U.PORTO

FEUP FACULDADE DE ENGENHARIA UNIVERSIDADE DO PORTO

STRENGTHENING OF REINFORCED CONCRETE ELEMENTS WITH UHPFRC

AURÉLIO GUILHERME SINE

A dissertation presented to the Faculty of Engineering of the University of Porto for the degree of Doctor in Civil Engineering - Structures

Adviser: Doctor Mário Jorge de Seixas Pimentel
Co-Advisers: Doctor Sandra da Conceição Barbosa Nunes
Doctor Américo Ocua Dimande

FUNDAÇÃO CALOUSTE GULBENKIAN

LEM LABORATÓRIO DE ENGENHARIA DE MOÇAMBIQUE

COMPETE 2020

PORTUGAL 2020

UNIÃO EUROPEIA Fundo Europeu de Desenvolvimento Regional

FCT Fundação para a Ciência e a Tecnologia

APRIL 2021

Intentionally blank

U.PORTO

FEUP FACULDADE DE ENGENHARIA
UNIVERSIDADE DO PORTO

STRENGTHENING OF REINFORCED CONCRETE ELEMENTS WITH UHPFRC

AURÉLIO GUILHERME SINE

A dissertation presented to the Faculty of Engineering of the University of Porto for the degree of Doctor in Civil Engineering - Structures

Grant: FUNDAÇÃO CALOUSTE GULBENKIAN

Support: LABORATÓRIO DE ENGENHARIA DE MOÇAMBIQUE

Funding:

- project UHPGRADE (PTDC/ECI-EST/31777/2017) financed by FEDER through COMPETE2020-POCI and by national funds through FCT/MCTES (PIDDAC)
- project HiperSlab (PTDC/ECI-EST/30511/2017) funded by national funds through FCT/MCTES (PIDDAC)
- Base (UIDB/04708/2020) and Programmatic (UIDP/04708/2020) funding of CONSTRUCT financed by national funds through the FCT/MCTES (PIDDAC)

APRIL 2021

Intentionally blank

Jury Members

Humberto Salazar Amorim Varum (Head of the jury)
Full Professor at Faculty of Engineering of University of Porto (FEUP), Portugal

Eugen Brühwiler
Full Professor at École Polytechnique Fédérale de Lausanne (EPFL), Switzerland

António Manuel Pinho Ramos
Associate Professor at School of Science and Technology of NOVA University of Lisbon (FCT-UNL), Portugal

Vítor Manuel do Couto Fernandes da Cunha
Assistant Professor at School of Engineering of University of Minho (EEUM), Portugal

Rui Manuel Carvalho Marques de Faria
Full Professor at Faculty of Engineering of University of Porto (FEUP), Portugal

Mário Jorge de Seixas Pimentel (Adviser)
Assistant Professor at Faculty of Engineering of University of Porto (FEUP), Portugal

Intentionally blank

Aos meus pais, Feliciano e Aurélia,

e irmãos, Hélder, Felício, Sofia e Jiquina.

Intentionally blank

"*It always seems impossible,*

until it's done."

- Nelson Mandela (1918-2013)

Intentionally blank

Acknowledgements *"Agradecimentos"*

Gostaria de expressar, em primeiro lugar, o meu apreço às pessoas e instituições, que sem o seu apoio esta jornada seria impossível de concretizar.

Aos Professores Mário Pimentel e Sandra Nunes pelo apoio académico e pessoal incondicional e pela disponibilidade e ensinamentos transmitidos. Igualmente, pelo afeto e amizade. Pelas discussões e dedicação contínua na orientação do trabalho.

Ao Dr. Américo Dimande, que marcou profundamente o meu percurso académico e profissional. Pela sua mentoria, suas lições e conselhos valiosos.

Ao Professor Joaquim Figueiras, que no início da minha chegada a Portugal me direcionou e pela atenção dispensada.

Ao Laboratório de Engenharia de Moçambique, Instituto Público (LEM, IP), principalmente ao Diretor Geral, o dr. Henrique Filimone, pela confiança e disponibilização dos meios necessários do LEM, IP para que fosse possível a minha deslocação a Portugal para esta formação.

Ao Serviço de Bolsas da Fundação Calouste Gulbenkian, especialmente à Dra. Margarida Abecassis e à Dra. Margarida Cunha, pela assistência prestada no processo da atribuição da bolsa que tornou possível a concretização dos meus estudos em pós-graduação.

Ao CONSTRUCT-LABEST, liderado pelo Professor Rui Faria, pelos meios técnicos disponibilizados e oportunidades criadas para a participação em conferências, formações e sobretudo para a realização de ensaios laboratoriais. Agradeço, igualmente, pela oportunidade concedida de integrar as equipas dos projetos de investigação BETOFIBRA, UHPGRADE e HiperSlab.

Às empresas LimpaCanal, pelo excelente trabalho de hidrodemolição prestado e a Gabriel Couto, particularmente ao Eng.º José Pedro, por se oferecerem a produzir as lajes que serviram para os estudos realizados no âmbito deste programa.

À Eng.ª Paula Silva e Cláudio Ferraz, pela amizade, entrega e paciência. O resultado deste trabalho deve-se muito ao vosso empenho. Igualmente, a minha estima estende-se à colaboração do Sr. Guilherme e Nuno Pinto.

Ao Dr. Amin Abrishambaf, pela prontidão sempre demonstrada, sempre bem disposto para esclarecer as minhas dúvidas.

Aos valiosos amigos internacionais que fiz na FEUP, especialmente "Tia" Tuba Tatar, Despoina Skoulidou, Ana Mafalda Matos, Araliya Mosleh, Gemma Rojo, Nathália Rabelo, JianJian Mou, Cilísia Ornelas, Arsénio Mindu, Rui Valente, entre outros, por tornarem a minha estadia no Porto memorável.

À ti Cristalina, minha querida "mon chéri", à nossa entreajuda e por teres sido o meu maior suporte quando mais precisei, principalmente durante a fase final deste processo.

À minha família pelo vosso apoio moral e amor incondicional, que essencialmente me manteve firme durante as fases difíceis.

À Zaquia, ambos sabemos o quanto esta busca nos custou. O teu apoio incondicional, mesmo diante das privações foi inestimável.

Aos meus amigos PANDAS, que mesmo distantes me acompanharam nesta caminhada.

À todos que por lapso não foram aqui citados, mas cujo contributo direta ou indiretamente impactou positivamente este processo, endereço a minha profunda gratidão.

Abstract

The present work addresses the structural behaviour of reinforced concrete (RC) beams and slabs strengthened with a thin layer of ultra-high performance fibre-reinforced cementitious composites (UHPFRC) over the top surface. This layer can either be plain (U) or reinforced with steel bars (RU), originating composite RC-U or RC-RU elements. This study is particularly relevant in the context of rehabilitation and strengthening of existing RC structures.

When no steel bars are used, the tensile behaviour of thin UHPFRC elements depends on the fibre content and orientation. These can be assessed using a non-destructive test (NDT) method based on the magnetic properties of the fibres. A mathematical description of the fibre orientation is developed and used together with a physical model of the composite supporting the methodology for determining the fibre volumetric fraction and the anisometric fibre orientation factor from the NDT measurements. An extensive experimental campaign is developed to validate the method and quantify the influence on the fibre content estimates of the element thickness, surface finishing, fibre settlement, and boundary effects. The method is also used to estimate the anisotropic post-cracking tensile strength of the UHPFRC, showing good agreement with the results of mechanical tests.

The behaviour of composite RC-(R)U beams and slabs are studied under flexural, one-way shear and punching shear actions. Three extensive experimental campaigns on slabs strips, beams and flat slabs were developed. The experimental data supported the validation of theoretical models that can be used for assessing the flexural behaviour of RC-(R)U composite cross-sections up to peak strength, the one-way shear strength of RC-(R)U beams and slabs without shear reinforcement and the punching shear strength of RU-(R)U flat slabs.

Key-words: Ultra-High Performance Fibre-Reinforced cementitious Composites (UHPFRC), reinforced concrete, fibre content and anisometry, tensile strength, NDT method, strengthening, beams, flat slabs, flexure, shear, punching shear

Resumo

O presente trabalho aborda o comportamento estrutural de vigas e lajes de betão armado reforçadas com uma camada fina de compósitos cimentícios de ultraelevado desempenho reforçados com fibras (*UHPFRC* sigla em inglês) sobre a superfície superior. Esta camada pode ser simples ou reforçada com armaduras de aço, originando elementos compostos. Este estudo é particularmente relevante no contexto da reabilitação e reforço de estruturas existentes de betão armado.

Quando não são utilizadas armaduras, o comportamento à tração dos elementos finos de *UHPFRC* depende do conteúdo e da orientação das fibras. Estes podem ser avaliados por meio de um método de ensaio não-destrutivo baseado nas propriedades magnéticas das fibras de aço. Uma descrição matemática da orientação das fibras é desenvolvida e utilizada juntamente com um modelo físico do compósito que suporta a metodologia para determinar a fração volumétrica e o fator de orientação das fibras a partir das medições pelo método não-destrutivo. É desenvolvida uma extensa campanha experimental para validar o método, bem como para quantificar a influência nas estimativas do conteúdo de fibras da espessura do elemento, do acabamento superficial, da segregação das fibras e dos efeitos de bordo. O método é também utilizado para estimar a resistência à tração anisotrópica pós-fracturação do elemento de *UHPFRC*, mostrando uma boa concordância com os resultados dos ensaios mecânicos.

O comportamento de vigas e lajes compostas é estudado sob ações de flexão, corte unidirecional e de punçoamento. Foram desenvolvidas três extensas campanhas experimentais sobre faixas de lajes, vigas e lajes fungiformes. Os dados experimentais sustentaram a validação de modelos teóricos que podem ser utilizados para avaliar o comportamento de flexão de secções compostas até à resistência de pico, a resistência ao corte unidirecional de vigas e lajes sem armaduras transversais e a resistência ao punçoamento de lajes fungiformes.

Palavras-Chave: Compósitos cimentícios de ultraelevado desempenho reforçados com fibras (*UHPFRC)*, betão armado, conteúdo e anisometria de fibras, resistência à tração, método não-destrutivo, reforço, vigas, lajes fungiformes, flexão, corte, punçoamento.

List of Contents

List of Figures

List of Tables

Notation and Symbols

ABBREVIATIONS

1D	One-Dimensional
2D	Two-Dimensional
3D	Three-Dimensional
ADM	Advanced Cementitious Materials
CSCT	Critical Shear Crack Theory
CFC	Composite Failure Criterion
DEWST	Double-Edge Wedge Splitting Test
EC	EuroCode
fib	The International Federation of Structural Concrete
FE	Finite Element
FEA	Finite Element Analysis
FPBT	Four-Point Bending Test
FRC	Fibre Reinforced Cementitious Composites
FRP	Fibre Reinforced Polymer
LoA	Level-of-Approximation
LVDT	Linear Variable Differential Transducer
MC	Model Code
NDT	Non-Destructive Test
NIC	Near Interface Crack
NLFEA	Nonlinear Finite Element Analysis
NSC	Normal Strength Concrete
RC	Reinforced Concrete
RC-U	RC substrate strengthened with plain UHPFRC layer
RC-RU	RC substrate strengthened with RU layer
RC-(R)U	RC substrate strengthened with plain UHPFRC or RU layer
RPC	Reactive Powder Concrete
RU	Reinforced UHPFRC

SLS	Service Limit State
SPM	Sand Patch test Method
UHPC	Ultra-High Performance Cementitious Composites
UHPFRC	Ultra-High Performance Fibre Reinforced Cementitious Composites
ULS	Ultimate Limit State
UTT	Uniaxial Tensile Test
TPBT	Three-Point Bending Test

SUBSCRIPTS/ SUPERSCRIPTS

Exp	experimental
R	resistance
Rc	RC substrate resistance
Simp	Simplified
U	UHPFRC
Uc	UHPFRC compressive strength
Ute	UHPFRC elastic tensile property
Utu	UHPFRC pos-cracking tensile property
c	concrete
cm	concrete average compressive strength
crit	critical
ct	concrete tensile strength
eq	equivalent
f	fibre
flex	flexural
i	steel or UHPFRC tensile reinforcement
pred	predicted
pc	Post-critical
ref	reference
s	steel
sU	steel tensile reinforcement in the UHPFRC
sc	steel tensile reinforcement in the concrete substrate
sy	yielding of steel

LATIN UPPER CASE

A	Area
B	The side length of the isolated square slab specimen
EI	Flexural stiffness
E	Young's modulus (of elasticity)
E	East
F	Load
G_c	Compressive fracture energy
G_F	Tensile fracture energy
I	The second moment of area
L	Inductance
L	Span
M	Bending moment
m	Unit bending moment
N	Number of turns in the coil
N	North
N_f	Number of fibres crossing a surface
R_t	Average texture depth
S	South
UHPFRC	Ultra-High Performance Fibre Reinforced Cementitious Composites
V	Shear force
V_f	Fibre content
V_{flex}	Flexural resistance
W	West
W	Work of external forces

LATIN LOWER CASE

a	shear span
a_0	Free distance between the loading and supporting plates
b	beam width
b_0	critical control perimeter for punching shear set at $d_{sc}/2$ from the column face
C	the side length of the column
d_f	Fibre diameter
d	Effective depth
e	Eccentricity
f	The probability density function of fibres crossing a surface
f	Tensile resistance
h	height
h_c	concrete substrate height
h_U	UHPFRC layer thickness
k_e	Coefficient of eccentricity
k_α	The slope of the regression line of the relation between the fibre orientation factor and fibre orientation indicator
k_g	Parameter of the sharpness of fibre distribution
k_v	The slope of the regression line of the relation between the fibre content and fibre content indicator
l	Lenght
l_f	Fibre length
n_f	Number of fibres per unit area
p	Unit vector collinear with the fibre
r	Radius
r_c	The radius of the circular column
r_q	Contraflexure radius
r_s	The radius of the circular slab
x	Compression depth
w	Crack opening

GREEK LOWER CASE

α_0	Fibre orientation factor
α_1	Fibre efficiency factor
α_c	Critical shear crack angle
β	Orientation of a cracking plane/axis
β_0	Fibres preferential orientation
γ	Fibres discontinuity parameter
δ	Deflection
ε	Strain
η_θ	Fibre orientation number
θ	The polar fibre orientation angle
κ	Curvature
λ	Fibre structure parameter
μ	The magnetic permeability of a material
μ_r	Relative magnetic permeability
$\mu_{r,mean}$	Mean relative magnetic permeability
ν	Normalized shear resistance
ξ_{seg}	Degree of fibres segregation
ρ_{ij}	Fibre orientation indicator
ρ	Reinforcement ratio
σ	Stress
τ_f	Fibre-to-matrix bond stress
φ	Azimuthal fibre orientation angle
χ_f	Workability parameter
ψ	The probability density function of fibre orientation
ψ	Rotation
Ψ	Fibre orientation distribution

1. Introduction

1.1. MOTIVATION

> "*Strengthening is an intervention made to increase the strength* (*load resistance/capacity*) *and/or possible the stiffness of a structure or its components, and/or to improve overall structural stability and/or the overall robustness of the structure to a performance level above that adopted by the designer* (fib 2012a)."

The built heritage is one of the wealth indicators of a country and constitutes identity symbols of historical, sociocultural, or architectural value. Independent of the material made upon, any structure is subjected to natural ageing and/or external environmental conditions that lead to degradation and, consequently, threaten its conservation. The preservation of a structure includes maintenance, reparation, rehabilitation and strengthening, or worst-case scenario, substitution, which are generally associated with large investments.

The construction industry is an important economic sector. However, in the last decades, the rehabilitation and/or strengthening of existing structures is growing significantly to the detriment of new constructions. Sustainable structures are those designed for long service life with minimum preservation interventions in the meantime (Brühwiler and Denarié 2013). This is in line with 3 of the 17 United Nations (UN) Sustainable Development Goals (SDG): goal 9-Industry, innovation and infrastructure; goal 11-Sustainable cities and communities; and goal 12-Responsible consumption and production (UN 2015).

Compared to other solutions and materials, the reinforced concrete (RC) structures dominate the construction industry thanks to the equilibrium between performance and cost.

Global warming has become a worldwide concern as its effects started taking place in our time due to CO_2 emission into the atmosphere, being concrete/cement usage one of the main contributors. As stated by Matthews (2021), "*a reduction in the future carbon footprint of construction could be achieved by repurposing* [and renovating] *existing buildings, rather than* [by demolishing and] *building new ones*. *Re-use/adaptation of existing buildings and other constructed assets offers a potentially sustainable way to extend their useful life*".

Nowadays, with the increasing population growth, tourism, or transportation, just to cite a few, the existing structures are subjected to service conditions beyond those expected on their original design. Besides that, even in new structures, construction and designing errors are frequently reported as the reason for bad structural performance and accidents, including human loss (Lew et al. 1982; Gardner, Huh, and Chung 2002; Wood 2003; King and Delatte 2004; H. D. P. Fernandes 2019; Rocha 2012; Nhumaio 2015).

The fast technological and scientific development cause continuous updates and revisions of the structural code provisions, not only for a new design but also for the existing concrete structures, for instance, the future *fib* Model Code for Concrete Structures 2020 (MC2020) (Matthews 2021).

The jacketing with RC, or the addition of an RC layer, is one of the most common strengthening techniques of existing RC structures. Other strengthening techniques involve the fixation of metallic plates or fibre-reinforced polymers (FRP), and external post-tensioning (Koppitz, Kenel, and Keller 2013; Lapi, Ramos, and Orlando 2019; D. M. V. Faria et al. 2014), among others. A more recent technology consists of adding a new layer of ultra-high-performance fibre-reinforced cementitious composites (UHPFRC) (SAMARIS D22 2005; Brühwiler and Denarié 2013; Denarié et al. 2013). This technique is being consistently developed in the last two decades, mainly at the École Polytechnique Fédérale de Lausanne (EPFL) (Habel 2004; Wuest 2007; Redaelli 2009; Oesterlee 2010; Noshiravani 2012; Bastien-Masse 2015) and is selected as the scope of the present thesis.

The performance of the RC structures strengthened with a new RC layer is continuously affected by time, being necessary periodic interventions during the structure service life. Whereas with the addition of a new UHPFRC thin layer, the long-term performance is

expected to improve and the eventual interventions reduced to a minimum (Habel 2004; Denarié and Brühwiler 2006), as illustrated in Figure 1, where the performance of both strengthening techniques on an RC structure during its service life are compared.

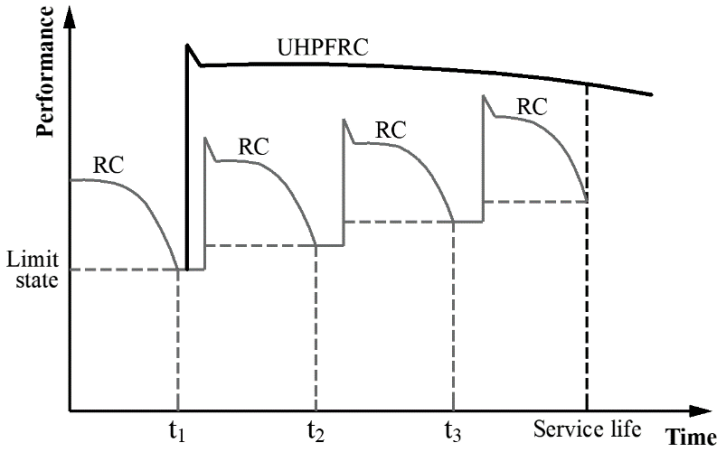

Figure 1. Conceptual illustration of performance enhancement of an RC existing member with normal strength concrete and UHPFRC (SAMARIS D22 2005).

The election of the UHPFRC as a structural strengthening material lies upon its outstanding mechanical strength and durability properties. Therefore, the concept is to use this advanced material only in the zones of a structure where the UHPFRC properties are fully exploited, like in structures exposed to severe environmental conditions and high mechanical loading (Brühwiler and Denarié 2013).

Adding a 30 to 50 mm thick UHPFRC layer to an RC element presents competitive costs, as it minimizes the additional self-weight to the existing structure relative to the RC strengthening technique. Its installation does not need intensive work, nor sophisticated equipment, besides that used for concrete, and the intervention time is even shorter (Habert et al. 2013; Haber et al. 2018). However, the UHPFRC is more expensive than concrete. Only the fibres represent 2/3 to 3/4 of the total cost of the material (Haber et al. 2018; Matos et al. 2019). Nevertheless, the overall cost of a UHPFRC strengthening intervention is competitive, in some cases representing construction cost savings of 30-40% (Brühwiler 2020) compared to competing alternatives.

1.2. BACKGROUND

1.2.1. Definition of UHPFRC

The Ultra-High Performance Fibre-Reinforced Cementitious Composites (UHPFRC) belong to the family of Advanced Cementitious Materials (ACM), particularly to the sub-group of Fibre Reinforced Cementitious Composites (FRC). Including the Normal Strength Concrete (NSC), they all belong to the Cementitious Materials.

The UHPFRC is essentially constituted by two phases, the cementitious matrix (UHPC) and steel fibres (Naaman 2008). The UHPC high-density matrix allows the material to be self-compacting in the fresh state and practically impermeable when hardened (Charron, Denarié, and Brühwiler 2007).

The original precepts for conceiving the UHPFRC, initially introduced as Reactive Powder Concrete (RPC), are basically: homogeneity – enhanced by removing the coarse aggregate; compacity – thanks to the optimization of the fine particles (e.g. sand, cement, limestone filler, silica fume, glass powder); and ductility – introduced by the short steel fibres (Richard and Cheyrezy 1995).

Typical UHPFRC compositions can be found elsewhere (Naaman and Wille 2012; Haber, De La Varga, and Graybeal 2018). Regarding the constituents, the differences between the UHPFRC and the NSC are on the volume of the paste phase, size and volume of the aggregate, and the fibres. Figure 2 presents the comparison of constituent proportions and their appearance in the hardened state.

The fibres must have high strength and superficial treatment to ensure a better bond with the matrix. Although the shape may vary from straight, twisted or hooked (Park et al. 2012; Naaman 2008; Wille and Naaman 2010), straight, smooth steel fibres are generally adopted. The fibres are characterized by its length, l_f, and diameter, d_f, varying from 6 to 13 mm and 0.15 to 0.33 mm, respectively, or according to the aspect ratio l_f/d_f from 40 to 100 (Trüb 2011; Haber, De La Varga, and Graybeal 2018; Park et al. 2012; Nunes, Pimentel, and Carvalho 2016a).

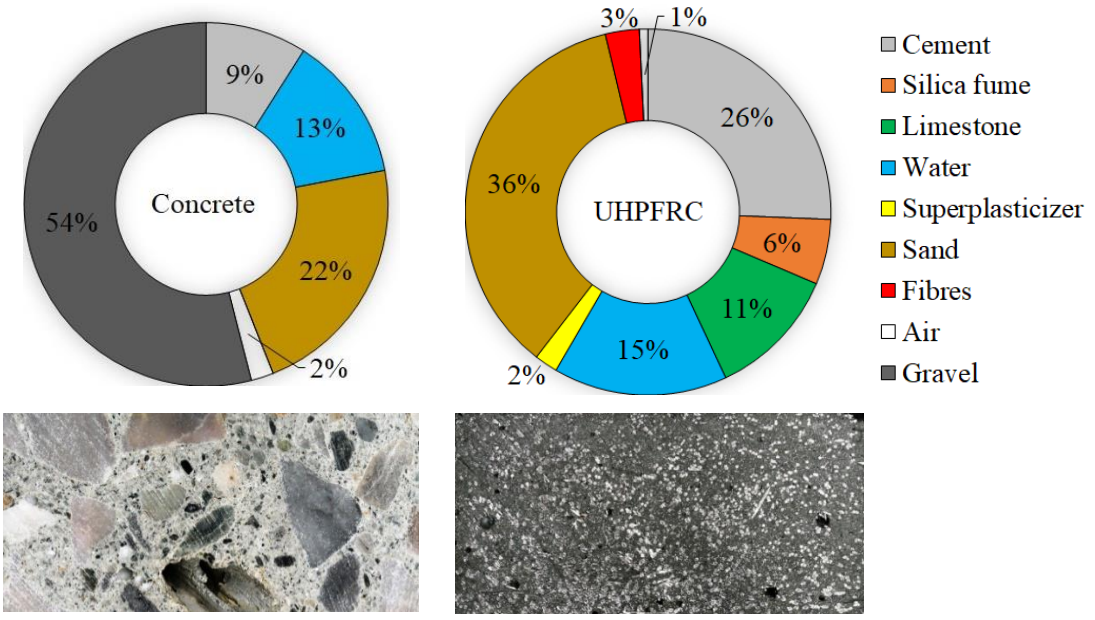

(a) (b)

Figure 2. Example of constituent proportions and appearance (Brühwiler 2017) of (a) Concrete and (b) UHPFRC.

Whenever hybrid fibre cocktails are used, containing fibres of different sizes, larger dimensions (l_f/d_f=30/0.3, for instance) are considered (Markovic 2006; Nguyen et al. 2013; Kwon et al. 2014; Park et al. 2012; Haber, De La Varga, and Graybeal 2018). The fibre content is expressed through mass per unit volume (kg/m^3) or according to the volume fraction in the mixture, V_f. Common fibre contents go up to V_f =3% (Richard and Cheyrezy 1995; Oesterlee 2010; Habel 2004; Pimentel and Nunes 2016c; Meda, Mostosi, and Riva 2014; di Prisco, Ferrara, and Lamperti 2010; Haber, De La Varga, and Graybeal 2018). The increase of the fibre content affects the workability of the fresh mixture (Markovic 2006; Wille and Naaman 2010), which is a function of the parameter $\chi_f = V_f . l_f/d_f$. Significant workability losses were reported by (Nunes et al. 2012) for χ_f>2. A maximum of χ_f=2.5 was recommended by (Markovic 2006).

The compression strength varies from f_{Uc}=120 to 250 MPa, the Young's modulus is in the range E_U=45-65 GPa, and the Poisson coefficient is 0.2 (AFNOR 2016a; SIA 2016). The absence of fibres in the UHPC makes it highly fragile (Redaelli 2009; Wille, El-Tawil, and Naaman 2014; fib 2012a), being recommend a minimum of V_f=2% (AFGC 2013).

The tensile behaviour of the UHPFRC is decisive for many applications. It is not an intrinsic material property, as it is affected by extrinsic factors, such as the fibre orientation, the casting method, and the geometry of the element (Babut 1985; Stähli and van Mier 2007; Zhou and Uchida 2017a; Stähli, Custer, and van Mier 2008; Wuest 2007; Ferrara and Meda 2007; Abrishambaf, Barros, and Cunha 2013; Laranjeira et al. 2012). Three types of tensile constitutive laws can be achieved: strain-softening, low strain-hardening, and large strain-hardening behaviour (AFGC 2013; Abrishambaf, Pimentel, and Nunes 2019).

The direct tensile behaviour of a strain-hardening UHPFRC is schematized in Figure 3. It is characterized by an elastic phase up to f_{Ute}, at which the microcracking of the matrix develops. Then the hardening branch may be observed, depending on the fibre content, orientation and fibre-to-matrix bond. In this stage, multiple microcracks are formed until the post cracking tensile strength, f_{Utu}, is reached. This marks the onset of the softening stage accompanied by the localization of the deformations in a macroscopic crack. During this stage, the fibres continuously pull-out from the matrix until the full stress release. Typical values of f_{Utu} are in the range 5 to 15 MPa, although values exceeding 20 MPa have been reported (Naaman and Wille 2012).

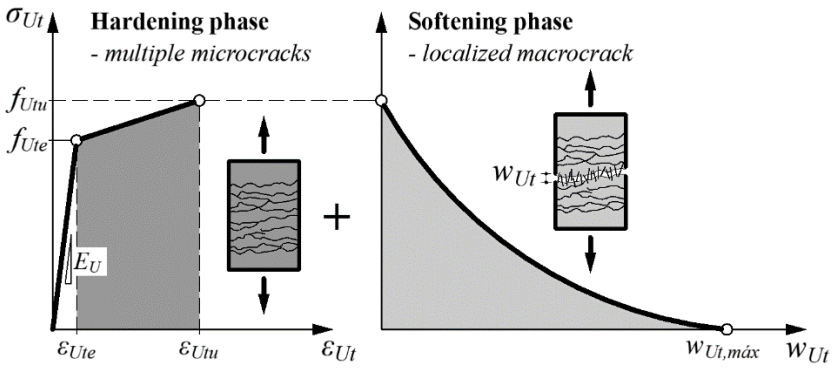

Figure 3. UHPFRC constitutive law with hardening under uniaxial tension.

The tensile response of the UHPFRC is directly related to its durability performance. For strains up to ε_{Ut}=0.15%, the material has the self-healing ability when exposed to water. At these strain levels, the UHPFRC permeability is even smaller than the non-cracked NSC (Charron, Denarié, and Brühwiler 2008; 2007; Matos, Nunes, and Aguiar 2019).

1.2.2. Concept

In the context of rehabilitation and strengthening of existing RC structures, the easiest way to cast a UHPFRC layer is directly over the top surface. This allows significant flexural strengthening ratios in the hogging moment region, exemplified in Figure 4 for structures submitted to combined bending and shear. However, the same technique must also ensure substantial shear strength and punching shear strength enhancements, besides increasing the flexural strength.

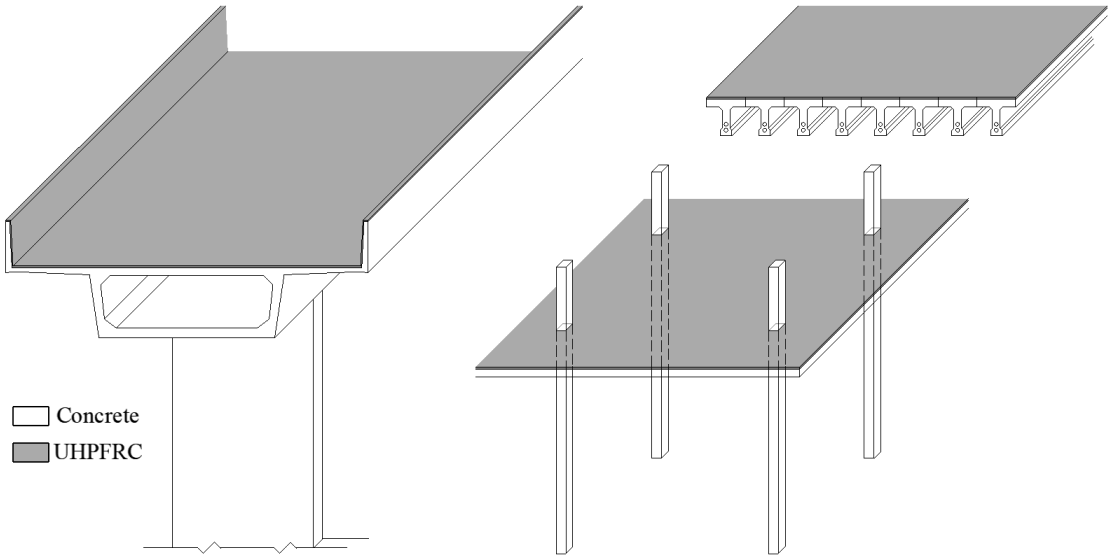

Figure 4. Structures submitted to combined bending and shear: (a) cantilever on a box girder bridge; and (c) flat slabs on columns (Bastien-Masse and Brühwiler 2016b).

The use of a thin layer of UHPFRC as tensile reinforcement has been conceptualized by (Habel 2004; Brühwiler and Denarié 2013). A plain UHPFRC layer of only 10 to 30 mm can be used to provide protection (configuration P: RC-U). Small diameter reinforcement bars with minimum cover can be added when significant strengthening is required (configurations R: RC-RU or PR: C-RU) (Figure 5).

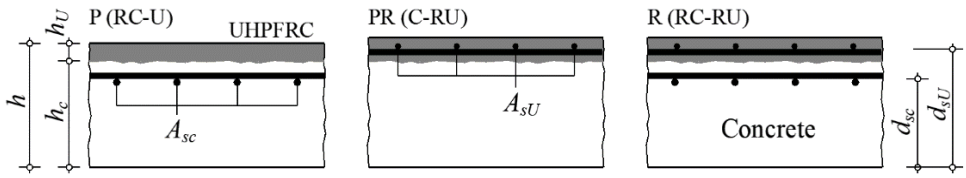

Figure 5. Conceptual idea basic configurations (Habel 2004).

For configurations R and PR, the cover and the distance to the substrate interface should not be smaller than 10 mm or the rebar diameter, whatever is larger, for sufficient stress

transmission between the new reinforced UHPFRC (RU) tension chord and the existing concrete substrate. Furthermore, the bond between both cementitious materials is achieved only by roughening the substrate, in which case mechanical connectors can be neglected (Habel 2004; Bastien-Masse 2015; Youm and Hong 2018; Pimentel and Nunes 2016c; Haber et al. 2018; Noshiravani 2012).

1.2.3. Practical applications

The UHPFRC is being used to cast architectural elements, such as façade panels, due to the possibility of materializing complex geometries elements. The structural applications in new construction are used in landmark structures with remarkably slender shapes (AFGC 2013). The more rational use of the material involves composite structures, where the UHPFRC is employed in zones where a high concentration of forces or cyclic effects are expected (Haber, De La Varga, and Graybeal 2018; Perry and Mathew 2010; Perry and Seibert 2013). The first UHPFRC structure, belonging to the RPC type was a pedestrian bridge in Sherbrooke (Quebec, Canada) built in 1997, having a 60 m span, made of six prefabricated segments (Blais and Couture 1999).

Regarding rehabilitation (and widening) of existing structures, the first application of the UHPFRC ($CEMTEC_{multiscale}^{®}$) cast *in situ* was in 2004 in a 10 m span bridge, originally built in the 1940s (SAMARIS D22 2005; Denarié and Brühwiler 2006).

Worldwide, France, Switzerland, Canada and the USA are the countries with more applications of the UHPFRC, mainly on bridges (AFGC 2013; Brühwiler and Denarié 2013; Perry and Seibert 2013; Haber et al. 2018), followed by South Korea, Malaysia, Japan, Germany, Czech Republic and China (B. Graybeal et al. 2020).

Figure 6 presents 247 structural applications of the UHPFRC in Switzerland, growing since 2003, distributed according to the type of structure in the map of Figure 6(a), and kind of intervention in Figure 6(b), where the majority refers to the usage as a protective layer, followed by strengthening (MCS-EPFL 2021). In addition, a map from the USA can be seen elsewhere (B. Graybeal et al. 2020; FHWA 2021).

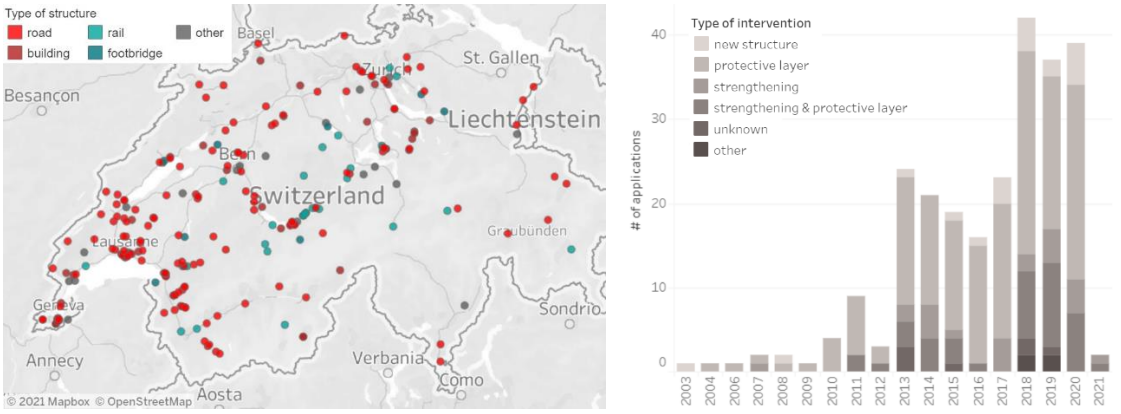

(a) (b)

Figure 6. Structural application of UHPFRC in Switzerland: (a) distribution map per structure type and (b) the number of interventions per type (MCS-EPFL 2021).

1.2.4. National recommendations and norms

In 2000 were presented in Australia the guidelines for designing prestressed beams made by DUCTAL® (Gowripalan and Gilbert 2000) compatible with the ultimate limit state philosophy of concrete structures of the norm AS3600-1994.

The joint workgroup formed by the French Association of Civil Engineering (AFGC) and the Department of Studies on Transport, Roads and Maintenance (SÉTRA) produced the temporary recommendations (AFGC 2002), aiming to create a reference document for using the UHPFRC in civil engineering applications. A decade later, a new version was issued (AFGC 2013), having as the primary goal the compatibility with the Eurocodes. These recommendations paved the way for elaborating the French norms NF P 18-470:2016-Concrete-UHPFRC-Specifications, performance, production and conformity (AFNOR 2016b), 18-710:2016-National addition to Eurocode 2-Design of concrete structures: specific rules for UHPFRC (AFNOR 2016c) and 18-451-Concrete-Execution of concrete structures-particular rules for UHPFRC (under public inquiry to date).

In Japan, the recommendations for designing and construction with the HPFRCs were introduced in 2008 (JSCE 2008).

The project norm prSIA 2052:2014-04 (SIA 2014) was submitted for public consultation and gave birth to the Swiss norm SIA 2052:2016 UHPFRC–Materials, Designing and Execution (SIA 2016).

In North America, more specifically in the USA and Canada, working groups were created in 2015 and 2016, respectively, for producing technical recommendations regarding the use of the UHPFRC. In the USA, the ASTM C1856 establishes the standard practice for fabricating and testing specimens of UHPFRC. In addition, the American Concrete Institute (ACI) committee 239C is responsible for elaborating the norm on the "structural design of UHPFRC" (Perry, White, and Ahlborn 2016). In Canada, two working groups were created under committee A23.1. The first deals with materials and methods standards for UHPFRC, and the second deals with the structural design guideline for bridges for tension softening and hardening FRCs (Perry and Habel 2017).

The worldwide efforts that have been made concerning the production of the national technical recommendations and norms related to the structural application of the UHPFRC represent, on the one hand, the potential of this material, and on the other hand, the attempt to raise awareness and provide design-like provisions to designers.

Almost all the documents available to date focus only on UHPFRC to design new structures. However, the Swiss norm (SIA 2016) includes provisions regarding the RC-UHPFRC composite structures, compatible with rehabilitation and strengthening of existing RC structures.

In the *fib* Model Code 2010 (MC2010), there is a section dedicated to FRC. In 2015 the MC2020 Core Group was formed. It was established that the new code would deal with both new and existing concrete structures, where materials, including the UHPFRC and associated technologies for the protection, repair, rehabilitation and enhancement of the current condition/performance, are considered as "*fertile areas of technological advance*" (fib 2021).

1.3. OBJECTIVES

This thesis presents significant experimental content, ranging from the material mechanical characterization of plain UHPFRC thin elements to structural tests of RC members (beams and slabs) strengthened with a UHPFRC layer, with or without steel reinforcement. This allowed fulfilling the following specific objectives:

a) To describe the "in-structure" anisotropic tensile behaviour of UHPFRC thin layers based on an NDT method. This is particularly relevant for elements without rebars, which are on the tensile response of the UHPFRC. As previously discussed, the latter depends on the local fibre content and orientation, which may vary throughout the structure depending on the material's rheology, casting procedures, and element shape.

b) To evaluate the flexural behaviour of RC-(R)U composite beams and describe corresponding moment-curvature relation through an analytical model suited for engineering practice.

c) To evaluate the one-way shear behaviour of composite RC-(R)U slabs and beams without shear reinforcement and validate analytical models for determining the corresponding shear strength. In addition, provide experimental data for evaluating the size-effect and the influences of the longitudinal reinforcement content in the RC substrate and the UHPFRC layer, the thickness of the UHPFRC layer and the location of the UHPFRC layer (tension or compression side).

d) To evaluate the punching shear behaviour of RC-(R)U composite flat slabs and calculate the corresponding punching shear strength through suitable numerical and analytical methods. In addition, provide experimental data for evaluating the influence of essential variables that affect the contribution of the UHPFRC for the punching shear strength of the composite slabs, namely the reinforcement ratio in the existing concrete substrate, the reinforcement in the strengthening layer, the shape of the column and the eccentricity of the force.

1.4. ORGANIZATION

The illustration of the intertwining between chapters in Figure 7 is relevant for establishing their links.

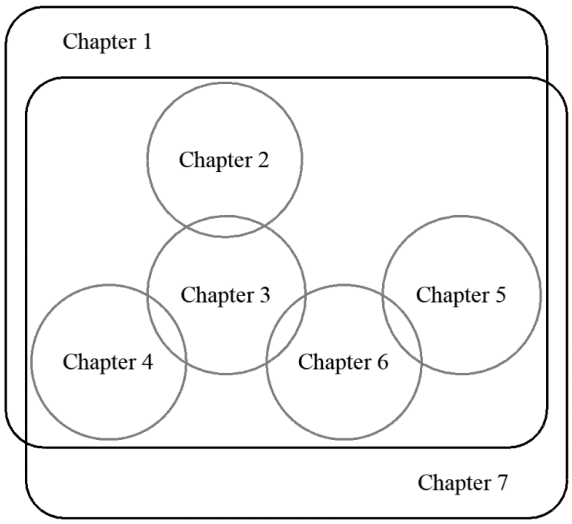

Figure 7. The connection between chapters.

Chapter 1 refers to the introduction. It encompasses the most relevant aspects of applying the UHPFRC as a strengthening layer for RC existing elements. Including a short literature review, the motivation and objectives that outline the thesis.

Chapter 2 deals with the non-destructive test method for evaluating the fibre content and anisometry in thin UHPFRC elements. The method allows the estimation of the anisotropic post-cracking tensile strength of the material and can be used in the scope of quality control procedures.

Chapter 3 describes the flexural behaviour of composite RC-(R)U beams or slabs using simplified analytical and layered numerical models and validated by experimental tests.

Chapter 4 presents an extensive experimental investigation on the shear behaviour of composite RC-(R)U beams. A methodology is proposed to determine the shear force corresponding to the instant when the critical shear crack forms and the beams can no longer be considered a monolithic element. In some cases, this event is shown to correspond to the shear failure. However, significant shear strength is generally available after the propagation of the diagonal crack, for which the accuracy of an existing model is evaluated.

Chapter 5 presents the experimental campaign on RC-(R)U composite flat slabs failing in punching shear, including one reference slab and a slab strengthened with an RC layer. An existing methodology for determining the punching shear strength is evaluated based on the intersection of the force-rotation curve with a composite failure criterion.

In Chapter 6, the results from chapter 5 and others from the literature validate a punching shear strength calculation method. A Nonlinear Finite Element Analysis (NLFEA) model using layered curved shell elements is adopted to determine the force-displacement and force rotations curves. The punching shear strength is determined as the intersection of the latter with suitable failure criteria. Finally, the validation is extended to a simplified analytical approach suited for design practice, and a parametric study is undertaken.

2. Fibre Content and Anisometry in UHPFRC Thin Layers

2.1. INTRODUCTION

The high mechanical resistance and the high unit cost of the material make it suitable for materializing thin structural elements, such as slender bridge deck slabs or beams with thin webs (Blais and Couture 1999; Lopez et al. 2016; Kolisko et al. 2017). UHPFRC can be prestressed or reinforced with ordinary steel bars. In many structural concepts, the prestress strands (or the reinforcement bars) are placed on longitudinal and/or transversal ribs, delimiting thin (40 to 60 mm thick) panels of unreinforced UHPFRC. The strengthening and rehabilitation of existing reinforced concrete (RC) structures through application of thin (generally 30 to 60 mm thick) layers of UHPFRC (Habel, Denarié, and Brühwiler 2006; Brühwiler and Denarié 2013; Denarié et al. 2013) constitutes another relevant field of application, especially when subjected to severe environmental exposure conditions (Figure 4). When the objective is waterproofing and protecting the existing RC substrate, unreinforced UHPFRC layers can be used. However, when significant strengthening is pursued, it is advantageous to incorporate small diameter reinforcement bars.

The tensile response of the UHPFRC schematically represented in Figure 3 is critical for the performance of the thin unreinforced UHPFRC elements. In general, the composite remains crack-free until the limit of elasticity in tension (f_{Ute}) is reached. Then, depending on the fibre content and orientation, a strain hardening phase may be achieved characterized by the formation of a stable microcrack pattern, with crack widths bellow 50 μm (Kang and Kim 2011; Bastien-Masse, Denarié, and Brühwiler 2016; Abrishambaf, Pimentel, and Nunes 2017; Duque and Graybeal 2017). When the post-cracking tensile strength (f_{Utu}) is reached, the deformations localize in a macrocrack that can still carry significant residual tensile stresses until the full stress release. This behaviour is thoroughly discussed elsewhere (Wuest 2007; Abrishambaf, Pimentel, and Nunes 2019). The post-cracking tensile strength along the *i*-direction, $f_{Utu,i}$, can be determined using the Eq. (1) first proposed by Naaman (1972; 2008):

$$f_{Utu,i} = \tau_f \, \alpha_{0,i} \, \alpha_{1,i} V_f \, \frac{l_f}{d_f} = \tau_f . \lambda_i \tag{1}$$

where τ_f is a representative value of the fibre-to-matrix bond strength; $\alpha_{0,i}$ and $\alpha_{1,i}$ are the fibre orientation and efficiency factors, respectively; V_f is the volumetric fibre fraction, l_f and d_f are the length and diameter of the fibres. Thus, the fibre parameters related to orientation, efficiency, content and geometry can be lumped on the directionally dependent fibre structure parameter, λ_i. Eq. (1) was validated for UHPFRC with varying fibre content and orientation profiles (Nunes et al. 2017; Abrishambaf, Pimentel, and Nunes 2017; 2019).

The tensile constitutive law of UHPFRC can be directly obtained from the uniaxial (direct) tensile test (UTT) (Pyo, El-Tawil, and Naaman 2016; B. A. Graybeal and Baby 2013; Abrishambaf, Pimentel, and Nunes 2017), or from the four-point bending test (FPBT) using inverse analysis (Qian and Li 2007; Baby et al. 2012; 2013; López et al. 2015; AFGC 2013; AFNOR 2016b). The double-edge wedge-splitting test (DEWST) has also been shown to be a suitable test for the direct determination of the post-cracking tensile strength f_{Utu} (di Prisco, Ferrara, and Lamperti 2010; 2013; Pimentel and Nunes 2016d). Moreover, the distribution of the fibres in a UHPFRC element depends on the rheology of the composite in the fresh state and the casting procedure (Babut 1985; Stähli and van Mier 2007; Zhou and Uchida 2017a; Stähli, Custer, and van Mier 2008; Wuest 2007; Ferrara and Meda 2007; Abrishambaf, Barros, and Cunha 2013; Laranjeira et al. 2012). Usually, self-compacting mixtures are considered, potentially leading to flow-induced fibre orientation of the fibres (Ferrara, Ozyurt, and di Prisco 2011; L. Martinie and Roussel 2011; Deeb, Karihaloo, and Kulasegaram 2014) and the anisotropic tensile behaviour of the material (Stroeven and Hu 2006; Stroeven 1986; Nemati and Stroeven 2001; Stroeven 2009). The latter is the direct consequence of anisometric fibre distribution that can be described using stereological principles and geometric probability theory (Bastien-Masse, Denarié, and Brühwiler 2016; Aveston and Kelly 1973; Stroeven 2009). It is also known that mixes with excessive fluidity may lead to fibre sedimentation across the thickness of horizontally cast elements or towards the base of vertically cast panels. Moreover, uneven fibre distribution may occur whenever two casting fronts meet and are not conveniently disturbed, using, for instance a rake for promoting its intersection by the fibres, creating a weak discontinuity in the element which may govern

the behaviour (Pimentel and Nunes 2016b; Nunes, Pimentel, and Carvalho 2016b; Ferrara et al. 2017; Zhou and Uchida 2017b). All this makes the tensile response of the material in the structure to differ from that obtained with laboratory specimens. The use of test specimens cut from larger panels provides one way to assess these effects (Oesterlee 2010; Zhou and Uchida 2017b; Shen and Brühwiler 2020; Duque and Graybeal 2017; Abrishambaf, Barros, and Cunha 2013), but is both costly and time-consuming.

Suitable quality control methods providing reliable indicators of the "in-structure" fibre content and orientation are necessary to ensure that the envisaged structural performance is achieved. Non-destructive test (NDT) methods pursuing this objective have been developed based on measurements of the electric resistivity (Lataste, Behloul, and Breysse 2008; Sirieix et al. 2007; Barnett et al. 2010; Laetitia Martinie, Lataste, and Roussel 2015), AC-impedance spectroscopy (AC-CS) (Woo et al. 2005) and magnetic properties of the fibres (Ferrara, Faifer, and Toscani 2012; Ferrara et al. 2012; Faifer et al. 2013; Torrents et al. 2012; Cavalaro et al. 2016; Nunes, Pimentel, and Carvalho 2016a; Ferrara et al. 2017). In particular, the NDT methods based on the magnetic inductance measurements provided by U-shaped probes placed over the surface of thin UFPFRC elements have shown great potential (Ferrara, Faifer, and Toscani 2012; Ferrara et al. 2012; 2017; Nunes, Pimentel, and Carvalho 2016a) for field applications.

This work presents further developments on the NDT method proposed by Nunes et al. (2016a; 2017) and recently adopted by other researchers (Shen and Brühwiler 2020; Li et al. 2020), substantiating its use for the determination of the fibre content and orientation in thin UHPFRC elements and allowing the estimation of the directionally dependent "in structure" post-cracking tensile strength. The physical model of the magnetic circuit composed of a U-shaped probe and the composite initially proposed in Nunes et al. (2016a) is generalized. The relations between the fibre content and orientation indicators determined from two orthogonal magnetic inductance measurements and the volumetric fibre fraction and the fibre orientation factor, respectively, are derived considering probabilistic descriptions of the fibre orientation. A second-order tensor approximation of the composite's relative magnetic permeability is proposed to determine the in-plane fibre orientation factor along any direction based on any three non-collinear measurements. Experimental evidence is presented supporting the theoretical developments. The factors that may affect the measurements are experimentally

quantified, namely the thickness of the UHPFRC element, the distance of the probe to the edges, the segregation of fibres, and the roughness of the measuring surface. This Chapter concludes with an application example illustrating the relevance of the method.

2.2. DESCRIPTION OF THE FIBRE ORIENTATION

In the three-dimensional space (3D), a fibre can freely rotate according to the angles θ (polar) and φ (azimuthal), and all possible orientations describe the surface of a sphere (Figure 8 (a)). On the other hand, in the two-dimensional case (2D), the fibres are considered to lie on parallel planes, thus all possible orientations of a fibre describe a circumference (Figure 8 (b)) and are defined only by the angle, θ. However, the fibre rotation can be limited depending on the element thickness and the fibre position relative to its depth. For this reason, the fibre distribution on actual thin elements is not precisely represented in 2D or 3D distribution (Lu and Leung 2017; Dupont and Vandewalle 2005). In fact, it can be taken as a 3D distribution with truncated limits expressing the so-called "wall effects".

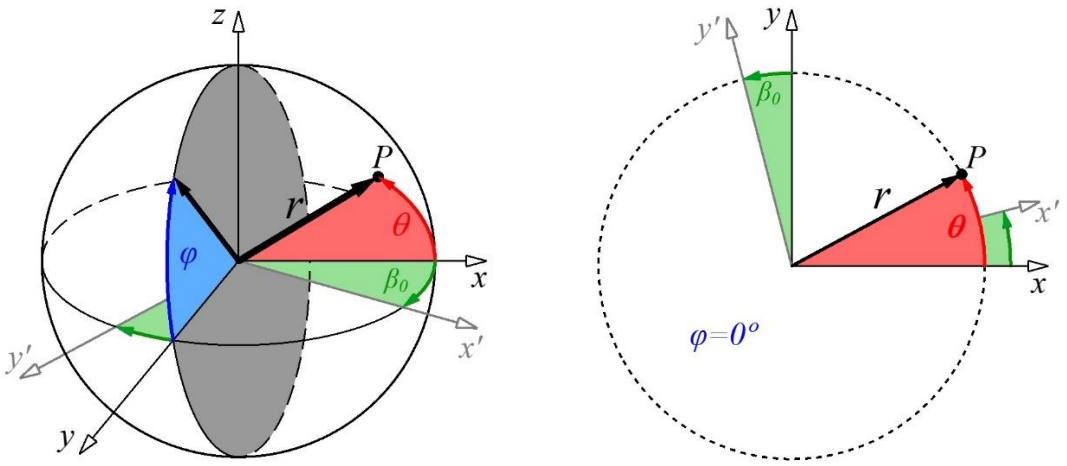

(a) (b)

Figure 8. Representation of fibre orientation in (a) 3D and (b) 2D.

According to French norm NF P18-710 (AFNOR 2016a), UHPFRC thin elements are considered those with a thickness not greater than three times the length of fibres, $h_U/l_f \leq 3$ (where l_f is the length of the longest fibres contributing to ensuring non-brittleness). In this work, it is considered that in these elements, the fibre orientation distribution varies

essentially in *xy*-plane, perpendicular to the element thickness (Figure 9). In particular, it is assumed that the direction of preferential fibre orientation is parallel to the *xy* plane.

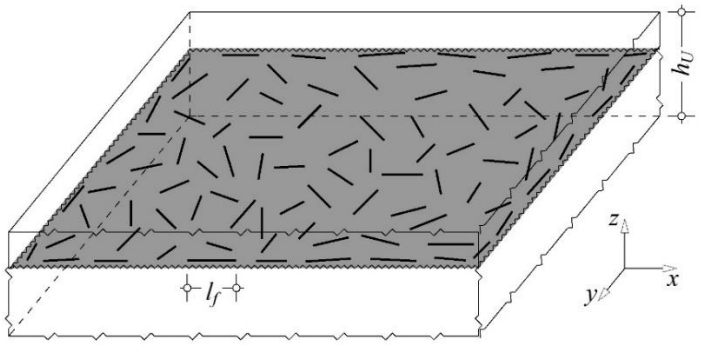

Figure 9. Fibre distribution in the xy-plane.

2.2.1. Probability density function

The fibre orientation state in 3D or 2D can be described using the probability density function, ψ. Some hypotheses have to be taken into account: the fibres are rigid cylinders, uniform in length and diameter, and are uniformly distributed in space or plane, i.e., the number of fibres per unit volume or area, respectively, is constant (Advani and Tucker 1987). The orientation of fibre in 3D can be described using a spherical coordinate system (Figure 8 (a)) or in a polar coordinate system in 2D (Figure 8 (b)).

Since a fibre oriented at any angles (θ,φ) is indistinguishable from another oriented at the (π-θ, φ+π), the probability density function of the fibre orientation, $\psi(\theta,\varphi)$ is π-periodic. To account for this property, Guenet (2016) used the following bell-shaped function:

$$\Psi(\theta,\varphi) = \cosh(k_g \cos\theta) \tag{2}$$

where k_g is a parameter that characterizes the sharpness of the function: k_g=0 defines a uniform distribution, and when $k_g \to \infty$, Ψ tends to Dirac Delta function, i.e., the orientation becomes unidirectional (1D). Eq. (2) is expressed in such a way that the default preferential orientation of the fibres (maximum value of Ψ) is along the *x*-axis. By rotating the *xy*-plane around the *z*-axis, the preferential in-plane orientation becomes defined by the angle β_0 (Figure 8). The distribution function for any preferential orientation β_0 is given by:

$$\Psi(\theta,\varphi) = \cosh\left\{k_g\left[\cos\theta\cos\beta_0 + \sin\theta\cos\varphi\sin\beta_0\right]\right\} \tag{3}$$

The function $\Psi(\theta,\varphi)$ must be normalized so that the integration over the domain is a unit value, as stated by Eq. (4) for the 3D case:

$$\int_{\varphi=0}^{\varphi=2\pi}\int_{\theta=0}^{\theta=\frac{\pi}{2}}\psi(\theta,\varphi)\,\sin\theta\,d\theta\,d\varphi = 1 \tag{4}$$

The final probability density functions of the fibre orientation in the 3D and 2D cases are given in Eq. (5) (a) and (b), respectively:

$$\text{3D:}\quad \psi(\theta,\varphi) = \frac{k_g}{2\pi\,\sinh k_g}\cosh\left[k_g\left(\cos\theta\cos\beta_0 + \sin\theta\cos\varphi\sin\beta_0\right)\right] \quad \text{(a)}$$

$$\text{2D:}\quad \psi(\theta) = \frac{\cosh\left[k_g\left(\cos\theta\cos\beta_0 + \sin\theta\sin\beta_0\right)\right]}{\int_{\theta=0}^{\pi}\cosh\left[k_g\left(\cos\theta\cos\beta_0 + \sin\theta\sin\beta_0\right)\right]d\theta} \quad \text{(b)} \tag{5}$$

The derivations of Eqs. (3) and (5) are presented in A. 1. In the 2D case, the denominator in Eq. (5) (b) requires numerical evaluation.

Figure 10 shows the representation of different 3D-probability density functions in the Cartesian coordinate system considering k_g=0, 2, 10 and the preferential in-plane orientation of the fibres β_0=30º.

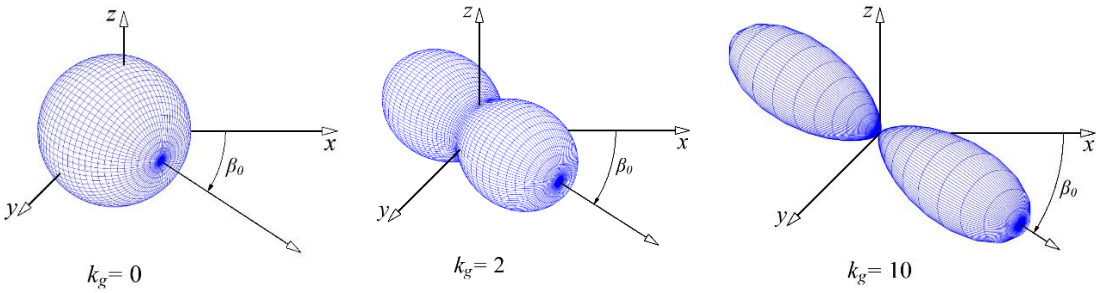

Figure 10. 3D-Probability density function representation on the Cartesian coordinate system.

By applying Eq. (5) (b) and the same parameters as Figure 10, the corresponding graphic representations of the 2D-probability density functions are presented in Figure 11.

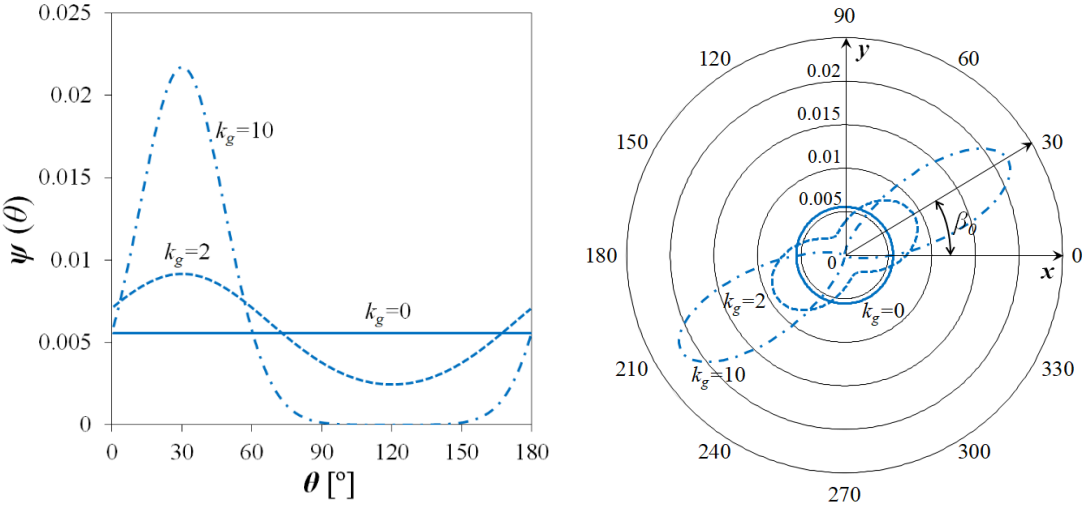

Figure 11. 2D-Probability density functions: (a) ψ as a function of the polar coordinate θ; (b) Polar representation.

2.2.2. Scalar descriptors

2.2.2.1. Fibre orientation factor

The fibre orientation factor, $\alpha_{0,i}$, is the probability of a single fibre to intersect a random planar surface normal to a given i-axis (Krenchel 1975) and can be experimentally determined by:

$$\alpha_{0,i} = n_{f,i} \frac{A_f}{V_f} \tag{6}$$

where $n_{f,i}$ is the number of fibres per unit area crossing the plane normal to the i-axis, and A_f is the cross-section of a single fibre. Considering the probability density function defined before and the projection along the i-axis of the unit vector collinear with the fibre, p_i, the fibre orientation factor along the i-direction is calculated by Eq. (7):

$$\text{3D:} \quad \alpha_{0,i} = \int_{\varphi=0}^{\varphi=2\pi} \int_{\theta=0}^{\theta=\frac{\pi}{2}} \psi(\theta,\varphi)\, p_i(\theta,\varphi) \sin\theta \, d\theta \, d\varphi \tag{a}$$

$$\text{2D:} \quad \alpha_{0,i} = \int_{\theta=0}^{\theta=\pi} \psi(\theta)\, p_i(\theta)\, d\theta \tag{b}$$

(7)

When the fibre orientation distribution is uniform (k_g=0), the Eq.s (7) (a) and (b) lead to the well-known values of $\alpha_{0,i}$=0.5 or 0.64 for 3D and 2D fibre distributions, respectively, independently of the direction i.

Considering the i-direction to lie in the xy-plane being defined by the angle β, the variation of $\alpha_{0,i}$ with respect to β is shown in Figure 12. In Figure 12 (a), besides $\alpha_{0,i}$, the variation of $\alpha_{0,z}$, where z refers to the out-of-plane direction, is shown for the 3D case considering k_g=5 and the fibres' preferential orientation defined by β_0=30º. It is seen that when $k_g \neq 0$, $\alpha_{0,i}$ increases as the i-direction approaches the direction of preferential fibre orientation while $\alpha_{0,z}$ remains invariant.

The effect of k_g on the variation of $\alpha_{0,i}$ is shown in Figure 12 (b) for the 2D and 3D cases. As k_g increases, the values corresponding to 2D and 3D fibre distributions become closer.

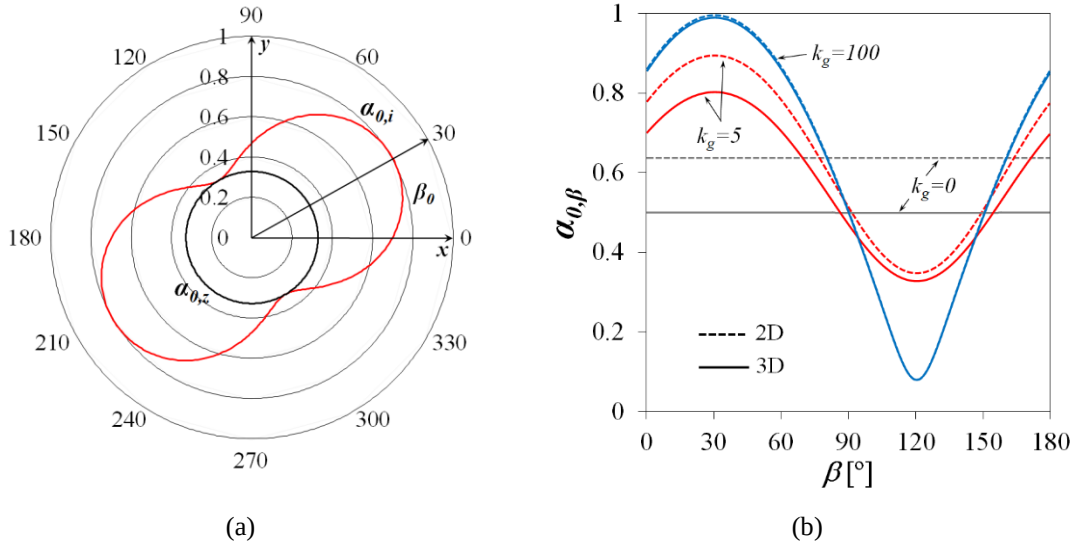

(a) (b)

Figure 12. Fibre orientation factor for β_0=30º: (a) $\alpha_{0,i}$ and $\alpha_{0,z}$ considering 3D fibre distribution and k_g=5; (b) effect of the variation of k_g on $\alpha_{0,i}$ considering both 2D and 3D fibre distributions.

In-plane isotropic behaviour is achieved when $\alpha_{0,j}/\alpha_{0,i}$=1.0 for any two orthogonal directions i and j within the xy plane. According to the probability density function adopted in this work, this condition implies k_g=0, in which case the fibre distribution is isometric. When k_g>0, the fibre distribution is anisometric, leading to the directional dependence of the fibre orientation factor and consequently to the anisotropic tensile behaviour. The ratio $\alpha_{0,i}/\alpha_{0,j}$ is a good indicator of the degree of anisotropy of the tensile response of the material. According to Eq. (7) and the experimental evidence, the comparison between the calculations is presented in Figure 13. The continuous lines were

determined varying k_g between 0 and 100, considering the i-direction aligned with the x-axis, and β_0=0º or 90º for obtaining for $\alpha_{0,j}/\alpha_{0,i}<0$ or $\alpha_{0,j}/\alpha_{0,i}>0$, respectively. The experimental data is taken from the works by Babut (1985), Wuest (2007), Oesterlee (2010), Ferrara, Ozyurt and di Prisco (2011), Bastien-Masse, Denarié and Brühwiler (2016). New data collected in the present work in DEWST specimens are also included and referenced as DEWST2. The corresponding values are tabulated in A. 3. For each data point, the number of fibres per unit area was determined on two orthogonal surfaces (i- and j-) using image analysis procedures like those described in Nunes et al. (2017), and then Eq. (6) was used to determine the corresponding orientation factors. It is noted that in most cases, the volumetric fibre fraction, V_f, was taken as that adopted in the mix design, not accounting for local variations in the extracted samples over which the image analysis was performed.

The experimental data covers a wide range of fibre distributions. The ratio of the thickness of the element over the fibre length, h_U/l_f, is indicated for reference. It can be seen that the experimental trend is well reproduced and that the theoretical curves for the two limiting cases corresponding to 3D ($h_U/l_f \to \infty$) and 2D ($h_U/l_f \to 0$) delimit most of the experimental points.

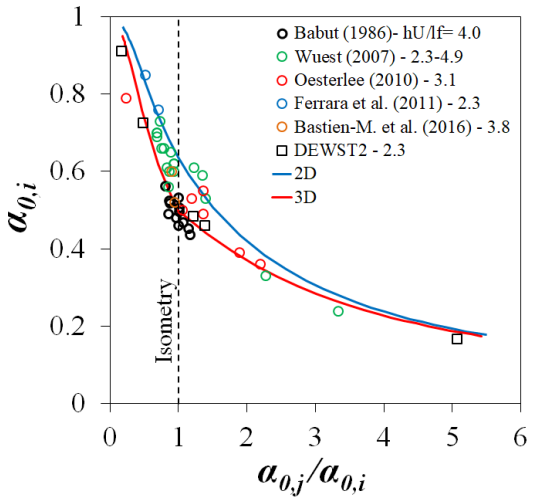

Figure 13. Fibre anisometry: analytical (Eq. (7)) vs experimental results.

2.2.2.2. Elements with finite thickness

On elements with finite thickness, the upper and lower boundaries constrain the range of possible fibre orientations. As shown in Figure 14, two regions can be accounted

concerning the location of the centre point of the fibres: *w*–subjected to wall effect and where the distance to the border is not greater than $l_f/2$; and *c*–the interior region where the fibre orientation is not constrained and follows a 3D distribution.

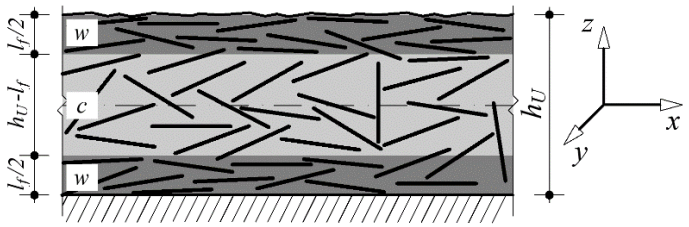

Figure 14. Fibres randomly distributed in UHPFRC thin elements.

For the case of the uniform probability density function of fibre orientation, that is k_g=0. The fibre orientation factor can be determined weighting the contribution of the two zones:

$$\alpha_{0,i}=\begin{cases}\dfrac{\alpha_{0,i}^{w}.l_f+\alpha_{0,i}^{c}\left(h_U-l_f\right)}{h_U} & ; \quad \text{for } h_U > l_f \\ \alpha_{0,i}^{w} & ; \quad \text{for } h_U \le l_f\end{cases} \tag{8}$$

The calculations are presented in A. 2 by applying Eq. (7) (a) and considering k_g=0 in Eq. (5) (a). Figure 15 shows the variation of fibre orientation factor with ratio h_U/l_f. As expected, when $h_U/l_f \to 0$, the fibre orientation factor approaches the theoretical value for a 2D distribution, that is $\alpha_{0,i} \to 2/\pi \approx 0.64$. On the other hand, when $h_U/l_f \to \infty$, the wall effects become less critical, and the fibre orientation factor tends to the value corresponding to a 3D distribution, $\alpha_{0,i} \to 0.5$.

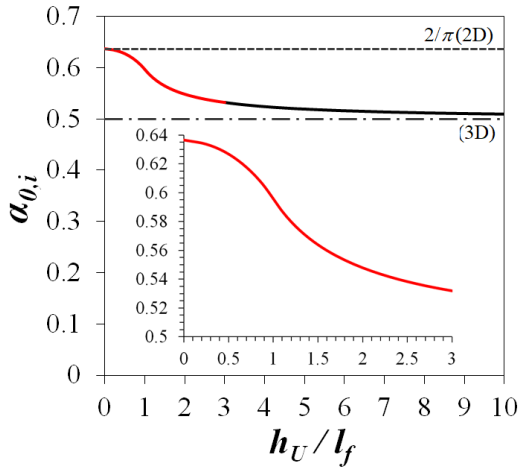

Figure 15. Fibre orientation factor considering uniform probability density function (k_g=0) according to the ratio h_U/l_f.

2.2.2.3. Fibre orientation number

The probability density function, $f_i(\theta)$, of the fibres crossing the surface normal to *i*-direction is given by Eq. (9).

$$f_i(\theta) = \frac{1}{\alpha_{0,i}} \int_0^{2\pi} \psi(\theta,\varphi) p_i(\theta,\varphi) \sin\theta \, d\varphi \tag{9}$$

The fibre orientation number, $\eta_{\theta,i}$, can be defined as the expected value of the projection along the *i*-direction of the unit vectors collinear with the fibres that intersect the cross-section normal to *i*:

$$\eta_{\theta,i} = \int_0^{\frac{\pi}{2}} \cos\theta f_i(\theta) d\theta \tag{10}$$

It can also be determined experimentally using image analysis:

$$\eta_{\theta,i} = \frac{1}{N_f} \sum_{n=1}^{N_f} \cos\theta_n \implies 0 \le \eta_{\theta,i} \le 1 \tag{11}$$

where N_f is the total number of fibres intersecting the surface normal to *i*; $\theta_n = cos^{-1}(d_2/d_1)$ is the orientation angle of the n^{th} fibre with respect to the *i*-direction; and d_1 and d_2 are, respectively, the greater and smaller diameters of the ellipse resulting from the intersection of the cylindrical fibres with the surface. Differently to the $\alpha_{0,i}$ calculated according to Eq. (6), the determination of $\eta_{\theta,i}$ according to Eq. (11) does not require the knowledge of V_f. Therefore, although not intervening in the calculation of the post-cracking tensile strength (Eq. (1)), $\eta_{\theta,i}$ is a more reliable scalar descriptor of the fibre orientation when using the image analysis.

Figure 16 shows the theoretical relations between the two scalar descriptors (α_0 and η_θ^2), using 2D and 3D-probability density functions varying k_g from 0 to 100. Also shown are the experimental data points obtained through image analysis (Eq. (11)) of specimens taken after UTT and DEWST tests being carried out by Duque and Graybeal (2017) (UTT1), Abrishambaf, Pimentel and Nunes (2017) (UTT2), Nunes et al. (2017) (DEWST1), the aforementioned DEWST2, and specimens cut from a large plate followed by an FPBT, as it will be presented in 2.3.8. The specimens cover a wide range of fibre contents of orientations. The corresponding values are tabulated in A. 4.

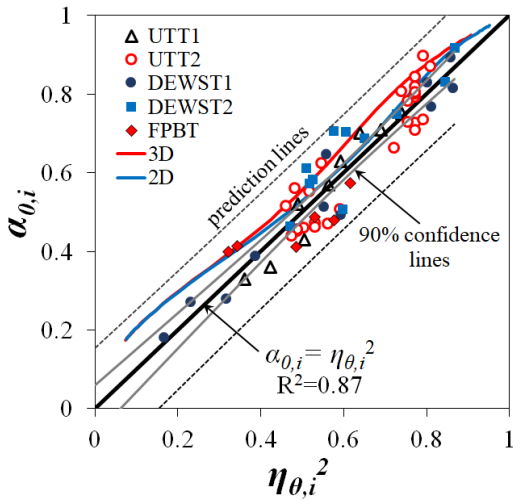

Figure 16. Experimental validation of the relation $\alpha_{0,i}$ vs $\eta_{\theta,i}^2$.

A regression analysis indicates that the simple model $\alpha_0=\eta_\theta^2$ first suggested by Nunes et al. (2017) provides a good fit for the experimental results, and the theoretical lines fall outside the 90% confidence band of the regression line.

2.2.3. Fibre efficiency factor

The fibre efficiency factor, $\alpha_{1,i}$, is defined as the expected value of fibre efficiency function, $g(\theta)$ (Bastien-Masse, Denarié, and Brühwiler 2016):

$$\alpha_{1,i} = \int_0^{\frac{\pi}{2}} g(\theta) f_i(\theta) d\theta \tag{12}$$

where $g(\theta)$ is the relation between the pull-out force of a fibre oriented at θ and that of a well-oriented fibre (Abrishambaf, Pimentel, and Nunes 2017). It has been suggested (Nunes et al. 2017; Abrishambaf, Pimentel, and Nunes 2017; 2019) to use a stepped function for $g(\theta)$, with a unit value for $\theta \in [0^o, 60^o]$, or zero otherwise. Thereby, Eq. (12) becomes:

$$\alpha_{1,i} = F_i(\theta = 60^o) \tag{13}$$

where F_i is the cumulative distribution function of fibres crossing the surface normal to i-direction. This allows $\alpha_{1,i}$ to be experimentally obtained by image analysis of polished surfaces counting the fibres with an orientation not greater than 60º.

The relations of the fibre efficiency factor with the fibre orientation indicators are presented in Figure 17, where the experimental data points are compared to the theoretical estimates. It can be seen that the theoretical lines quite well represents the relation between $\alpha_{1,i}$ and $\eta_{\theta,i}$ in Figure 17(a) and that the scatter in the experimental data is low. The linearization proposed in Nunes et al. (2017) is also shown to represent the variation of $\alpha_{1,i}$ with $\eta_{\theta,i}$ accurately. However, the scatter increases significantly when it comes to the relation between $\alpha_{1,i}$ and $\alpha_{0,i}$, as shown in Figure 17(b), and the quality of the fitting between the theoretical lines and the experimental data decreases. The increased scatter can be because its experimental determination relies on the nominal amount of fibres used in the mix design and not on the number of fibres of the sample. Resorting to the approximation $\alpha_{0,i} \approx \eta_{\theta,i}^2$, Eq. (14) can be derived as proposed originally by Nunes et al. (2017) and shown in Figure 16. It is also noted that the theoretical lines for the 2D and 3D fibre distributions are nearly coincident, which means that the relation between α_1 and α_0 is independent of the thickness of the element.

$$\alpha_{1,i} = 1.686\sqrt{\alpha_{0,i}} - 0.406 \Longrightarrow 0 \leq \alpha_{1,i} \leq 1 \tag{14}$$

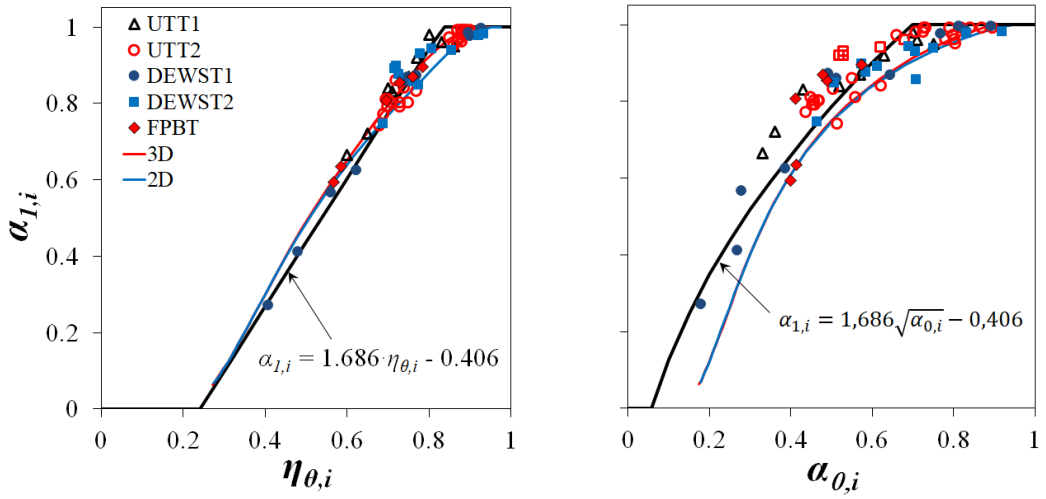

(a) (b)

Figure 17. Experimental validation of the relation between (a) $\alpha_{1,i}$ vs $\eta_{\theta,i}$ and (b) $\alpha_{1,i}$ vs $\alpha_{0,i}$. The corresponding values are tabulated in A. 4.

2.3. NON-DESTRUCTIVE TEST METHOD

2.3.1. Fundamentals

The magnetic permeability of a material, μ, can be defined as the constant of proportionality between the magnetizing field strength to which the material is subjected and the resultant magnetic flux density inside the material. In isotropic mediums, μ is a scalar, becoming a second-order tensor in anisotropic mediums. It can be more conveniently expressed in terms of relative magnetic permeability μ_r, which is the factor by which the material permeability exceeds that of free space, μ_0: $\mu=\mu_r\mu_0$. Since the UHPFRC is a composite constituted by two phases: the matrix, with a relative magnetic permeability μ_{rm}=1.0, similar to that of the air and independent of the mix composition and age; and the fibres, which show ferromagnetic behaviour, i.e., μ_{rf} >>1.0, it makes the measurement depending on the magnetic permeability of the composite a good candidate for providing information on both the amount and orientation of the fibres.

In a previous work by Nunes et al. (2016a), an inductor was developed consisting of a U-shaped ferrite core with a copper wire coil around both legs (Figure 18). A magnetic field is generated when an electric current passes through the copper winding. The inductance, L, is the ratio of the magnetic flux to current and can be measured using an LCR meter, as depicted in Figure 18 (b). If the U-shaped inductor is placed over a UHPFRC layer, the inductance of the resulting magnetic circuit depends on the relative magnetic permeability of the composite according to the equation derived in Nunes et al. (2016a):

$$L_i=\frac{N^2\mu_0}{\frac{l_c/A_c}{\mu_{rc}}+\frac{l/A}{\mu_{r,i}}} \tag{15}$$

where the subscript i refers to any in-plane direction along which the inductance is being measured; N is the number of turns in the coil; l_c/A_c is the ratio between the length of the magnetic path through the U-shaped core and its cross-sectional area; μ_{rc} is the relative magnetic permeability of the core material (ferrite); and $\mu_{r,i}$ is the relative magnetic permeability of the composite along the i-direction. The ratio l/A relates to the geometrical properties of the magnetic field path through the composite layer. Knowing that μ_{rc} and $\mu_{r,i}$ differ by three orders of magnitude, and assuming that the ratio l/A remains

approximately unchanged when the inductance L_{air} is measured placing the probe in the air, away from any magnetic object, the relative magnetic permeability of the composite can be estimated experimentally according to:

$$\mu_{r,i} \approx \frac{L_i}{L_{air}} \tag{16}$$

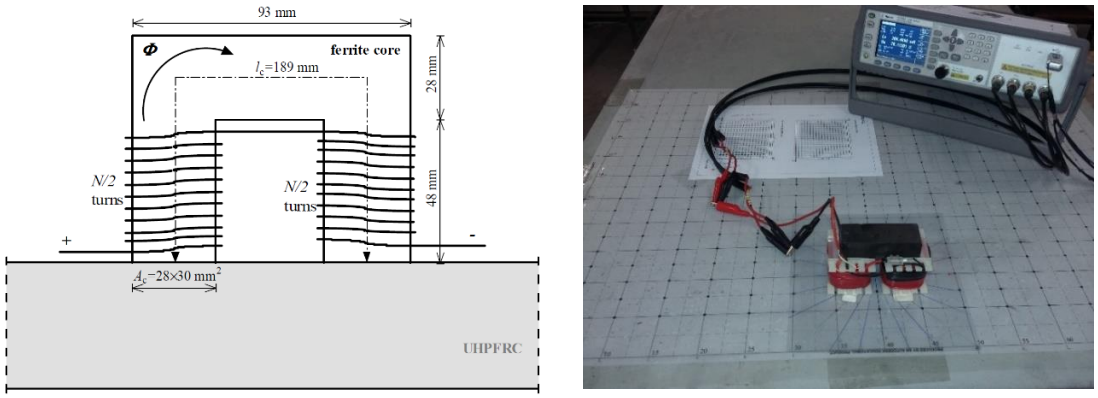

(a) (b)

Figure 18. NDT method (a) schematic representation of the magnetic circuit constituted by probe and UHPFRC layer (Nunes, Pimentel, and Carvalho 2016a); and (b) measurements on a UHPFRC thin element.

2.3.2. Simplified physical model of the composite

A simple model of the composite supporting the NDT method was developed Nunes et al. (2016a). As previously mentioned, the composite is considered a two-phase material, matrix and fibres, with relative magnetic permeability equal to μ_{rm}=1.0 and μ_{rf}, respectively. Negligible interaction is assumed between the fibres. Furthermore, the fibres are assumed to lie on parallel planes and be aligned in the same direction. That is, the orientation is 2D and is described by a Dirac delta function. This model is herein generalized. Instead of a Dirac delta, the 2D probability density function given by Eq. (5) (b) is adopted instead, allowing for a more realistic in-plane distribution of fibres in thin UHPFRC elements.

The angle β defines the orientation angle of the probe (alignment of the legs), and the orientation angle of the fibres is defined by θ and both are measured with respect to the x-axis as reference, according to Figure 19. Let $dV_{fn} = \psi(\theta_n)V_f\, d\theta$ be the volumetric fraction of fibres oriented between θ_n and $(\theta_n + d\theta)$. Likewise, in reference (Nunes,

Pimentel, and Carvalho 2016a), the fibre volume is divided into two parts. However, in this generalized model, this division is made for each infinitesimal group of fibres, such that $dV_{fn} = dV_{f,n,//} + dV_{f,n,\perp}$

- $dV_{f,n,//} = dV_{f,n}.\cos^2(\beta-\theta_n)$ corresponds to the part $dV_{f,n}$ parallel to the measuring direction;
- $dV_{f,n,\perp} = dV_{f,n}.\sin^2(\beta-\theta_n)$ corresponds to the part $dV_{f,n}$ perpendicular to the measuring direction.

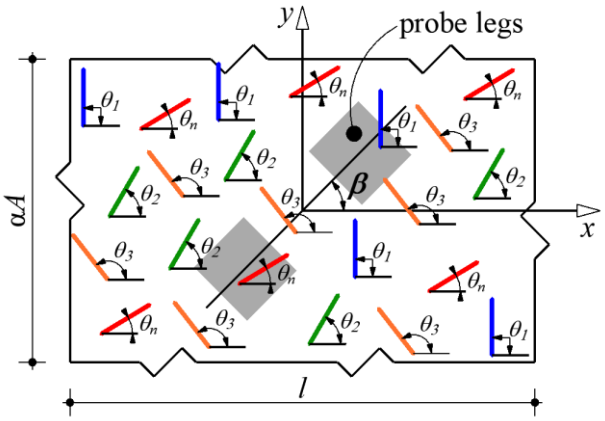

Figure 19. Definition of in-plane orientation angles of fibres.

The relative magnetic permeability of a thin UHPFRC element for any alignment β of the probe can be calculated according to the in-plane generalized simplified physical model as follows (see (Nunes, Pimentel, and Carvalho 2016a) and A. 5 for further details):

$$\mu_{r,\beta} = \left\{ \frac{(1-\gamma) V_{f,\perp}}{\gamma+\mu_{r,f}.(1-\gamma)} + \frac{\left[1-(1-\gamma) V_{f,\perp}\right].\left(\mu_{r,f}.\gamma+1-\gamma\right)}{\left[1-(1-\gamma) V_{f,//}\right].\left(\mu_{r,f}.\gamma+1-\gamma\right) + \mu_{r,f}.(1-\gamma) V_{f,//}} \right\}^{-1} \quad (17)$$

where γ is a model parameter expressing the fact that the fibres are discontinuous steel filaments, $V_{f,//} = V_f \int \psi(\theta) \cos^2(\beta-\theta)\, d\theta$ and $V_{f,\perp} = V_f \int \psi(\theta) \sin^2(\beta-\theta)\, d\theta$.

The polar representation of relative magnetic permeability is shown in Figure 20, considering the probability density functions of fibre orientation of Figure 11, γ=0.35 and μ_{rf}=2000. It is evident the alignment of the maximum relative magnetic permeability with the direction of preferential fibre orientation. It is also noticed that the model predicts that the average of the relative magnetic permeability along with any two orthogonal directions β and $\beta+\pi/2$ is independent of k_g, that is, independent of the fibre orientation profile.

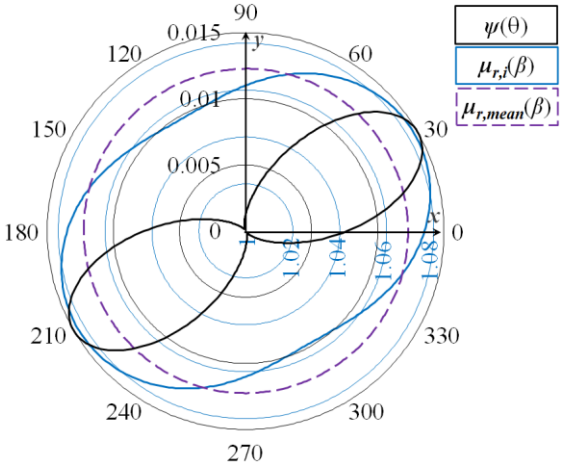

Figure 20. Polar representation of relative magnetic permeability for k_g=5 and β_0=30º.

2.3.3. Approximation via a 2nd order tensor

A 2nd order tensor can approximate the relative magnetic permeability of the theoretical model. Thus, the relative magnetic permeability for any alignment defined by the angle β, $\mu_{r,\beta}$, can be retrieved from the relative magnetic permeability along with any three non-collinear directions. In particular, knowing $\mu_{r,i}$, $\mu_{r,j}$ and $\mu_{r,i+\pi/4}$ (Figure 21), $\mu_{r,\beta}$ can be determined using Eq. (18):

$$\mu_{r,\beta} = \mu_{r,i} \cdot \cos^2\beta + \mu_{r,j} \cdot \sin^2\beta + \left[\mu_{r,i+\pi/4} - \mu_{r,mean}\right] \sin 2\beta \tag{18}$$

where $\mu_{r,mean}$ is the mean relative magnetic permeability between the orthogonal directions, *i* and *j*.

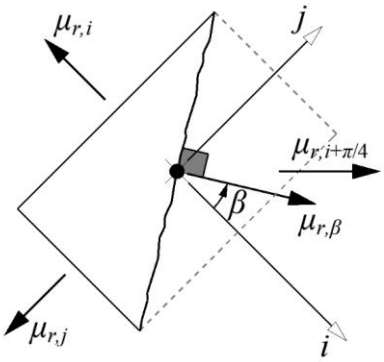

Figure 21. 2nd order tensor approximation of the relative magnetic permeability.

The directions of maximum and minimum magnetic permeability can also be determined using the usual tensor operations. These provide the visualization of the directions of the

preferential fibre orientation in larger specimens where inductance measurements are performed in a grid of points. This will be exemplified in section 2.3.8.1.

2.3.3.1. Validation

An NDT campaign was conducted in 24 DEWST specimens with 150x150x30 mm^3, containing volumetric fibre fractions of 1, 2, 3 and 4% of fibres with l_f/d_f=13/0.2 (mm/mm) and three fibre orientation profiles: oriented (β_0=0º and 90º) and not-oriented. As depicted in Figure 22 (a), each mould has 304x150x30 mm^3 and is cut along the centreline to produce two identical DEWST specimens. A single batch is used to fill each mould to guarantee the nominal fibre content. The mix composition is provided in the A. 6. Following the procedure and the setup detailed in Nunes, Pimentel and Carvalho (2016a) and Nunes et al. (2017), the orientation of the fibres is achieved by casting specimens within a magnetic field capable of orienting the fibres while the material is in the fresh state. The specimens without preferential fibre orientation were cast by placing the material in the centre and flowing until the mould is filled.

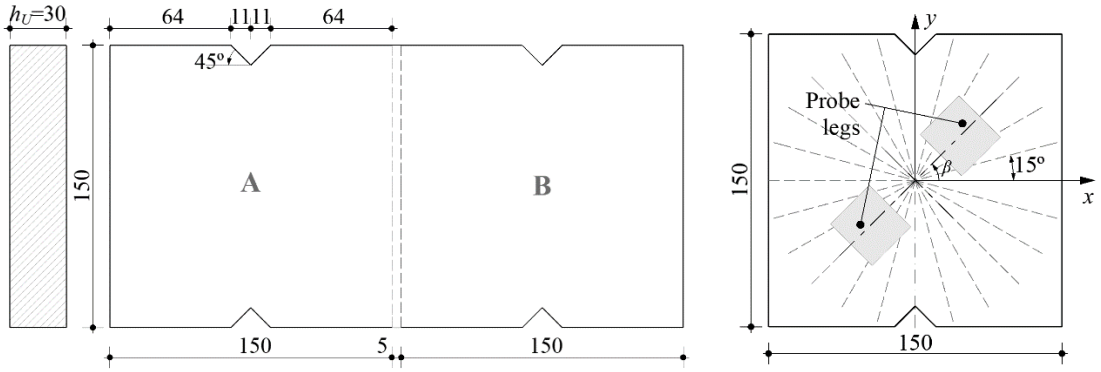

Figure 22. DEWST specimens: (a) Dimensions of the mould for two identical specimens; (b) scheme of the probe measurement and notation.

The inductance measurements L_i were taken every 15º over the moulded face (Figure 22 (b)), and the relative magnetic permeability was determined according to Eq. (16). The dots in Figure 23 represent the average of the measurements taken on the two identical specimens in each mould, and the lines provide the tensor approximation according to Eq. (18). The agreement is noticeable. In the specimens with no preferential orientation of the fibres, the polar representation of the relative magnetic permeability shows a nearly

constant radius (Figure 23 (a)). However, in the specimens with preferential fibre orientation along β_0=0º (or 90º), the radius is clearly variable, being maximum at β=β_0=0º and minimum in the perpendicular direction (Figure 23 (b)).

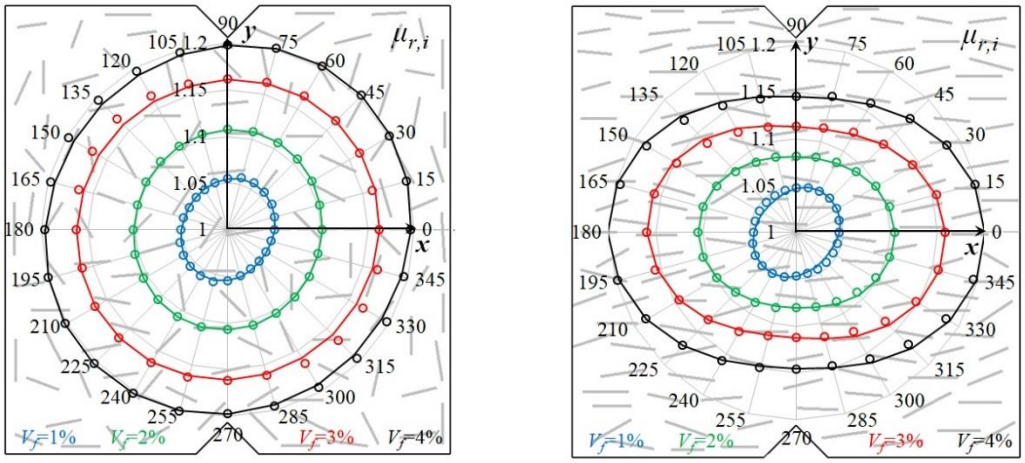

(a) (b)

Figure 23. Relative magnetic permeability of DESWT2 plates (a) not oriented and (b) β_0=0º.

2.3.4. Determination of the fibre content

As shown in section 2.3.2, the model predicts that the mean relative magnetic permeability along two orthogonal directions given by Eq. (19) is nearly insensitive to the fibre orientation distribution and may serve as an indicator of the fibre content.

$$\mu_{r,mean}=\frac{1}{2}\left(\mu_{r,i}+\mu_{r,j}\right) \tag{19}$$

Additionally, Nunes, Pimentel and Carvalho (2016a) propose that $\mu_{r,mean}$ increases linearly with the fibre volumetric fraction:

$$V_f = \frac{\mu_{r,mean}-1}{k_v} \tag{20}$$

where k_v is the proportionally constant and depends on the length and magnetic permeability of the fibres. This can be accounted for in the model through the parameters γ and μ_{rf}. For example, Figure 24 shows the model predictions considering a fibre distribution with k_g=5 and β_0=0º, and the parameters γ=0.35 and μ_{rf}=2000, confirming the Eq. (20). However, as will be discussed in section 2.3.6, other factors have a direct influence on k_v which cannot be described by this simple model, such as the element

thickness, the finishing of the surface, the fibre segregation across the thickness and the distance of the probe to the border of the element.

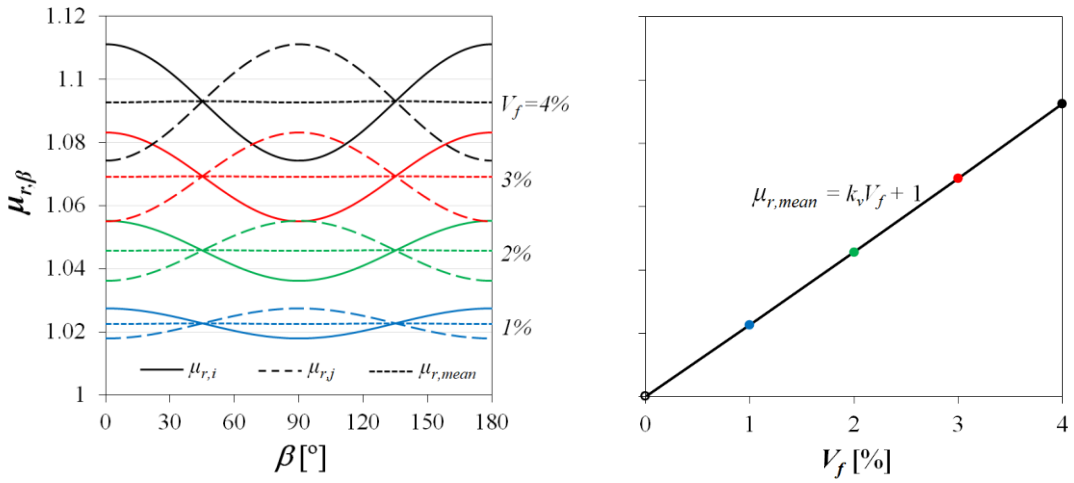

(a) (b)

Figure 24. Model predictions: (a) Relative magnetic permeability variation with V_f and β; (b) relation between V_f and $\mu_{r,mean}$.

2.3.4.1. Validation

The experimental validation of the Eq. (20) is made with data from three experimental campaigns, totalizing 58 specimens and varying the fibre volumetric fraction, the fibre orientation profiles, the fibre geometry and the element thickness. The experimental data are summarized in Table 1. The measurements were made on the moulded face of DEWST specimens with the same in-plane dimensions 150x150 mm^2. The specimens of the series DEWST1 and DEWST3 are from Nunes, Pimentel and Carvalho (2016a), and the DEWST2 are those mentioned in section 2.3.3.1.

The results are shown in Figure 25. It can be seen that Eq. (20) is within the 90% confidence lines of the linear regression model, further confirming its validity. A more refined analysis indicates that the scatter in the series DEWST1 and DEWST3 increases noticeably above V_f=3%. The most likely explanation relies on the fact that the inductance measurements are pretty sensitive to the uneven distribution of the fibres across the thickness of the specimens, most often due to fibre segregation. This will be discussed in detail in section 2.3.6.3. It is recalled that the measurements were performed over the moulded (bottom) face, and it cannot be ruled out that this may have contributed to at least part of the observed scatter in some specimens.

Table 1, it is also shown k_v providing the best fit to the data of each experimental series. As expected, k_v increases with the length of the fibres.

Table 1. Specimens used to validate Eq. (20).

Ref.	h_U [mm]	l_f [mm]	d_f [mm]	V_f [%]	Fibre orientation			k_v [-]
					x	*y*	Not-orient.	
DEWST1	25	9-12 [a])	0.175	0.5	2	2	2	4.12
				1.5	2	2	2	
				3.0	2	2	2 [b])	
DEWST2	30	13	0.2	1.0	2	2	2	4.68
				2.0	2	2	2	
				3.0	2	2	2	
				4.0	2	2	2	
DEWST3	25	10	0.175	1.0	2	-	2	3.90
				2.0	2	-	2	
				3.0	2	-	2	
				4.0	2	-	2	

[a]) 50% of each; [b]) $\mu_{r,mean}$ measurements on these specimens were identified in Nunes, Pimentel and Carvalho (2016a) as outliers and are not considered here for the determination of k_v indicated in the table.

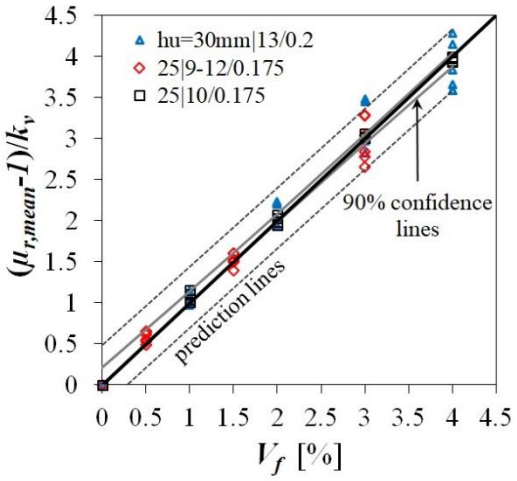

Figure 25. Normalized fibre content indicator versus the volumetric fibre fraction.

2.3.5. Determination of the fibre orientation factor

The fibre orientation indicator, ρ_{ij}, given by:

$$\rho_{ij} = \frac{\mu_{r,i} - \mu_{r,j}}{2\left(\mu_{r,mean} - 1\right)} \tag{21}$$

was introduced by Nunes, Pimentel and Carvalho (2016a) as being practically independent of the fibre content. Positive values of ρ_{ij} indicate the orientation of the fibres along the *i*-direction and along the *j*-direction, otherwise. Values close to zero indicate no preferential orientation. Later, Nunes et al. (2017) identified a linear relation between ρ_{ij} and the fibre orientation factor, $\alpha_{0,i}$. allowing its determination from the NDT measurements. This is here further explored using the model introduced in section 2.3.2. Figure 26 presents the theoretical results concerning the relation between $\alpha_{0,i}$ and ρ_{ij} using the 2D-probability density function. Different orientation profiles were obtained varying the parameter k_g and inserted in Eq. (17) (γ=0.35 and μ_{rf}=2000) to calculate the corresponding relative magnetic permeability $\mu_{r,\beta}$. The angle β was varied between 0º and 90º to obtain the full range of possible ρ_{ij} values for each fibre orientation profile. The corresponding values of $\alpha_{0,i}$ were determined according to Eq. (7) (b). It can be seen that the relation between $\alpha_{0,i}$ and ρ_{ij} becomes closer to linear as k_g approaches values representative of fibre orientation profiles that can be found in practice (k_g=3.65), for which k_g=10 can be considered as an upper bound. It is noticed that the slope of linear fit to the modelled nonlinear relation only slightly changes with the k_g value.

For a 2D uniform distribution of fibre orientation (k_g=0) we get ρ_{ij}=0 and α_0=0.64. For elements with finite thickness, it has been shown in section 2.2.2.2 that α_0 is a function of h_U/l_f. Therefore, the general form of linear relation is:

$$\alpha_{0,i} = k_\alpha \rho_{ij} + \alpha_0\left(h_U/l_f\right) \tag{22}$$

with k_α being the slope of the linear regression and $\alpha_0(h_U/l_f)$ determined according to Eq. (8) considering a uniform distribution of the fibre orientation.

Figure 26 (b) shows that the influence of the fibre volumetric fraction can be neglected for practical purposes.

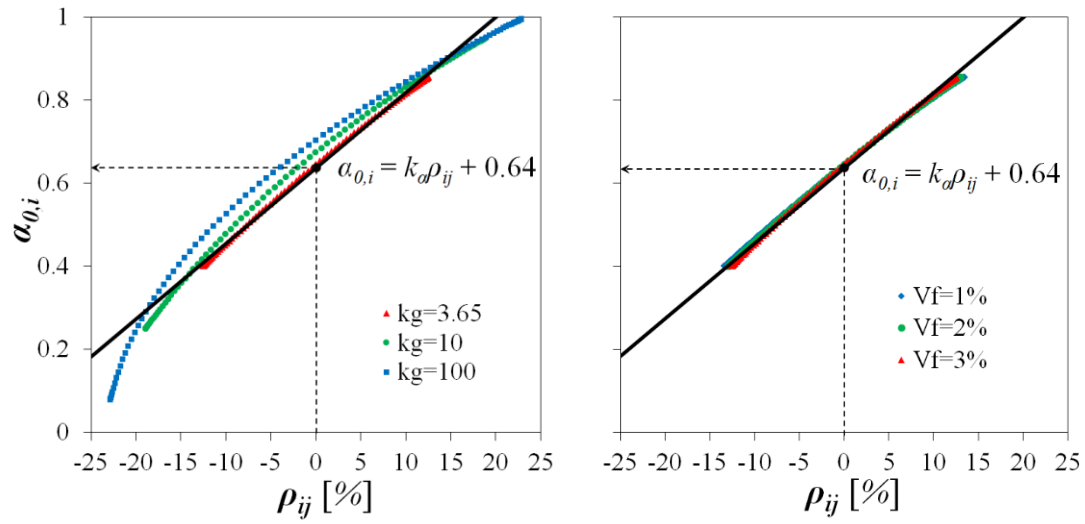

Figure 26. Theoretical results for the relation between fibre orientation factor and fibre orientation indicator with the variation of (a) k_g and (b) V_f.

2.3.5.1. Validation

The validation of the linear relation expressed by Eq. (22) and the determination of the slope k_α is made using the methodology adopted in Nunes et al. (2017). After the mechanical testing of the DEWST specimens over which the NDT measurements reported in section 2.3.3.1 were made, a cubic sample of 30x30x30 mm^3 was cut in the central part of selected specimens, at a distance greater than $l_f/2$ from the crack section to ensure that no fibres were pulled out from the sample. These samples were then used for the determination of $\alpha_{0,i}$ according to Eq. (6), following the image analysis procedures described in detail in Nunes et al. (2017). The corresponding values are tabulated in A. 5 and shown in Figure 27, jointly with the linear regression line and its 90% confidence band. The data covers a wide range of ρ_{ij} and $\alpha_{0,i}$ values and confirms the adequacy of the linear model. Figure 27 (a) shows that no discernible effect of fibre volumetric fraction can be detected. All this is in agreement with the trends predicted by the theoretical model. In Figure 27 (b), the data is labelled according to the orientation profile. The non-oriented specimens present smaller ρ_{ij} values and populate the central part of the regression. The two data points corresponding to oriented specimens located in this central region correspond to samples cut at 45º from the direction of preferential fibre orientation.

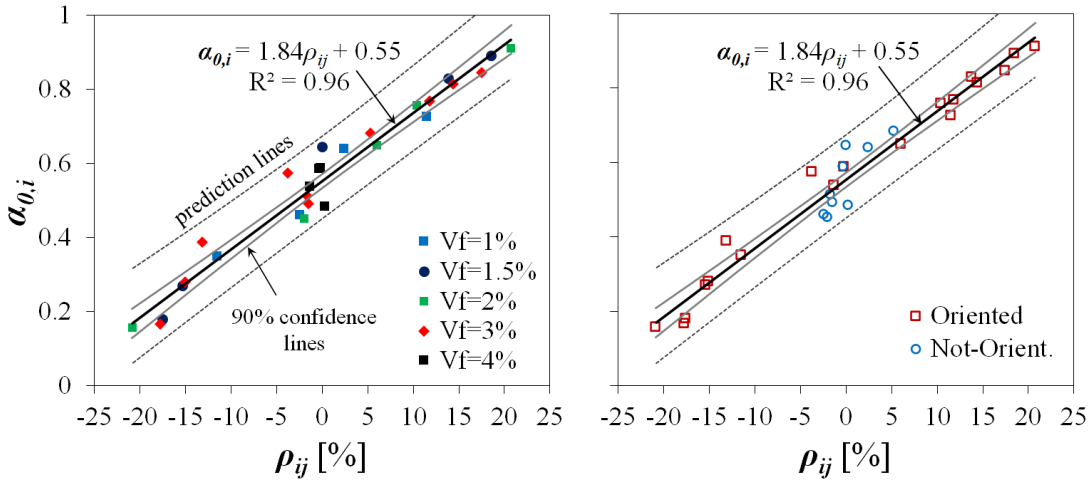

(a) (b)

Figure 27. Relation between fibre orientation factor and fibre orientation indicator. Specimens labelled according to the: (a) fibre volumetric fraction, V_f ;(b) orientation profile.

The slope of the regression line indicates that k_α=1.84 with a narrow 90% confidence band. The intersection at the origin is α_0=0.55, quite close to the values calculated using the methodology described in section 2.2.2.2, considering uniform fibre orientation distribution in elements with finite thickness. In fact, noting that the ratios h_U/l_f =2.1 for DEWST1 and 2.3 for DEWST2, α_0=0.546 and 0.542 can be obtained from Figure 15 (or A. 2).

The linearization of the relation between ρ_{ij} and $\alpha_{0,i}$ and the fact that, by definition, ρ_{ij} =- ρ_{ji} implies that:

$$\alpha_{0,i} = \frac{2\,\alpha_0}{1 + \alpha_{0,j}/\alpha_{0,i}} \tag{23}$$

This equation is independent of the slope k_α and is plotted in Figure 28 jointly with the experimental data already included in Figure 13. It is seen that the equation fits the data at least as well as the more complex Eq. (7) and provides further indication of the adequacy of the linearized model relating ρ_{ij} and $\alpha_{0,i}$.

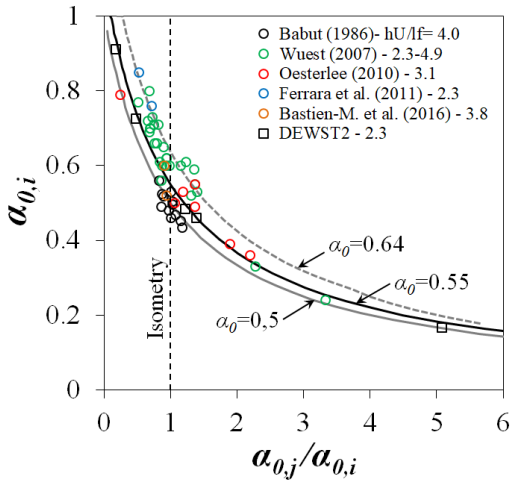

Figure 28. Fibre anisometry: Eq. (23) vs experimental data.

2.3.6. Factors influencing the inductance measurements

The simplified model of the magnetic circuit cannot account for the influence of some factors on the inductance measurements, such as the thickness of the element, the area surrounding the measuring point, the segregation of the fibres and the roughness of the surface. In the following sections, the effects are quantified based on experimental data.

2.3.6.1. Element thickness

The magnetic field developed through the UHPFRC element depends on its thickness and so the inductance measurements. In thicker elements, more ferromagnetic material is intersected, and higher values of the inductance are expected. This has a direct impact on the calibration of the regression line relating V_f and $\mu_{r,mean}$. Four 150 mm diameter and 100 mm tall cylinders were cast to study this effect, with steel fibre volumetric fractions of 1, 2, 3, and 4%. The fibre cocktail was constituted by a blend of 9 mm and 12 mm long fibres (50% each) with 0.175 mm diameter. The matrix composition is similar to the DEWST specimens presented in A. 6. The inductance measurements on these cylinders were always performed at the centre of the top surface. The thickness effect was evaluated by successively slicing the cylinder from the base, thus decreasing its height from h_U=100 mm down to h_U=20 mm.

The variation of the slope k_v of the regression line relating V_f and $\mu_{r,mean}$ with the element thickness h_U is shown in Figure 29. The results are normalized by the slope of the line for h_U=50 mm. It becomes apparent that the measurements are no longer affected for thicknesses beyond h_U=70 mm. Whenever the thickness of the element under analysis does not match the thickness of the specimens used in the laboratory, k_v should be corrected using the following equation:

$$\frac{k_v}{k_{v,ref}} = \sqrt{\frac{1-e^{-0.0642h_U}}{1-e^{-0.0642h_{U,ref}}}} \tag{24}$$

where k_v and $k_{v,ref}$ are the slopes of the regression lines obtained in specimens with the thickness h_U and $h_{U,ref}$, respectively, expressed in millimetres, the equation is particularized in the figure for $h_{U,ref}$=50 mm.

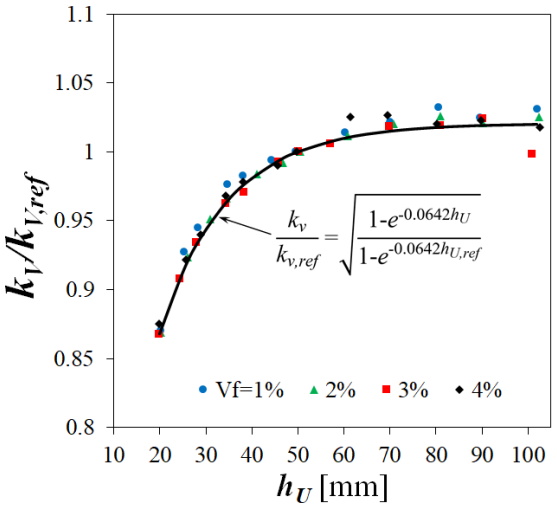

Figure 29: Dependence of k_v with the thickness of the element.

2.3.6.2. The area surrounding the probe

Three plates of 350x350x30 mm^3 with a total fibre content of 3% were cast to study the effect on the inductance measurements of the in-plane boundary conditions. The mix and fibre types are identical to those used in the cylinders of the previous section. The plates were cut sequentially of about 10 to 25 mm on each side (Figure 30 (a)) to reduce the area of the element. In all the stages, the NDT measurements were made at the same location: the plate's centre, as shown in Figure 30 (b). The first two plates were cast horizontally from the centre, one with free-flow (SP1) and the other with disturbance of the flow (SP2).

The third plate (SP3) was cast vertically. Finally, the non-destructive measurements were performed on the smooth moulded surfaces.

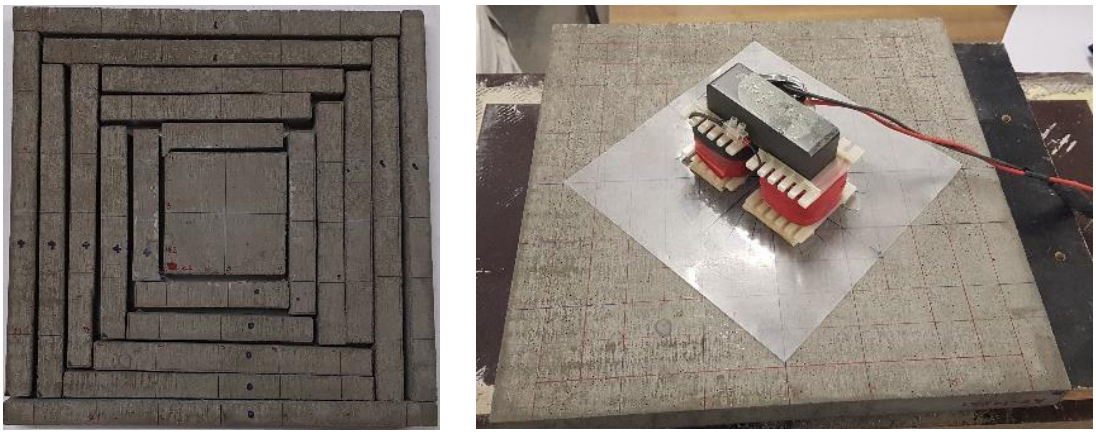

(a) (b)

Figure 30. (a) the final state of the plate after all cuts, and (b) NDT measurement in the centre of the SP1.

The results in Figure 31 show that the $\mu_{r,mean}$, and so the V_f, estimates are affected by the variation of the area surrounding the measuring point. This effect becomes negligible for the specimen sides not smaller than 200 mm. The error using the 150 mm side DEWST specimens mentioned in section 2.3.4.1 is around 2%, which can still be considered acceptable. It also means that when performing measurements in a real element, the centre of the probe should be at least 100 mm away from the edges of the element.

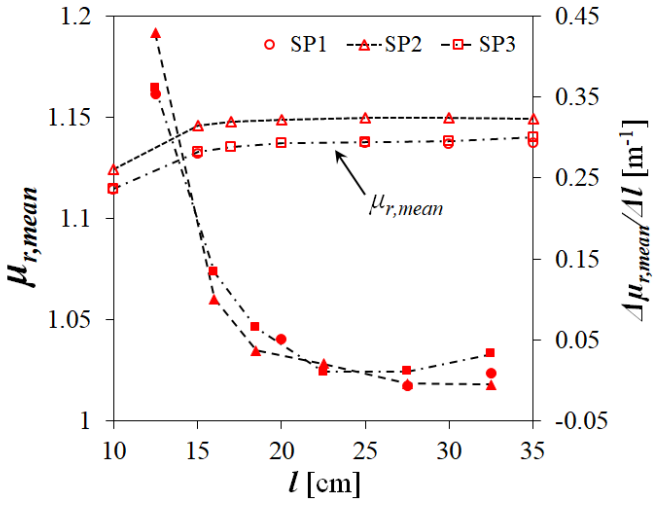

Figure 31. Effect of the area surrounding the probe on the estimate of the mean relative magnetic permeability.

The results in the figure show another essential effect. Although the trend is identical, the $\mu_{r,mean}$ values of the plate SP2 are higher than the others. This is due to the fibre

sedimentation (or in-depth segregation) caused by flow disturbance, which is further studied in the next section.

2.3.6.3. Segregation of the fibres

As the inductance measurements are performed on one face of the UHPFRC element, it is expected that if the fibres are not evenly distributed across the thickness and more concentrated towards one of the surfaces, the $\mu_{r,mean}$, and so the V_f, estimates may be affected. To analyse this effect, 12 plates with dimensions 200x200x30 mm^3 and fibre content of 1, 2, 3 and 4% were cast. The mix is identical to that used in the previous sections. The groups of plates are considered: HO*k* – Horizontal cast with fibres oriented with external magnetic field; HR*k* – Horizontal cast without forced orientation of the fibres; and VR*k* – Vertically cast without forced orientation of the fibres. The index *k* refers to the fibre content (1, 2, 3 and 4%). It is worth pointing that the *x*-axis in HO*k* plates refers to preferential orientation of the fibres, whereas in VR*k* refers to the vertical casting direction.

The NDT measurements were performed at the centre of the moulded surfaces (bottom surface in the case of the HO*k* and HR*k* specimens. Afterwards, 30x30x30 mm^3 cubes were extracted for determining the number of fibres (N_f) intersecting a cross-section normal to *x*- or *y*-axis through image analysis. The degree of segregation, ξ_{seg}, along the thickness h_U was computed using Eq. (25) (Babut 1985):

$$\xi_{seg} = \frac{1}{h_U N_f} \sum_{i=1}^{N_f} z_i \tag{25}$$

where the z_i refers to the distance of the centre of each fibre crossing the section to the top (casting) surface. As no fibre segregation across the thickness is expected in the vertically cast specimens, in these cases, z_i is the distance to one of the vertical surfaces. The value ξ_{seg}=0.5 corresponds to a specimen with fibres distributed symmetrically in respect to its midplane. The sedimentation of the fibres towards the bottom surface leads to ξ_{seg}>0.5. The results are summarized in Table 2. The variation of the number of fibres through the thickness of the elements is shown in Figure 32.

Table 2. Summary of the test results to evaluate the effect of fibre segregation.

Specimen	*i*-direction [°]	N_f	h_U [mm]	ξ_{seg}	$\mu_{r,i}$	$\mu_{r,mean}$
HO1	0	212	29	0.53	1.0532	1.0455
HO2	90	158	29	0.64	1.0744	1.0900
HO3	0	747	29	0.50	1.1442	1.1239
HO4	0	953	29	0.52	1.1971	1.1683
HR1	0	89	29	0.62	1.0526	1.0574
HR2	0	354	30	0.61	1.1011	1.1102
HR3	90	639	29	0.54	1.1793	1.1650
HR4	0	481	29	0.63	1.2117	1.2148
VR1	0	217	30	0.48	1.0488	1.0468
VR2	90	152	30	0.52	1.0834	1.0887
VR3	0	731	30	0.52	1.1244	1.1258
VR4	90	583	29	0.55	1.1690	1.1674

The results show that the HR*k* specimens exhibit fibre segregation towards the bottom surface. This is evident in the graphs of Figure 32 and the values of $\xi_{seg.}$ As shown in Figure 33, this affects directly the slope of the regression line relating V_f and $\mu_{r,mean}$.

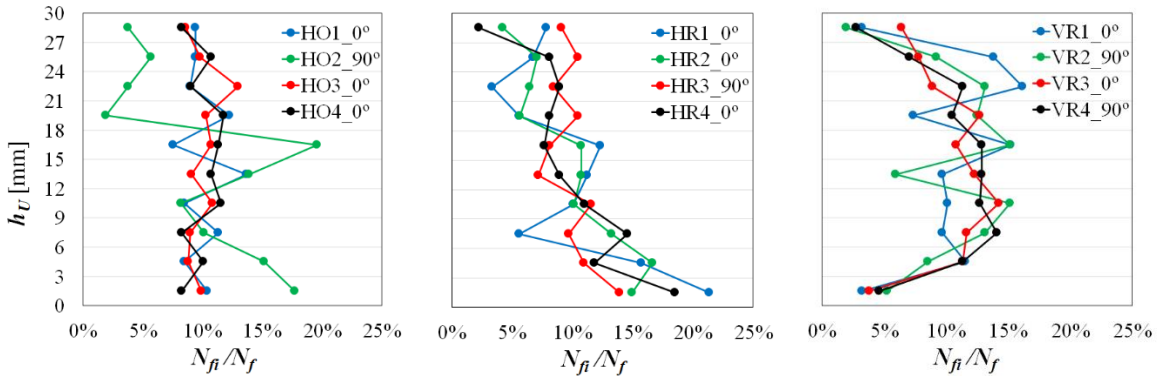

(a) (b) (c)

Figure 32. Distribution of the fibres through the thickness: (a) HOk series; (b) HRk series; (c) VOk series

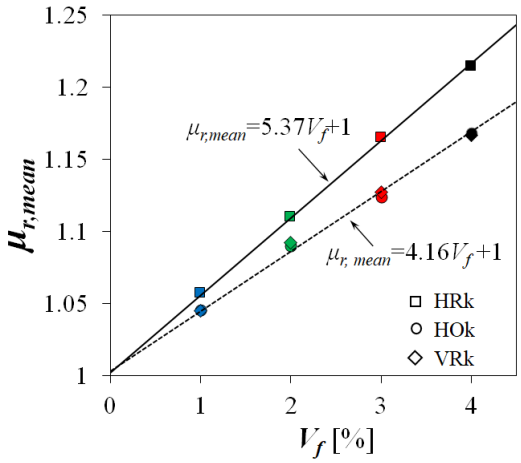

Figure 33. Effect of the segregation on the relation between V_f and $\mu_{r,mean}$.

2.3.6.4. Surface finishing

Poor contact between the probe and the UHPFRC surface introduces magnetic leakage and affects the inductance measurements. The best measuring conditions are always obtained over moulded surfaces, which have smooth finishing. The opposite occurs over rough casting surfaces. A remedial measure is to smooth the surface before performing the inductance measurements, as depicted in Figure 34 (a).

The plates of the series HO*k* mentioned in the previous section were selected for evaluation of this effect. As shown in Figure 33, these plates did not show fibre segregation, with $\mu_{r,mean}$ values measured over the moulded surface identical to those of the vertically cast plates. Therefore, the specimens are now labelled according to the surface type where the measurements were performed: C – casting, natural finishing, S – casting, smoothed finishing and M – moulded. It becomes apparent that the smoothing improves the contact between the probe and the UHPFRC surface, but it was not enough to achieve the same $\mu_{r,mean}$ values as in the moulded surface. Therefore, the calibration of the regression to be used in the measurements in an actual structure must be made on the same type of surface.

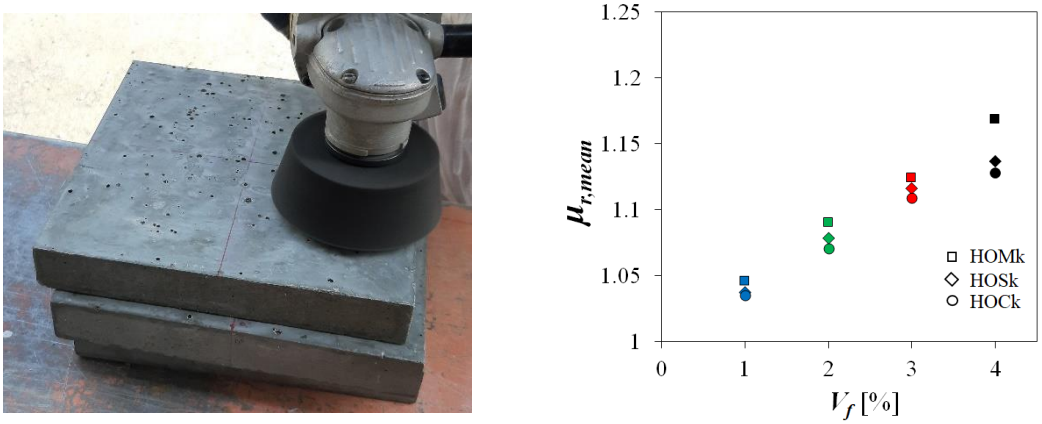

(a) (b)

Figure 34. Surface effect on $\mu_{r,mean}$: (a) mechanical smoothing of the casting surface; (b) regression lines for the different surface types.

2.3.7. Estimation of the tensile strength

The flowchart summarizing the procedure for estimating the post-cracking tensile strength, f_{Utu}, of a UHPFRC thin element using the NDT method is depicted in Figure 35.

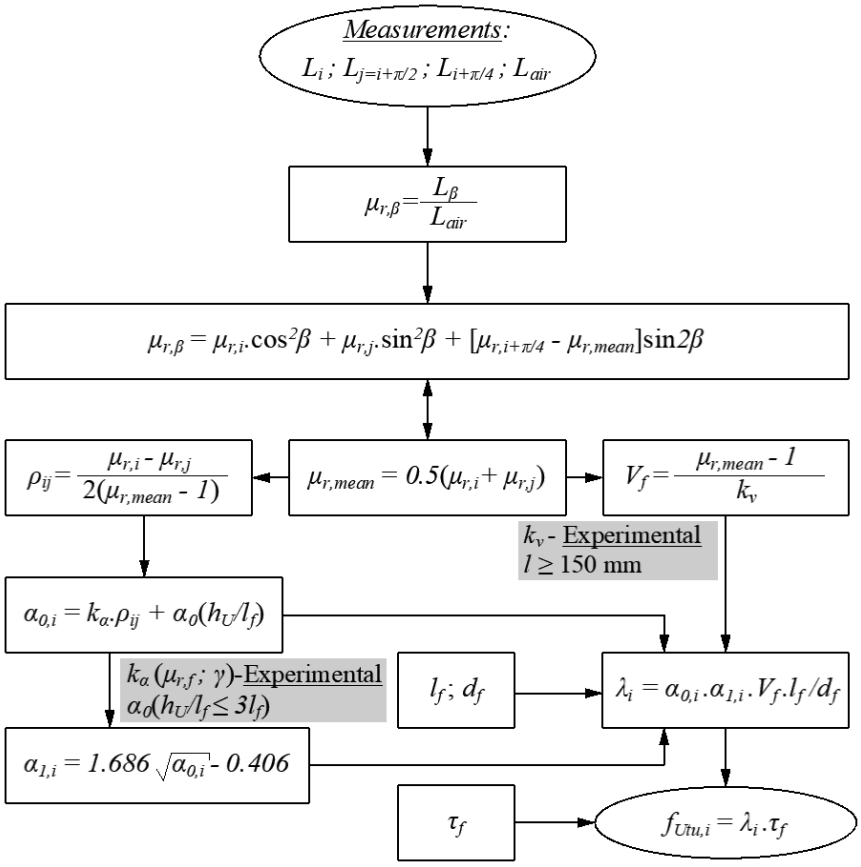

Figure 35. Flowchart for the estimation of the tensile strength of UHPFRC.

2.3.7.1. Validation on small specimens

In previous works, the validity of Eq. (29) was assessed performing direct tensile tests (UTT) (Abrishambaf, Pimentel, and Nunes 2017; 2019) and double-edge wedge splitting tests (DEWST1) (Nunes et al. 2017) to determine f_{Utu}, accompanied by image analysis (IA) to determine $\alpha_{0,i}$ (Eq. (6)) and $\alpha_{1,i}$ (Eq. (13)), and so the fibre structure parameter, λ_{IA}. As shown in Figure 36 (a), this allowed estimating the representative fibre-to-matrix bond strength, τ_f=11.1 MPa, for the UHPFRC mix used in this work.

According to the procedures described elsewhere (2010; 2013; Pimentel and Nunes 2016d), additional double-edge wedge splitting tests on the specimens designated as DEWST2 were carried out. Instead of using image analysis, the NDT measurements were used to determine the fibre structure parameter λ_{NDT}: Figure 36 (b) shows the results obtained for the test series DEWST1 and DEWST2, together with the 90% confidence band for the regression. Compared to Figure 36 (a), the scatter has increased, with some data points lying outside the 90% prediction band, but it is noteworthy since the line f_{Utu}=11.1λ is within the 90% confidence band of the regression, which further confirms the applicability of the NDT method. The data points corresponding to specimens with V_f=4% were excluded from the regression. These points are systematically below the regression line from λ>1, which may indicate that the validity of the linear model $f_{Utu}=\tau_f \lambda$ for such high fibre contents becomes questionable. This is expected since signs of fibre agglomeration were observed for these specimens.

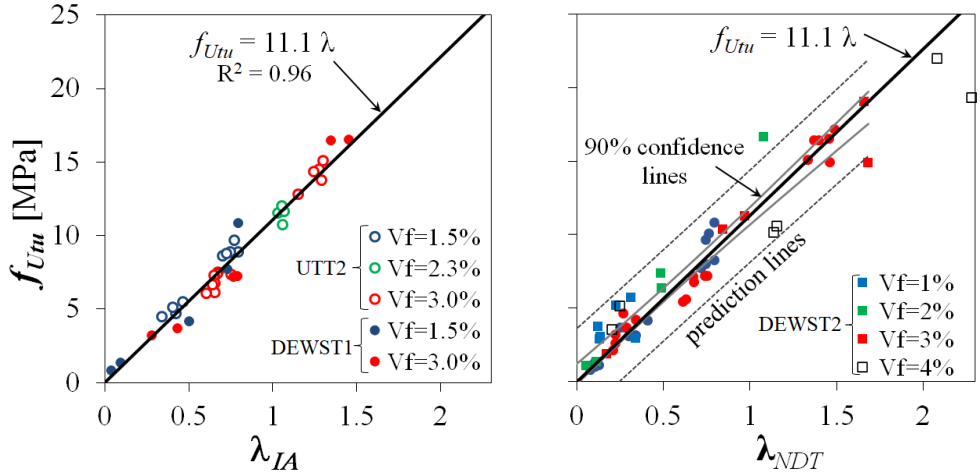

Figure 36. Relations between fUtu and λ from (a) image analysis (Abrishambaf, Pimentel, and Nunes 2017) and (b) NDT method.

2.3.8. Tensile strength prediction of a thin UHPFRC plate

2.3.8.1. Non-destructive measurements

A thin plate of 900x1100x30 mm^3 was cast horizontally using a mixture with 3% fibre content. The mix is characterized elsewhere (Abrishambaf, Pimentel, and Nunes 2017; 2019; Nunes et al. 2017) (UTT and DEWST1 specimens in Figure 36) and in the experiments described in section 2.3.6. The fresh mixture was poured in the point (CP: x=400, y=500 mm) and then vibrated on a vibrating table to help the material fill the mould (Figure 37).

Figure 37. Casting the plate.

Following the flowchart depicted in Figure 35, the NDT measurements were performed over an area of 700x900 mm^2 (respecting a 100 mm clearance from each border to avoid the boundary effects). The measuring grid of 50x50 mm^2 contained 285 points (15x19). Three non-collinear measurements were made on each point and always on the moulded (bottom) surface.

The directions of preferential fibre orientation were determined through the usual tensor operations and are represented by ellipses in Figure 38 (a). The major and minor radius are proportional to the corresponding fibre orientation factors. These were determined using the Eq. (22) with k_α=1.84 and α_0=0.54, resulting from Figure 15 considering the ratio h_U/l_f=2.5. Thus, the fibres tended to be preferentially oriented from the CP towards the bottom-left and top-right corners. Among all points and directions, the maximum orientation factor reached 0.88 and the minimum 0.19. The average values along x and y-directions equal 0.48 and 0.60, respectively.

The fibre content was determined using k_v=4.1. The colour map with V_f variation throughout the plate is shown in Figure 38 (b). The overall dispersion is 0.12%, with a

range from 2.76 to 3.47%. The global average is 3%, confirming the adequacy of the adopted k_v value.

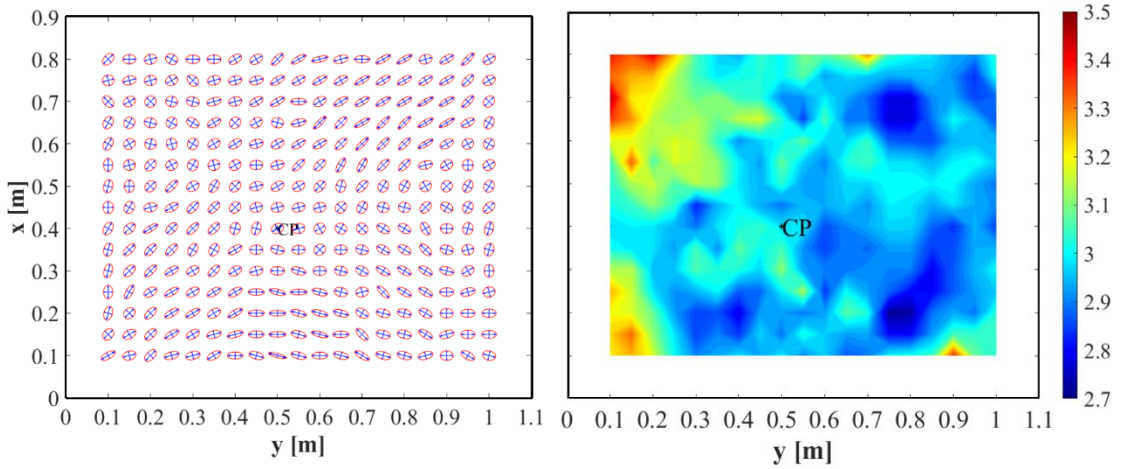

(a) (b)

Figure 38. NDT results: (a) fibre anisometry and (b) contour maps with the volumetric fibre fraction [%].

The post-cracking tensile strengths in the x-direction, $f_{Utu,x}$ and y-direction, $f_{Utu,y}$, were estimated applying the regression line of Figure 36 (a), with λ_i determined based on the known geometry of the fibres (l_f/d_f=60), V_f and $\alpha_{0,i}$ determined from NDT and $\alpha_{1,i}$ from Eq. (14). The contour maps are presented in Figure 39 and a large variability can be seen with values in the range 3-15 MPa. It is remarked that the 2nd order tensor approximation allows the determination $f_{Utu,i}$ not only in the x and y-directions but along any direction of interest.

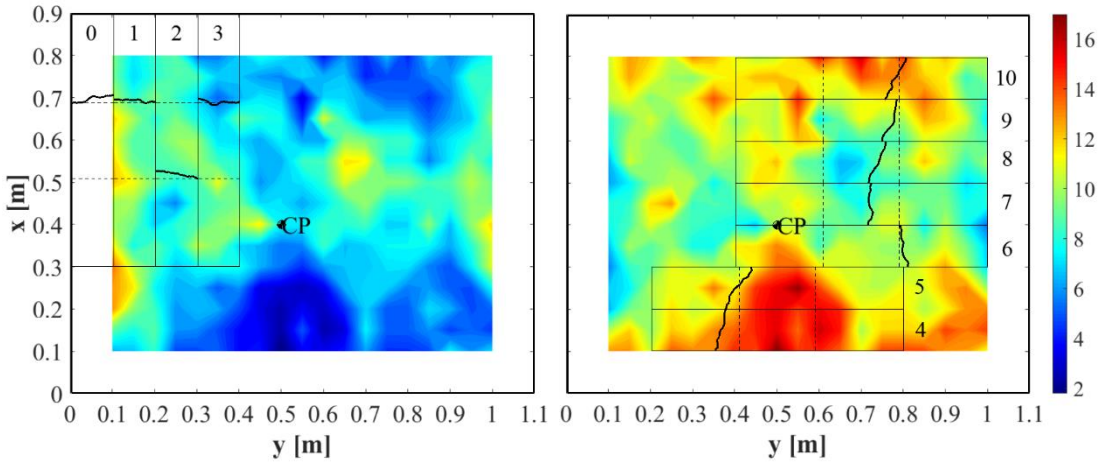

(a) (b)

Figure 39: NDT tensile strength [MPa] contour maps and FPBT cracks of LP1 (a) $f_{Utu,x}$ and (b) $f_{Utu,y}$.

2.3.8.2. Four-point bending test

After the NDT measurements, the plate was cut to obtain 10 specimens with approximately 100x600x30 mm^3 to be tested under four-point bending according to the French norm NF P18-470 (AFNOR 2016b) recommendations for thin elements. The location, orientation and numbering of the specimens are marked in Figure 39. The dashed lines delimit the region of constant bending moment. The tests were conducted under vertical displacement control with a rate of 0.25 mm/min. Two LVDT's were placed at mid-span to measure displacements, according to the setup depicted in Figure 40.

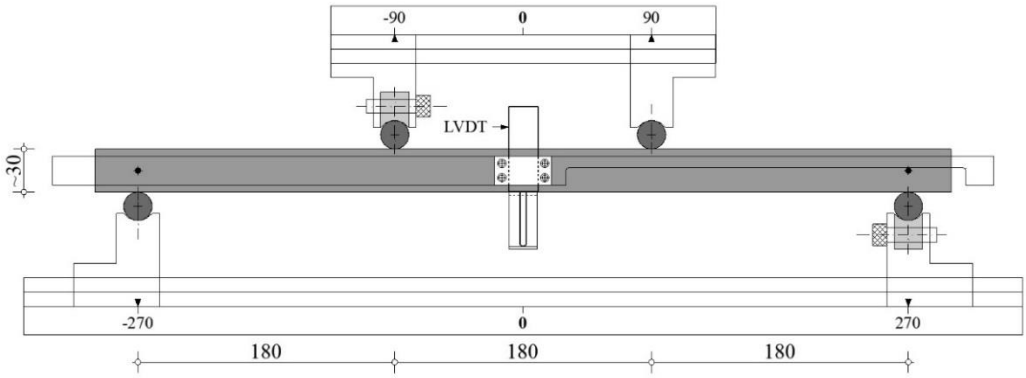

Figure 40. Four-point bending test scheme of the test setup.

The locations of the cracks are marked in Figure 39. In most cases, it is evident that the cracks formed within, or close to, the segment with the maximum moment, but following the regions identified by the NDT method as having lower values of $f_{Utu,i}$. The clear exception is specimen 8. However, it should be noted that due to the viscosity of the material, the casting surface was somewhat irregular, and crack localization may have been affected by the surface irregularities. The average thickness of each of the specimens is indicated Table 3. It is notable that in specimens 4 and 5, the shape of the cracks clearly suggests that they formed following the path of least resistance.

The bending moment versus the average midspan displacement curves are plotted in Figure 42. As expected from the NDT results, the variability is significant. Therefore, a simplified inverse analysis following the procedures indicated in the French norm (AFNOR 2016b) was developed to derive the simplified elastic-plastic UHPFRC constitutive law up to the onset of strain localization. The outcomes of the analysis are f_{Utu} and the strain at the onset of crack localization, ε_{Utu}. The elasticity modulus E_U=42 GPa was determined using the average slope at the origin of the M-δ curves of Figure 42, taking into account the actual average thickness of each specimen.

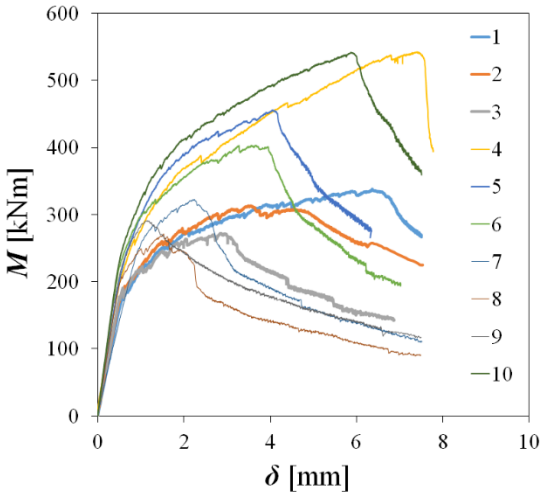

Figure 41. Four-point bending test results of plates 1-10.

The results from the simplified back analysis and the post-cracking tensile strength estimate from the NDT method are presented in Table 3. The latter refers to the average values over the crack cross-section and along the respective direction, i.e., $f_{Utu,x}^{NDT}$ for specimens 1, 2 and 3, and $f_{Utu,y}^{NDT}$, otherwise. The value of $\alpha_{0,i}$ was similarly derived. The agreement is noticeable, except for specimens 8 and 9. The average ratio $f_{Utu,i}^{NDT}/f_{Utu}^{FPBT}$=1.08, with a standard deviation of 0.11.

Table 3. Results from simplified back analysis of FPBT and NDT method.

Specimen	h_U **[mm]**	$\alpha_{0,i}^{NDT}$	M **[N]**	δ **[mm]**	χ **[m^{-1}]**	ε_{Utu} **[‰]**	f_{Utu}^{FPBT} **[MPa]**	$f_{Utu,i}^{NDT}$ **[MPa]**	$f_{Utu,i}^{NDT}/f_{Utu}^{FPBT}$
1	30.24	0.51	338	6.36	0.205	4.30	9.49	9.33	0.98
2	30.33	0.54	313	3.55	0.114	2.03	9.09	8.91	0.98
3	31.39	0.50	272	2.84	0.091	1.66	7.72	8.38	1.09
4	32.19	0.67	542	7.40	0.238	5.15	13.35	12.58	0.94
5	32.67	0.63	456	4.04	0.130	2.49	11.18	11.32	1.01
6	34.14	0.59	403	3.56	0.115	2.34	9.64	10.32	1.07
7	33.74	0.54	323	2.24	0.072	1.29	7.92	9.00	1.14
8	33.66	0.54	271	1.52	0.049	0.74	7.05	8.94	1.27
9	34.26	0.60	291	1.14	0.037	0.38	7.98	10.13	1.27
10	33.86	0.67	542	5.87	0.189	4.18	12.19	12.73	1.04
Min.	30.24	0.50	271	1.14	0.037	0.38	7.05	8.38	0.94
Max.	34.26	0.67	542	7.40	0.238	5.15	13.35	12.73	1.27
								Average	1.08
								Standard deviation	0.11

2.4. CONCLUSIONS

This Chapter presented further developments on the NDT magnetic method proposed by Nunes et al. (2016a; 2017) for quality control of thin UHPFRC elements containing short steel fibres. The method allows determining the fibre content and the fibre orientation factor, which can be used to estimate directionally dependent post-cracking tensile strength. A mathematical description of the fibre orientation was presented and used to derive the directional variation of the scalar descriptors of the fibre orientation usually adopted in engineering models. The simplified physical model of the composite was generalized to accommodate more realistic 2D fibre orientation distributions. The model predicts that the in-plane relative magnetic permeability of the composite is well approximated by a second-order tensor, which allows describing the anisometry of the fibre distribution in thin elements based on only three non-collinear inductance measurements. The validity of the fibre content and fibre orientation indicators was assessed using the developed model, substantiating the equations relating these indicators with V_f and $\alpha_{0,i}$. All this was validated with extensive experimental data.

The influence on the relative magnetic permeability estimates of factors that cannot be described by a simple model, such as the element thickness, surface finishing, the fibre sedimentation across the thickness and the distance of the probe to the boundaries, were assessed experimentally. It was shown that the magnetic probe used in this study can evaluate the fibre content and fibre orientation in the UHPFRC up to a depth of 70 mm measured from the contact surface and that the measurements should be taken 100mm away from the nearest border. An equation was proposed to correct the slope of the line relating V_f and $\mu_{r,mean}$ to account for the effect of the thickness of the element. The measurement should be taken preferably on moulded surfaces. In case this is not possible, the surface unevenness should be smoothed. The magnetic measurements are highly sensitive to fibre settlement across the thickness due to excessive agitation during casting or excessive fluidity of the material in the fresh state.

A methodology was systematized for using the NDT method for estimating the post-cracking strength of the UHPFRC. The procedure was validated, and good agreement with the experiments was achieved. Therefore, it can be concluded that the NDT method used here is a valuable tool for quality control on real applications.

3. Flexural Behaviour of Composite Beams and Slabs

3.1. INTRODUCTION

The strengthening of reinforced concrete (RC) substrate with a UHPFRC thin layer working in tension leads to a significant increase in the flexural stiffness and higher load-bearing capacity of the resulting composite RC-(R)U (RC-U or RC-RU) element. After the peak load is reached, a softening behaviour is observed due to the tensile contribution of the UHPFRC. In general, the element's ductility is reduced compared to that of the RC reference element of equal cross-section and equivalent reinforcement ratio (Pimentel and Nunes 2016c). As observed by Habel, Denarié and Brühwiler (2006), Oesterlee (2010) and Pimentel and Nunes (2016c), when testing beams with composite cross-section, the shape of the resulting force-displacement, or moment-curvature curve shows resemblance to the force-displacement curve of plain or reinforced UHPFRC ties under direct tension. The rebars significantly increase the resistance and improve the deformation capacity and the strain-hardening behaviour of the UHPFRC. The global tensile behaviour of an RU element can be described by the linear superposition of the reinforced steel and the UHPFRC tensile behaviours (Figure 42) (Redaelli 2009; Oesterlee 2010).

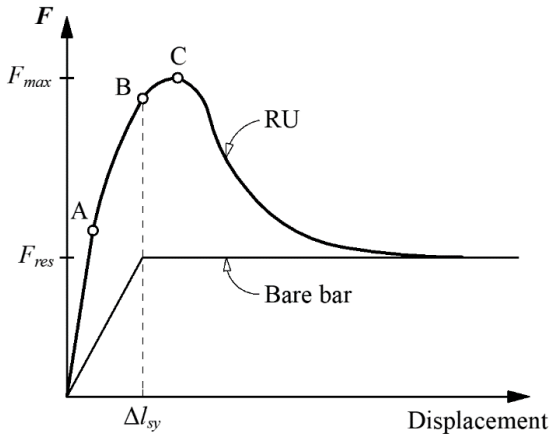

Figure 42. Characteristic tensile behaviour of RU element (Oesterlee 2010)

Flexural tests of RC-(R)U beams or one-way slabs strips under monotonic loading (Habel 2004; Oesterlee 2010; Meda, Mostosi, and Riva 2014; Pimentel and Nunes 2016c;

Bastien-Masse and Brühwiler 2016b; Al-Osta et al. 2017) showed the behaviour depicted in Figure 43. The following description refers to composite elements with or without reinforcement bars in the UHPFRC layer. Ordinary ribbed reinforcement steel is considered and, whenever the rebars are not present, the UHPFRC is assumed to have strain-hardening behaviour under direct tension:

a) The elastic behaviour of the materials is observed until the concrete cracks near the interface and micro-cracks start to form in the UHPFRC surface (Figure 43 (a)). Micro-crack formation in the UHPFRC layer marks its entry into the hardening domain, with the reinforcements still operating in the elastic domain. The UHPFRC layer presents micro-cracks openings generally below 50μm and remains practically impermeable. In general, at the end of this stage, the load reaches about 70% of the maximum load resistance, which generally exceeds the upper limit of the Service Limit State (SLS) loading level;

b) Depending on the existence, or on the extent, of the hardening branch of the UHPFRC, one of the following cases is observed (Figure 43 (b)):

   i. When a low strain hardening UHPFRC is used (or even a strain-softening UHPFRC) combined with a suitable minimum amount of rebars, the onset of strain localization in the R-UHPFRC layer coincides with reinforcement yielding. Therefore, it may be assumed that the post-cracking tensile strength, f_{Utu}, is fully mobilized at the onset of yielding and that $\varepsilon_{Utu} = \varepsilon_{syU}$;

   ii. When a UHPFRC with large strain-hardening is employed, the reinforcement starts yielding before the UHPFRC layer ends the hardening phase ($\varepsilon_{Utu} > \varepsilon_{syU}$), like point B in Figure 42.

c) Then follows the appearance of a localized macro-crack (visible to the naked eye) in the UHPFRC surface and its development towards the interface (Figure 43 (c));

d) The maximum flexural strength is reached at the onset of yielding the reinforcement embedded in the concrete substrate, with the UHPFRC layer already in the softening domain (Figure 43 (d)). The softening branch of the moment-curvature relation is governed by the post-peak tensile behaviour of the UHPFRC and by the bond stress transfer between the rebars and the surrounding UHPFRC;

e) The failure occurs either by breaking the reinforcement embedded in the composite (Figure 43 (e)) or crushing the concrete under compression. If full

UHPFRC tensile stress release is achieved before the rebars break, the residual capacity of the composite element corresponds to that of the RC beam with an equal reinforcement amount.

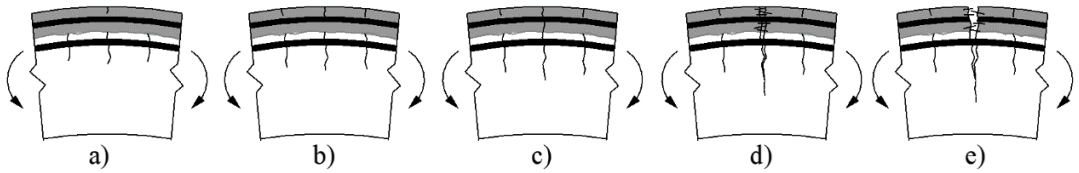

Figure 43. Flexural cracking development in RC-(R)U, adapted from (Habel 2004)

When the UHPFRC layer is under compression, its strength is not fully exploited since the compressive strength of the concrete substrate near the interface is about 3 to 6 times lower. Thus, the conventional concrete may crush before the UHPFRC (Brühwiler 2017). Adding the UHPFRC layer on the compression side increases the reinforcement effective depth, similar to what happens with the addition of the normal strength concrete. In these conditions, the gain in resistance is equivalent, but because of the higher compressive strength of UHPFRC, the eventual failure by concrete crushing will be delayed. In general, the sectional analysis of the flexural strength under Ultimate Limit State (ULS) can be made using linear UHPFRC behaviour. Avoiding the crushing of the adjacent concrete becomes the determinant design criterion rather than the UHPFRC reaching its compressive strength (Brühwiler 2020).

In this Chapter, the flexural behaviour of composite RC-(R)U elements is discussed, and the influence of the tensile properties of the UHPFRC layer on the behaviour of the composite cross-section is evaluated. Based on the analysis of cross-sections resorting to a layered discretization through Nonlinear Finite Element Analysis (NLFEA) and realistic stress-strain constitutive laws for the materials, a simplified analytical model was derived for obtaining the most relevant points of the moment-curvature (M-κ) relation. The models are validated with experimental results.

The UHPFRC layer is assumed to be in tension, simulating the hogging bending moment region of an existing RC slab or beam over which a UHPFRC layer has been poured. Thus, the effects of the previous loading are neglected, and the RC substrate is considered initially uncracked.

3.2. SIMPLIFIED ANALYTICAL MODEL

The determination of the cross-sectional flexural response of a composite element is performed considering the following assumptions:

a) Plane sections remain plane after the deformation (Bernoulli hypothesis),
b) Perfect bond between the materials (monolithic behaviour);
c) The material behaviour is described according to the respective stress-strain constitutive laws; and
d) Translational and rotational static equilibrium of the cross-section is ensured.

Habel (2004) introduced a cross-sectional analysis model involving an iterative procedure to establish the equilibrium of the normal forces acting in the cross-section. This was simplified by Bastien-Masse and Brühwiler (2016a), who proposed multilinear moment-curvature relation in which the coordinates of the vertices correspond to notable points of the material constitutive laws. Furthermore, the multilinear curve was generalized to accommodate the case where the bending moment vector is not orthogonal to the flexural reinforcement. Following the same line of thinking, Figure 44 shows the multilinear moment-curvature approximation of the moment-curvature curves of both RC and RC-(R)U cross-sections. The multilinear curves are defined up to point C, referring to the maximum bending resistance.

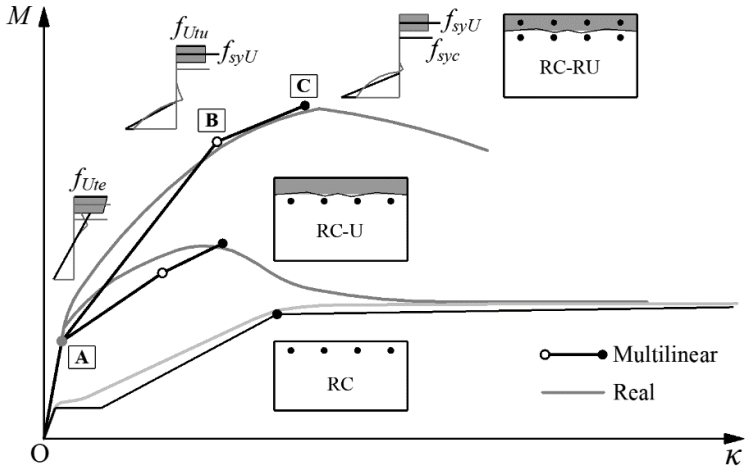

Figure 44. Bending moment-curvature relations.

The calculations are made obeying the equilibrium of forces in the composite cross-section as shown in Figure 45, according to the material constitutive laws of Figure 46. It

is also noted that the concrete tensile strength is neglected after point A. As the forces are assumed to act at the cracked section, no tension stiffening effects are accounted for. Linear concrete compressive is considered, and the contribution of the reinforcement in the compressive zone is neglected. Moreover, the reinforcement in the UHPFRC is considered to be placed in the middle of the layer, that is, $d_U=d_{sU}$.

Due to the synergetic behaviour of the rebars and the fibres, it is assumed that the strain localization in the UHPFRC occurs at onset of reinforcement yielding, that is, $\varepsilon_{Utu}=\varepsilon_{syU}$, regardless of whether the UHPFRC itself has a strain-softening or -hardening tensile behaviour (Redaelli 2009; Oesterlee 2010; Valente, Pimentel, and Nunes 2021).

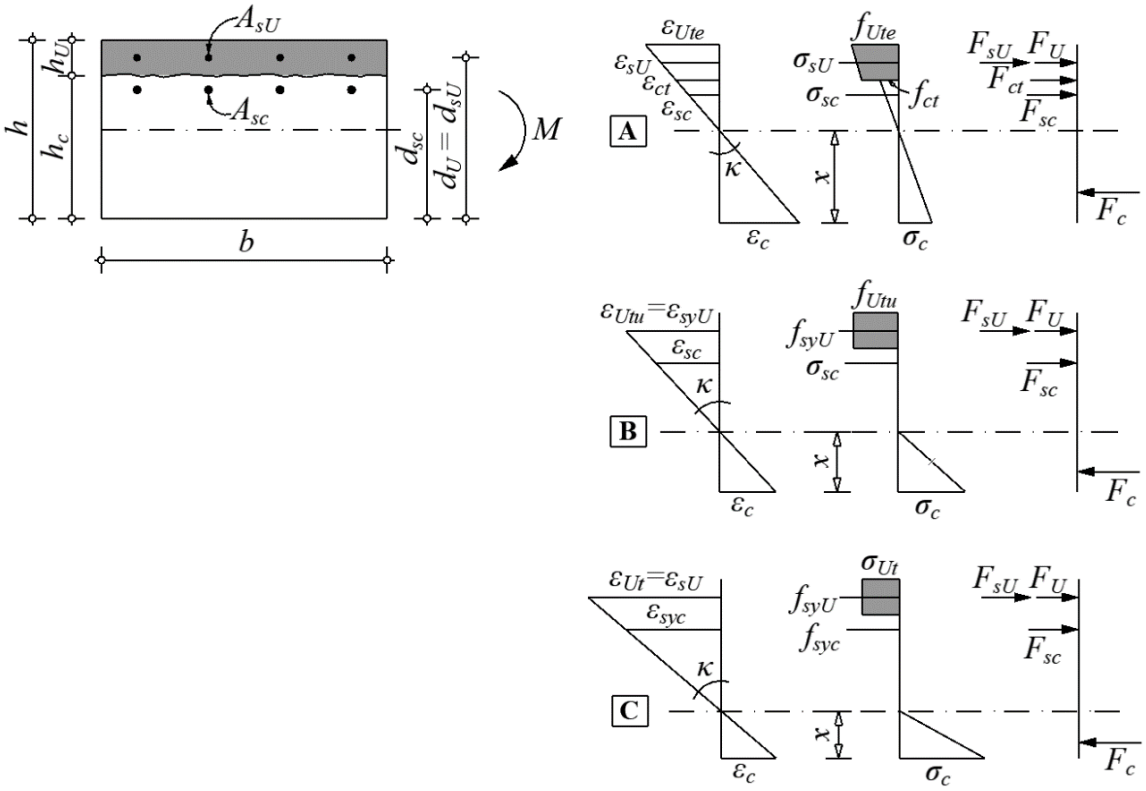

Figure 45. Analytic model of the hybrid (a) cross-section and (b) equilibrium of forces.

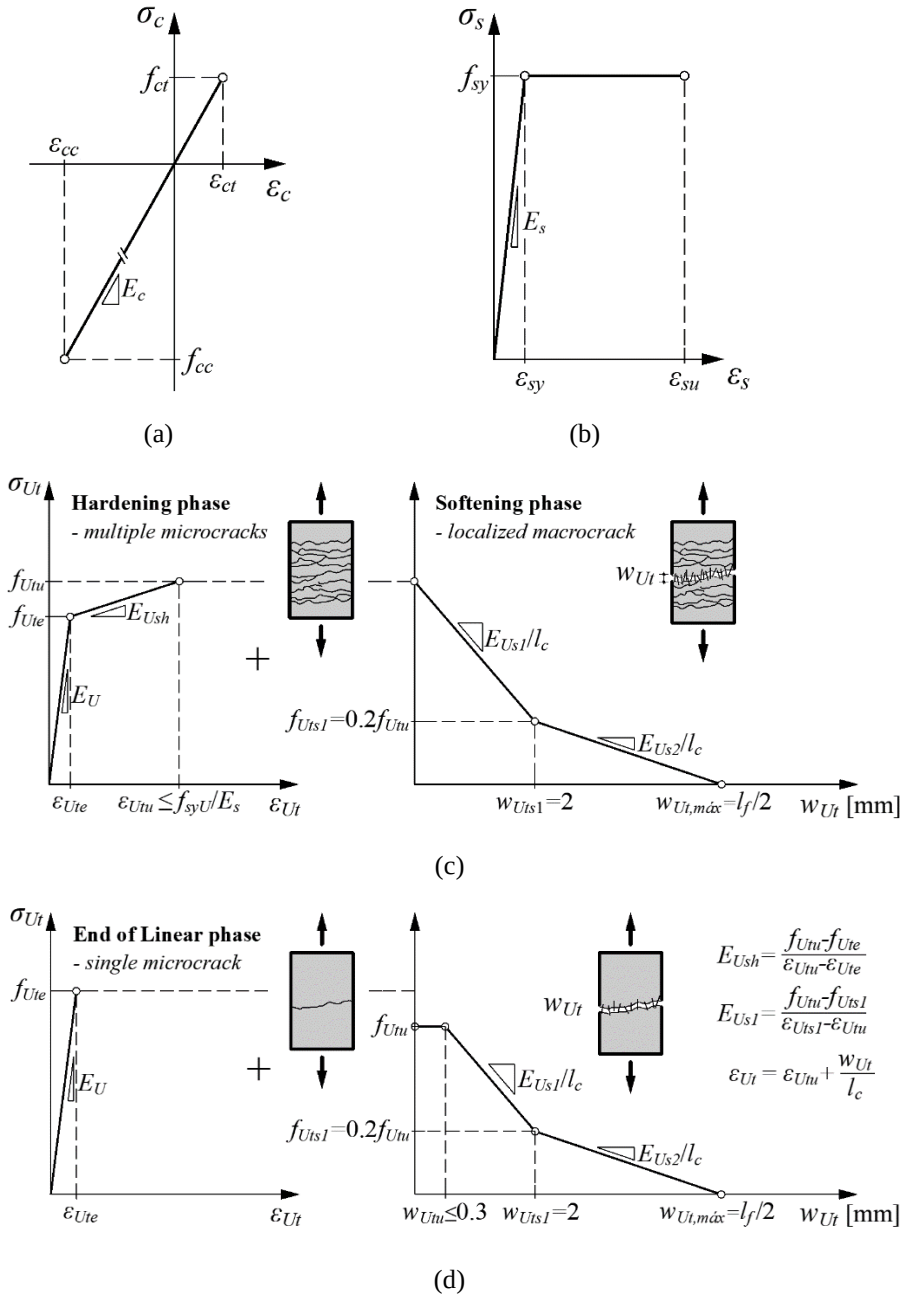

Figure 46. Materials constitutive laws (a) concrete, (b) steel, and UHPFRC with (c) strain-hardening and (d) strain-softening behaviour.

The multilinear moment-curvature curve is defined by the points A to C, schematically identified in Figure 44, can be described as follows:

a) Elastic phase (O to A - $\sigma_{Ut} \leq f_{Ute}$): The conventional limit of elasticity in bending, denoted by point A, can simply be determined considering that all the materials are elastic until the first crack appears on the UHPFRC surface;

b) Hardening phase (A to B - $\sigma_{Ut}=f_{Utu}$): This phase develops when most RC-(R)U composite cross-sections operate under service loads. Therefore, a reasonable simplifying assumption consists in defining point B as the instant when the UHPFRC reaches its post-cracking tensile strength, f_{Utu}. Since for the reinforced UHPFRC layer, it is assumed that the $\varepsilon_{Utu}=\varepsilon_{syU}$, then $\sigma_{sU}=f_{syU}$: The reinforcement in the RC substrate is still elastic;
c) Yielding phase (B to C - $\sigma_{sc}=f_{syc}$): In this phase, the reinforcement in the UHPFRC layer is experiencing plastic deformations, and the UHPFRC layer is in the softening regime. Point C corresponds to the onset of yielding of the reinforcement in the RC substrate.

In most common situations, the maximum bending moment is achieved at yielding of the reinforcement in the RC substrate (point C). Only when very ductile UHPFRC layers ($\varepsilon_{Utu}>>\varepsilon_{syc}$) are used, the moment can still increase. This case is not considered in the proposed equations. Besides, whenever high strength steel is used in the UHPFRC layer, the resistance occurs at point B, and it can be determined considering the UHPFRC tensile strength (again $\varepsilon_{Utu}=\varepsilon_{syU}$) and the yielding stress of both reinforcements.

Table 4 presents the equations defining points A, B and C. Before point A, the bending moment for any given curvature, κ, is calculated considering its product with the elastic flexural stiffness, EI_0, using Eq. (26). Next, the bending moments corresponding to points B and C are calculated performing the equilibrium of moments in the cross-section applying Eq. (27).

A: $$M=\sum E_i I_i \kappa = EI_0 \kappa \tag{26}$$

B and C: $$M=(F_U+F_{sU})\left(d_U-\frac{x}{3}\right)+F_{sc}\left(d_{sc}-\frac{x}{3}\right) \tag{27}$$

where the subscript *i* refers to each material (concrete, UHPFRC and reinforcement steel), *E* is the elasticity-modulus, and *I* the second moment of the area around the axis passing through the centroid of the homogenized section.

Table 4. Analytical model equations.

Points	Forces		x	κ
A	$F_U=f_{Ute}h_Ub$ $F_{sU}=\varepsilon_{sU}E_{sU}A_{sU}$ $F_{sc}=\varepsilon_{sc}E_{sc}A_{sc}$ $F_{ct}=0.5f_{ct}(h_c-x)b$ $F_c=0.5\varepsilon_cE_cxb$		$\frac{\sum E_iA_id_i}{\sum E_iA_i}$	$\frac{f_{Ute}}{E_U(h-x)}$
B	$F_U=f_{Utu}h_Ub$ $F_{sU}=f_{syU}A_{sU}$ $F_{sc}=\varepsilon_{sc}E_{sc}A_{sc}$ $F_c=0.5\varepsilon_cE_cxb$		$\frac{\sqrt{C_1^2+C_2C_c}-C_1}{2C_c}$	$\frac{\varepsilon_{Utu}}{d_U-x}$
C	$F_U=\left\{f_{Utu}+E_{Us1}\left[\varepsilon_{Utu}-\frac{(d_U-x)}{(d_{sc}-x)}\varepsilon_{syc}\right]\right\}h_Ub$ $F_{sU}=f_{syU}A_{sU}$ $F_{sc}=f_{syc}A_{sc}$ $F_c=0.5\varepsilon_cE_cxb$			$\frac{\varepsilon_{syc}}{d_{sc}-x}$
Coefficients				
B	$C_{sc}=\varepsilon_{Utu}E_{sc}A_{sc}$ $C_c=0.5\varepsilon_{Utu}E_cb$		$C_1=F_U+F_{sU}+C_{sc}$ $C_2=(F_U+F_{sU})d_U+C_{sc}d_{sc}$	
C	$C_c=0.5\varepsilon_{syc}E_cb$ $C_{U1}=f_{Utu}h_Ub$	$C_{U2}=\varepsilon_{Utu}E_{Us1}h_Ub$ $C_{U3}=\varepsilon_{syc}E_{Us1}h_Ub$	$C_1=C_{U1}+C_{U2}-C_{U3}+F_{sU}+F_{sc}$ $C_2=(C_{U1}+C_{U2}+F_{sU}+F_{sc})d_{sc}-C_{U3}d_U$	

The assumption of linear concrete compressive behaviour leads to underestimating the height of the compression zone and the maximum concrete compressive strain. However, and as will be seen later on, this is only significant for highly reinforced members, typically beams, in which case the concrete compressive stress, σ_c, determined under the linear behaviour assumption, may exceed the compressive strength, f_c. In these cases, the moment capacity (point C) needs to be verified using the equivalent concrete stress block distribution, considering the maximum compressive strain $\varepsilon_{cu}\leq 3.5‰$ (IPQ 2010), as per Eq. (28). As a simplification, shown in Figure 47, F_U may be determined assuming constant stress distribution within the UHPFRC layer equal to f_{Utu}.

$$M_R=(F_U+F_{sU})(d_U-0.4x)+F_{sc}(d_{sc}-0.4x) \quad (28)$$

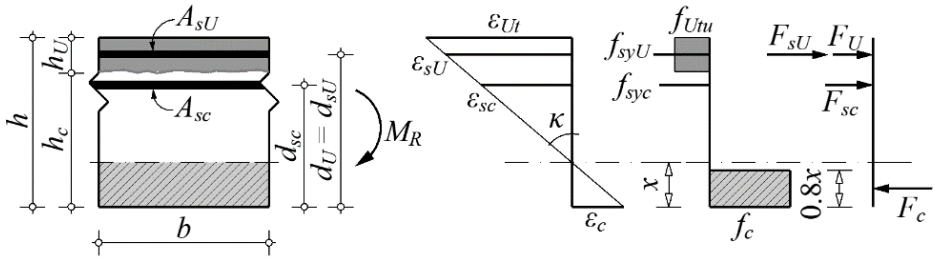

Figure 47. Sectional analysis with concrete stress block.

3.3. NUMERICAL LAYERED DISCRETIZATION

A numerical model based on a layered discretization of the cross-section may be used to verify some of the simplifying assumptions of the multilinear moment-curvature relation described in the previous section. Each layer is assumed to follow a nonlinear stress-strain law according to the correspondent material. Rebars can be added where appropriate. Besides the equilibrium of the forces along the normal to the cross-section, the compatibility conditions are fulfilled, corresponding to the usual assumption that plane sections remain plane and that the composite cross-section is monolithic. The shear deformations are neglected.

The numerical modelling was performed using the software DIANA FEA 10.5. The model comprehends a finite beam element of 3 nodes, as depicted by Figure 48. For the integration along the axis, the Gauss quadrature of 2 nodes was considered, whereas, across the depth, the Simpson method (11 layers for each 50 mm) was adopted. The beams are fixed in one end, and the bending moment is applied to the other.

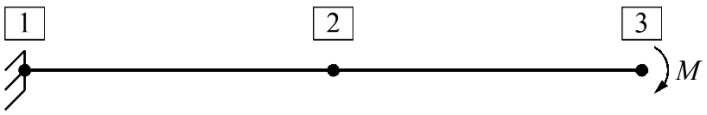

Figure 48. Unidimensional finite element of 3 nodes.

Concrete is assumed to follow a parabolic stress-strain curve in compression (Figure 49 (a)) and the exponential tension-softening law (Figure 49 (b)). As for the UHPFRC in tension, a quadrilinear relation is adopted, as previously shown in Figure 46 (c-d). The characteristic length allowing the transformation of the crack-opening into strains was

assumed to be l_c=2/3h (AFGC 2013), with h= h_c+h_U being the total cross-section depth. An elasto-plastic law is adopted for the steel rebars (Figure 46 (b)). The reinforcement is modelled as embedded truss elements sharing the displacement field of the embedding concrete element.

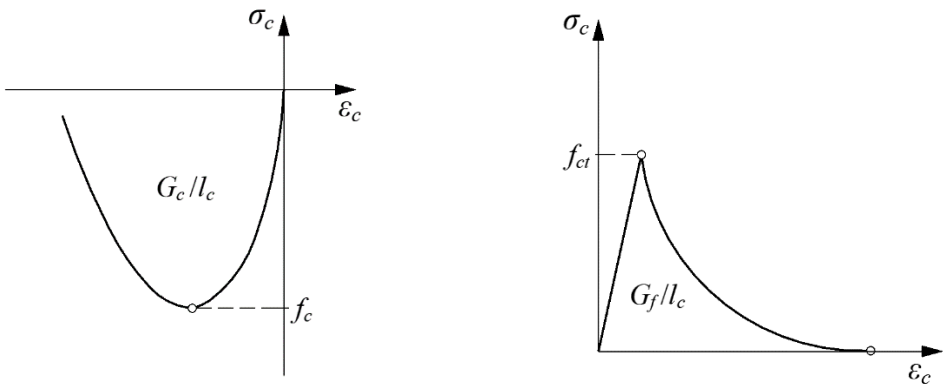

(a) (b)

Figure 49. Concrete nonlinear behaviour: a) parabolic compression curve and b) exponential tension-softening curve.

3.4. EXPERIMENTAL VALIDATION

An experimental campaign consisting of two series, LA and LB, was carried out to simulate the flexural behaviour of one-way composite and reference RC slabs strips. The results of the campaign are used to validate both the simplified analytical model and the layered discretization.

3.4.1. Specimens specifications

The series LA was initially presented elsewhere (Pimentel and Nunes 2016c) and comprises four slabs, two reference RC, one with a single reinforcement layer (LSA) and another with double (LDA), and two composite slabs, one without reinforcement in the UHPFRC layer (LSA-U) and another with reinforcement (LSA-RU1). Series LB also consists of four slabs, one LDB similar to the LDA, one LSB-U similar to the LSA-U, and two with reinforcement in the UHPFRC layer, LSB-RU1 and LSB-RU3.

The test series differ from each other essentially in the static system. In both series, the UHPFRC layer is under tension. As shown in Figure 50 (a), the LSA series slab strips were tested in a TPBT cantilevered setup, with a maximum shear span a=1.0 m, corresponding to a/h_c=5. On the other hand, the slab strips of the LSB series were tested in four-point bending, with a shear span a=0.65m, corresponding to a/h_c=3.25, see Figure 50 (b). The specimen specifications are summarized in Table 5. The reinforcement ratio in the RC substrate is determined as $\rho_{sc}=A_{sc}/(b.d_{sc})$ and the reinforcement ratio in the UHPFRC layer as $\rho_{sU}=A_{sU}/(b.h_U)$.

And for the reinforcement ratio on the UHPFRC layer, ρ_{sU}=1.57%, 2.26% and 0.76% for LSA-RU, LSB-RU1 and LSB-RU2, respectively. All slabs have the same reinforcement ratio in the substrate, ρ_{sc}=0.47%, except LDA e LDB that have ρ_{sc}=0.81%. The slabs have a width b=400 mm. The composite cross-sections have h_c=180 mm, h_U=50 mm and d_{sU}=225 mm. The resulting total depth, h=250 mm, of the composite cross-sections is equal to that of the LDA and LDB. The latter two have the same reinforcement as LSA-RU. The cross-sections geometric specifications are illustrated in Figure 50 (c). All specimens are shear reinforced in almost half-length.

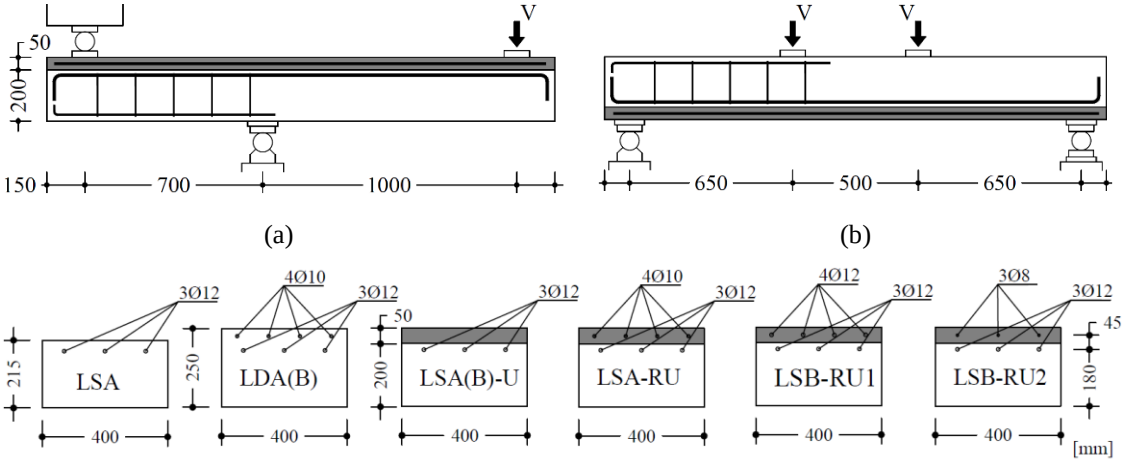

Figure 50. Specimens geometric specifications (a) series LA side view, (b) series LB side view and (c) cross-sections.

Table 5. Specimen specifications.

Series	Specimens	Cross-section type	h [mm]	a [mm]	Concrete substrate				UHPFRC layer			
					h_c [mm]	d_{sc} [mm]	Bars	ρ_{sc} [%]	h_U [mm]	$d_U = d_{sU}$ [mm]	Bars	ρ_{sU} [%]
LA	**LSA**	RC	215	1000	215	180	3ϕ12	0.47	-	-	-	-
	LDA	RC	250		250	200	3ϕ12 + 4ϕ10	0.81	-	-	-	-
	LSA-U	RC-U	250		200	180	3ϕ12	0.47	50	225	-	-
	LSA-RU	RC-RU	250		200	180	3ϕ12	0.47	50	225	4ϕ10	1.57
LB	**LDB**	RC	250	650	250	180	3ϕ12 + 4ϕ10	0.81	-	-	-	-
	LSB-U	RC-U	250		200		3ϕ12	0.47	50	225	-	-
	LSB-RU1	RC-RU	250		200		3ϕ12	0.47	50	225	4ϕ12	2.26
	LSB-RU2	RC-RU	250		200		3ϕ12	0.47	50	225	3ϕ8	0.75

3.4.2. Materials

The material mechanical properties are presented in Table 6. All the specimens were cast with ready-mix concrete with maximum aggregate size, d_g=14 mm. The compressive and splitting tensile strength in Table 6 were determined at 28 days as the average of three tests in standardized Ø150x300 (mm) cylinders. The ribbed reinforcement belongs to S500, a high ductility class steel, presenting strains at peak stress over 7.5%.

The UHPFRC was produced in the laboratory, and it contained V_f=3% of smooth and straight high-steel fibres (f_y=2100 MPa) with lengths l_f=9 and 12 mm (half of each) and diameter d_f=0.175 mm. The detailed characterization of the tensile response of the UHPFRC is presented elsewhere (Abrishambaf, Pimentel, and Nunes 2017; 2019) for a wide range of fibre contents and orientation profiles. For V_f=3% and well-oriented fibres corresponding to a fibre orientation factor α_0=0.73, the UHPFRC exhibited large strain-hardening behaviour reaching f_{Utu}=15.0 MPa and ε_{Utu}=5‰. In the case of poorly oriented fibres (α_0<0.44), only strain-softening with f_{Utu}=6.1 MPa was registered. As for the specimens with α_0=0.48-0.50 corresponding to a fibre distribution with no preferential orientation (random), the tensile strength was about 7.4 MPa, and ε_{Utu} ranged between 2.1 and 2.7‰ (Abrishambaf, Pimentel, and Nunes 2017). Considering the results presented in Chapter 2, where the fibre orientation factor is defined according to the ratio h_U/l_f, the value $\alpha_0(h_U/l_f$=4.2)=0.52 is achieved. The structure parameter is determined as λ=0.75,

which leads to f_{Utu}=8.3 MPa. The other parameters are derived, resorting to the meso-mechanical model described elsewhere (Abrishambaf, Pimentel, and Nunes 2019).

Table 6. Material mechanical properties.

Concrete			**UHPFRC**				**Steel**		
E_c	f_c	$f_{ct,sp}$	E_U	f_{Ute}	f_{Utu}	ε_{Utu}	f_{sy} **[MPa]**		
[GPa]	**[MPa]**		**[GPa]**	**[MPa]**		**[‰]**	ϕ8	ϕ10	ϕ12
31	35	3.1	45	7.2	8.3	3.0	513	605	537

3.4.3. Specimens preparation

For the composite slabs, the interface of the substrate was roughened, exposing the coarse aggregate to ensure proper bonding between both layers. For that regard, a pneumatic hammer was used to demolish the 15 mm cover of the existing concrete (Figure 51 (a)), whereas for the LSB-RU slabs, a retarder was used, then washed with a low-pressure water jet (Figure 51 (b)).

Before applying the UHPFRC strengthening layer, the substrate surface was saturated. Figure 51 (c-d) shows the casting procedure of the self-compacting UHPFRC.

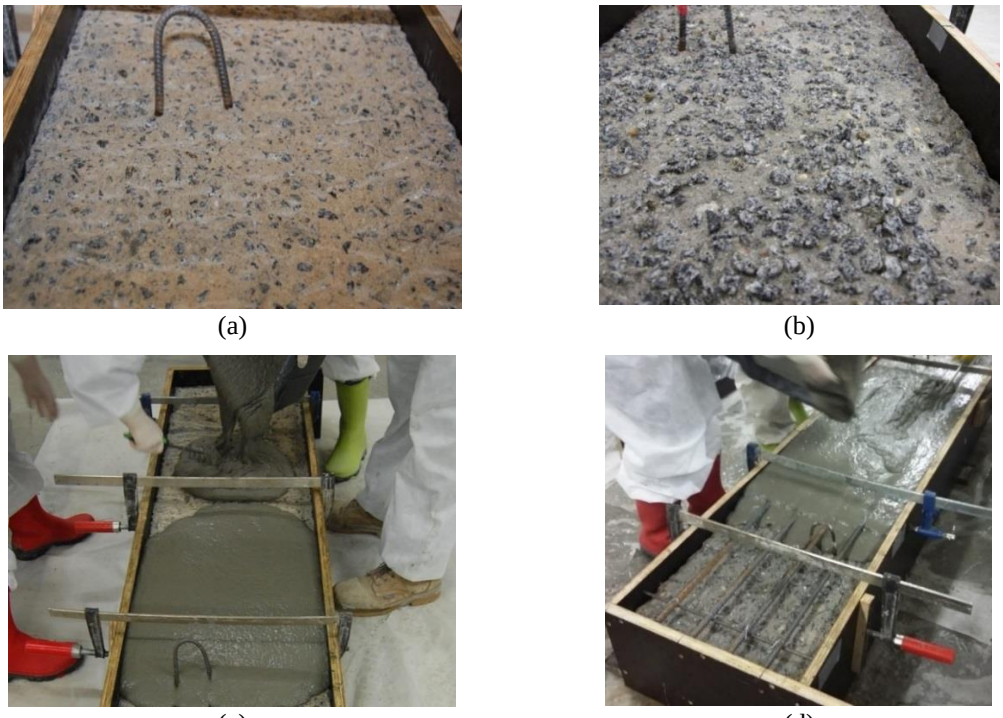

(a) (b) (c) (d)

Figure 51. Hybrid specimen preparation (a) surface roughened by hammer (b) and by washing after applying hardening retarder, and (c-d) casting procedure.

3.4.4. Test setup, instrumentation and procedure

As aforementioned, the test setup consisted of a three-point bending (TPBT) for the LA series and four-point bending (FPBT) for series LB. The former had a 1000 mm long cantilevered span with the tension side facing the top, as shown in Figure 50 (a). The latter was simply supported with two similar shear spans, a=650 mm, and the central region of a constant bending moment with 500 mm.

The slabs were instrumented with horizontal and vertical LVDTs, according to Figure 52. The horizontal LVDTs were used to determine the curvature.

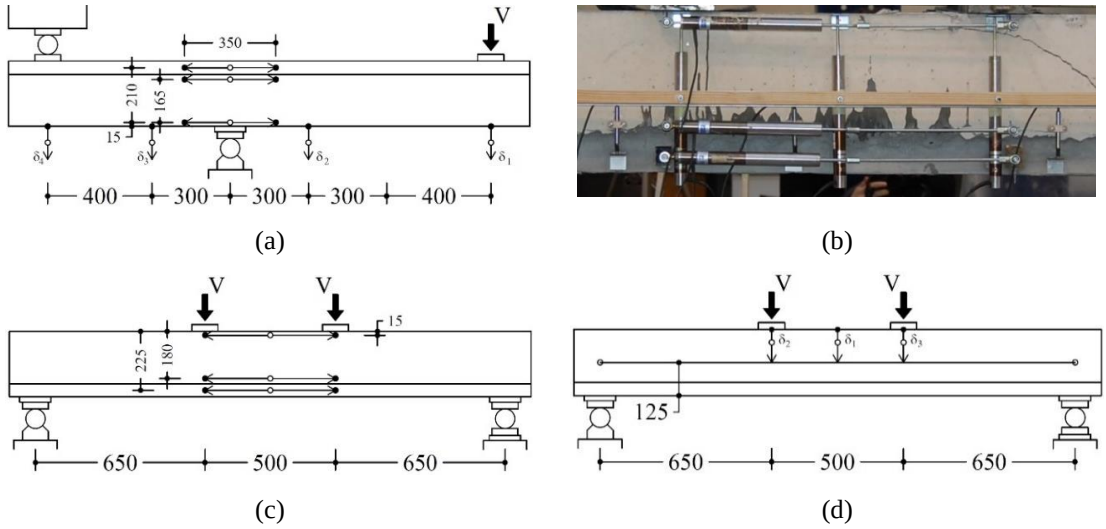

Figure 52. Instrumentation (a) series LA (Pimentel and Nunes 2016c) and (b-d) series LB.

3.4.5. Results

The bending moment-vertical displacement (M-δ) relations are presented in Figure 53 and the cracking patterns after failure in Figure 54 and Figure 55. The vertical displacement of the LA series refers to the load application alignment, whereas the LB series refers to the mid-span. All LA slabs exhibited flexural failures, whereas, in LB, the predominant failure mode was shear, even in the case of LBD, this occurred after longitudinal reinforcement yielding. The specimen LSB-U failed in flexure but with the main crack localized outside the constant bending moment region.

The slab LSA-RU was considerably stiffer than the reference slabs and resisted 2.48 and 1.15 times more than LSA and LDA. This comes at the expense of smaller ductility. The reinforcement bars in the UHPFRC layer broke at $0.86M_R$ and $2.4\delta_R$, with M_R and $2\delta_R$

being the moment and the vertical displacement at peak load. After the rebars broke, the residual moment followed the reference LSA (Figure 53 (a)). The maximum displacements up to the failure of the LSA and LDA were 4.3 and 5.6 times larger than the LSA-RU deflection at the maximum bending moment, respectively. The rupture of the rebars was also observed in RU ties tested by (Redaelli 2009) and RC-RU composite beams tested by (Oesterlee 2010).

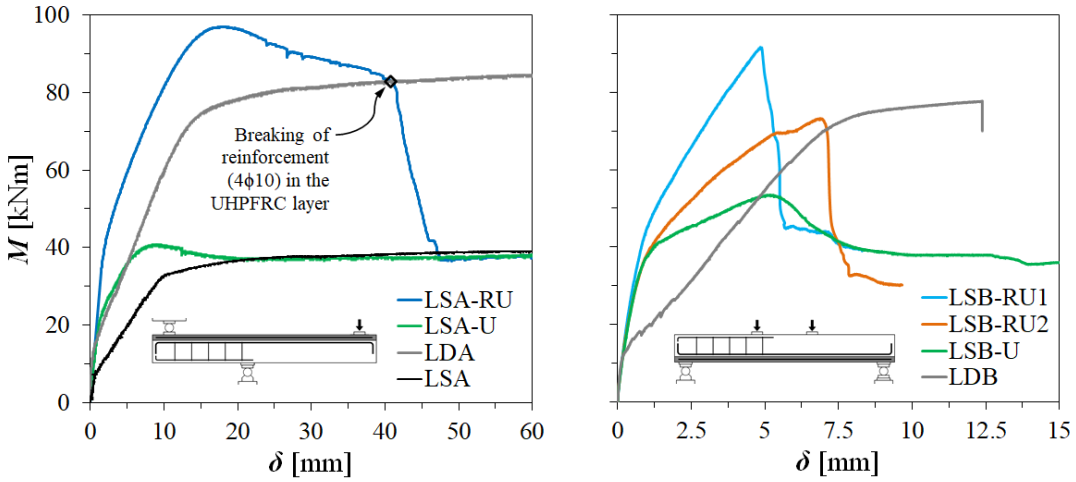

Figure 53. Experimental results (a) series LA (Pimentel and Nunes 2016c) and (b) series LB.

In the composite slabs, the flexural cracks were primarily observed on the concrete substrate near the interface. Only with additional loading, the cracks appeared on the UHPFRC strengthening layer.

The LDB specimen failed in shear while the reinforcement was already yielding. In this slab, the critical shear crack crossed the full depth. In the composite slabs LSB-RU1 and LSB-RU2, the diagonal shear crack is arrested at the interface and propagates along the interface (Figure 54). This failure mode will be discussed in detail in Chapter 4. Compared to the beams of Chapter 4, it is apparent that the use of a pneumatic hammer over a wider surface does not seem to ensure the same adhesion of the UHPFRC to the RC substrate as the hydro jetting.

The flexural capacity of slabs LSB-RU1 and LSB-RU2 was not reached. Nevertheless, a macro-crack crossing all the width on the face of the UHPFRC layer was observed. Furthermore, the crack appeared almost in the same alignment as the tip of the critical shear crack near the interface.

LSA:
M_R=39 kNm

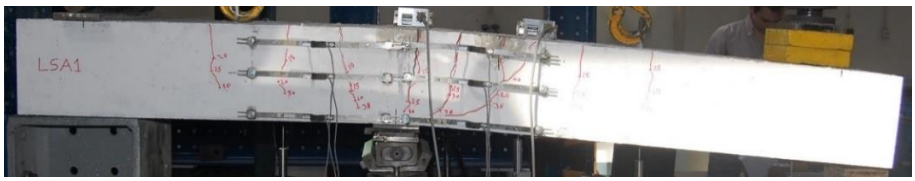

LDA:
M_R=84 kNm

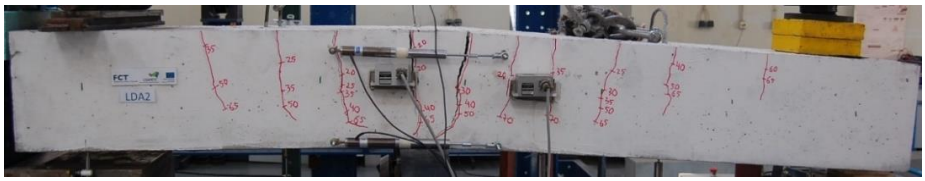

LSA-U:
M_R=42 kNm

LSA-RU:
M_R=97 kNm

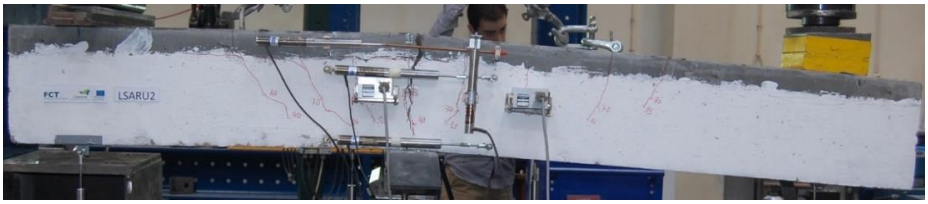

Figure 54. Cracking pattern after the failure of LA slabs.

LDB:
V_R=118 kN;
M_V=77 kNm

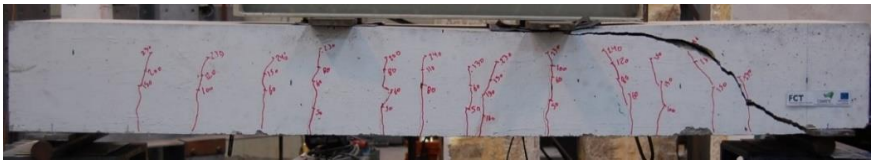

LSB-U:
M_R=53 kNm

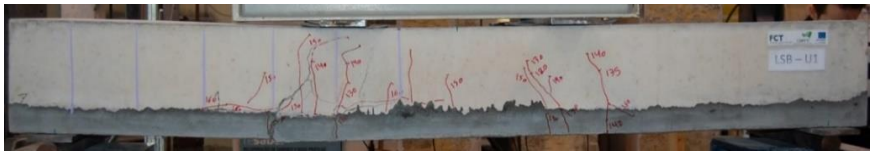

LSB-RU1:
V_R=141 kN;
M_V=92 kNm

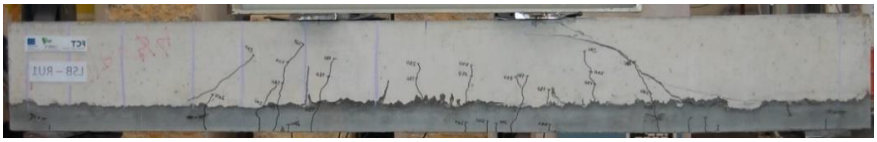

LSB-RU2:
V_R=112 kN;
M_V=73 kNm

Figure 55. Cracking pattern after the failure of LB slabs.

No visible micro-cracks were detected with the naked eye on the plain UHPFRC layers of LSA-U and LSB-U, and the failure macro-cracks have deviated from the maximum

bending cross-section (LSA-U) or region (LSB-U) to a section where the local fibre content and orientation were unfavourable (Nunes, Pimentel, and Carvalho 2016b; Pimentel and Nunes 2016b). The weak section was originated due to the discontinuous casting process illustrated in Figure 51 (c).

Furthermore, the maximum moment in slab LSB-U was 26% larger than that of LSA-U, even though the cross-sections of both slabs are the same. In fact, plain UHPFRC layers are susceptible to fibre content and anisometry, as discussed in chapter 2.

3.4.6. NDT on the UHPFRC layers of slabs LSA-U and LSB-U

To understand the results of slabs LSA-U and LSB-U, the tensile strength estimates provided by the NDT method in the vicinity of failure macro-cracks are presented, following the framework developed in Chapter 2. The 25x25 mm^2 measurement grids are depicted in Figure 56. The grids are centred on the maximum bending moment alignments, y=0.85 and 0.75 m for LSA-U and LSB-U, respectively. Note that the right side of the latter is under a constant moment.

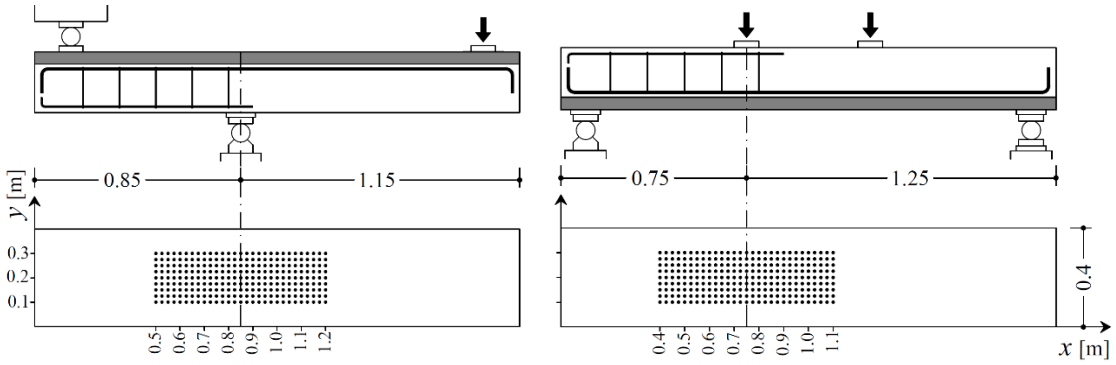

(a) (b)

Figure 56. NDT measurement grid (a) LSA-U (Pimentel and Nunes 2016b) and (b) LSB-U.

The macrocrack of slab LSA-U opened along the alignment x=0.8 m, only 50 mm on the left side of the maximum bending moment alignment (Figure 57 (a)), whereas in slab LSB-U, it opened along the alignment x=0.6 m, 150 mm on the left side of the constant maximum bending moment region (Figure 57 (b)).

The average fibre content and orientation factor along the alignment x=0.8 m of LSA-U are V_f=2.93%, and $\alpha_{0,x}$=0.42 (below the global average, 0.48). The resulting tensile

strength is $f_{Utu,x}$=5.9 MPa, below the average of the slab in the interval [x=0.5, 1.2 m], 7.6 MPa, and falling within the range of the strain-softening behaviour (Figure 57(a)).

As for the LSB-U, the averages along alignment x=0.6 m are V_f=2.96%, and $\alpha_{0,x}$=0.47 (below the global average, 0.57), and the resulting tensile strength is $f_{Utu,x}$=7.1 MPa (λ=0.75), also below the average of the slab in the interval [x=0.4, 1.1 m] 9.95 MPa, but within the strain-hardening range (Figure 57 (b)). The dark red area of the $f_{Utu,x}$ map refers to a region over which the NDT measurements could not be performed due to the existence of embedded steel hooks (on the x=0.55 m alignment) used to lift the slab. The NDT results show that the cracks appeared in the regions with lower tensile strength for both slabs.

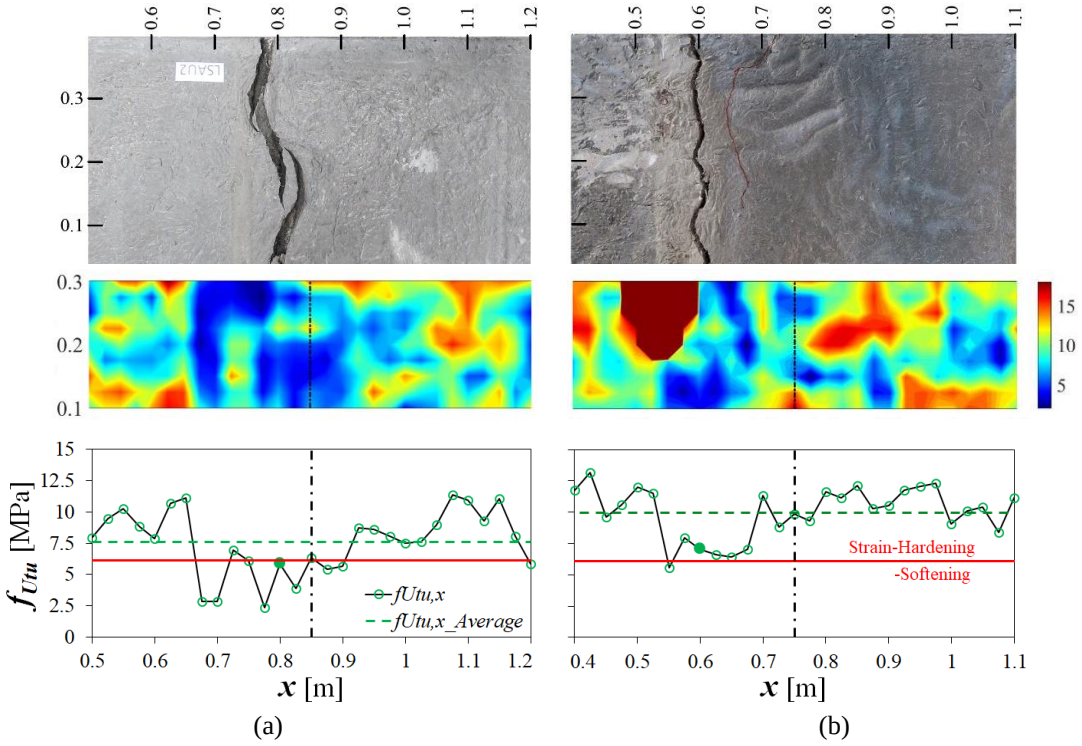

Figure 57. $f_{Utu,x}$ [MPa] prediction by NDT method and macro-crack on the UHPFRC surface (a) LSA-U (Pimentel and Nunes 2016b; Nunes, Pimentel, and Carvalho 2016b) and (b) LSB-U.

3.4.7. Validation of analytical and layered models

Both analytical and nonlinear numerical layered models for describing the flexural behaviour of the RC and RC-(R)U slabs were validated using the experimental results from the current campaign and the beams tested by (Oesterlee 2010).

Oesterlee (2010) tested beams under FPBT with a 4.8 m span and constant bending moment along the central 1.8 m. Three beams were selected from this work, including one reference RC (B RC), one RC-U (B RCU) and one RC-RU (B 4x50R), comprising the B series. Whenever applicable, according to the cross-section type, these beams had the following geometric characteristics: b=150 mm, h_c=250 mm, h_U=50 mm, h_U/h_c=0.2, d_{sc}=237 mm, d_{sU}=275 mm, ρ_{sc}=0.66% (3ϕ10) and ρ_{sU}=2.68% (4ϕ8). The concrete and reinforcement refer to class C30/37 and cold-formed steel ribbed rebars from class B500B. The UHPFRC tensile properties for the B RCU beam were f_{Ute}=f_{Utu}=6 MPa with strain-softening behaviour according to Figure 46 (a), whereas for the B 4x50R, it was f_{Ute}=7 MPa and f_{Utu}=9 MPa with strain-hardening behaviour (Figure 46 (b)). All the beams failed in flexure.

The experimental and the calculated moment-curvature relations are depicted in Figure 58. The coloured lines refer to the experimental data, the light grey to the layered numerical model and the black to the multilinear model. In the composite slabs of the type RC-RU, the numerical and analytical curves were calculated considering expected tensile properties of the UHPFRC, that is, the properties shown in Table 6 for the series LA and LB. The good fit indicates that the flexural behaviour of RC-RU slabs is not affected by eventual local fibre content and orientation variations.

This is not the case in composite slabs of the type RC-U, with a plain UHPFR layer. These have shown to be susceptible to local defects when the casting procedures are not carefully controlled. For that matter, the UHPFRC tensile properties in LSA-U and LSB-U were defined based on the NDT results. For the slab LSA-U, the constitutive law was first derived using the NDT results along the macro-crack alignment, which led to a value of f_{Utu}=5.9 MPa. Then, a second derivation was made considering the information of two more alignments in the vicinity of the crack, resulting in f_{Utu}=4 MPa. This is more realistic since the crack is curvilinear and follows the path of least resistance. As expected, the second law provided better agreement with the experimental result than the first, which overestimated the experimental curve (Figure 58 (b)).

Two constitutive laws for the UHPFRC were also considered in the analysis of the slab LSB-U. The first law was obtained considering NDT measurements along the macro-crack alignment, which resulted in f_{Utu}=7.1 MPa. The second law was the same as that of the RC-RU slabs, defined in Table 6. Thus, the weakest section's strength governs the

beams' capacity, corresponding to the crack localized outside the constant (maximum) bending moment region. However, the curvature was measured with horizontal LVDTs placed within the constant bending moment region. Therefore, the corresponding *M*-*κ* relation is governed by the tensile response of the UHPFRC in this region and not that of the weakest section. This is reflected in Figure 58 (d).

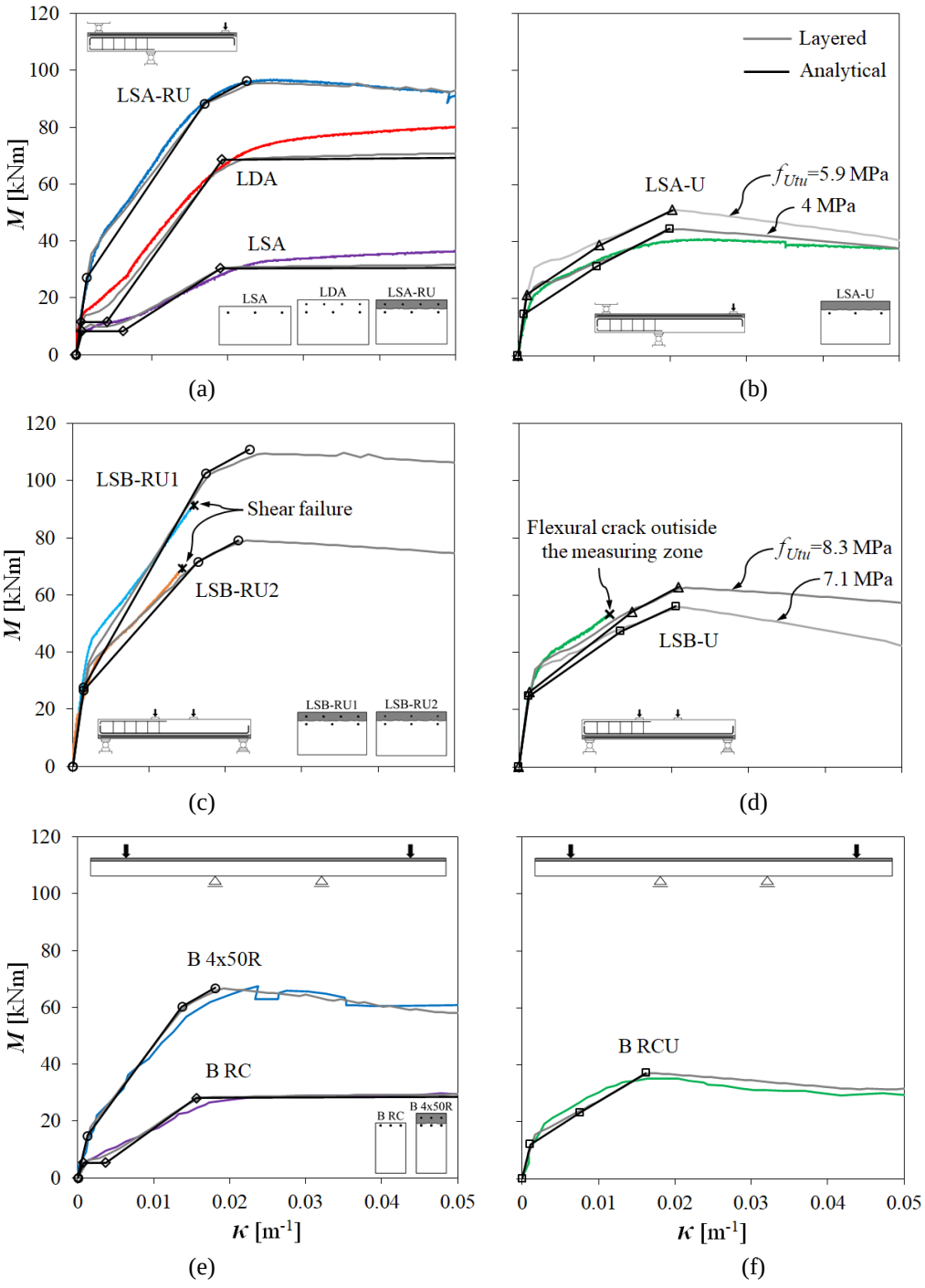

Figure 58. Validation of moment-curvature relations (a-b) LSA series (c-d) LSB series and (e-f) B series.

As shown in Figure 58 (e) and (f), good agreement with the experimental curves is achieved for the B series tested by Oesterlee (2010).

Overall, the fitting is quite good, at least with similar levels of accuracy as those achieved for the reference RC beams. Despite slabs LSB-RU1 and LSB-RU2 failed in shear, the respective bending moment-curvature relations are still relevant for validating the cross-sectional analysis models. However, since the tensile strength of concrete after the elastic phase (point A) and the tension stiffening effect are neglected in the analytical (multilinear) model, the stiffness in the elastic cracked stage is generally somewhat underestimated compared to the experimental data.

Table 7 presents the maximum experimental bending moment and the corresponding calculated values using the layered and analytical models. The ratio between the experimental and the layered model resistance, $M_{R,Exp}/M_{R,layered}$, refers to the slabs/beams that failed in flexure, and its average is about 0.97. The ratio between the layered and analytical model, $M_{R,layered}/M_{R,analytic}$, refers to all elements, and its average is 1.0. This shows good compatibility between both models, at least for the equivalent reinforcement ratio up to $\rho_{s,eq}$=1%, which cover the range of values typically used in slabs.

Table 7. Validation of the maximum bending moment results.

Specimen	$\rho_{s,eq}$ **[%]**	$M_{R,Exp}$ **[kNm]**	$M_{R,layered}$ **[kNm]**	$M_{R,anlt}$ **[kNm]**	$M_{R,exp}/M_{R,layered}$	$M_{R,layered}/M_{R,analytic}$
LSA-U	0.47	41.6	44.5	44.5	0.94	1.00
LSB-U	0.47	-	62.6	62.8	-	1.00
LSA-RU	0.81	96.6	95.7	96.4	1.01	0.99
LSB-RU1	0.96	-	109.9	111.0	-	0.99
LSB-RU2	0.63	-	79.0	79.1	-	1.00
B RCU	0.66	34.2	37.1	37.2	0.92	1.00
B 4x50R	1.15	68.3	66.6	66.9	1.03	1.00
				Average	0.97	1.00

3.5. PARAMETRIC STUDY

A parametric study was carried out to assess the range of applicability of the analytical model. The influence of following parameters were analysed: ρ_{sU} (Figure 59 (a)); h_U/h_c (Figure 59 (b)); f_{Ute} (Figure 59 (c)); f_{Utu}/f_{Ute} (Figure 59 (d)); and ε_{Utu} (Figure 59 (e)). The reference values for the geometric and material properties are as follows:

Geometry:

b=1000 mm; h_c=200 mm; d_{sc}=180 mm

h_U=50 mm; d_{sU}=225 mm; h_U/h_c = 0.25

$\rho_{sc}=A_{sc}/(b.d_{sc})$=0.3%

$\rho_{sU}=A_{sU}/(b.h_U)$=1.0%

$\rho_{s,eq}=(A_{sc}+A_{sU})/d_{s,eq}$=0.5%

$d_{s,eq}=\sum A_{si}.f_{syi}.d_{si}/\sum A_{si}.f_{syi}$

Materials:

E_c=33 GPa; f_{ct}=2.9 MPa; f_c=38 MPa

E_s=200 GPa; f_{sy}=500 MPa; ε_{su}=100‰

E_U=45 GPa; f_{Ute}=7.0 MPa; f_{Utu}=7.9 MPa

ε_{Utu}=2.5‰; ε_{Uus1}=22.5‰; $\varepsilon_{Ut,máx}$=47.5‰

For a fair comparison, the brittle tensile concrete behaviour was considered in the layered model. However, differently from the analytical model, the concrete tensile contribution is not entirely neglected after cracking. Moreover, since the analytical model does not account for $\varepsilon_{Utu}>\varepsilon_{su}$, no comparison is made in Figure 59 (e), in which only the results from the layered model are shown.

The progressive increase in the geometric (ρ_{sU} and h_U/h_c) and material (f_{Ute} and f_{Utu}/f_{Ute}) properties of the UHPFRC layer implies the direct increase in stiffness and bearing capacity, as it is shown in Figure 59 (a-d). The elastic phase (O-A) is extended by increasing either h_U or f_{Ute}, whereas the bearing capacity is enhanced with the h_U and/or mostly ρ_{sU}. From the mechanical and economic point of view, the latter is more effective.

The hardening domain of the UHPFRC influences increases the ductility after yielding the reinforcement in the RC substrate (Figure 59 (e)). Thus, for large strain hardening composites, a yield plateau can be observed before the onset of softening.

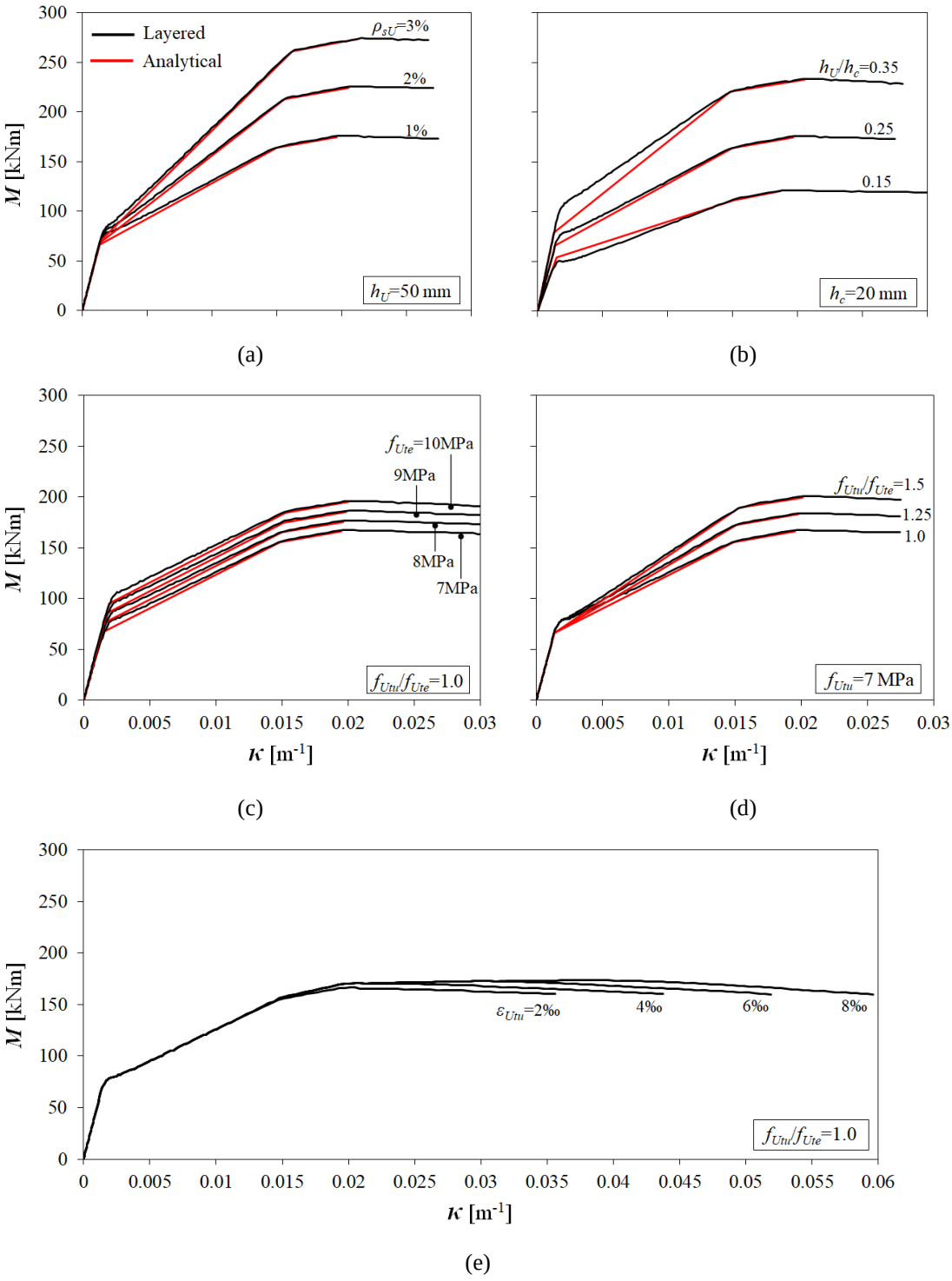

Figure 59. Analytical and layered moment-curvature variations with (a) ρ_{sU}, (b) h_U/h_c, (c) f_{Ute}, (d) f_{Utu}/f_{Ute}, and (e) ε_{Utu}.

The analytical multilinear model fits quite well the results of the layered model. However, the stiffness in the elastic-cracked phase (A-B) is generally underestimated, similarly to what was observed on the experimental validation of the LSA and LSB series (Figure 58 (a-d)).

The stress and strain diagrams in the composite cross-section obtained using both models presented in Figure 60 refer to the reference slab. The diagrams are coincident in point A. Regarding points B and C, the tensile stress on the UHPFRC layer is nearly uniform, while on the opposite side, the concrete compression is slightly overestimated with the analytical model. Moreover, the strains and the compressive depth are slightly smaller.

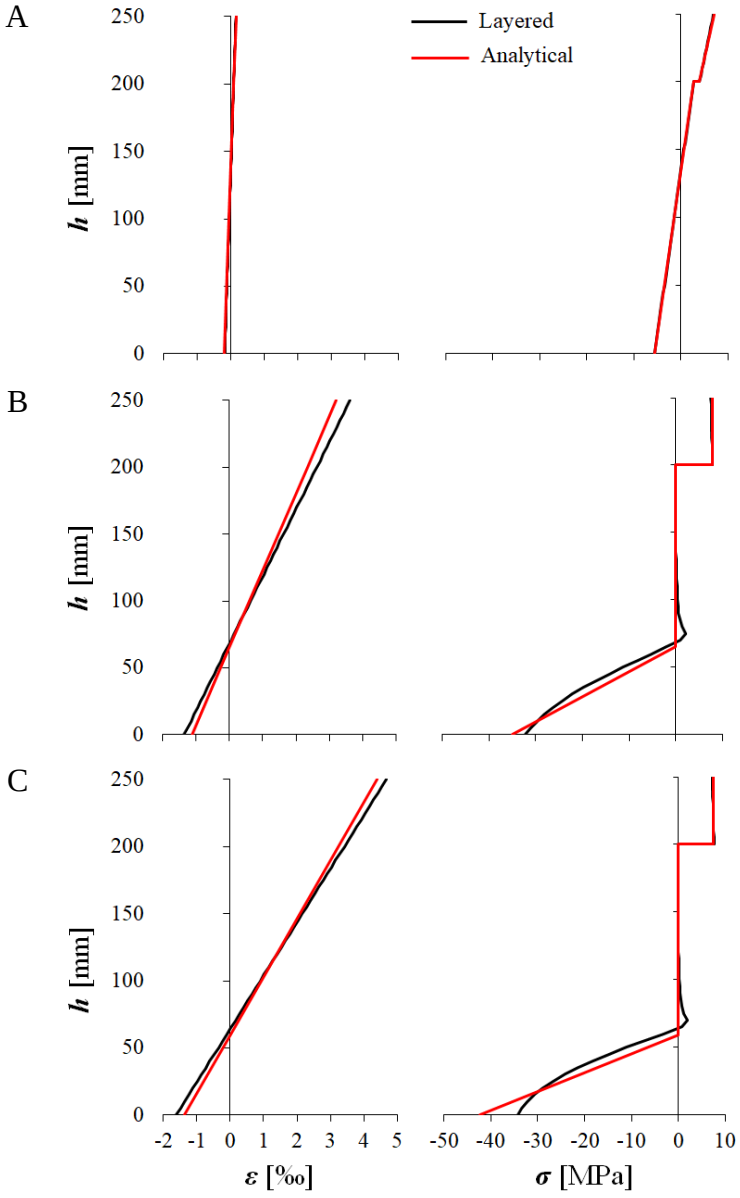

Figure 60. Stress and strain diagrams in the hybrid cross-section for points A, B and C.

Figure 61 presents an evaluation of the accuracy of the multilinear model, defining its range of applicability by showing the ratio $M_{R,layered}/M_{R,analytic}$. It is observed that for $\rho_{s,eq}$=1.5% the ratio is still 99%, decreasing down to 94% for $\rho_{s,eq}$=2.5%. These results indicate that the analytical model is well suited for the analysis of most slabs and slightly overestimates the resistance for highly reinforced beams.

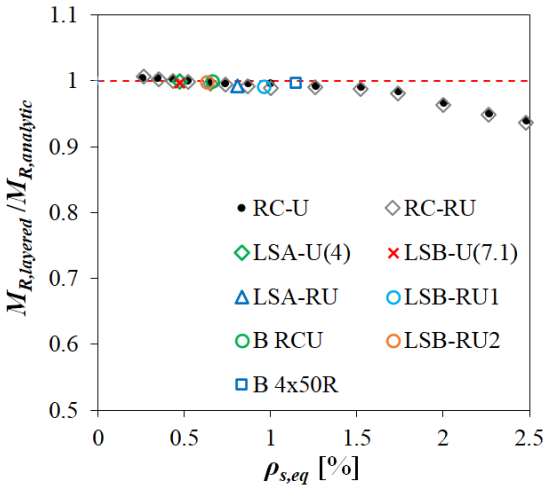

Figure 61. Accuracy of the analytical model for increasing reinforcement ratios.

3.6. CONCLUSIONS AND RECOMMENDATIONS

The results of flexural tests on RC-U and RC-RU slab strips with the UHPFRC layer under tension were presented. The moment-curvature curves could be well reproduced using a layered cross-sectional model with realistic material stress-strain laws. A simplified analytical model relying on a multilinear approximation of the real curve was developed for use in engineering practice, which shows good agreement with the experiments. The NDT method was revealed to be essential to allow the correct estimation of the flexural behaviour of RC-U elements.

The use of reinforcement bars in the UHPFRC layers has several benefits and is recommended whenever strengthening is the main objective of the UHPFRC layer. The strengthening ratio is higher, but the behaviour becomes insensitive to local fibre content, and orientation variations originated during the casting procedure. In practice, reasonable estimates of the structural behaviour are obtained using the tensile properties of the UHPFRC corresponding to random fibre orientation.

The casting of plain UHPFRC layers requires special cautions to avoid defects like those in the beams LSA-U and LSB-U. The casting process should be continuous, and joints should be avoided or located away from the regions with the highest forces.

The roughening method by pneumatic hammer is intrusive, and the coarse aggregate is broken in the process. As further will be shown in Chapter 4, removing the concrete cover through hydro-jetting provides better results and improves the adhesion between the concrete and the UHPFRC. The use of the retarder is suitable in the scope of laboratory tests or prefabrication.

4. Experimental Investigation of One-way Shear Behaviour

4.1. INTRODUCTION

As the hogging flexural capacity increase can be very significant, mainly when a UHPFRC layer reinforced with ordinary steel bars is used, the shear strength must be conveniently assessed since it may govern the load-bearing capacity of the strengthened element. It is noted that in many cases, the slab to be strengthened does not contain shear reinforcement. The available experimental evidence regarding the shear capacity of composite RC-U or RC-RU beams and slabs indicates that it is also greatly improved by the addition of a thin UHPFRC layer (Noshiravani and Brühwiler 2013a; 2013b; Pimentel and Nunes 2016c). The UHPFRC layer acts as a stiff longitudinal tensile reinforcement improving the efficiency of the shear transfer mechanism in the RC substrate and as a secondary load-bearing system after the formation of the critical shear crack (Noshiravani and Brühwiler 2014; Bastien-Masse and Brühwiler 2016c). The response of the composite members is governed by the formation of the near interface cracking (NIC) zone that softens the connection between both layers, as depicted in Figure 62, allowing the opening of the critical shear crack. The latter is a flexural-shear crack propagating from the tensile side of the element towards the support, and which only becomes cinematically admissible once the element behaviour is no longer monolithic. In fact, while the UHPFRC layer is macro-crack free the opening of this flexural shear crack requires the formation of the NIC to promote the separation between the RC substrate and the UHPFRC layer.

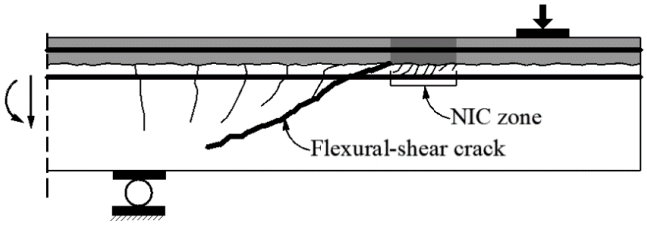

Figure 62. Typical crack pattern at continuous support of RC-(R)UHPFRC composite beams under large shear forces (adapted from Noshiravani and Brühwiler (2013a)).

Noshiravani and Brühwiler (2013a) presented the results of an experimental campaign of composite beams failing under flexure-shear, where the effect of adding an RU layer on the tensile side is evaluated. The other studied variables were the effect of pre-existing shear reinforcement and the type and amount of longitudinal steel in the UHPFRC layer (smooth, ribbed, high- or normal strength). Pimentel and Nunes (2016) evaluated the effect of rebars in the UHPFRC layer. Both studies showed that the shear strength of an RC beam (or slab strip) can be more than doubled and that, contrary to what occurs in RC beams without shear reinforcement, significant shear capacity is available after the formation of the critical shear crack. Additionally, Noshiravani and Brühwiler (2013b) evaluated the effect of the UHPFRC layer on the shear behaviour of internal spans of continuous beams with changing moment signs. However, some crucial aspects remain to be addressed so that the available experimental evidence allows the validation of design methods, namely the effect of the longitudinal reinforcement content in the RC substrate and the UHPFRC layer, the size-effect, the thickness of the UHPFRC layer and the effect of the UHPFRC layer when placed on the compression side. These are investigated in the present work.

4.2. SHEAR STRENGTH OF RC-(R)UHPFRC BEAMS

4.2.1. Flexural behaviour

The moment-curvature relation of RC-(R)U composite cross-sections is schematically depicted in Figure 44 (Chapter 3). The formulas presented in Table 4 consider the elastic behaviour of the compressed concrete and describe quite well the cross-section behaviour for total reinforcement ratios up to 1%. Above that ratio, the curvatures corresponding to the yielding of the reinforcements are slightly underestimated and the corresponding moments overestimated. However, the assumption of linear elastic behaviour for the compressed concrete greatly simplifies the formulation and still provides reasonable estimates of the cross-section before reinforcement yielding, which is the domain of interest for predicting the shear strength.

As shown in Figure 44, point A corresponds to the end of the elastic phase when $\sigma_{Ut}=f_{Ute}$ and points B and C correspond to the reinforcement's yielding in the UHPFRC layer and the RC substrate, respectively.

The tensile strain-hardening behaviour of UHPFRC is schematically represented in Figure 46 (c). In the present work, a mix exhibiting strain hardening under direct tension was employed. When UHPFRC is reinforced with steel bars, the strain at the onset of the macro-crack localization (ε_{Utu}) can be taken equal to the yielding steel strain (Valente, Pimentel, and Nunes 2021). This means that point B marks the onset of the softening stage in the UHPFRC material.

4.2.2. Critical shear crack propagation - V_{crit}

The hereby designated critical shear force for RC-(R)U members, V_{crit}, is defined as the value of the shear force at the development of the critical shear crack. This event is characterized by a sudden drop of the shear force, generally followed by its recovery (Figure 63 (a)) (Pimentel and Nunes 2016c; Noshiravani and Brühwiler 2013a). However, in some cases, the shear force cannot be further increased, in which case V_{crit} is equal to the shear strength, V_R.

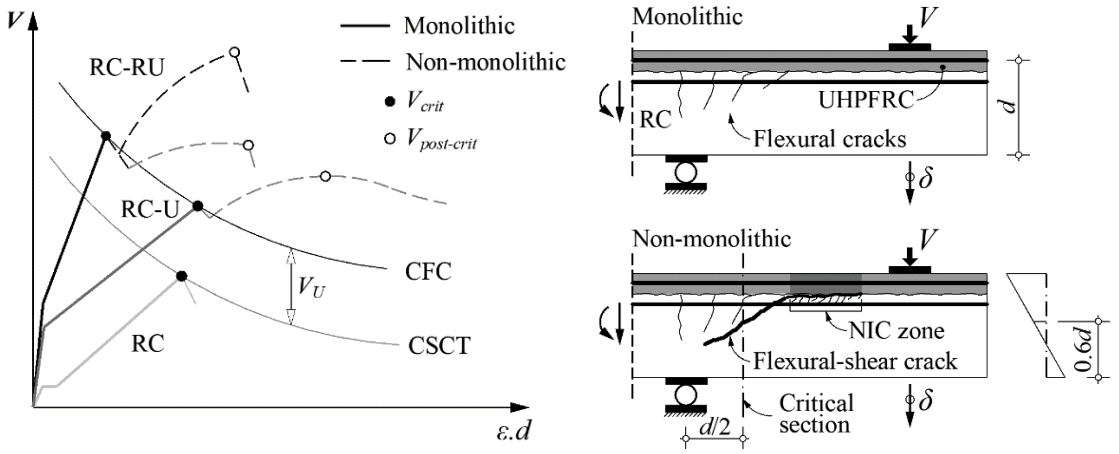

(a) (b)

Figure 63. Determination of V_{crit}: (a) failure criterion for RC and RC-(R)U members; (b) Crack patterns before and after the NIC formation.

Following the proposal of Bastien-Masse and Brühwiler (2016a) for determining the punching shear resistance of RC-(R)U flat slabs, it is here suggested to determine V_{crit} for

beams and slabs without shear reinforcement using a composite failure criterion based on the Critical Shear Crack Theory (CSCT) (Muttoni and Fernández Ruiz 2008):

$$V_{crit}=V_c+V_U \tag{29}$$

where V_c is the contribution of the RC substrate given by the CSCT and V_U is the contribution of the UHPFRC layer.

According to Muttoni and Ruiz (2008), the CSCT failure criterion is defined by Eq.(30). The shear strength of RC members without transverse reinforcement is proportional to the square root of the concrete compressive strength and depends on the critical shear crack width ($w \propto \varepsilon.d$) and its roughness accounted by the maximum aggregate size, d_g (mm):

$$\frac{V_c}{bd_{sc}\sqrt{f_c}}=\frac{1/3}{1+120\frac{\varepsilon.d}{16+d_g}} \tag{30}$$

For RC-(R)U members, the effective depth d refers to the midplane of the UHPFRC layer, $d_U=h_c+h_U/2$ (or the RU layer reinforcement effective depth, d_{sU}), and b is the width of the cross-section. V_c is calculated at the critical section, located at a distance $d/2$ from the support. The critical shear crack width is correlated to the strain, ε, calculated at $0.6d$ from the compression face (Figure 63 (b)), and ε is determined based on a cracked section analysis assuming Bernoulli's hypothesis. In the RC-(R)U members, the equations in Table 4 are suggested, as mentioned in section 4.2.1.

As previously discussed, the development of the critical shear crack occurs with the NIC formation, which promotes the separation between the concrete substrate and the UHPFRC layer (Figure 63(b)). Noting that these cracks occur mostly at the concrete substrate, just below the interface with the UHPFRC layer, and adapting the proposal of Bastien-Masse and Brühwiler (2016a) for punching shear, the additional contribution of the UHPFRC layer to V_{crit} is determined considering that the prying force, V_U, necessary to separate the two materials is given by:

$$V_U=f_{ct}h_U b \tag{31}$$

where h_U is the thickness of the UHPFRC layer, and f_{ct} is the tensile strength of the concrete substrate (Figure 64). At the onset of the critical shear crack development, the minimum length of the debonded zone is set to h_U.

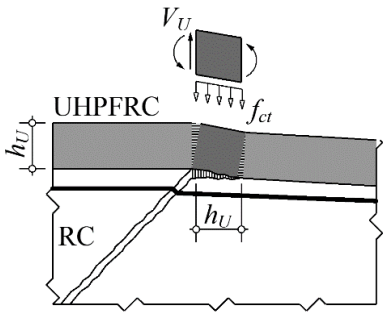

Figure 64. The critical shear crack formation of composite elements (Bastien-Masse and Brühwiler 2016b).

The concrete tensile strength adopted in the calculations presented in this work was determined according to Eq. (32) given by the Eurocode 2 (IPQ 2010):

$$f_{ct}=0.3\left(f_c-8\right)^{2/3} \tag{32}$$

The addition of V_U to the CSCT failure criterion given by Eq. (30) gives place to the composite failure criterion (CFC). Consequently, the intersection of the V-ε curve determined from a cross-sectional analysis of the RC-(R)U element with the CFC allows predicting the critical shear force (Figure 63 (a)). It is noted that the effect of the UHPFRC layer is twofold: first, its stiffening effect decreases the value of ε, that is, the opening of the critical shear crack, therefore increasing V_c; second, the additional term V_U introduces the force necessary to separate the layer from the substrate, allowing the development of the critical shear crack. Additionally, the model includes provisions for the size effect according to the CSCT (Fernández Ruiz, Muttoni, and Sagaseta 2015).

4.2.3. Post-critical shear crack load-bearing mechanism - $V_{post\text{-}crit}$

An analytical model was proposed to calculate the shear strength after developing the critical shear crack, $V_{post\text{-}crit}$ (Noshiravani and Brühwiler 2014; Bastien-Masse and Brühwiler 2016b). This model is the basis of the shear safety provisions for RC-(R)U composite elements in the Swiss code (SIA 2016). The shear capacity is determined using the upper bound theorem of the theory of plasticity considering the failure mechanism

schematized in Figure 65. Assuming rigid plastic behaviour at failure, the following work equation can be written:

$$V_{post\text{-}crit}\,\delta_u = W_{i,slid} + W_{i,U} \tag{33}$$

where δ_u is the assumed vertical translation. The left-hand side represents the work of the external forces, and on the right-hand side, the energy dissipated during failure. The latter consists of two contributions: $W_{i,slid}$ and $W_{i,U}$. It is noted that the displacement δ_u is vertical because no dissipation occurs in the flexural reinforcement, which is assumed to remain elastic. The term $W_{i,slid}$ corresponds to the dissipation along the line of discontinuity developing in the compressed portion of concrete. Assuming a Mohr-Coulomb material with an associated flow rule, it is possible to show that:

$$W_{i,slid} = \frac{1}{2} f_{ce}\, b \left[\frac{x}{\sin\alpha_c} (1-\cos\alpha_c) \right] \delta_u \tag{34}$$

where f_{ce} is the effective (or plastic) compressive strength of concrete; x is the depth of the compression zone calculated considering the equilibrium of forces in the composite cross-section; α_c is the angle of the line of discontinuity (Figure 65). Thus, the dissipation along the portion of the line of discontinuity developing in the tensile zone of the beam is neglected.

The term $W_{i,U}$ corresponds to the dissipation occurring in the UHPFRC layer, which according to the assumed failure mechanism, is bending in double curvature, given by:

$$W_{i,U} = 2 \frac{M_U}{l_{NIC}} \delta_u \tag{35}$$

where l_{NIC} is the length of the NIC zone and M_U is the plastic bending moment in the UHPFRC layer developing at each of the two plastic hinges at the extremities of the NIC. The rotation of each of these hinges is assumed to be the same and given by δ_u / l_{NIC}.

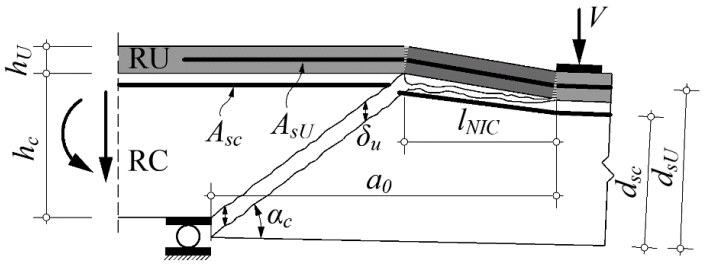

Figure 65. The flexure-shear failure mechanism of composite elements, adapted from Bastien-Masse (2015).

Inserting Eqs. (34) and (35) into Eq. (33), it is possible to obtain:

$$V_{post\text{-}crit}=V_{pc,c}+V_{pc,U} \tag{36}$$

with

$$V_{pc,c}=\frac{1}{2} f_{ce} b \left[\frac{x}{\sin\alpha_c}(1-\cos\alpha_c)\right] \tag{37}$$

and

$$V_{pc,U}=2\frac{M_U}{l_{NIC}} \tag{38}$$

The depth of the neutral axis x can be estimated at the point corresponding to the peak flexural moment (point C of Figure 44) using the equations in Table 4. According to Bastien-Masse and Brühwiler (2016b), the effective concrete compressive strength can be assumed $f_{ce}=0.8f_{c,}$ and the plastic bending moment M_U can be conservatively estimated by:

$$M_U=f_{syU}\rho_{sU}h_U b(h_U/2-x_U/2)+f_{Utu}b(h_U-x_U)(h_U/2-x_U) \tag{39}$$

where x_U, is calculated as follows:

$$x_U=\begin{cases}\dfrac{h_U f_{Utu}}{0.5f_{Uc}+f_{Utu}} \; ; \rho_{sU}=0 \\ \dfrac{\rho_{sU}h_U f_{syU}}{0.5f_{Uc}} \; ; \rho_{sU}>0\end{cases} \tag{40}$$

with ρ_{sU} being the reinforcement ratio in the UHPFRC layer; f_{Uc} and f_{Utu} are the compressive and post-cracking tensile strength of the UHPFRC.

This is a model based on the upper bound theorem. The mechanism leading to the minimum collapse load must be found. Noting that the free distance between the support and the loading plates, a_0, is related to l_{NIC} according to the equation:

$$l_{NIC}=a_0-\frac{d_{sc}}{\mathrm{tg}\alpha_c} \tag{41}$$

The angle α_c must be found iteratively until the minimum $V_{post\text{-}crit}$ is reached. The shorter l_{NIC}, the larger the $V_{pc,U}$ and smaller the $V_{pc,c}$. In general, α_c varies between 25º and 45º, with the value 30º being recommended in Bastien-Masse and Brühwiler (2016b) as a reasonable estimate for avoiding the minimization procedure.

The model described above provides the shear strength of the RC-(R)U member when it is no longer monolithic (Figure 63). Depending on the thickness, the reinforcement ratio in the UHPFRC layer, and the boundary conditions, the resistance may be achieved at the critical shear crack formation. Therefore, the shear strength is given by:

$$V_R = max\{V_{crit};\ V_{post\text{-}crit}\} \tag{42}$$

It is remarked that $V_{post\text{-}crit}$ is determined based on the theory of plasticity and therefore cannot reproduce any type of size-effect, which is a limitation of the current formulation.

4.3. EXPERIMENTAL INVESTIGATION

4.3.1. Specimens and test setup

The cross-sections and static system of the tested beams are schematically depicted in Figure 66. In addition, the geometric and reinforcement layout specifications are presented in Table 8. As for the notation used in Figure 66 and Table 8, the subscripts *c*, *U*, *sc*, and sU refer to concrete, UHPFRC, and reinforcements in concrete and UHPFRC layers.

The series VT was used to evaluate the effect of the reinforcement ratio in the UHPFRC layer, with $\rho_{sU}=A_{sU}/(b.h_U)$=0.0, 2.1, 3.2 and 4.5%. This series includes four beams tested by Pimentel and Nunes (2016): VT1, VT2, VT-U5 and VT-RU2. The reinforcement ratio in the RC substrate was kept constant at $\rho_{sc}=A_{sc}/(b.d_{sc})$=1.26%. Two reference (unstrengthened) beams were included: the beam VT1, representing the RC substrate containing one reinforcement layer with ρ_{sc}=1.26%; and the beam VT2, containing two reinforcement layers, with a total reinforcement ratio ρ_{sc}=1.93% equal to that of the beam VT-RU2. The beam VT-U3 contains a 30 mm thick UHPFRC layer (h_U/h_c=0.15), while the others have 50 mm (h_U/h_c=0.25).

The VB series was defined to evaluate the influence of the longitudinal reinforcement ratio in RC substrate, with ρ_{sc}=0.21, 0.58 and 0.84%, while ρ_{sU}=4.5% and h_u=50 mm were kept constant.

The VS series was developed to evaluate the size effect and contains RC-RU geometrically similar scaled specimens, with the total heights h=230, 460 and 690 mm. In this series, the ratio of the UHPFRC layer thickness to substrate depth was maintained at h_U/h_c=0.15. The reinforcement ratios in the VS series are ρ_{sc}=1.26% and ρ_{sU}=2.24%. Reference beams without any strengthening layer were also tested.

Finally, the VC series shows the shear strength near pinned end supports, where the top UHPFRC layer is under compression. The reinforcement ratio in the substrate is ρ_{sc}=1.26%, identical to that of the VT series. The UHPFRC layer is unreinforced and is 35 and 50 mm thick for VC-U3 and VC-U5, respectively.

All beams have the same width b=150 mm, shear span $a=L/2$=600 mm and height of the concrete substrate h_c=200 mm, except for the medium and large beams of the series VS that have twice and triple shear span and height of the small one, respectively. In addition, one half of each beam contained transversal reinforcement (Figure 66 (b)) to ensure that shear failure occurs on the other half.

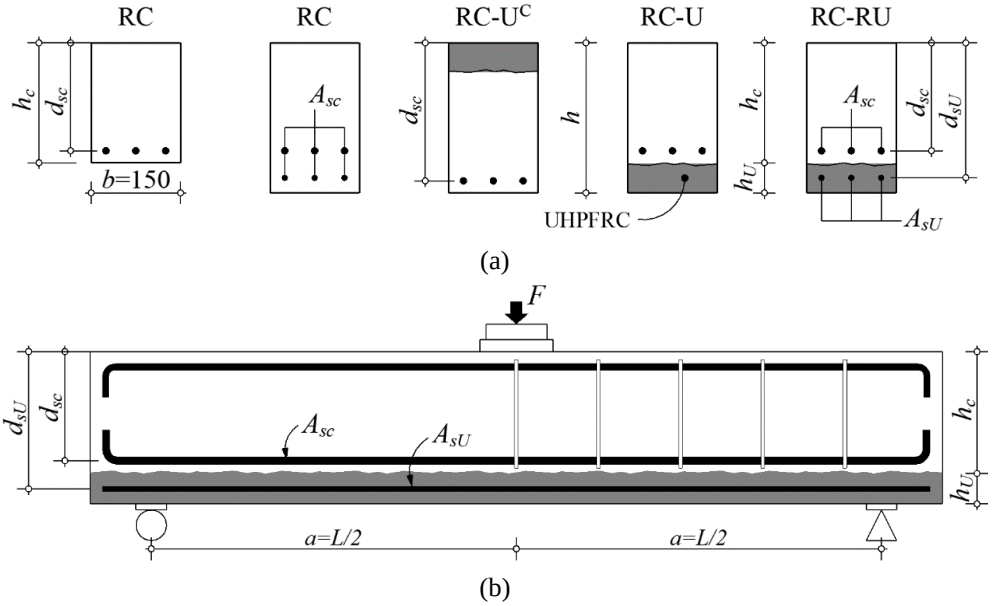

Figure 66. Tested beams: (a) cross-sections type and (b) three-point bending test setup.

Except for beams VT1, VT2 and VT-U5 and VT-RU2, which were tested with a cantilevered static system (Pimentel and Nunes 2016c), all the other beams were tested under a three-point bending (TPBT), with a point load, F, applied at mid-span, as schematized in Figure 66.

Table 8. Geometrical specifications of the specimens.

Series	Specimens	Cross-section type	h [mm]	$a=L/2$ [mm]	Concrete substrate				UHPFRC layer			
					h_c [mm]	d_{sc} [mm]	Bars	ρ_{sc} [%]	h_U [mm]	$d_U=d_{sU}$ [mm]	Bars	ρ_{sU} [%]
VT	**VT1**	RC	215	600	215	180	3ϕ12	1.26	-		-	-
	VT2	RC	250	600	250	200	3ϕ12 +3ϕ10	1.93	-	-	-	-
	VT-U3	RC-U	230	600	200	180	3ϕ12	1.26	30	215	-	0.00
	VT-U5		250						50	225		
	VT-RU1	RC-RU	250	600	200	180	3ϕ12	1.26	50	225	2ϕ10	2.09
	VT-RU2										3ϕ10	3.15
	VT-RU3										3ϕ12	4.52
VC	**VC-U3**	RC-U^C	235	600	200	210	3ϕ12	1.08	35	-	-	-
	VC-U5		250			230		0.98	50			
VB	**VB0-RU**	RC-RU	250	600	200	180	2ϕ6	0.21	50	225	3ϕ12	4.52
	VB1-RU						2ϕ10	0.58				
	VB2-RU						2ϕ12	0.84				
VS	**VS1**	RC	200	600	200	180	3ϕ12	1.26	-	-	-	-
	VS2		400	1200	400	360	6ϕ12					
	VS3		600	1800	600	540	9ϕ12					
	VS1-RU	RC-RU	230	600	200	180	3ϕ12	1.26	30	215	2ϕ8	2.24
	VS2-RU		460	1200	400	360	6ϕ12		60	430	4ϕ8	
	VS3-RU		690	1800	600	540	9ϕ12		90	645	6ϕ8	

4.3.2. Materials properties

The mechanical properties of the concrete and the UHPFRC are presented in Table 9. The beams were cast with a ready-mix normal strength concrete with a maximum aggregate size of d_g=14 mm for the VT series and 16 mm otherwise. The compressive strength in standard 150 mm diameter cylinders at the age of testing (between 220 and 280 days) is

given in Table 9. The concrete of series VS exhibited a significant increase in compressive strength from 28 to 280 days.

Table 9. Material mechanical properties of RC layer.

Series	Concrete (age of testing)			UHPFRC (28 days)					
	E_c [GPa]	f_c [MPa]	$f_{ct,sp}$ [MPa]	E_U [GPa]	f_{Uc} [MPa]	f_{Ute} [MPa]	f_{Utu} [MPa]	ε_{Utu} [‰]	w_{Ut} [mm]
VT[a)]	31	35	3.1	45	135	7.2	8.3	2.5	4.5
VB, VC	28	37	2.8						
VS	33	50	3.8						

[a)] except VT2. For VT2, f_c=28 MPa and $f_{c,sp}$=2.6 MPa.

The UHPFRC consists of a self-compacting mixture, with the proportions presented in Table 10. It contains fibre volumetric ratio V_f=3% of straight high-strength steel fibres with length l_f=9 and 12 mm (50% of each) and diameter d_f=0.175 mm. The characterization of the tensile behaviour of this mix is presented elsewhere (Abrishambaf, Pimentel, and Nunes 2017; 2019). The tensile properties at 28 days indicated in Table 9 correspond to random fibre orientation. In this case, the post cracking tensile strength is expected to be slightly below f_{Utu}=8 MPa with tensile strain-hardening behaviour up to the peak strain in the range of 2.0-3.0‰.

Ordinary hot-rolled ribbed S500 steel bars were used as reinforcement, except for the ϕ6 S400 bars in specimen VB0-RU.

Table 10. UHPFRC mix proportions.

Constituents	Specific gravity	Mix-proportions [kg/m^3]	
		VT	VB, VC, VS
CEM I 42.5 R	3.10	794.9	794.9
Silica fume [a)]	1.38	79.5	79.5
Limestone	2.68	311.4	311.4
Water	1.00	153.8	145.4
Superplasticizer	1.08	22.2	30.0
Sand	2.63	941	941
Fibres (l_f/d_f = 9/0.175)	7.85	117.8	117.8
Fibres (l_f/d_f = 12/0.175)	7.85	117.8	117.8

[a)] Slurry with 50% solid content.

4.3.3. Preparation of the specimens

The specimens from each series were cast on the same day to warrant similar mechanical properties of the concrete during the test. To ensure a good bond between the substrate and the UHPFRC layer, the top surface of the former was hydro-jetted, and about 15 mm depth was removed to expose the coarse aggregate (Figure 67). This procedure was adopted in all specimens except for the VT series, where a pneumatic hammer was used instead (Pimentel and Nunes 2016c). In all cases, the surface was cleaned, and before pouring the UHPFRC layer, the substrate was kept saturated. The casting of the UHPFRC overlay over hydro-jetted surfaces is illustrated in Figure 68.

Figure 67. Concrete surface preparation by hydro jetting.

To avoid flow-induced orientation of the fibres, the fresh UHPFRC mixture was not allowed to have a free flow, being placed with random movements of the tray, and disturbed with a small rake making smooth movements to be as less intrusive as possible to avoid sedimentation of fibres, Figure 68 (a).

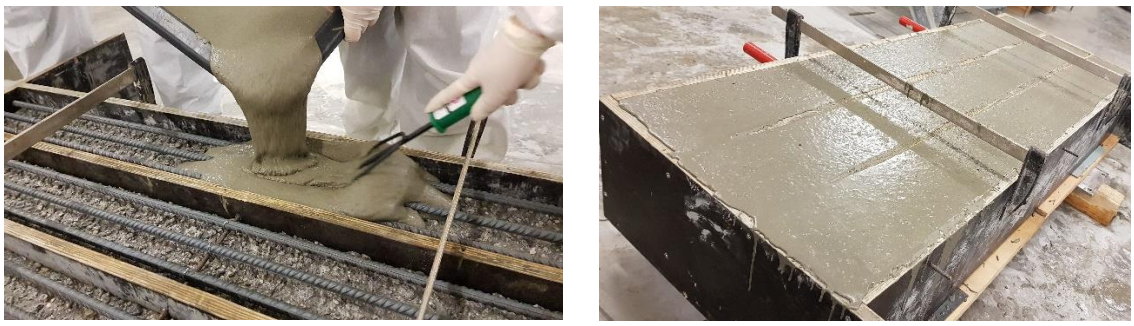

(a) (b)

Figure 68. Casting of the RU layer in Series VB: (a) pouring the UHPFRC; (b) final aspect.

4.3.4. Instrumentation and testing procedure

The instrumentation setup was symmetrical. Vertical and horizontal Linear Variable Differential Transducers (LVDTs) were installed to measure displacements, as schematically depicted in Figure 69, showing the installation in a small scale beam. In the case of the larger beams of the VS series, the reference lengths of the horizontal LVDTs were taken two or three times larger, as was the case of beams VS2/VS2-RU and VS3/VS3-RU, respectively. The horizontal LVDTs t_i were placed in the top face (compression face), while $b_{i,j}$ were placed in the bottom face (tensile face). The vertical LVDTs w_i were placed to measure the opening of the NIC.

The load was applied through a servo-hydraulic actuator under displacement control at a rate of 0.02 mm/s.

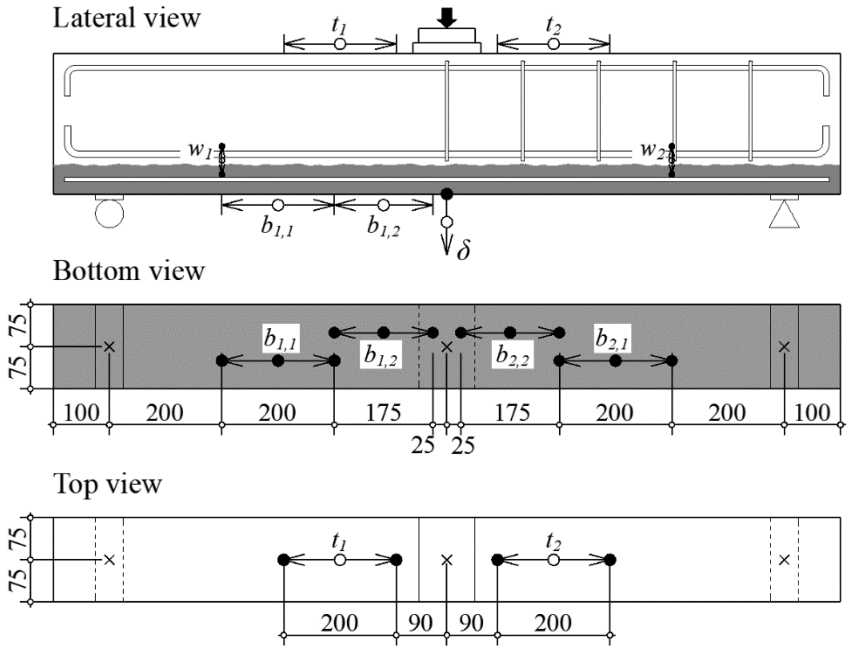

Figure 69. Instrumentation setup in the small scale beams.

4.4. RESULTS AND DISCUSSION

4.4.1. General observations

Figure 70 shows the shear force, *V*, versus vertical mid-span deflection, *δ*, curves for each series of beams. The strengthened beams have shown the typical behaviour observed in most composite RC-(R)U beams failing in flexural-shear (Noshiravani and Brühwiler 2013a; Pimentel and Nunes 2016c).

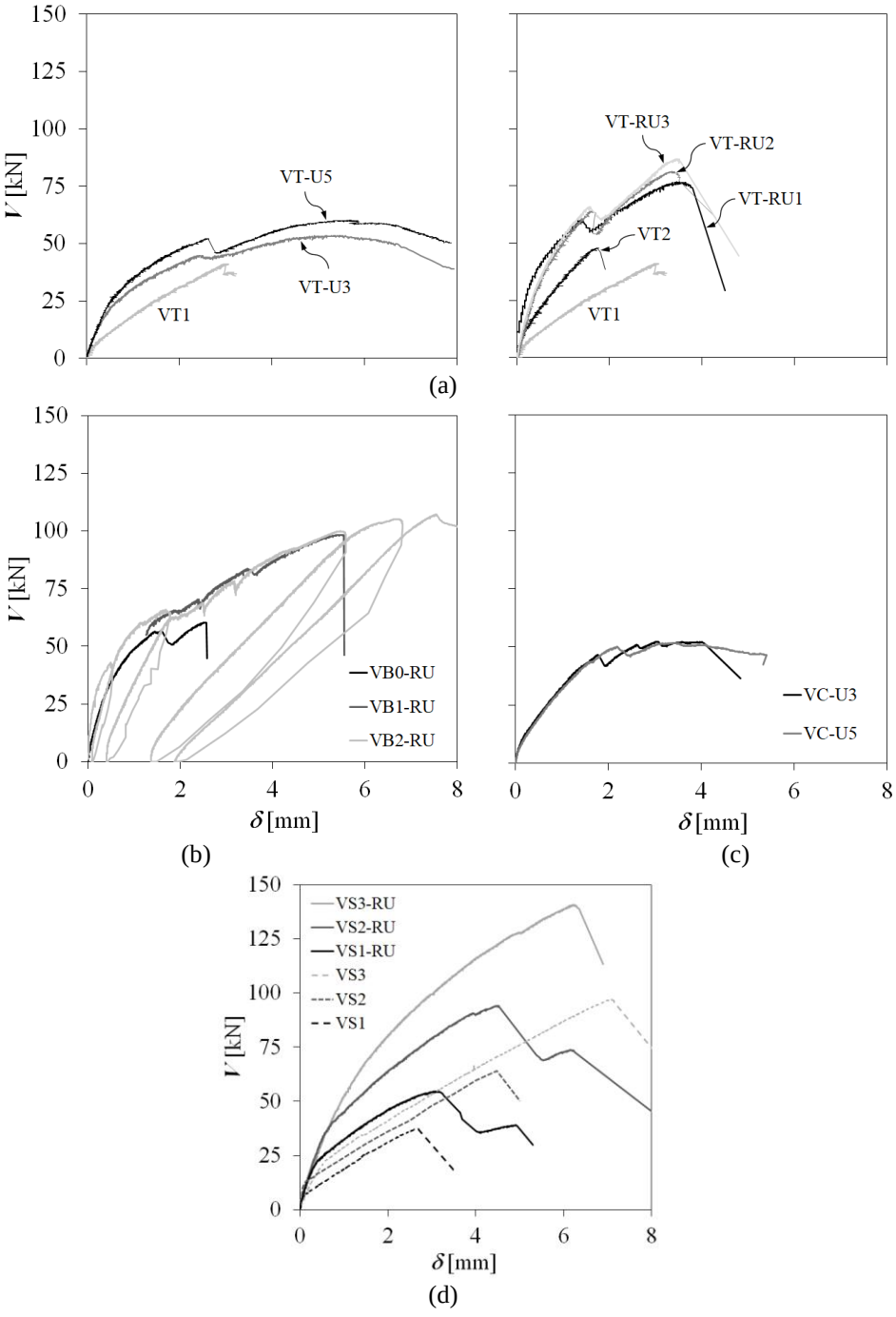

Figure 70. Experimental force-deflection curves of series (a) VT, (b) VB, (c) VC and (d) VS.

The event corresponding to NIC and diagonal shear crack propagation is noticeable in the force-deflection curves and marks the end of the monolithic behaviour between the UHPFRC layer and the RC substrate. This phenomenon is illustrated using the results from beam VB0-RU presented in Figure 71. The readings provided by the vertical LVDTs w_1 and w_2 shown in Figure 71 (b) allow determining the instant when the NIC starts developing (point A). It can be seen that the NIC already exhibited a small opening before the load drop (point B). The results from the horizontal LVDTs in the compression and tensile zones evidence this behaviour by providing readings that cannot be explained by the classical beam theory and considering a monolithic behaviour of the cross-section. As shown in Figure 71 (c), the deformations measured by LVDT $b_{1,1}$, located far away from the maximum bending moment section, start growing faster than those measured by the LVDT $b_{1,2}$ after point A. This confirms Noshiravani and Brühwiler (2013) observation that the UHPFRC layer is bending with double curvature after the NIC has propagated and promoted the partial detachment of the strengthening layer along the NIC zone (Figure 65). The measurements provided LVDTs t_1 and t_2 in the compressive side show evidence of the development of the elbow-shaped strut described by Muttoni and Fernandez Ruiz (2008) and supporting the stress field developing after the NIC formation suggested by Noshiravani and Brühwiler (2014). The LVDT t_1 exhibits a sharp decrease of the absolute values of the deformation from point B onwards (Figure 71(d)). After force recovering, failure occurred in point C with LVDT t_1 measuring tensile deformations.

The behaviour described above was observed in all the strengthened beams of the series VT and VB. In addition, and as can be exemplified in Figure 71(a)), the NIC systematically forms above the interface, i.e., in the concrete substrate.

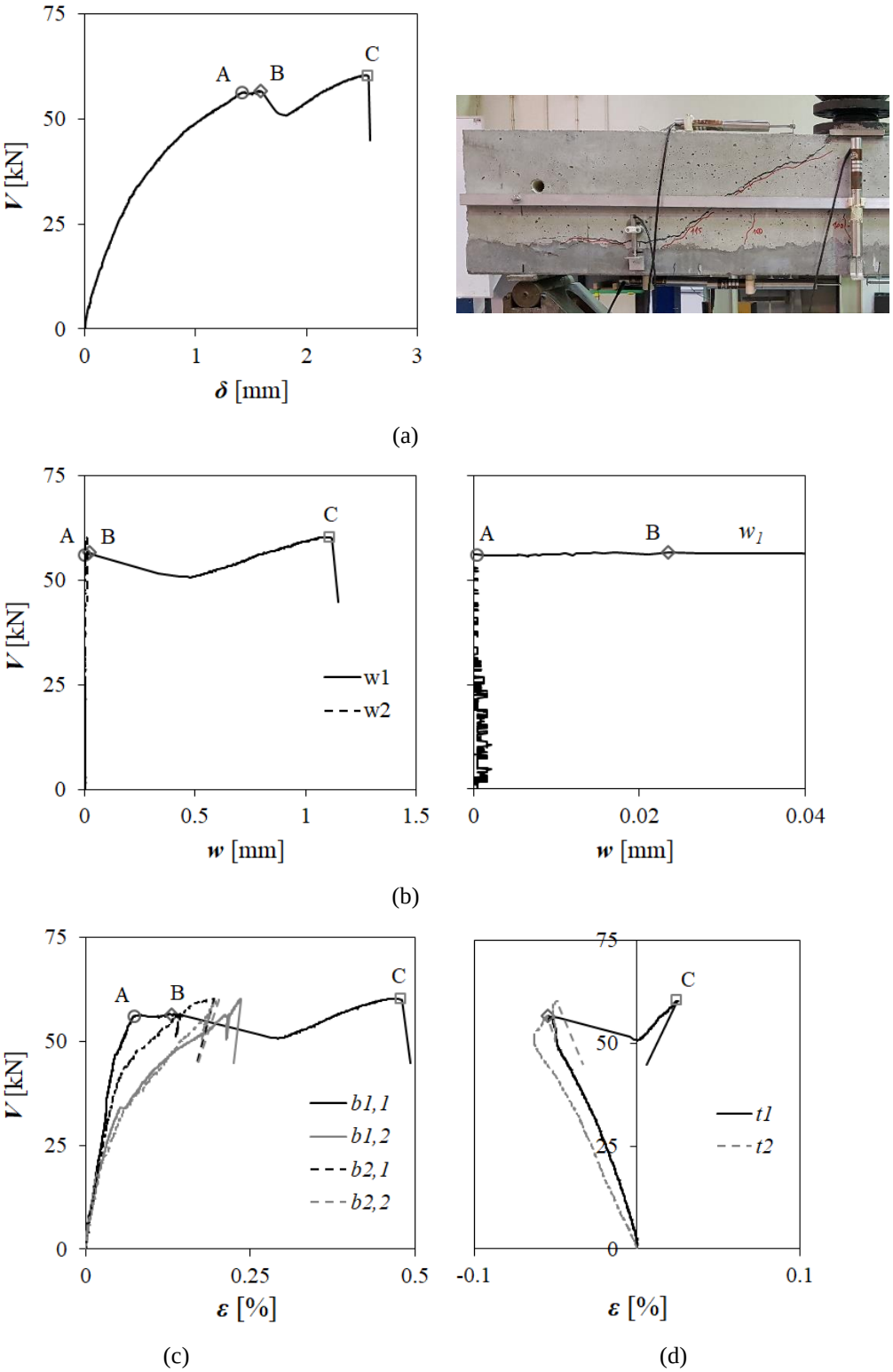

Figure 71. Beam VB0-RU: Shear force-displacements in the LVDTs located in the (a) mid-span and the cracking pattern and (b) interface, -horizontal strains in the LVDTs located in the (c) tensile and (d) compressive side.

4.4.2. Series VT – Influence of the (R)U layer under tension

The shear force-deflection curves of the VT series are depicted in Figure 70 (a). The reference beams VT1 and VT2 failed in a brittle manner short after the visible (to the naked eye) propagation of the critical shear crack. As it is typical in this type of failure, this crack is "S" shaped, with a more or less horizontal branch propagating just above the reinforcement, the sometimes called "doweling crack", and another flatter segment propagating above the neutral axis where the bending theory would predict compressive stresses in the longitudinal direction. The shape of the diagonal crack is different in the strengthened specimens. In these cases, the "S" shape cannot be identified, and the crack is closer to the assumptions of the failure mechanism in Figure 65. As for the strengthening layer, a vertical crack always develops in the UHPFRC starting from the bottom of the layer, roughly at the section where the diagonal shear crack intersects the interface, confirming the assumptions of the failure mechanism identified by Noshiravani and Brühwiler (2013a; 2014). The distance between this section and the face of the support defines l_{NIC}. This supports the fact that the readings of the LVDT $b_{1,1}$ are always larger than those of the other $b_{i,j}$ after the formation of the critical shear.

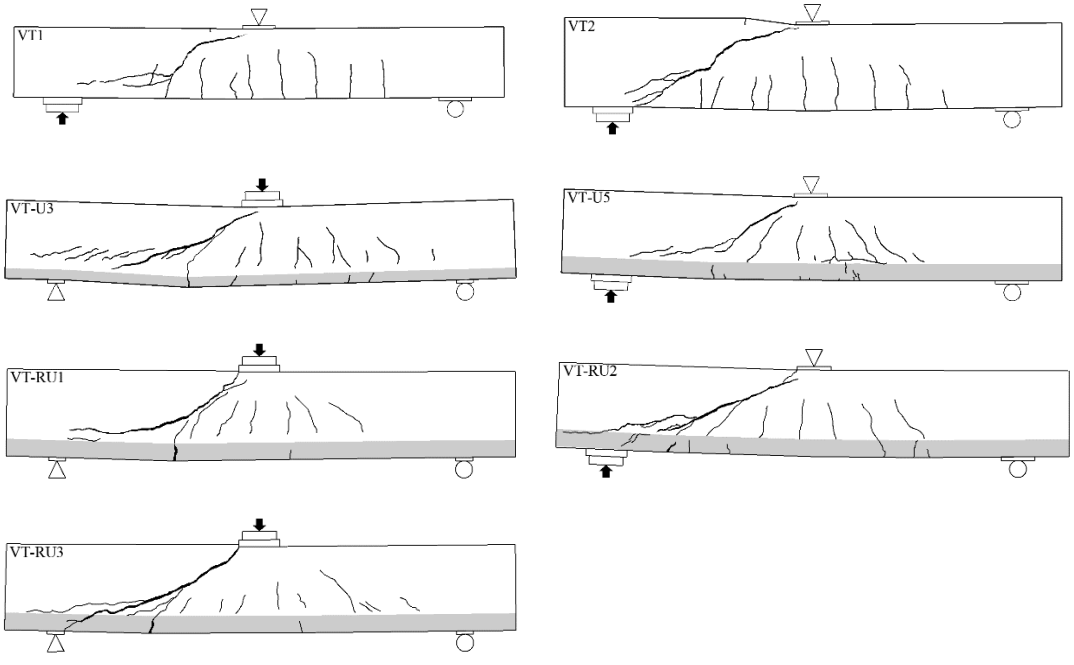

Figure 72. VT series cracking pattern.

Compared to the reference beam VT1, the shear strength could be roughly doubled in the specimens with steel reinforced UHPFRC layer. In the specimens with plain UHPFRC (VT-U3 and VTU5), the shear strength is close to the corresponding flexural strength and

the ductility is significantly increased compared to the reference beam VT1, i.e., the failure mode is no longer brittle. The effect of the reinforcement ratio in the UHPFRC layer is evidenced in the results but not clearly in the crack patterns.

4.4.3. Series VB – Influence of reinforcement in the RC substrate

The results of the series VB are depicted in Figure 70 (b). These results show a strong dependency of shear strength V_R on the RC substrate's reinforcement ratio. Figure 73 shows the cracking pattern of the beams of the series VB and a tendency for the critical shear crack to develop at a flatter angle (decreasing l_{NIC}) with increasing ρ_{sc} is observed. Likewise, in the VT series, the NIC occurs in the concrete substrate, propagating from the inclined critical shear crack base towards the support. Also, the same visible macro-crack in the UHPFRC layer, located below the base of the critical shear crack and starting from the bottom surface of the UHPFRC layer, is present in all three specimens of this series.

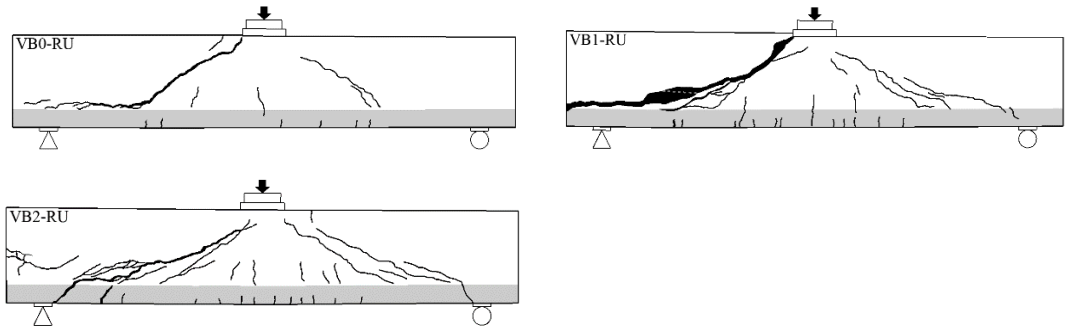

Figure 73. VB series cracking pattern.

4.4.4. Series VC – Influence of UHPFRC layer under compression

The shear force-deflection curves of the VC series are depicted in Figure 70 (c). Despite the UHPFRC layer of beam VC-U5 being 15 mm thicker than VC-U3, both beams resisted similar values and were about 1.26 times more than the reference VT1. The instant propagation of the diagonal shear crack is evidenced in the shear force-deflection curves by a sudden drop of the force, which could be recovered and increased afterwards. This marks a significant difference with respect to the brittle behaviour of the reference beams VT1 and VT2. Although the force-displacement curve may suggest that longitudinal reinforcement yielding has occurred, the peak load reached only 83% and

76% of the theoretical flexural failure load obtained for the monolithic cross-section of the beams VC-U3 and VC-U5, respectively.

As depicted in Figure 74, the critical shear crack presented an "S" shape, like the reference RC beams. However, the flatter segment close to the compressed side propagates below the interface between the two materials and not diagonally towards the loading plate as in the reference beams. This is due to the larger tensile strength and toughness of the UHPFRC. Moreover, compared to the reference beams, the critical shear crack is shifted towards the support such that the doweling crack developing along with the tensile longitudinal reinforcement nearly vanishes. Thus, after the critical shear crack is formed in both beams, the UHPFRC layer is bending with double curvature with positive bending moment close to the loading plate and negative bending moment at the section where the steeper branch of the diagonal crack would meet the interface. Likewise, in the beams with the layer in tension, a fraction of the shear force is carried by the UHPFRC layer, and an alternative load path is formed in the post-critical stage.

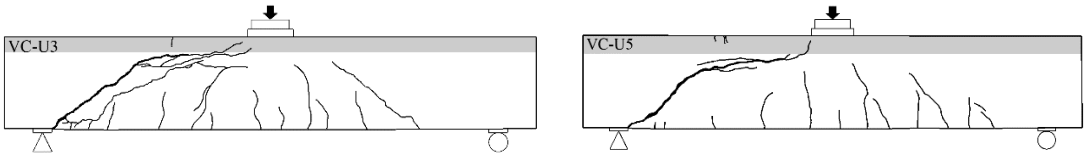

Figure 74. VC series cracking pattern.

4.4.5. Series VS – Size effect

The shear force-deflection curves of the VS series are shown in Figure 70 (d). All the reference specimens (VS1, VS2, and VS3) exhibited a brittle shear failure triggered by the sudden propagation of the diagonal shear cracks depicted in Figure 76 (a). These cracks had similar "S" shapes in all three scaled specimens. Contrary to what was observed in all the other test series, the strengthened specimens (VS1-RU, VS2-RU, and VS3-RU) also failed suddenly, right after the visible propagation of the critical shear crack, reaching a shear strength roughly 1.45 times larger than those of the unstrengthened counterparts. The main differences to the other two series are the lower relative thickness of the UHPFRC layer (h_U/h_c=0.15 in the VS series and 0.25 in the VB and VT series) and the higher concrete strength of the substrate. Beams tested in similar conditions by Noshiravani and Brühwiler (2013a), with h_U/h_c=0.20 and f_c=42 MPa, presented curves

like those of the VT-RU and VB-RU beams. The cracking patterns at failure are shown in Figure 76 (b). Again, the diagonal shear cracks of the three VS-RU scaled beams show similar shapes and, likewise, the beams in series VT and VB are less curvilinear than in the reference specimens.

The size effect is the reduction of the normalized shear strength for geometrically identical specimens with increasing size (Muttoni 2008). The shear-stress versus normalized mid-span deflection curves are shown in Figure 75.

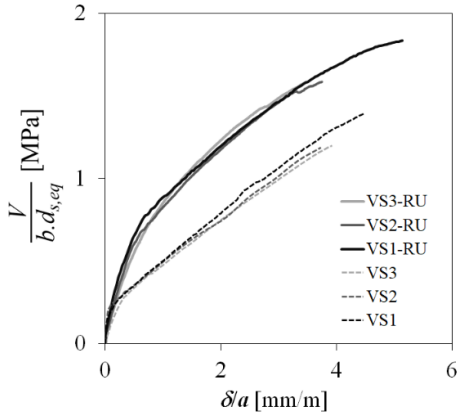

Figure 75. Series VS normalized force-deflection curves.

As expected for perfectly scaled specimens, the normalized stress-displacement curves are nearly coincident and evaluate the size effect. An apparent decrease in the ultimate shear stress is observed from the small scale (VS1/VS1-RU) to the intermediate scale (VS2/VS2-RU) beams. However, the ultimate shear stress of the large-scale and intermediate-scale beams are close. The trend of the size effect is similar on the reference and strengthened specimens.

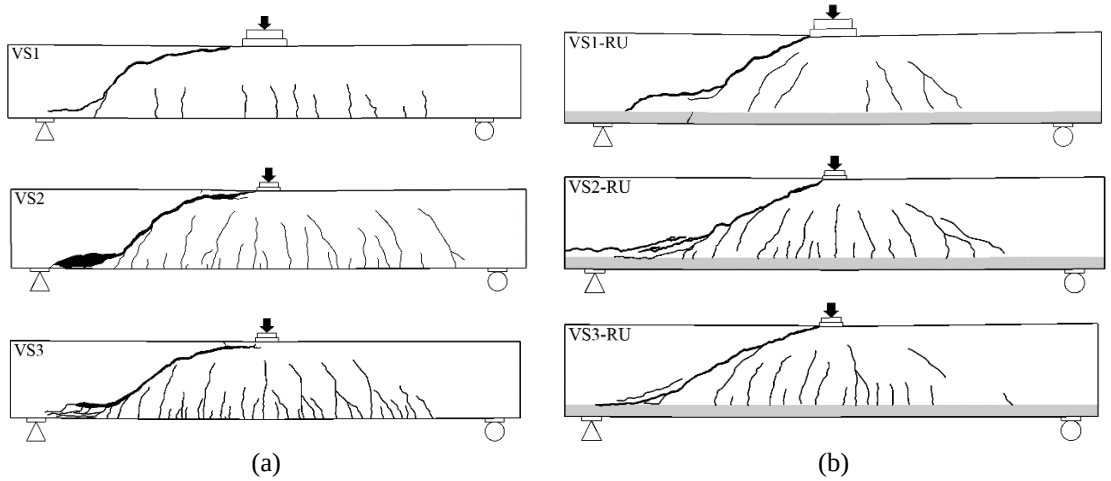

Figure 76. VS series cracking pattern (a) RC and (b) RC-RU beams.

4.4.6. Shear strength calculation

The summary of results obtained experimentally (superscript ^{exp}) and analytically (without any superscript) are presented in **Erro! Fonte de referência não encontrada.**. These results can be analysed considering two main instants: the propagation of the critical shear crack when V_{crit} is reached and the failure when the shear strength, $V_R=max\{V_{crit};V_{post\text{-}crit}\}$, is reached. In addition, the results of four RC-RU beams, MW3, MW4, MW5 and MW6 and an RC beam, MW0, tested by Noshiravani and Brühwiler (2013a) and referred to as series MW, are also presented in **Erro! Fonte de referência não encontrada.**. These beams have a shear span of a=800 mm with RC substrate height of h_c=250 mm and strengthened with RU layer of h_U=50 mm (h_U/h_c=0.20). However, despite being shear reinforced, the stirrup spacing was such that the diagonal shear crack did not activate the stirrups. Likewise, the beams of the series VT, VB, VC and VS, the beams of the MW series, failed in flexural-shear mode.

Figure 77 exemplifies the calculation of V_{crit} in the VS beams by determining the intersection point between the flexural response obtained from the simplified analytical model in Table 4 and the CSCT failure criterion for the RC, or the CFC for the RC-(R)U composite beams. A similar procedure was performed for the other series. As for the series VC, with the UHPFRC layer on the compression side, the CSCT failure criterion for RC members was adopted, which happens to be a conservative approach.

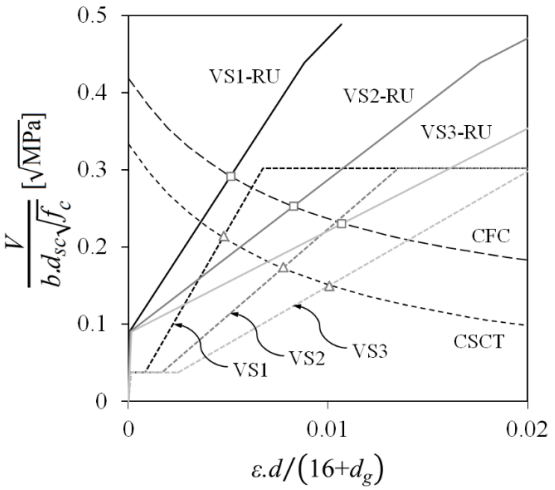

Figure 77. Prediction of critical shear force in VS series.

For the calculation of $V_{pc,c}$ (Eq. (37)) and $V_{pc,U}$ (Eq. (38)), the distance l_{NIC} was derived considering the geometric conditions of Figure 65 and Eq.(41) according to the angles

that lead to a minimum shear strength value. As indicated in **Erro! Fonte de referência não encontrada.**, α_c ranged from 24 to 31º.

Erro! Fonte de referência não encontrada. also presents the flexural resistance of the beams, which in the case of the RC-(R)U specimens with the UHPFRC in the tensile side were estimated according to the analytical model in Table 4 (point C). Moreover, the ratio $V_R^{exp}/V_{R,FPBT}^{exp}$ (in parentheses) for the MW series is also presented, where $V_{R,FPBT}^{exp}$ refers to the experimental flexural resistance of MW beams firstly tested under four-point bending (FPBT) by Oesterlee (2010) and then tested by Noshiravani and Brühwiler (2013a) using the undamaged ends which failed in flexure-shear. The ratio $V_R^{exp}/V_{flex} \geq 1.0$ indicates that the shear failure occurred when all the longitudinal reinforcements yielded.

It can be seen that the model described in section 4.2.2 for calculating V_{crit} in the RC-(R)U beams show very good agreement with the experimental results, with an average and a standard deviation of the V_{crit}^{exp}/V_{crit} ratio equal to 1.02 and 0.06, respectively. This is further evidenced in **Erro! Fonte de referência não encontrada.**, where dots correspond to V_{crit}^{exp} (with the corresponding strains ε calculated with the cross-sectional model) and the lines to the CSCT or CFC, depending on if the specimens are an RC or an RC-(R)U element, respectively.

The results are normalized according to the respective effective depth in the RC layer, d_{sc}, even for RC-(R)U configurations. In these circumstances, it is noted that while the line corresponding to the CSCT failure criterion is the same for all RC members in the different test series, the same does not occur for CFC and the RC-(R)U beams. In the composite failure criterion, the value of V_U depends on the concrete tensile strength given by Eq. (32) and on the UHPRFC layer thickness. As shown in **Erro! Fonte de referência não encontrada.**, the model for calculating V_{crit} captures well the effect of the studied variables, namely the reinforcement ratios and the size effect. Also, the thickness of the UHPFRC layer in tension is well reproduced (**Erro! Fonte de referência não encontrada.** (b)).

Table 11. Critical and post-critical shear force calculation.

Beam	α_c [°]	V_U [kN]	V_{crit} [kN]	V_{crit}^{exp} [kN]	$V_{pc,c}$ [kN]	$V_{pc,U}$ [kN]	$V_{post\text{-}crit}$ [kN]	V_R^{exp} [kN]	V_R^{exp} / V_{flex}	V_{crit}^{exp}/ V_{crit}	V_R^{exp} / $V_{post\text{-}crit}$
VT1	-	-	35.1	41.1	-	-	-	41.1	0.83	1.17	
VT2	-	-	39.7	46.9	-	-	-	46.9	0.51	1.18	
VT-U3	30	12.2	44.7	44.8	35.1	3.3	38.4	53.4	0.91	1.00	1.39
VT-U5	26	20.3	52.1	52.1	31.6	12.3	43.9	60.2	0.91	1.00	1.37
VT-RU1	30	20.3	56.7	61.0	40.7	23.8	64.5	76.8	0.82	1.08	1.19
VT-RU2	30	20.3	59.1	63.0	43.1	25.9	69.0	81.3	0.76	1.07	1.18
VT-RU3	30	20.3	61.5	66.9	45.2	26.8	71.9	86.8	0.70	1.09	1.21
VC-U3	30	14.8	41.1	46.5	-	-	-	52.3	0.83	1.13 [a)]	-
VC-U5	30	21.1	44.6	50.0	-	-	-	51.7	0.76	1.12 [b)]	-
VB0-RU	31	21.1	59.8	56.3	40.5	25.7	66.2	60.3	0.72	0.94	0.91
VB1-RU	30	21.1	61.4	57.5	43.0	26.3	69.2	98.3	1.01	0.94	1.42
VB2-RU	30	21.1	62.2	65.8	45.6	26.9	72.5	107.1	1.01	1.06	1.48
VS1	-	-	40.8	37.6	-	-	-	37.6	0.74	0.92	
VS2	-	-	66.3	64.0	-	-	-	64.0	0.63	0.97	
VS3	-	-	85.7	97.1	-	-	-	97.1	0.64	1.13	
VS1-RU	24	16.3	55.6	54.5	41.2	13.1	54.3	54.5	0.71	0.98	1.00
VS2-RU	24	32.5	96.4	94.1	82.9	26.2	109.0	94.1	0.62	0.98	0.86
VS3-RU	24	48.8	131.5	140.6	124.3	39.3	163.6	140.6	0.61	1.07	0.86
MW0 [d)]	-	-	40.0	43.2	-	-	-	43.2	1.09 (1.08 [e)])	1.08	
MW3 [d)]	28	28.5	72.4	78.0	60.2	26.5	86.7	91.7	1.06 (1.05 [e)])	1.08	1.06
MW4 [d)]	27	28.5	74.8	75.0	63.0	26.9	89.9	90.7	1.07 (1.05 [e)])	1.00	1.01
MW5 [d)]	28	28.5	75.3	82.5	63.3	28.8	92.1	99.6	1.03 (1.09 [e)])	1.10	1.08
MW6 [d)]	27	28.5	82.1	77.5	70.9	30.2	101.2	90.9	0.72 (0.67 [e)])	0.94	0.90
Average [c)]									0.85	1.02	1.13
Standard deviation [c)]									0.16	0.06	0.21
Minimum [c)]									0.61	0.94	0.86
Maximum [c)]									1.07	1.10	1.48

[a)] The model for $V_{post\text{-}crit}$ is not applicable. In this case, V_{Rexp}/V_{crit}=1.27

[b)] The model for $V_{post\text{-}crit}$ is not applicable. In this case, V_{Rexp}/V_{crit}=1.16

[c)] Only composite beams, except VC series for which the model for $V_{post\text{-}crit}$ is not applicable.

[d)] Tested by Noshiravani and Brühwiler (2013a)

[e)] From $V_R^{exp}/V_{R,FPBT}{}^{exp}$. $V_{R,FPBT}{}^{exp}$ is the experimental flexural resistance from FPBT by (Oesterlee 2010).

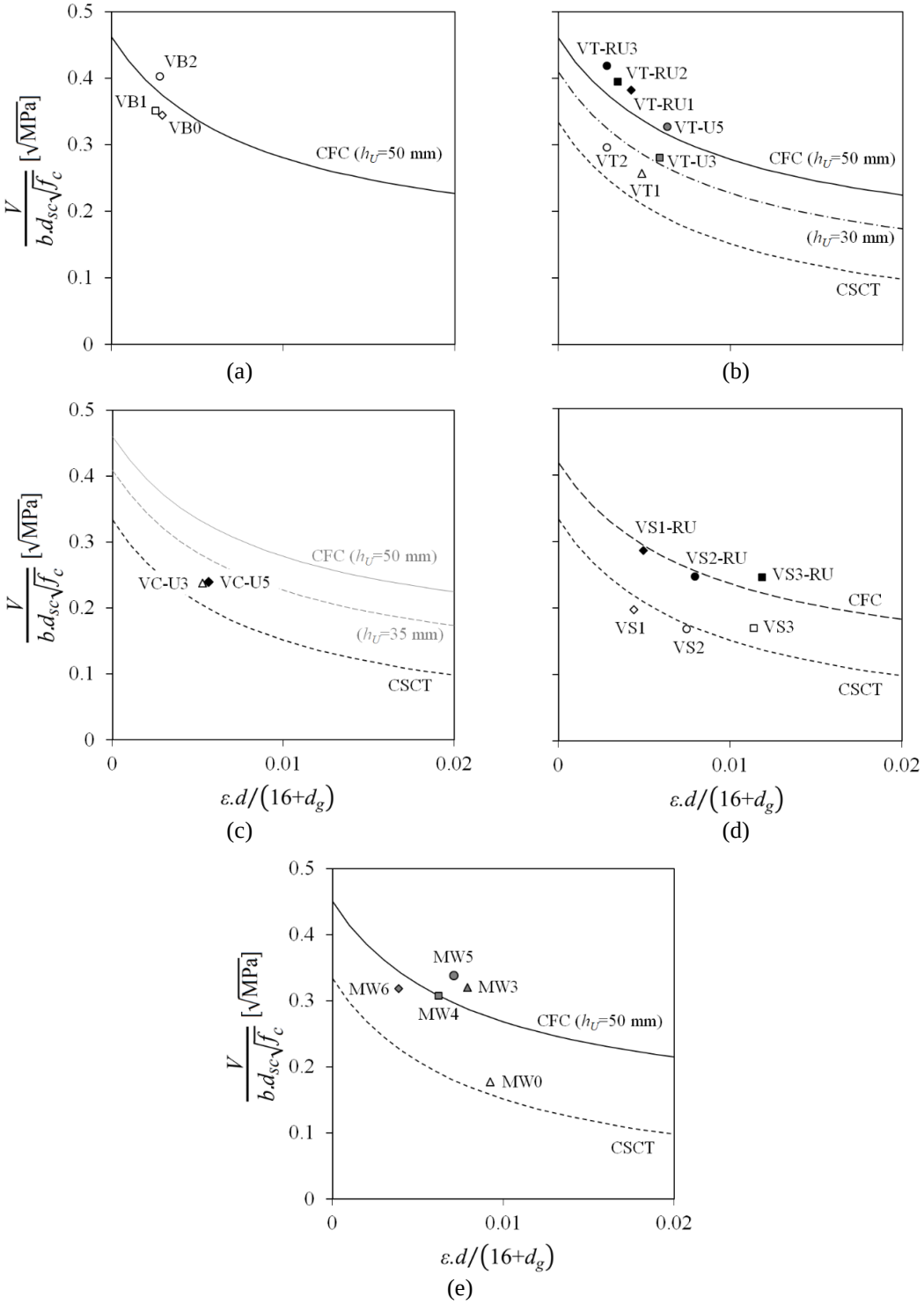

Figure 78. Comparison between the V_{crit} and the CSCT and CFC failure criteria: (a) VB series; (b) VT series; (c) VC series; (d) VS series; (e) MW series.

The prediction of post-critical shear strength of the composite beams using the model proposed by Bastien-Masse and Brühwiler (Noshiravani 2012) is generally conservative for small scale beams representing the typical thickness of building or bridge deck slabs, with an average and a coefficient of variation of the $V_{R,exp}/V_{post\text{-}crit}$ ratio equal to 1.13 and

0.21, respectively. The standard deviation value indicates important scatter in the predictions. This is further evidenced in Figure 79. The model seems to capture well the trend due to the reinforcement ratio in the UHPFRC layer (Figure 79 (a)). The predicted effect of the reinforcement ratio in the substrate (Figure 79 (b)) is mild, although the experimental trend is somewhat difficult to reproduce since it is not monotonic. Whether this can be explained by the mechanics of failure or just a consequence of the intrinsic variability associated with the involved phenomena is still to be clarified through further experimental evidence and more refined interpretative models. As for the size effect, it becomes apparent that the model for $V_{post\text{-}crit}$ cannot reproduce the decreasing shear stress at failure with increasing size (Figure 79 (c)).

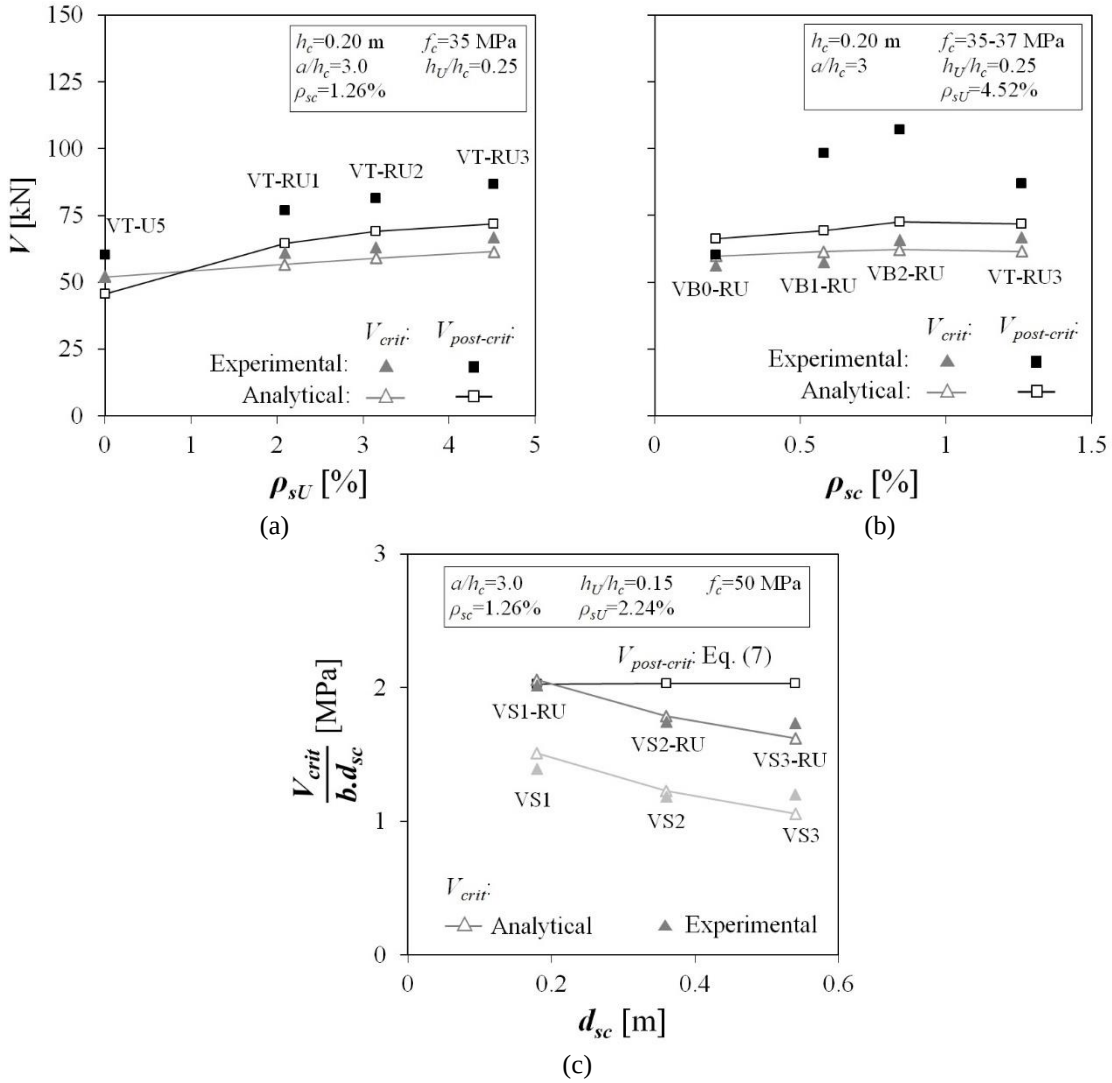

Figure 79. Experimental versus analytical trends for V_{crit} and $V_{post\text{-}crit}$: (a) effect of the reinforcement ration in the UHPFRC layer; (b) effect of the reinforcement ration in the substrate; (c) size effect.

4.5. CONCLUSIONS

An experimental campaign was carried out to test composite RC-(R)U and reference RC beams failing in shear. The analysed variables were the reinforcement ratios in the RC substrate and the UHPFRC layer, the location of the UHPFRC layer (tension or compression side), the UHPFRC layer thickness and the size effect.

In all cases, a significant stiffness and shear strength increase could be achieved with respect to the reference beams. In the specimens with the UHPFRC layer under tension and h_U/h_c=0.25, the strength (and ductility) increase were more significant, with the development of an alternative load-bearing mechanism after the formation of the diagonal shear crack and the NIC zone, as first described by Noshiravani and Brühwiler (2013a). The effect of the reinforcement ratio in the substrate on the shear strength of the composite beams is shown to be significant, as well as that in the UHPFRC layer. The size effect was similar in the strengthened and the reference beams. The specimens with the UHPFRC layer cast on the compressive side have also exhibited the formation of an alternative load-bearing mechanism after the formation of the critical shear crack, which allowed a substantial ductility increase with respect to the reference beams.

A composite failure criterion based on the CSCT contemplating the contribution of the UHPFRC layer was shown to accurately predict the shear force V_{crit} corresponding to the sudden propagation of the diagonal flexural-shear crack. In the specimens with a thinner UHPFRC layer (h_U/h_c=0.15) and stronger substrate concrete (f_c=50MPa), V_{crit} coincided with the failure load. The model well reproduced the influence of all the studied variables. Therefore, the CSCT can also be safely applied for estimating the shear strength of slabs and beams with the UHPFRC layer on the compressive side.

The model proposed by (Noshiravani and Brühwiler 2014; Bastien-Masse and Brühwiler 2016b) and adopted in the Swiss code (SIA 2016) was employed for determining the shear strength corresponding to the load-bearing mechanism developing after the NIC and critical shear crack propagation. This model is shown to provide safe estimates of the shear strength for the small scale specimens representing the thickness of typical building or bridge deck slabs. However, being rooted in the plasticity theory, the model is by definition size-independent and provided unsafe predictions of the failure load for the larger specimens of the series VS.

5. Experimental Investigation of Punching Shear Behaviour

5.1. INTRODUCTION

Reinforced concrete (RC) flat slabs are commonly used in multi-storey buildings due to the ease of construction, increased headroom, and improved flexibility in coordinating the structure design with the architecture and building equipment. However, the punching shear strength often dictates the design of RC flat slabs for the ultimate limit state (ULS). Since punching shear is associated with a brittle failure mode and may trigger a progressive global collapse of the structure, design or construction deficiencies can lead to collapse scenarios (Lew et al. 1982; Gardner, Huh, and Chung 2002; Wood 2003; King and Delatte 2004).

Strengthening techniques of existing RC flat slabs against punching shear include the enlargement of the support region, post-installed shear reinforcement (Ruiz, Muttoni, and Kunz 2011), post-tensioning (D. M. V. Faria, Lúcio, and Pinho Ramos 2012; Clément et al. 2014) or strengthening of the flexural reinforcement on the hogging moment region (Koppitz, Kenel, and Keller 2013; Lapi, Ramos, and Orlando 2019). Strengthening of the flexural reinforcement can be achieved by glueing fibre-reinforced polymers (FRP) (Farghaly and Ueda 2011; D. M. V. Faria et al. 2014; Torabian et al. 2020) or by casting a new RC overlay over the existing RC substrate (Lapi et al. 2018a; H. Fernandes, Lúcio, and Ramos 2017).

The application of a thin layer of ultra-high performance fibre reinforced cementitious composite (UHPFRC) over the top surface of existing RC slabs (Figure 80) has also been shown to be an effective punching shear strengthening method (Wuest 2007; Bastien-Masse and Brühwiler 2015; Youm and Hong 2018), allowing significant stiffness and strength enhancements. The UHPFRC layer can have the primary purpose of protection and/or strengthening. A plain UHPFRC layer suffices in the former case, turning the existing RC slab into an RC-UHPFRC composite slab (RC-U). In the latter, a reinforced UHPFRC layer is more efficient and less dependent on local variations of fibre content

and orientation (Pimentel and Nunes 2016a; 2016b). This strengthening approach improves both the flexural and punching shear behaviour, being possible to significantly increase the flexural hogging capacity of the RC-R-UHPFRC (RC-RU) composite slab (Figure 81 (a)) (Habel 2004; Oesterlee 2010). Moreover, the replacement of the existing concrete cover with the new UHPFRC layer results only in a slight increase of the slab self-weight, lower than using the traditional RC overlay (RC-RC), and improved durability in virtue of the UHPFRC excellent transport properties and ability to remain macro-crack free under service load levels. This strengthening technique also has the advantage of eliminating falsework, causing minimum disturbance of the structure below and allowing for brief interventions.

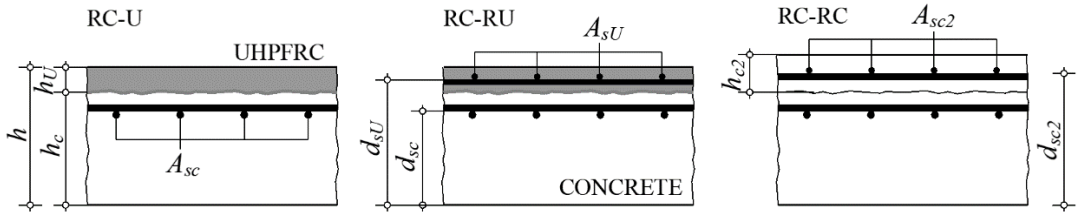

Figure 80. Composite RC-U and RC-RU, and RC-RC slab sections.

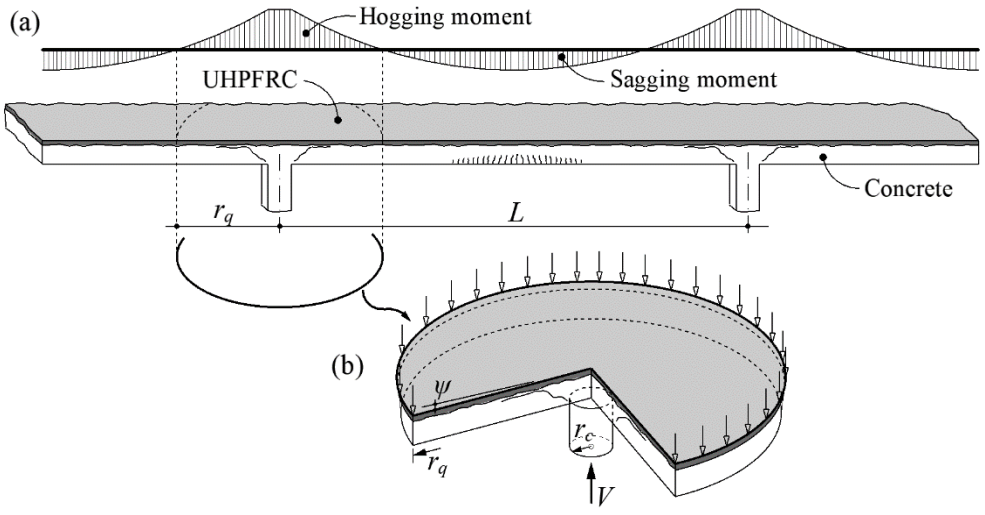

Figure 81. RC-(R)UHPFRC flat slab: continuous system and (b) isolated element, adapted from (Einpaul, Fernández Ruiz, and Muttoni 2015).

Some studies have been developed to evaluate the contribution of a UHPFRC overlay to the punching shear behaviour of flat slabs without transverse reinforcement. For example, Wuest (2007) tested an isolated (Figure 81 (b)) RC-U composite flat slab failing in punching shear. The slab was square with a 2000 mm side and a total height h=200 mm.

The 23 mm, thick UHPFRC overlay contained a fibre volume fraction V_f=6% of fibres with length l_f=10 mm and diameter d_f=0.2 mm. The reinforcement ratio in the RC substrate was $\rho_{sc}=A_{sc}/d_{sc}\approx0.75\%$. It was found that the substitution of the existing normal strength concrete cover layer by only 23 mm thick plain UHPFRC increased the flexural stiffness and the punching shear strength by 60% with respect to what should be expected in a reference RC slab.

Regarding the fibre distribution, it was concluded that its variability per unit area caused the non-symmetric cracking observed on the top layer. A similar slab, cited in Bastien-Masse and Brühwiler (2015), was tested, but with a reinforced 50 mm thick UHPFRC layer. The RC substrate's effective depth and reinforcement ratio were maintained, but the UHPFRC layer contained a reinforcement radio $\rho_{sU}=A_{sU}/h_U$=1.0%. The resistance of the RC-RU slab was 44% higher than that of the RC-U slab. However, the central displacement at failure was 30% smaller.

Bastien-Masse and Brühwiler (2015) also studied the contribution of the UHPFRC overlay (V_f=3% and l_f/d_f=13/0.2) on RC-U and RC-RU composite flat slabs without transverse reinforcement. The square slab panels had a 3000 mm side, total height h=260 mm and $\rho_{sc}\approx0.75\%$. The analysed parameters were the UHPFRC layer thickness (h_U=25 and 50 mm), its reinforcement ratio (ρ_{sU}=0.0 or 0.67%) and yield stress (f_{syU}=532 MPa or 772 MPa). The punching force was applied to the slab through a 260x260 mm^2 steel plate. The slabs with the 50 mm thick UHPFRC overlay resisted up to 75% more than the reference RC specimen in terms of normalized resistance. The slabs' punching shear strength and load-displacement behaviour were nearly identical irrespective of the presence and the type of the rebars in the UHPFRC layer.

Youm and Hong (2018) tested 2600x2600 mm^2 RC-U and RC-RU composite slabs. The substrate height (h_c=150 mm) and reinforcement ratio (ρ_{sc}=1.26%) were kept constant. The analysed parameters were the thickness of the UHPFRC layer (h_U=30 and 50 mm with V_f =2%, l_f/d_f=13/0.2) and its reinforcement ratio (ρ_{sU}= 0.0, 0.79 or 1.58%). The column with a 420x420 mm^2 cross-section was monolithically connected to the slabs. The column segment above the top surface of the slab was included such that the strengthening layer was not continuous over the load application area, reproducing the situation of a flat slab on an intermediate floor. Contrary to the other studies, the eight reactions points around the perimeter were fixed to the slabs with four bolts each, which may have

introduced partial rotational restraint, moving the perimeter of contraflexure towards the column. It was concluded that the influence of the reinforcement in the UHPFRC overlay was significant, leading to an increment of the punching shear resistance of up to 82% with respect to the reference RC slab, and that increasing amounts of reinforcement in the UHPFRC layer led to increasing punching shear resistance.

5.2. FAILURE CRITERIA

5.2.1. General

The punching shear provisions of RC flat slabs in the *fib*-Model Code 2010 (MC2010) (fib 2012b) are based on the Critical Shear Crack Theory (CSCT), where the failure criterion is a function of the slab rotation. On this basis, the punching shear strength can be predicted by the intersection of the failure criterion curve with the slab's force-rotation relation (Figure 82) (Muttoni 2008). Furthermore, it has shown to be generalizable to reproduce the effect of various strengthening techniques on the punching shear strength (Koppitz, Kenel, and Keller 2013; Lapi, Ramos, and Orlando 2019; D. M. V. Faria et al. 2014; Clément et al. 2014; Ruiz, Muttoni, and Kunz 2011; Lapi et al. 2018a). As for the composite flat slabs, the composite failure criterion, which considers the UHPFRC layer contribution, is employed (Bastien-Masse and Brühwiler 2016a).

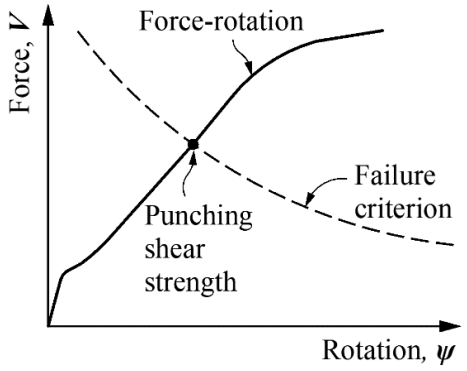

Figure 82. Failure criterion (Muttoni 2008).

According to the CSCT, the punching shear resistance, V_c, of the RC element depends on the opening of the critical shear crack, w, which can be assumed proportional to the product of the slab rotation, ψ, by its effective depth, d_{sc}. Therefore, the maximum

aggregate size, d_g, that accounts for the roughness of the critical shear crack; the concrete compressive strength, f_c; and the critical surface, obtained by the product of d_{sc} and the control perimeter, b_0, defined at a distance $d_{sc}/2$ from the column face are the remaining parameters involved in the failure criterion defined by Eq. (43).

$$\frac{V_c}{b_0 d_{sc}\sqrt{f_c}} = \frac{3/4}{1+15\frac{\psi d_{sc}}{d_{g0}+d_g}} \tag{43}$$

5.2.2. RC overlay

Lapi et al. (2018a) used the formulation of the CSCT for RC slabs strengthened with an RC overlay (RC-RC), considering that if the substrate is not cracked at the time of strengthening and that delamination of the RC overlay is prevented, the maximum crack width and the critical surface may be calculated using the effective depth of the overlay reinforcement, d_{sc2}. In these circumstances, the failure criterion becomes:

$$\frac{V_c}{b_{0,sc2} d_{sc2}\sqrt{f_c}} = \frac{3/4}{1+15\frac{\psi d_{sc2}}{d_{g0}+d_g}} \tag{44}$$

In Eq. (44), the compressive strength and maximum aggregate size refer to the substrate concrete, representing a conservative approach since using higher strength concrete for the overlay is common. This assumption leads to an enhanced failure criterion curve for determining the punching shear strength of the RC-RC cross-sections, as shown in Figure 83 Alternatively, more conservative estimates can be obtained using an average effective depth of the substrate and the RC overlay, d_{eq}, modifying the control perimeter, b_{eq} (D. M. V. Faria et al. 2014).

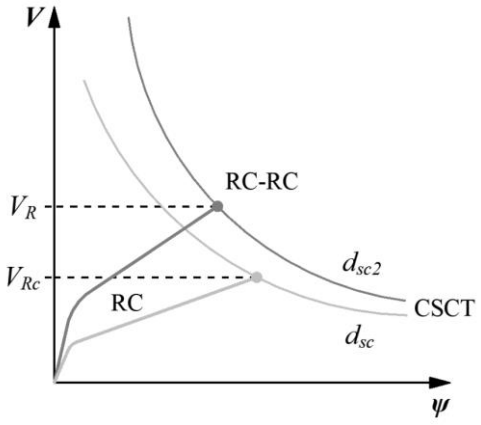

Figure 83. Determination of the punching shear strength of RC and RC-RC sections (Muttoni 2008).

5.2.3. Composite RC-(R)UHPFRC flat slabs

Bastien-Masse and Brühwiler (2016a) proposed and validated a composite failure criterion (CFC) model that includes the contribution of the UHPFRC layer to the punching shear resistance for RC-(R)U composite flat slabs. According to the CFC, the punching shear strength of the composite slab, V_R, is given by Eq. (45) (Figure 84):

$$V_R(\psi)=V_c(\psi)+V_U \tag{45}$$

where the superposition of the concrete, V_c, and the UHPFRC overlay, V_U, contributions are considered and determined according to Eqs. (43) and (46), respectively.

The UHPFRC overlay contribution to the CFC, V_U, depends upon the concrete tensile strength, f_{ct}, which controls the development of the near interface crack (NIC) at a radius r_U. This is based on the observation of the failure mode made by Bastien-Masse and Brühwiler (2015). Considering that the conical punching shear crack cannot intersect the UHPFRC layer, the formation and propagation of a horizontal crack promoting the separation between the concrete and the UHPFRC are required for the failure mechanism to become cinematically admissible. When the surface of the substrate is appropriately roughened, this crack is observed to propagate mainly through the concrete, just below the interface. If the inclination of the conical crack is conservatively taken as α_c=45º, then $r_U=r_c+h_c$ as schematically shown in Figure 85, where $r_c=(C_x+C_y)/\pi$.

Noting the limited extension of the NIC at the onset of failure, Bastien-Masse and Brühwiler (2016a) proposed that a minimum length equal to the thickness of the UHPFRC layer, h_U, is required, along which it is supposed that the stress at the onset of failure is uniform and equal to f_{ct}. Thus, the contribution of the UHPFRC overlay is given by:

$$V_U=b_U h_U f_{ct} \tag{46}$$

with b_U being the control perimeter in the UHPFRC layer defined at a distance $h_c+h_U/2$ from the column face.

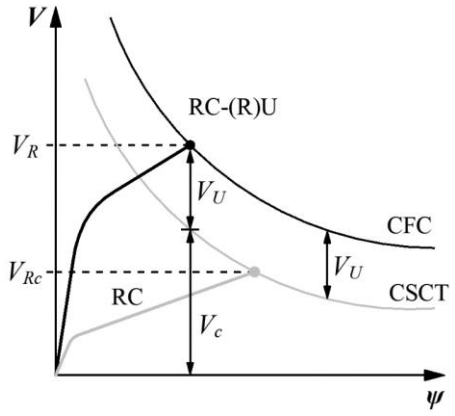

Figure 84. Determination of the punching shear strength of RC and RC-(R)U sections (Muttoni 2008; Bastien-Masse and Brühwiler 2016a).

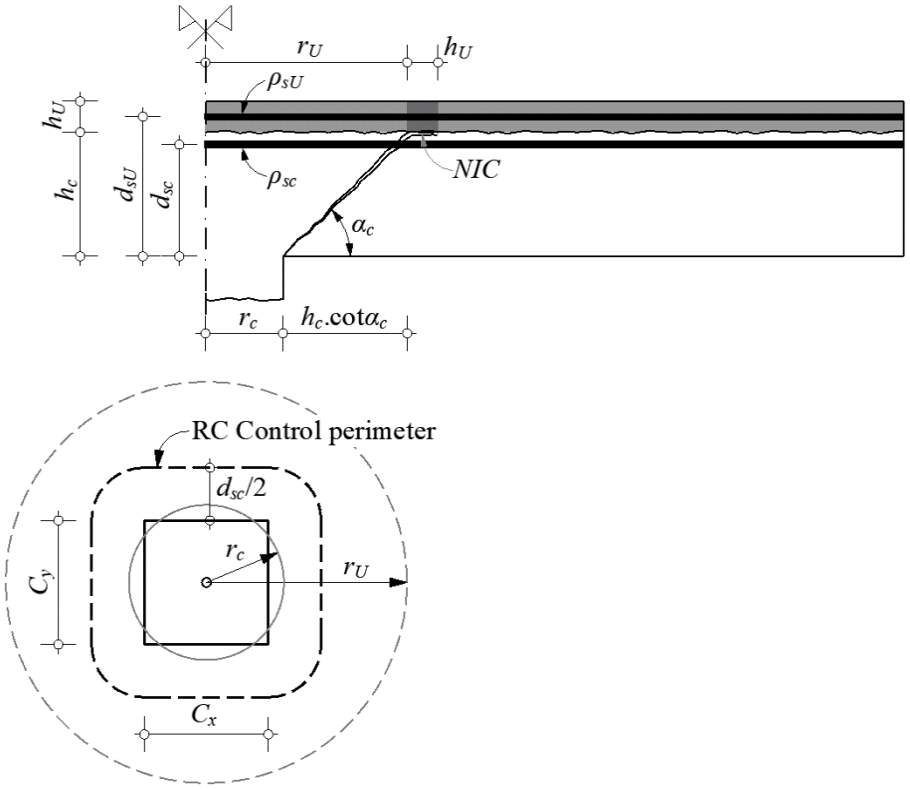

Figure 85. RC-(R)U slabs resistance mechanism and control perimeter.

In Eq. (46), no direct contribution of the UHPFRC strength is accounted for, and no distinction is made between the plain-U or reinforced-RU overlay. However, as schematically depicted in Figure 84, the (R)U overlay directly affects the slab flexural stiffness, allowing the intersection between the force-rotation curve and the CFC failure criterion to occur at higher load levels, therefore enabling significant punching shear strength enhancement.

The composite model was shown to provide exceptionally accurate estimates of the punching shear strength of the 6 six specimens (three RC-U and three RC-RU) tested by Wuest (2007) and Bastien-Masse and Brühwiler (2015).

5.3. EXPERIMENTAL INVESTIGATION

5.3.1. Specimens' specification and geometry

The experimental campaign presented herein focuses on the punching shear behaviour of strengthened RC flat slabs without transverse reinforcement, considering the following variations: the overlay cementitious material – RC (h_{c2}=60 mm, $\rho_{sc2}=A_{sc2}/h_{c2}$=1.31%, #$\phi$10@100) and UHPFRC (plain-U and reinforced-RU, h_U=40 mm, $\rho_{sU}=A_{sU}/h_U$=1.96%, #ϕ10@100); the substrate reinforcement ratio ($\rho_{sc}=A_{sc}/d_{sc}$=0.17%, #ϕ8@200 and 0.57%, #ϕ12@125); the shape of the loading area – square ($C_x=C_y$=250 mm) and rectangular ($2C_x=C_y$, 175x350 mm^2); the force eccentricity – concentric (e=0) and eccentric (e_y=150 mm). The slabs have an in-plane octagonal shape to allow rational materials use, as shown in Figure 66 (a). Figure 66 (b) and (c) show the side view of the concentrically and eccentric setups, respectively.

The specimens are organized in three test series: PC, with minimum reinforcement on the RC substrate; PRC, with normal RC substrate reinforcement; and PE, with a column segment cast monolithically to the slab, aiming to evaluate the influence of the eccentricity. The series PC reproduces those scenarios in which the effective depth or reinforcement ratio is significantly lower than necessary to resist the ULS loads. It can be caused by structural design and/or construction errors (Lew et al. 1982; Gardner, Huh, and Chung 2002; Lúcio, Ramos, and Faria 2008; Rocha 2012; Nhumaio 2015).

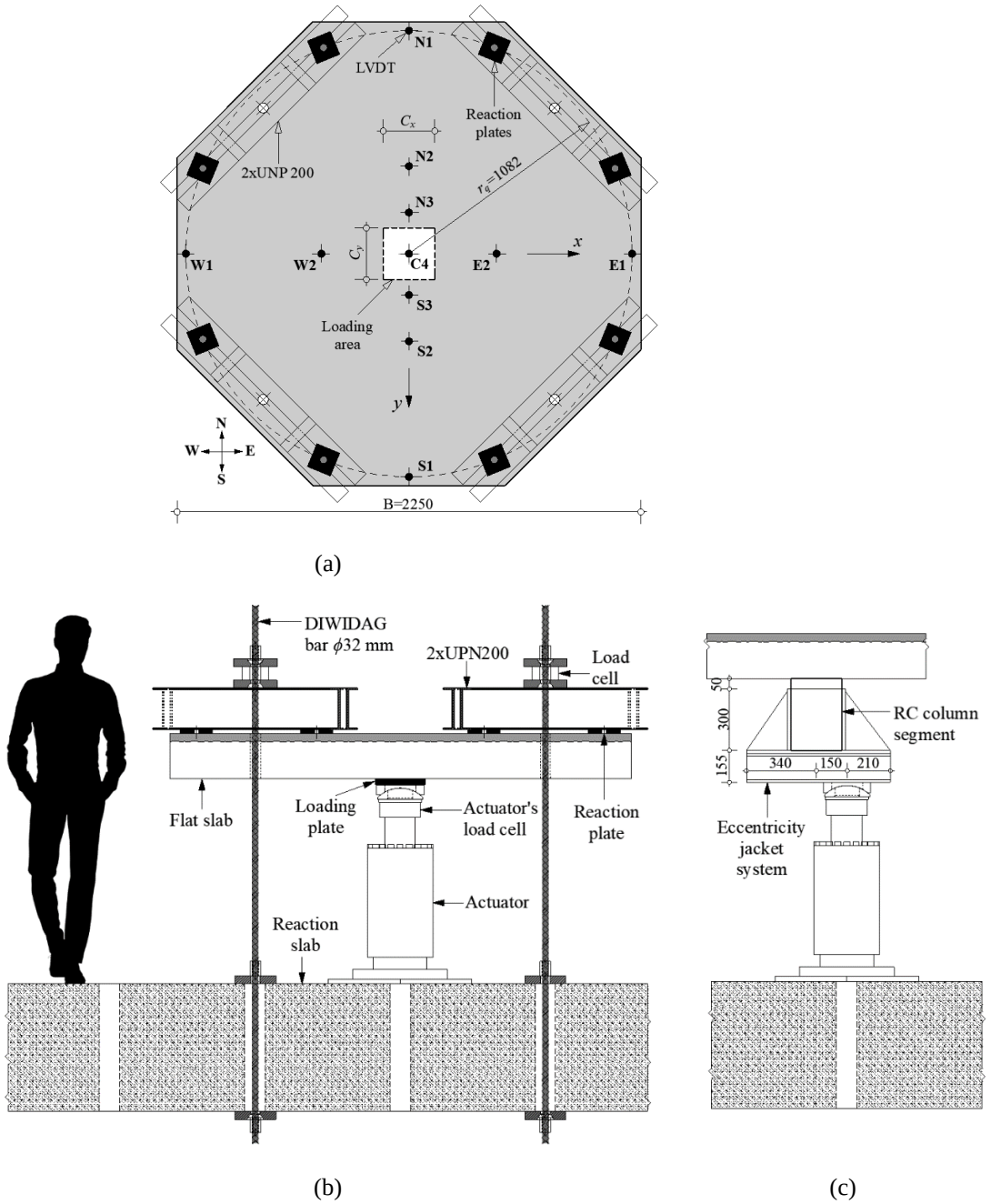

Figure 86. Punching test setup: (a) top and side view of (b) concentrically and (c) eccentrically loaded specimens.

The geometry and characteristics of the tested slabs are summarized in Table 12. h_U/h_{c2}=0.33 gives the overlay to substrate thickness ratios and h_U/h_c=0.22 for the RC and RU strengthening layers, respectively.

Table 12. Experimental programme.

Series	Specimens	Cross-section	B [mm]	r_q [mm]	C_xxC_y [mm^2]	RC substrate				U, RU or RC overlay			
						h_c [mm]	d_{sc} [mm]	*Bars*	ρ_{sc} [%]	$h_{U(c2)}$ [mm]	$d_{sU(c2)}$ [mm]	*Bars*	$\rho_{sU(c2)}$ [%]
PC	**PC-RC1**	RC-RC	2250	1082	250x250	180	154	#ϕ8 //200	0.16	60	210	#ϕ10 //100	1.31
	PC-RC2						150		0.17				
	PC-RU	RC-RU					151		0.17	40	200		1.96
PRC	**PRC ref.**	RC				190	142		0.64	-	-	-	-
	PRC-U	RC-U				180	146		0.62	40	200	#ϕ10 //100	1.96
	PRC-RU	RC-RU					159	#ϕ12 //125	0.57				
	PRC-R-RU				175x350		158		0.57				
PE	**PE-RU1**				250x250		154		0.59				
	PE-RU2 [a])						147		0.62				

[a]) – slab tested with force eccentricity e=150 mm

5.3.2. Material properties

The mechanical properties of the concrete and the UHPFRC are summarised in Table 13. The substrate's concrete and the overlay of slab PC-RC belong to two different batches of ready-mix normal strength concrete with maximum aggregate size d_g=16 mm.

Table 13. Material properties of RC substrate and RU overlay.

Specimens	RC substrate					RU overlay				
	E_c [GPa]	f_c [MPa]	$f_{ct,sp}$ [MPa]	f_{sy} [MPa]	*Age at test* [days]	E_U [GPa]	f_{Uc} [MPa]	f_{Ute} [MPa]	f_{sy} [MPa]	*Age at test* [days]
PC-RC	32	39	3.4	565	342	-	-	-	521	77
PC-RU					348	56	182	10.2		42
PRC (RC)	28	32	2.9	528	251	-	-	-	-	-
PRC-U	32	39	-		331	56	182	10.2	521	56
PRC-RU					335					55
PRC-R-RU					350					68
PE-RU1	28	32	2.9		355					67
PE-RU2					362					75

The concrete compressive strength (f_c), elasticity modulus (E_c) and splitting tensile strength ($f_{ct,sp}$) were determined as the average of three tests performed on standard Ø150 mm cylinders close to the date of the punching shear test. Despite being tested at different ages, the substrate (342 days) and overlay (77 days) concrete had the same properties.

The UHPFRC was produced in the laboratory using a commercial pre-mixture containing the powders and the sand. Straight steel fibres constitute the fibre fraction with an aspect ratio l_f/d_f =15/0.2 and a dosage of 2% in volume. The compressive strength f_{Uc} indicated in the table was determined at 33 days and is the average of three tests on 100 mm side cubic specimens. According to Graybeal and Davis (2008), this specimen shape provides the same UHPFRC compressive strength obtained in cylinders with height over diameter ratio h/Ø=2.0. The elasticity modulus was determined using cylinders with h/Ø=200 mm/100 mm. The tensile response of the UHPFRC was obtained through direct tensile tests on dog-bone shaped specimens with a 30x40 mm^2 cross-section, also at the age of 33 days, using a test setup where both ends are hinged (for details on the test setup, refer to Abrishambaf, Pimentel and Nunes (2020)). The results in the table are the average of five tests. All the specimens presented strain-softening behaviour after the elastic phase. The average values of the limit of elasticity in tension (f_{Ute}) and post-cracking tensile strength (f_{Utu}) are 11.7 MPa and 10.2 MPa, respectively. Image analysis on polished surfaces parallel to the main fracture surface revealed that the average fibre orientation factor in the dog-bone specimens was close to 0.53, representing a random fibre orientation in a thin UHPFRC layer with h_U=40 mm and l_f=15 mm.

Ordinary S500 hot-rolled ribbed steel bars were used as reinforcement.

5.3.3. Preparation of the slabs

5.3.3.1. The casting of the RC slabs (substrate)

The specimens were cast on a construction site close to the laboratory (Figure 87). The slabs of series PC and PRC were cast on the up-right position (flexural reinforcement close to top surface) as indicated in Figure 87 (a), whereas slabs of series PE were cast upside down due to the column segment (Figure 87 (b)). The slabs were cured on-site.

(a) (b)

Figure 87. Casting of RC slabs: (a) series PRC, and (b) series PE.

5.3.3.2. Preparation of the substrate concrete surface

The top surface of the existing RC slabs was hydro-jetted four to five months after being cast, as shown in Figure 88 (a). The slabs were initially cast with 190 mm thickness so that the top 10 mm were removed with the hydro-jetting process exposing the coarse aggregates (Figure 88 (b)). This procedure alone is sufficient to guarantee a good bond between the concrete of the existing substrate and the new UHPFRC layer, thus avoiding the use of mechanical connectors (Habel 2004; Bastien-Masse 2015; Youm and Hong 2018; Pimentel and Nunes 2016c; Haber et al. 2018; Noshiravani 2012). The slabs were transported to the laboratory after hydro-jetting.

(a) (b)

Figure 88. Concrete surface preparation: (a) hydro-jetting process and (b) surface roughness detail.

5.3.3.3. Casting of overlay

Before being strengthened with the new NSC/UHPFRC overlay materials, the roughened surface was saturated. The saturation process consisted of removing the dust and any other undesirable loose particles using a vacuum cleaner and a high-pressure air jet and finally covering the surface with moist cloths for a minimum of 20 hours before casting.

The PC-RC slab was strengthened with a new 60 mm RC overlay with a 20 mm cover to the reinforcement. Figure 89 (a) shows the reinforcement layout, and the casting process is presented in Figure 89 (b).

(a) (b)

Figure 89. The casting of RC overlay of the PC-RC specimen: (a) reinforcement layout; and (b) concrete placement.

Four hours after casting, the new concrete surface was covered with a plastic sheet for curing for seven days.

All the RC-(R)U composite slabs were strengthened with a 40 mm thick UHPFRC layer. As a result, the reinforcement of all RC-RU specimens had a 10 mm cover (Figure 90).

Figure 90. The casting of RU overlay

Shortly after finishing the new UHPFRC layer, the surface was covered with a plastic sheet to prevent water loss by evaporation. Here, the plastic cover was kept for a minimum of two days. After that, all the slabs were kept inside the laboratory until testing.

5.3.4. Interface concrete-to-concrete/UHPFRC mechanical characterization

5.3.4.1. Surface roughness characterization through SPM

The MC2010 (fib 2012a) provisions for interface shear between concretes cast at different times consider the influence of the substrate surface treatment (or roughness) on the cohesive and friction coefficients contributing to the bond resistance. The MC2010 considers the value of the average texture depth, R_t, derived from the sand patch test method (SPM) described in ASTM E965 (2001) guidelines to define whether the surface is rough ($R_t \geq 1.5$ mm) or very rough (≥ 3.0 mm). The SPM consists of pouring a known volume of sand on the surface to be assessed, spreading it to form a circular patch up to the peaks level. R_t is determined by the quotient between the volume of the sand and the area of the circular patch. An average R_t=6.3 mm was obtained from eight randomly spaced zones (Table 14). Therefore, according to the MC2010, the substrate surface can be considered very rough, resulting from the high-pressure water jetting employed in the present work.

Table 14. Average roughness depth of the surface subjected to hydro-jetting.

R_t [mm]									
i								**Average**	**Std. Dev.**
1	**2**	**3**	**4**	**5**	**6**	**7**	**8**		
4.8	6.6	6.3	8.4	5.6	6.8	5.9	5.9	6.3	1.04

5.3.4.2. Tensile bond strength - Pull-off test

The pull-off adhesion strength of the new strengthening layers was evaluated using the PROCEQ DYNA Z equipment, following the ASTM D 4541-85 standard. Failure occurs along the weakest plane within the system, which can be the substrate (A), the overlay (B), the interface between the substrate and the overlay (A/B), or the interface between the overlay and the aluminium disc (B/C). The pull-off tests were performed in the PC and PRC series, and the results are presented in Table 15. It can be seen that 3/4 of the RC-RC cores failed at the interface between the substrate and overlay concrete (Figure 91(a)), while all of RC-(R)U failed on the concrete substrate (Figure 91(b)). The results obtained in the RC-(R)U specimens confirm that the adhesion between the UHPFRC and the concrete is higher than the concrete tensile strength.

Table 15. Pull-off adhesion strength results and type of failure.

Slabs	σ [MPa]					
	i				Average	Std. Dev.
	1	2	3	4		
PC-RC	0.81 (A/B)	1.53 (A/B)	2.27 (A)	1.49 (A/B)	1.53	0.60
PC-RU	1.14 (A)	1.20 (A)	1.95 (A)	1.60 (A)	1.47	0.38
PRC-U	1.21 (A)	-	1.73 (A)	1.80 (A)	1.58	0.32
PRC-RU	1.86 (A)	2.15 (A)	2.23 (A)	2.38 (A)	2.15	0.22
PRC-R-RU	1.34 (A)	2.24 (A)	1.60 (A)	1.93 (A)	1.78	0.39

(a) (b)

Figure 91. Pull-off test cores: (a) PC-RC1; and (b) PRC-U.

5.3.5. Punching test setup, instrumentation, and testing procedure

5.3.5.1. Test setup

The load was applied upwards at the centre of the slabs (or eccentric in PE-RU2) using a 1500 kN capacity servo-hydraulic actuator equipped with a load cell. The test slabs were supported by eight equally spaced reaction points around the contraflexure line (Figure 86 (a)). The punching force was applied through a square (250x250 mm2) steel plate in the PC and PRC series (Figure 86 (b)), except in the PRC-R-RU slab (rectangular, 175x350 mm^2). In the PE slabs, the load was applied through a concrete column segment with a cross-section of 250x250 mm^2. In addition, a metallic L-shaped element previously developed by Afonso (2010) was used to introduce the eccentric load by jacketing it to the column segment (Figure 86 (c)).

The eight reaction points restrain the vertical displacement using steel plates of 120x120x25 mm^3 and ensure that the radius of the contraflexure circumference is r_q=1082 mm. A group of four 2xUPN200 steel beams receive the force from the reaction points and transmit it to four ϕ32 mm DYWIDAG bars anchored to the laboratory reaction slab. A load cell was placed on the top end of each DYWIDAG bar (Figure 86 (b)).

5.3.5.2. Instrumentation

LVDTs were installed according to Figure 86 (a), along two orthogonal alignments. The LVDTs were attached to an independent steel frame. Four LVDTs were positioned along the contraflexure line (N1, S1, W1 and E1), another four (N2, S2, W2 and E2) were installed at a distance $2d_{sc}$ (d_{sc}=150 mm) from the column face, and the two LVDTs N3 and S3 at $d_{sc}/2$. Finally, the eleventh LVDT, C4, was installed in the centre of the slab. The positioning of the LVDTs was maintained in all tests, except in slab PE-RU2 (with eccentric load e_y=150 mm), where the distance of N3 and S3 LVDTs to the centre of the slab was reduced 50 mm.

5.3.5.3. Testing procedure

The concentric (or eccentric) load was monotonically applied under displacement control at a rate of 0.01 mm/s. The punching failure was characterized by a sudden drop of the load soon after reaching the peak. From this point onward, the post-peak load barely increased for most specimens, and to avoid severe damage of the slabs, the tests were kept running for not more than 10 minutes.

The test with eccentric force (PE-RU2) had to be performed in two stages. In the first stage, the load was increased up to 674 kN, but excessive rigid body rotation was detected. Therefore, the test was stopped. After removing the steel encasing piece, it was found that the column was showing signs of failure, and there were gaps between the concrete and the steel encasing piece. The column was repaired, the gaps eliminated, and the test successfully conducted up to the punching shear failure (686 kN) without signs of column failure.

After testing, all slabs were transversally sawn through the symmetry planes along the *x*- and *y*-alignments so that the actual reinforcement depths and the critical shear punching crack angles could be measured and the internal crack patterns inspected.

5.4. RESULTS AND DISCUSSION

5.4.1. General observations

The experimental results are presented in Table 16, namely, the punching shear resistance (maximum force reached during the test) and the corresponding vertical displacement at the centre of the slab. Figure 92 shows the force-vertical displacement curves. All the slabs failed by punching shear.

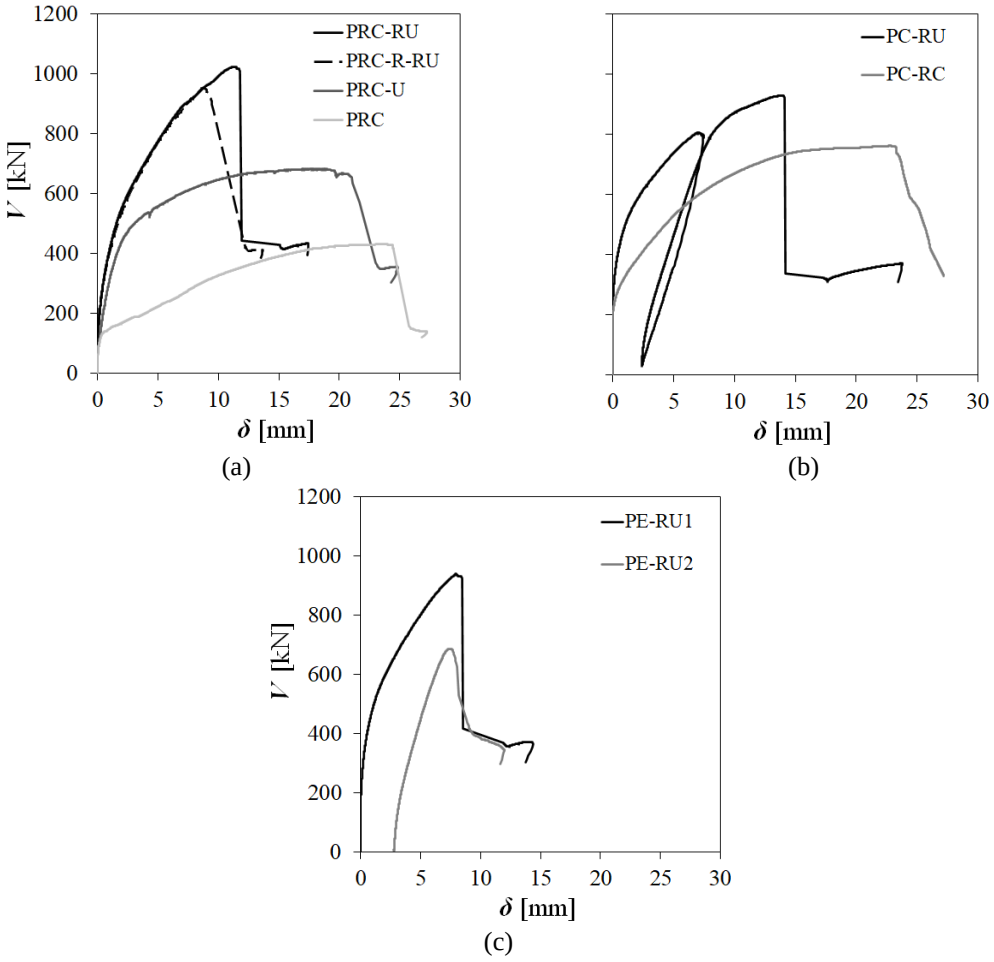

Figure 92. Experimental load-central deflection curves for (a) PRC, (b) PC and (c) PE series.

Table 16. Punching shear resistance and the corresponding vertical displacement

Specimens	**PRC**	**PRC-U**	**PRC-RU**	**PRC-R-RU**	**PC-RC**	**PC-RU**	**PE-RU1**	**PE-RU2**
V_R **[kN]**	431	682	1024	952	764	929	940	686
δ **[mm]**	23.8	17.6	11.4	8.7	22.7	13.9	8.0	7.4

The initial deflection and stiffness of the eccentric load test (PE-RU2 in Figure 92(c)) could not be assessed due to the aforementioned excessive rigid body rotations and premature column failure. Therefore, a NLFEA model duly calibrated in 6.2 with the results of the remaining tests was performed for estimating the residual deflection after the initial test stage for which no reliable deflections could be measured.

Figure 93 presents two typical saw cuts of the composite slabs, showing the diagonal critical shear crack crossing the substrate depth but not the UHPFRC layer. A horizontal crack is consistently seen propagating just below the interface between the concrete and the UHPFRC, the previously designated NIC (near interface crack). The inclination of the critical shear crack ranged from 18º to 44º.

(a) (b)

Figure 93. Typical detail of the critical shear crack and NIC in slab PE-RU1: (a) South and (b) East.

5.4.2. Influence of the UHPFRC overlay

The cross-sections of the slabs from the PRC series are presented in Figure 94. With an unreinforced 40 mm thick UHPFRC layer, the PRC U slab resisted 58% more than the reference PRC slab and reached similar displacement at failure. In the case of the PRC-RU slab, the punching shear resistance reached 138% and 52% with respect to the reference PRC and PRC-U slabs, respectively. As a consequence, the displacement at failure was reduced to about half of the reference slab.

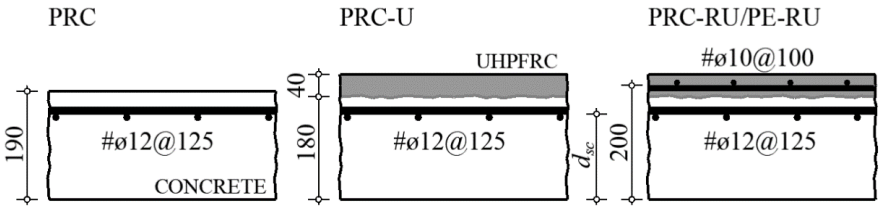

Figure 94. PRC, PRC-U, PRC-RU, PRC-R-RU, and PE-RU slabs' cross-sections.

The saw cuts evidencing the critical punching shear cracks and their inclination α_{ci} are shown in Figure 95 and Figure 96, together with the cracking patterns observed on the top surface. The subscript *i* denotes the cardinal directions. The inclination has been defined as the straight line connecting the edge of the loading plate and the intersection between the punching shear cracks with the reinforcement in the RC substrate.

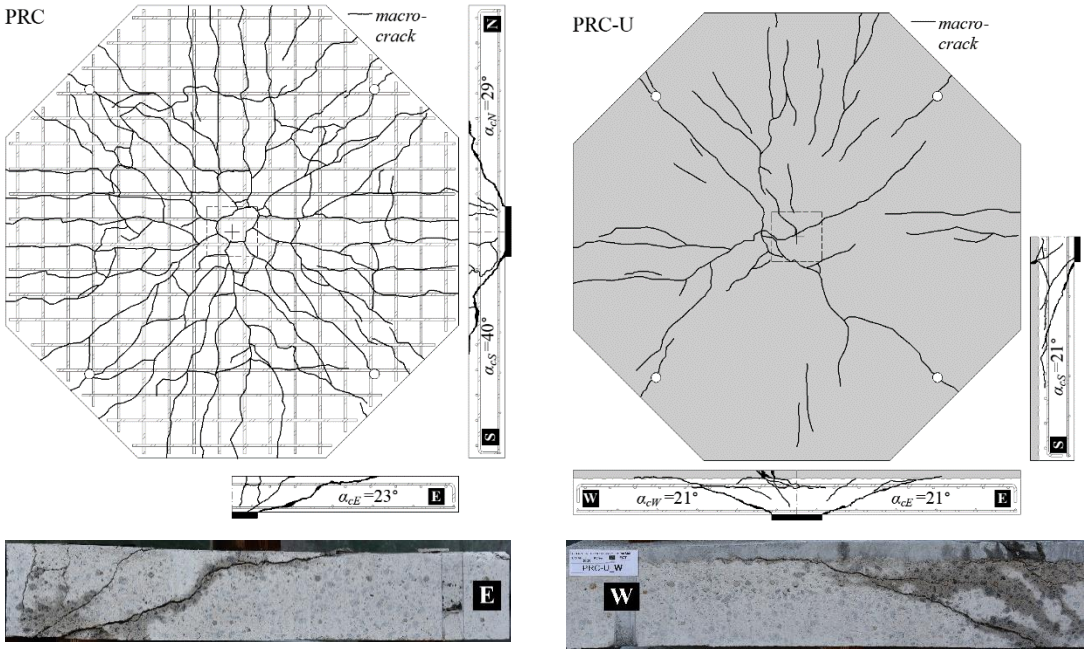

(a) (b)

Figure 95. Cracking pattern of series PRC (a) reference RC and (b) PRC-U.

The failure of the reference PRC slab occurred after reinforcement yielding but before the flexural capacity was achieved. A stabilized cracking pattern on the top surface of the slab is depicted in Figure 95 (a), where it can be seen that the distance between the rebars dictates the crack spacing. As for the PRC-U slab, a radial crack pattern was observed (Figure 95 (b)), indicating that the UHPFRC was in the softening regime, in which the deformations are already localized in macro-cracks visible to the naked eye. The results suggest that the flexural capacity of the slab might have been achieved. It is noted that the

peak force V_R was reached before the sudden drop attributed to the punching failure. Just before failure, the force was already reduced to $0.97V_{R,}$ and the central displacement increased 20% with respect to that at peak force (Figure 92 (a)).

The crack pattern of the PRC-RU slab shown in Figure 96 (a) was different, with a smaller number of cracks visible to the naked eye. The failure load is well below the flexural capacity of the slab. As shown in Figure 96 (b), a fine micro-crack pattern could be disclosed after spraying the surface with alcohol, with micro-cracks spaced every 10 to 20 mm. This micro-crack pattern was observed in all specimens with the reinforced UHPFRC overlay. Most of the macro-cracks observed on the RU strengthened specimens followed the direction of the top layer of bars, which can be attributed to the small cover of this reinforcement.

Youm and Hong (2018) also reported the micro-crack development in the reinforced UHPFRC overlays. Actually, it has been shown that RU ties may display a stable array of fine micro-cracks with spacing values close to the fibre length, l_f, even if the UHPFRC itself is a strain-softening material (Oesterlee 2010; Redaelli 2009; Leutbecher and Fehling 2012; Valente, Pimentel, and Nunes 2021). This is due to the synergetic effect between the reinforcement bars and the fibres, both concurring to bridge the tensile forces across the cracked UHPC cementitious matrix. It is also shown that, in general, the visible cracks are the consequence of the strain localization occurring at the onset of yielding of the reinforcement in the RU layer (Valente, Pimentel, and Nunes 2021).

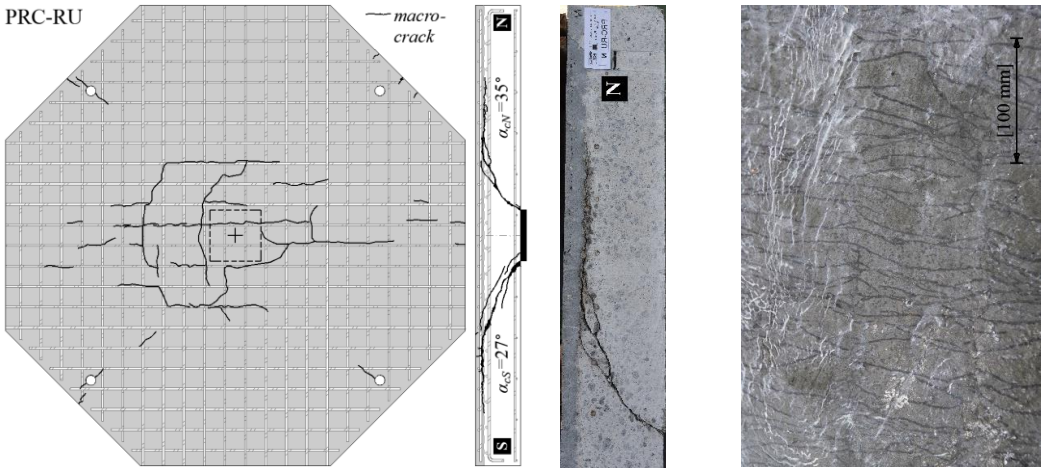

(a) (b)

Figure 96. Cracking pattern of PRC-RU slab (a) macro-cracks and critical shear crack and (b) micro-cracks detail.

5.4.3. Influence of the overlay cementitious material

The cross-sections of the slabs from the PC series are presented in Figure 97. In this series, the flexural reinforcement ratio in the RC substrate is close to the minimum, and the resistance increase compared to the hypothetical reference slab was quite significant in both slabs. The PC-RC slab failed after significant reinforcement yielding, and the peak load is the same as the theoretical flexural capacity. The crack pattern at the top surface depicted in Figure 98 (a) is similar to that of the reference slab. The saw-cuts revealed that the RC strengthening layer and the substrate bond was enough to prevent delamination cracks. The punching cracks are observed to cross the strengthening layer, likewise what would be expected in a monolithic slab.

Albeit the smaller total thickness and effective depth of the rebars in the overlay, the PC-RU slab showed higher bending stiffness and 22% larger punching shear strength than the PC-RC, but with a minor deflection at failure (Figure 92 (b)). Still, the failure load is below the flexural capacity due to the significant contribution of the UHPFRC to the flexural strength. The crack pattern on the top surface is depicted in Figure 98 (b). The visible cracks follow the alignments of the most superficial layer of rebars closely. As previously discussed, the existence and the extent of these visible cracks indicates the area where reinforcement is yielding.

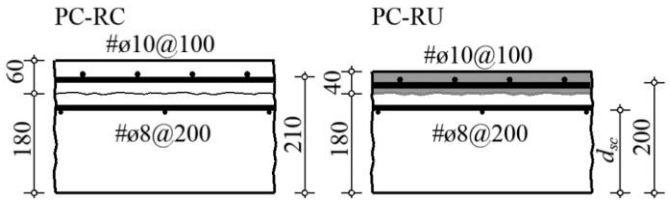

Figure 97. PC-RC and PC-RU slabs' cross-sections.

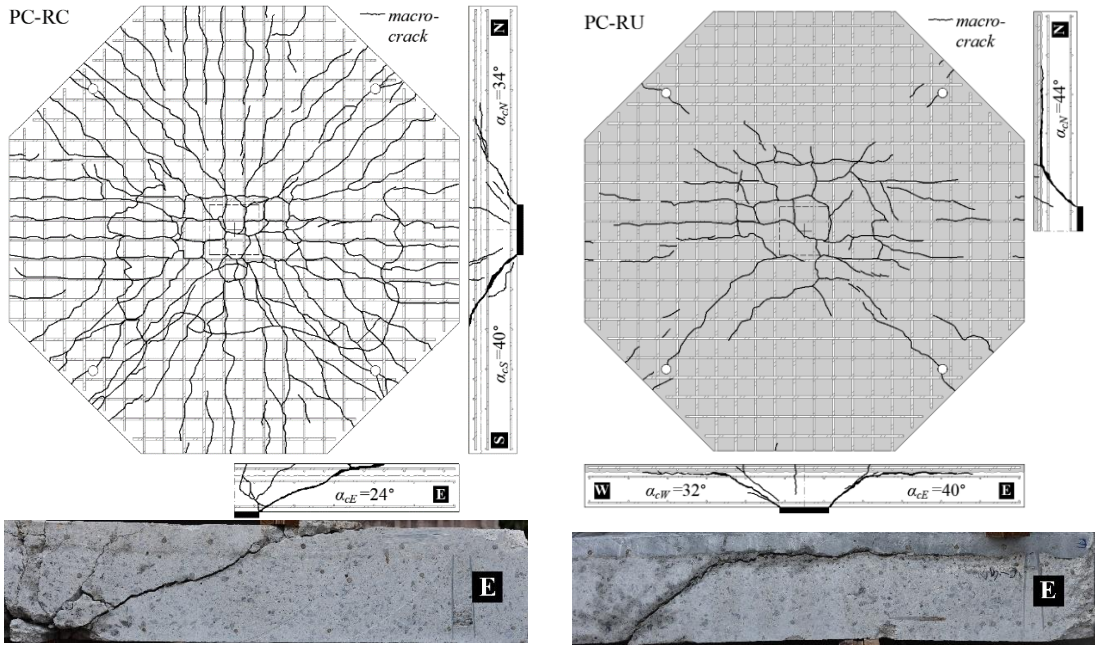

(a) (b)

Figure 98. Cracking pattern of series PC (a) PC-RC and (b) PC-RU.

5.4.4. Influence of the reinforcement ratio in the substrate

The slabs PRC-RU and PC-RU have the same RU overlay but different reinforcement ratios in the substrate, i.e., low ρ_{sc}=0.17% for the PC-RU and intermediate ρ_{sc}=0.57% for the PRC-RU (typical for RC flat slabs). Even though the latter resisted only 10% more than the former (Figure 92 (a-b)). The visible crack pattern in the top surface of the PC-RU (Figure 98 (b)) is clearly more developed than in the PRC-RU (Figure 96 (a)), indicating that the extent of the region over which rebar yielding has been reached is more significant on the former.

5.4.5. Influence of the loading area shape

The slabs PRC-RU and PRC-R-RU were tested using square and rectangular steel plates, respectively. The area of the rectangular plate is 2% smaller than that of the square one, but the perimeter is 5% larger. The slabs presented similar behaviour, with the punching shear strength of PRC-R-RU being 7% less than that of the PRC-RU (Figure 92 (a)), which is within the experimental scatter.

The rotations in the two orthogonal directions of the slab PRC-R-RU are similar, as shown in Figure 99 (a), which further confirms that the differences to the slab with square loading area should be negligible. The rotations were determined from the relative vertical displacements between the LVDTs located in positions 1 and 2 of each direction, N-S and W-E. The rotations along the N-S direction aligned with the largest dimension of the rectangle become marginally higher at the later loading stages (>0.85V_R).

Both slabs presented a similar cracking pattern. Figure 99 (b) shows the crack pattern at the top surface and the saw cuts of the PRC-R-RU slab. The column side did not seem to influence the inclination of the critical shear crack, that is $\alpha_{cN} \approx \alpha_{cW}$. This confirms that the punching shear strength RC-RU composite slabs is unaffected by the shape of the columns whenever the ratio between the greater and smaller sides of the column is $C_{max}/C_{min} \leq 2.0$.

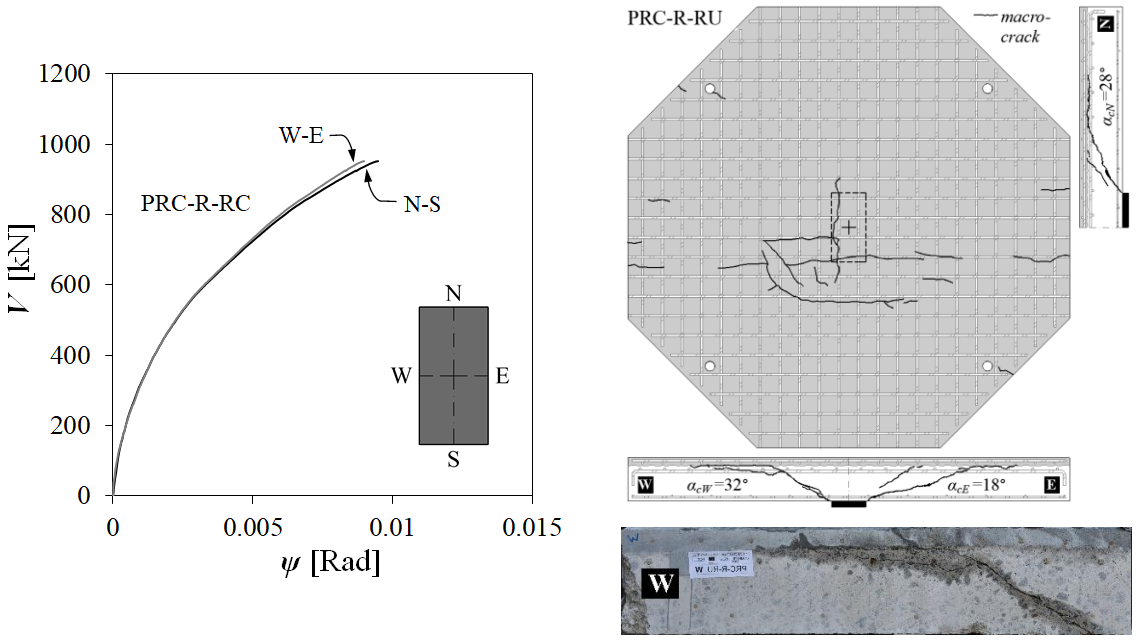

(a) (b)

Figure 99. PRC-R-RU slab (a) force-rotation curve and (b) cracking pattern.

5.4.6. Influence of force eccentricity

The slabs of the series PE contained a concrete column segment for load application. To better evaluate the influence of the eccentricity on composite flat slabs, the slab PE-RU1, with a concentric load, is considered here as the reference. An eccentricity e_y=150 mm of

the force was applied in the PE-RU2 specimen. The punching shear resistance of the PE-RU2 slab was 27% lower than in the concentrically loaded specimen.

The crack patterns of the two slabs are depicted in Figure 100. As expected, the crack pattern of the slab PE-RU1 was similar to that of the PRC-RU. As for the PE-RU2, only one crack visible to the naked eye could be detected on the top surface. However, a dense micro-crack pattern could be observed after spraying alcohol on the surface, like Figure 96 (b).

The inclination of the critical shear cracks of the PE-RU1 slab varies from 30º to 36º (Figure 100 (a)). It differs from that of the PE-RU2 slab. In the PE-RU2 slab, the crack inclination is 19º along with the S-direction, corresponding to the direction of the force eccentricity (Figure 100 (b)). In this slab, the near interface cracking was observed over the column's top and towards the N-direction.

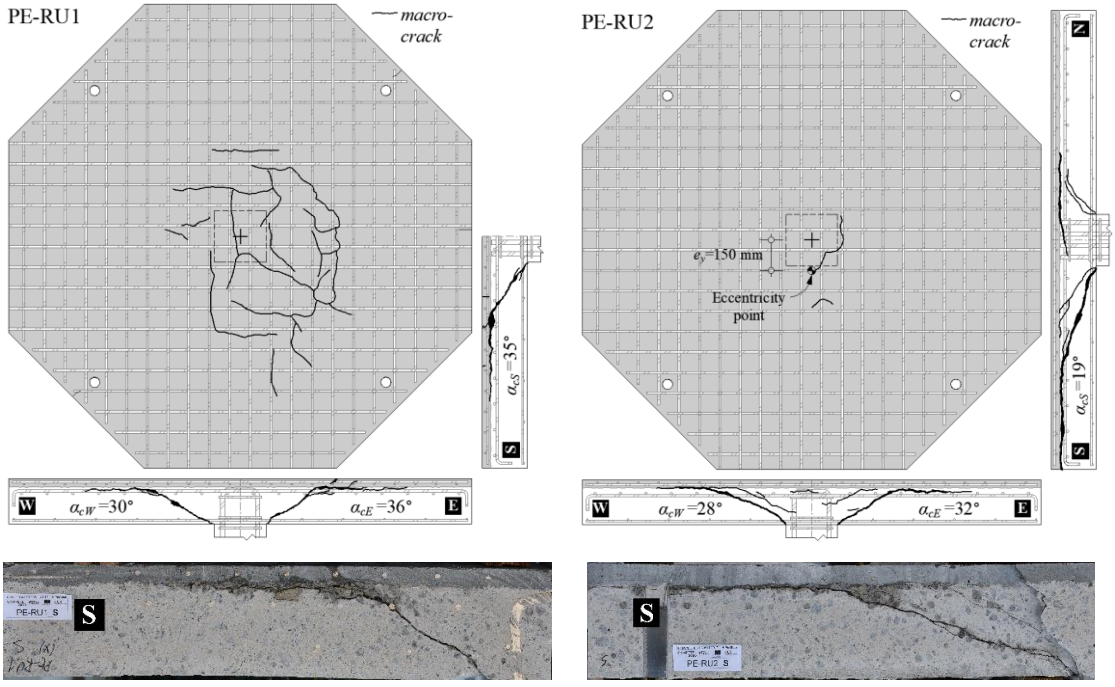

(a) (b)

Figure 100. Cracking pattern of series PE (a) PE-RU1 and (b) PE- RU2.

Figure 101 shows the deflected shape of the slab PE-RU2 at the onset of failure, along with two orthogonal directions. The effect of the eccentricity is noticeable. The results are compared to the estimates of a numerical NLFEA model.

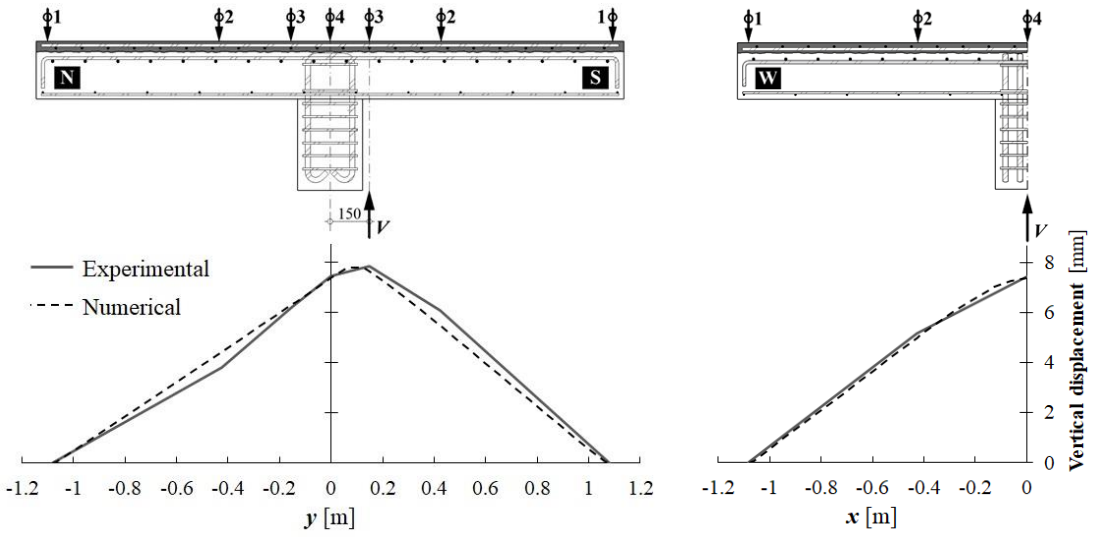

Figure 101. Deformation profile at the punching shear strength of the PE-RU2 slab (a) *y*- and (b) *x*-directions.

5.4.7. Experimental and calculated punching shear strength

The experimental failure loads, $V_{R,exp}$, are compared with the punching shear strength calculated through the intersection of the experimental force-rotation curves and the applicable failure criterion, as shown in Figure 102. The failure criterion is defined by Eq. (43) for the reference RC slab, by Eq. (44) for the RC-RC slab and by Eq. (45) for composite RC-(R)U slabs. The value of $f_{ct}=0.3(f_c-8)^{2/3}$ (fib 2012a) was used in Eq. (46). The results are summarized in Table 17.

The experimental rotations were determined by dividing the vertical central deflections by r_q-r_c (Guandalini 2005), where r_c is the circle's radius with the same perimeter as the square/rectangular column and r_q the radius of the contraflexure line. This procedure is also adopted for the slab with the rectangular loading plate since the differences in the rotations along the two orthogonal directions of the slab are negligible.

In the case of the slab PE-RU2 with eccentric loading, the control perimeters b_0 and b_U used to determine the contributions V_c and V_U to the composite failure criterion were reduced by a coefficient k_e, following the MC2010 provisions (fib 2012b):

$$k_e = \frac{1}{1+e_u/(2r_u)} \tag{47}$$

where e_u is the eccentricity of the resultant of shear forces with respect to the centroid of the control perimeter and r_u is the radius of the circle with the same surface as the region

inside the control perimeter. The coefficient k_e is equal to 0.75 and 0.80 for the perimeters b_0 and b_U, respectively. Figure 102(d) shows that the CFC corresponding to the PE-RU2 slab is lower than that of PE-RU1. The force-rotation curve was determined considering the maximum slope occurring along the S-direction: $\psi=(\delta_{v,S1}-\delta_{v,S2})/l_{12}$, where $\delta_{v,S1}$ and $\delta_{v,S2}$ are the relative vertical displacements measured by LVDTs S1 and S2, respectively, and l_{12} is the distance between them.

All the punching shear strengths were normalized with the product $b_0 d_{sc}\sqrt{f_c}$, thus obtaining the value v_R. The ratio $v_{R,exp}/v_{R,RC}$ shows the strengthening efficiency relative to the RC substrate. For the PRC and PE series, $v_{R,RC}$ was taken as the PRC reference slab. As for the PC series, with minimum reinforcement in the substrate, $v_{R,RC}$ was determined considering flexural strength of the substrate slab given by $V_{flex}=2\pi m_R r_s/(r_q-r_c)$, where r_s is the radius of the circle circumscribed in the octagonal-shaped slab and m_R is the unit moment capacity of the substrate slab section.

The average of the ratio $V_{R,exp}/V_R$ for the composite slabs is equal to 1.06 with a standard deviation of 0.04. This shows that the predicted resistance using the CFC proposed by Bastien-Masse and Brühwiler (2016a) agrees with the experiments, covering a substantial range of flexural reinforcement ratios and even considering rectangular loading areas and the effect of the eccentricity of the force.

Table 17. Comparison of the punching shear resistance.

Slabs	$V_{R,exp}$ **[kN]**	$\psi_{R,exp}$ **[‰]**	V_R **[kN]**	ψ_R **[‰]**	V_U **[kN]**	$v_{R,exp}/v_{R,RC}$	$V_{R,exp}/V_R$	$\psi_{R,exp}/\psi_R$
PRC	431	25.8	402	17.6	-	1.00	1.07	1.47
PRC-U	682	19.1	681	20.6	262	1.38	1.00	0.93
PRC-RU	1024	12.4	932	9.0	262	1.85	1.10	1.38
PRC-R-RU	952	9.6	949	9.4	268	1.68	1.00	1.02
PC-RC	764	25.1	708	13.3	-	4.76 [a)]	1.08	1.89
PC-RU	929	14.8	865	10.5	262	5.84 [a)]	1.07	1.41
PE-RU1	940	8.6	874	6.9	208	1.96	1.08	1.24
PE-RU2	686	8.0	618	8.1	172	1.92	1.11	1.14
						Average [b)]	1.06	1.19
						Standard deviation [b)]	0.04	0.17

[a)] Determined relatively to substrate flexural strength, V_{flex}.

[b)] Except reference PRC and PC-RC slabs.

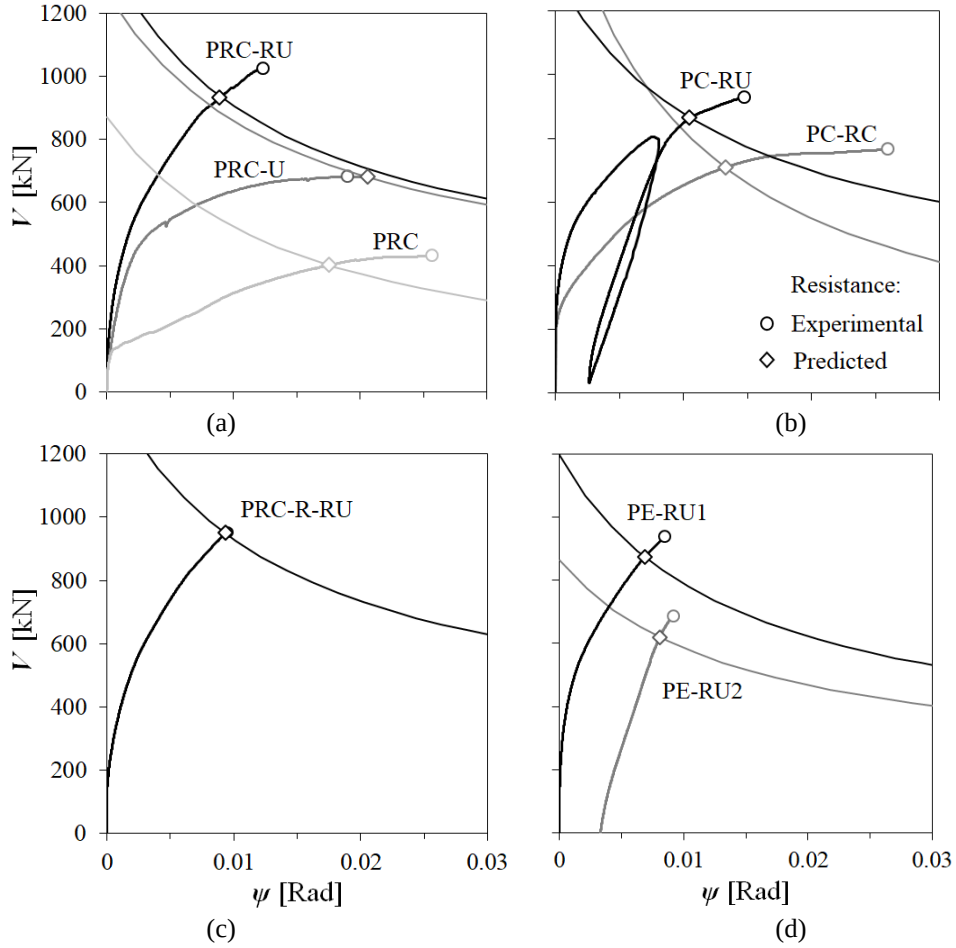

Figure 102. Comparison of punching shear strength of slabs (a) PRC, PRC-U and PRC-RU, (b) PC-RC and PC-RU, (c) PRC-R-RU and (d) PE-RU1 and PE-RU2.

Figure 103 shows the effect of the force eccentricity, which seems to be well reproduced by the model, including the reduction coefficient given by Eq. (47) applied to the control perimeters b_0 and b_U.

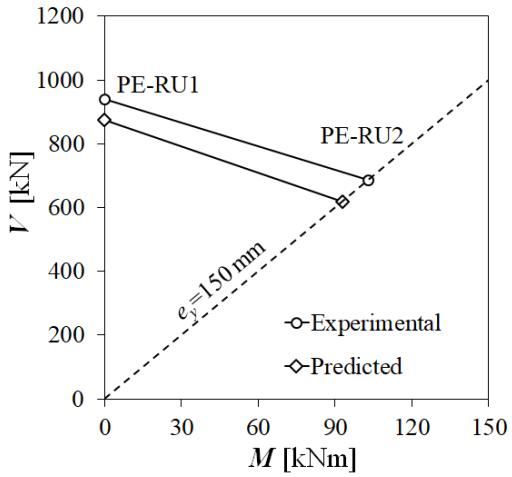

Figure 103. Effect of the force eccentricity on the punching shear strength of composite slabs.

5.5. CONCLUSIONS

An experimental investigation is presented herein comprising six RC flat slabs strengthened with a thin UHPFRC overlay failing under punching shear. Two additional reference slabs were tested for comparison: one unstrengthened RC specimen and one specimen strengthened with a new RC overlay. The investigation allowed studying important variables that affect the contribution of the UHPFRC for the punching shear strength of the composite slabs, namely the reinforcement ratio in the existing concrete substrate, the reinforcement in the strengthening layer, the shape of the column and the eccentricity of the force. In addition, the tests significantly extend the existing experimental evidence and provide a wide range of data for model validation.

All the composite RC-(R)U slabs failed in punching shear. Likewise, the observations made by other authors, the saw cuts, revealed that the conical punching shear cracks do not cross the UHPFRC layer. Instead, a horizontal crack propagates just below the interface between the UHPFRC and the concrete (the so-called near interface crack, NIC), promoting the separation between the two materials and allowing the development of the failure mechanism. In the case of the reinforced UHPFRC layers, a distinct crack pattern constituted by fine microcracks, only visible after spraying the surface with alcohol and spaced every 10 mm to 20 mm apart, could be observed on the slab top surface.

The failure loads were compared to the estimates obtained using the composite failure criterion (CFC) proposed by Bastien-Masse and Brühwiler (2016a). The CFC is based on the Critical Shear Crack Theory (CSCT) and considers the contribution of the UHPFRC to be twofold: first, the UHPFRC layer significantly decreases the opening of the critical shear crack, thereby increasing the punching shear strength of the substrate, V_c; second, an additional term, V_U, is added to V_c accounting for the force necessary to open the NIC.

The experimental results confirm the significant contribution of the UHPFRC thin overlay to the punching shear capacity. The addition of the 40 mm plain UHPFRC layer (h_U/h_c=0.22) allowed the resulting composite slab (PRC-U) to develop its flexural capacity and resist 1.58 times more than the unstrengthened reference RC slab (PRC) containing a flexural reinforcement ratio ρ_{sc}=0.57%. The reinforced UHPFRC overlay (PRC-RU) enhanced the resistance of the reference slab by 2.38 times. Regarding the

variation of the reinforcement ratio in the substrate, it was observed that the slab with a smaller reinforcement ratio (PC-RU, ρ_{sc}=0.17%) resisted only 10% less than that with a higher reinforcement ratio (PRC-RU, ρ_{sc}=0.57%) and about 5.4 times more than the flexural capacity of the original slab. This shows the efficiency of this strengthening technique in cases of existing slabs with serious construction/design errors. The CFC could well reproduce all these failure loads and trends.

The slab tested with a rectangular loading plate with a ratio between the maximum and minimum side C_y/C_x=2 has shown that the term V_U in the CFC can still be calculated assuming a uniform tensile stress distribution around rectangular columns at least $C_y/C_x \leq 2.0$. As for the effect of the load eccentricity, the hybrid slab tested with e=150 mm (=0.6 times the column side) resisted about 27% less than the force of the slab tested under concentric loading. In this case, reasonable estimates of the failure load were also obtained with the CFC considering suitably reduced control perimeters for taking into account the non-uniform stress distribution, following the recommendations of the *fib* Model Code 2010.

The observed failure mode of the RC-RU slabs and the excellent agreement of the CFC with the experimental failure loads confirm that the punching shear failure of the composite slabs is triggered by the formation of the NIC, which is still governed by the concrete tensile strength of the existing substrate. Therefore, despite the significant strength increase achieved in the RC-RU slabs, this suggests that if the NIC formation could be delayed or even prevented using suitable mechanical connection systems, the punching shear strength would be even higher and limited by concrete crushing in the vicinity of the column. Also, the ductility of the response would be more significant, which may be determinant in cases of column-to-slab connection subjected to cyclic loadings, such as those in buildings in earthquake-prone regions. This is a topic that requires further research.

6. Calculation of Punching Shear Strength

6.1. INTRODUCTION

The Composite Failure Criterion (CFC) that accounts for the UHPFRC layer contribution to the punching shear resistance of RC-(R)U hybrid sections was proposed by (Bastien-Masse and Brühwiler 2016a) has been previously introduced. The UHPFRC layer contribution is added to the RC substrate contribution, defined by the Critical Shear Crack Theory (CSCT) (Muttoni 2008). The CFC was successful validated using experimental results of six hybrid flat slabs (three RC-U and three RC-RU) from (Wuest 2007; Bastien-Masse and Brühwiler 2015). The intersection of the analytical shear force-rotation relations with the CFC predicted the shear strength accurately (Bastien-Masse and Brühwiler 2016a; 2016b). The main variables of these slabs refer to the plain UHPFRC overlay thickness and the additional reinforcement strength (standard and high).

Six more composite slabs were tested and presented in Chapter 5. The studied variables included the reinforcement ratios in the substrate and the overlay, the column shape and the force eccentricity. The CFC was successfully used together with the experimentally measured force-rotation curves to reproduce the observed punching shear strength. Additionally, two reference RC slabs were tested. One comprised the original substrate configuration, while the other simulated one RC slab with minimum reinforcement ratio strengthened with another RC layer, denoted as RC-RC.

In this Chapter, an NLFEA using layered shell elements is performed to obtain the load-rotation curves, following the procedure outlined in the punching shear provisions of the *fib*-Model Code 2010 (MC2010) fourth and the highest-level of approximation (LoA IV) (fib 2012b; Muttoni and Ruiz 2012). This procedure is here adopted for the composite slabs, likewise has been made by (Bastien-Masse and Brühwiler 2016a) based on a multilinear moment-curvature relation and assuming a conical deformed shape for the slab pane outside the control perimeter. The use of NLFEA, although being more time consuming, allows dealing with specimens with eccentric punching force, or rectangular

loading area. Additionally, following the MC2010 LoA II, a simplified approach suitable for practical applications is employed based on an analytical description of the force-rotation curve.

Structural codes provide design provisions considering a sound structure suitable for new structural elements, however, the reality is quite different. In most practical applications, the strengthening of existing RC flat slabs is carried out after the structure experiment the service loads (Lapi, Ramos, and Orlando 2019; Koppitz, Kenel, and Keller 2013; Ruiz, Muttoni, and Kunz 2011; D. M. V. Faria et al. 2014; Bastien-Masse and Brühwiler 2016a; Rocha 2012), as illustrated in Figure 104 for the cases of flexural reinforcement using a new RC or RU overlays. This effect is studied in the present chapter.

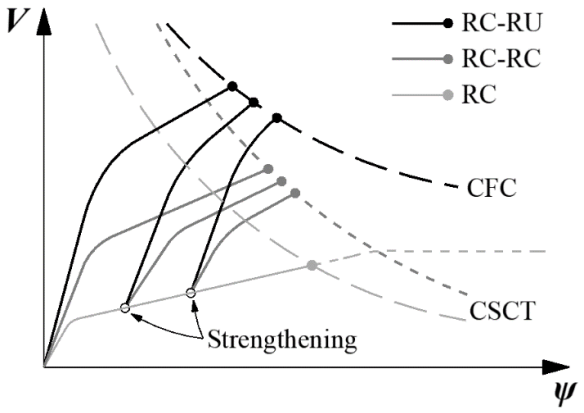

Figure 104. Force-rotation relations for RC considering post-installed RC and RU overlays (Bastien-Masse and Brühwiler 2016a; Lapi et al. 2018a).

At last, a parametric study involving the variation of the substrate concrete strength and reinforcement ratio, the geometrical (thickness and reinforcement ratio) characteristics of the RC and UHPFRC overlays, the basic tensile properties of the UHPFRC, the load eccentricity and the post-installed overlays was undertaken considering the LoA IV and whenever applicable, the LoA II.

6.2. VALIDATION

The NLFEA using the software DIANA 10.4 was performed on the premise that the punching shear strength for both RC and composite flat slabs can be predicted by considering the intersection point between the structural response through the force-rotation (V-ψ) curve and the corresponding failure criterion, the CSCT (Muttoni 2008)

and the CFC (Bastien-Masse and Brühwiler 2016a), respectively. Moreover, the force-rotation curve can be derived from the flexural behaviour of the slab. As stated before, this approach refers to LoA IV for RC slabs under punching shear (fib 2012b; Muttoni and Ruiz 2012) and has been applied successfully using bending shell elements (Belletti et al. 2015; Vaz Rodrigues 2007; J. Sagaseta, Fernández Ruiz, and Muttoni 2009). Its simplicity compared to 3D (brick) finite element models makes it attractive for practical applications.

On the other hand, the LoA II establishes a practical procedure to calculate the punching shear strength through simplified analytical formulas accounting for the internal forces and other geometrical and mechanical parameters, with the advantage of being less time-consuming and suitable for the design and assessment of existing structures (fib 2012a). Again, this approach was herein extended for the case of the composite flat slabs.

The validation of both approaches (the LoA II and IV) was made using the experimental results of the campaign carried in section 5.3 and those from Wuest (2007) and Bastien-Masse and Brühwiler (2015).

6.2.1.1. Geometry

Wuest (2007) tested two specimens, SAMD1 (RC-RU) and SAMD2 (RC-U), which are referred to as series SAMD. Series PMB comprises the slabs tested by Bastien-Masse and Brühwiler (2015), which consist of slabs PBM1 (RC-U), PBM2 and PBM3 (RC-RU) and PBM4 (RC-U). In both series SAMD and PBM, the slab elements were square, and the load application was concentrically through a square steel plate.

Table 18. Cross-section specifications of the specimens used in the validation.

Specimens	**Cross-section**	**RC substrate**				**RU layer**			
		h_c [mm]	d_{sc} [mm]	*Bars*	ρ_{sc} [%]	h_U [mm]	d_{sU} [mm]	*Bars*	ρ_{sU} [%]
SAMD1	RC-RU	150	136	#ϕ14@150	0.76	50	175	#ϕ10@150	1.05
SAMD2	RC-U	172				23	184	-	-
PBM1	RC-U	211	189	#ϕ16@150	0.71	47	-	-	-
PBM2	RC-RU	212				48	233	#ϕ10@150	0.7
PBM3									
PBM4	RC-U	239	211	#ϕ16@125	0.76	22	-	-	-

The in-plane geometric dimensions of all the series are summarized in Table 19 according to the notation presented in Figure 105.

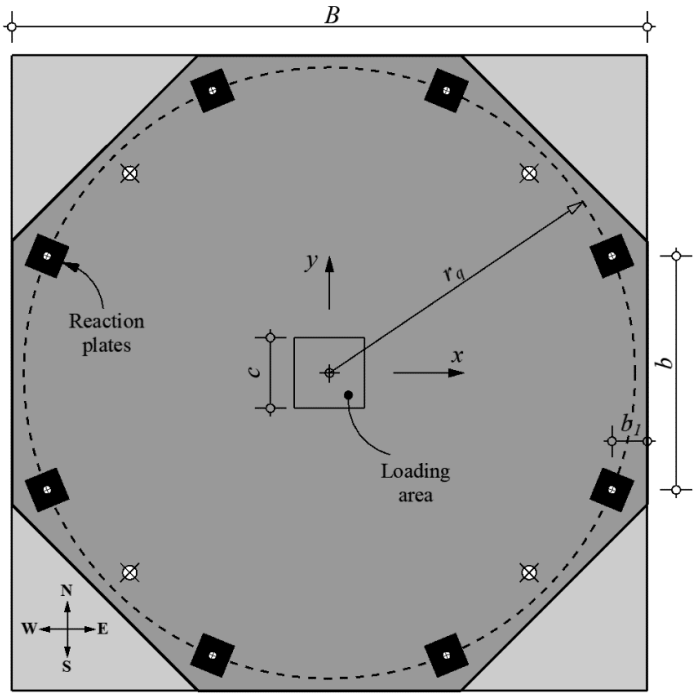

Figure 105. Geometry and notation of the specimens used in the validation.

Table 19. General dimensions of the specimens used in the validation.

Series	B [mm]	r_q [mm]	c [mm]	b [mm]	b_1 [mm]
PC/ PRC/ PE	2250	1082	250 [a)]	828	125
SAMD	2000	1000	200	870	100
PBM	3000	1505	260	1200	120

[a)] Except slab PRC-R-RU: 175x350 mm^2

6.2.1.2. Material mechanical properties

The material mechanical properties of both RC substrate and overlay are presented in Table 20 and Table 21, respectively. All concretes had a maximum aggregate size d_g=16 mm. Knowing that the results from the splitting test overestimate the tensile strength, more suitable values were used $f_{ct}=0.3(f_{cm}-8)^{2/3}$, considering the ageing and f_{cm}, as proposed by the Eurocode 2 (EC2) (IPQ 2010).

The UHPFRC of both SAMD and PBM series presented strain-hardening behaviour, and the reinforcement was ribbed. The typical UHPFRC constitutive laws and notation are shown in Figure 46 (c-d). The SAMD series used 6% of l_f/d_f =10/0.2 fibres, whereas the PBM used 3% of l_f/d_f=13/0.2 fibres (Bastien-Masse and Brühwiler 2016a).

Table 20. Substrate material mechanical properties used in the validation.

Specimens	E_c **[GPa]**	f_c **[MPa]**	f_{ct} **[MPa]**	E_s **[GPa]**	f_{sy} **[MPa]**
PC/ PRC (RC-(R)U)	32	39	2.9	200	565
PE/ PRC (RC)	28	32	2.3		528
SAMD	33.7	49	3.6		526
PBM	27.4	36.7	2.8		546

Table 21. Overlay material mechanical properties.

Specimens	E_U **[GPa]**	f_{Uc} **[MPa]**	f_{Ute} **[MPa]**	f_{Utu} **[MPa]**	ε_{Utu} **[mm]**	w_{Uts1} **[mm]**	f_{Uts1} **[MPa]**	$w_{Ut,max}$ **[mm]**	E_s **[GPa]**	f_{sy} **[MPa]**
PC-RU	46	182	11.4 [a]	10.2 [a]	[b]	2	0.2 f_{Utu}	7.5	200	521
PRC/PE										
SAMD1	50	150	8	11.5	[b]			5		937
SAMD2			9.5	12.8	1.3					-
PBM1			5.7	8.7	2.1			6.5		-
PBM2					[b]					532
PBM3					[b]					772
PBM4			6.9	10.1	2.6					-

[a] Average experimental results from UTT; [b] $\varepsilon_{Utu}=\frac{f_{sy}}{E_s}$, except PRC-U

6.2.2. Finite Element Model (FEM)

Quadrilateral layered shell elements with 8-nodes were used. In-depth, the elements were subdivided into layers to account for the substrate and the overlay, where each layer has its nonlinear material properties and is integrated separately according to 11 points for the Simpson integration scheme. In-plane, a 2x2 Gauss integration points was considered. The minimum mesh size was set to half of the column smaller side, i.e., 125 mm for all slabs tested herein, except PRC-R-RU, 87.5 mm. For the SAMD series, it was 100 mm and 130 mm for PBM.

The reinforcement was modelled as embedded grids elements, with null in plane shear stiffness and axial stiffness in the direction of the reinforcement bars. These elements share the displacement field of the embedding elements.

Due to the symmetric geometry and loading/reaction conditions, only a quarter of the slab was modelled (Figure 106), except for slab PE-RU2 because of the eccentric loading. In this case, half of the slab was modelled

Boundary conditions taking symmetry into account were applied, i.e., horizontal translations and rotations were restrained on the symmetry axes. On the place of reaction plates, only the vertical translation was restrained. For the concentrically loaded specimens, a vertical uniform distributed force was applied. A variable distributed force along the direction N-S was adopted to consider the eccentricity effect. Since no self-weight was considered, the slabs were assumed to be square for all campaigns, even for the specimens tested herein.

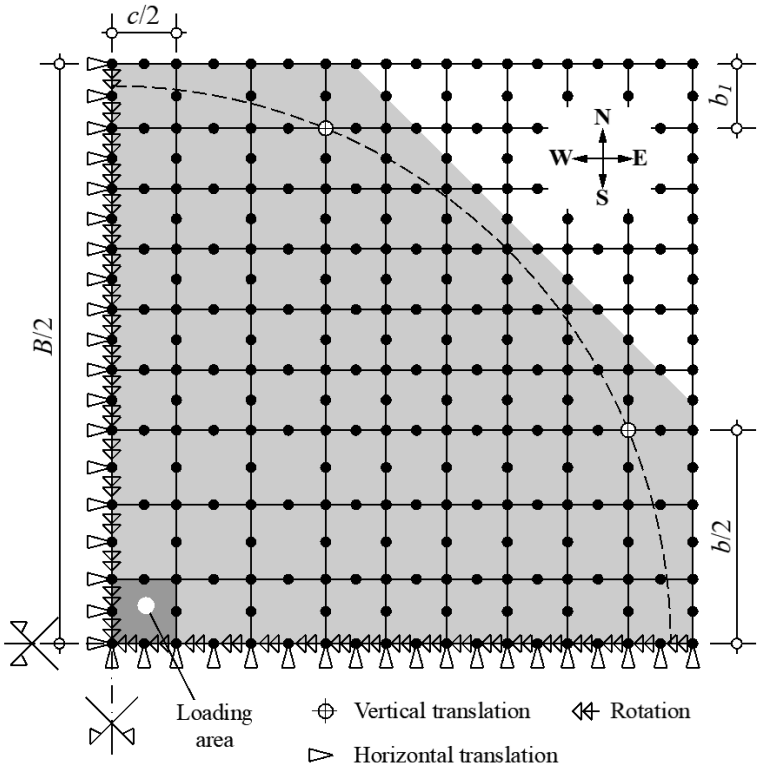

Figure 106. FEA discretization, mesh, and boundary conditions.

The loading incrementation was made up of 100 steps using the arch length procedure. The Regular Newton-Raphson method with the line-search technique was used for iteration. The convergence criteria was set to be the force-norm with a tolerance of 0.01.

6.2.3. Material constitutive laws

6.2.3.1. UHPFRC

For NSC and the UHPFRC, a total strain-based rotating smeared crack model with Poisson ratio ν=0.2 and a perfect bond between all material is assumed.

Since the UHPFRC layer is under tension, only the parameters describing the tensile response are discussed. Therefore, a reasonable approach is to use the UTT results as input parameters for the model, then compare the overall structural response with the experimental results, and secondly, perform an inverse analysis, adapting the UHPFRC tensile properties (Habel, Denarié, and Brühwiler 2007). Furthermore, to carry out this approach, uncertainty must be reduced by validating the RC substrate structural response alone. In the present study this was made for the reference slab, PRC.

The constitutive laws were defined according to the cracking pattern observed in the experiments, where discrete macrocracking, typical of UHPFRC with strain-softening, was shown on the surface of slab PRC-U. In contrast, the slabs with reinforced overlays presented continuous multiple-microcracking, typical of UHPFRC with strain-hardening (Figure 46 (d)). In fact, tests on reinforced UHPFRC ties have shown that the UHPFRC does not need to have tensile strain-hardening behaviour itself to achieve the overall strain-hardening response of the RU member (Oesterlee 2010; Redaelli 2009; Leutbecher and Fehling 2012; Valente, Pimentel, and Nunes 2021).

On the other hand, the UTT test specimens presented only a discrete macro-crack. The elastic tensile stress reached an average of f_{Ute}=11.4 MPa, whereas the macro-crack localization stress was f_{Utu} =10.2 MPa. Some scattering in the overall tensile behaviour of five specimens was observed (Figure 107). After validating the reference slab, the adopted tensile behaviour was derived following the approach mentioned above since the results from the UTT resulted in the overestimation of the flexural stiffness and resistance. Other authors also used this procedure (Wuest 2007; Bastien-Masse and Brühwiler 2016a; Sadouki, Denarié, and Brühwiler 2017), and the adopted law for numerical modelling presented lower resistance than that obtained with the UTT (Figure 107).

For that matter, only Young's modulus E_U=46 GPa was derived from the UTT results. The plain UHPFRC overlay was considered f_{Ute}=7.5 MPa, then a drop up to f_{Utu}=6 MPa. The remaining parameters were adopted (Abrishambaf, Pimentel, and Nunes 2019),

including the w_{Utu}=0.3 mm. Moreover, for the reinforced UHPFRC layer was considered the same value of f_{Utu} with the ratio f_{Utu}/f_{Ute}=1. The value of ε_{Utu} was assumed to be reached when the reinforcement in the layer yields, i.e., $\varepsilon_{Utu}=f_{syU}/E_s$. Finally, the remaining strains corresponding to the softening phase were transformed considering a crack-band width, l_c, and equal to side of the FE.

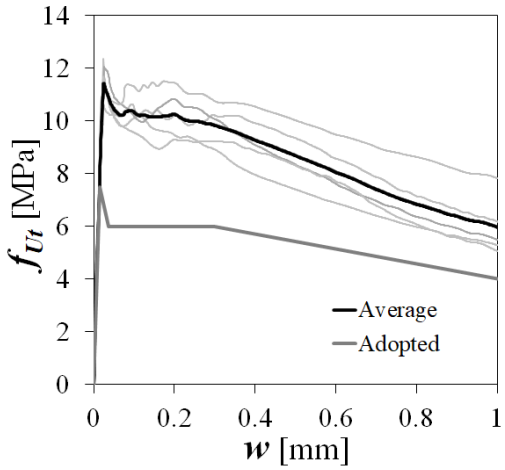

Figure 107. UHPFRC tensile constitutive law, UTT results and adopted.

6.2.3.2. Concrete and steel

For concrete under compression was considered the Parabolic stress-strain diagram, defined by the E_c and f_c presented in Table 20 and Table 21 and the compressive fracture energy, G_c=250G_F (Feenstra and De Borst 1996). Relatively to the tensile behaviour and noting that perfect bond is assumed between steel and concrete, the tension stiffening effect is considered in the tensile concrete stress-strain constitutive law by adopting the post-cracking average concrete stress $\beta \cdot f_{ct}$, with β = 0.4. The corresponding spatially averaged steel yield stress, f^*_{syc}, is determined by equilibrium, ensuring that the moment at yielding of the tensile reinforcement, M_y, determined in terms of the forces at the cracks or in terms of the average forces, is the same (Figure 108). The process is illustrated in Figure 108 for the RC section. A similar procedure has been adopted for the steel bars in the RC substrate of the RC-UHPFRC cross-section.

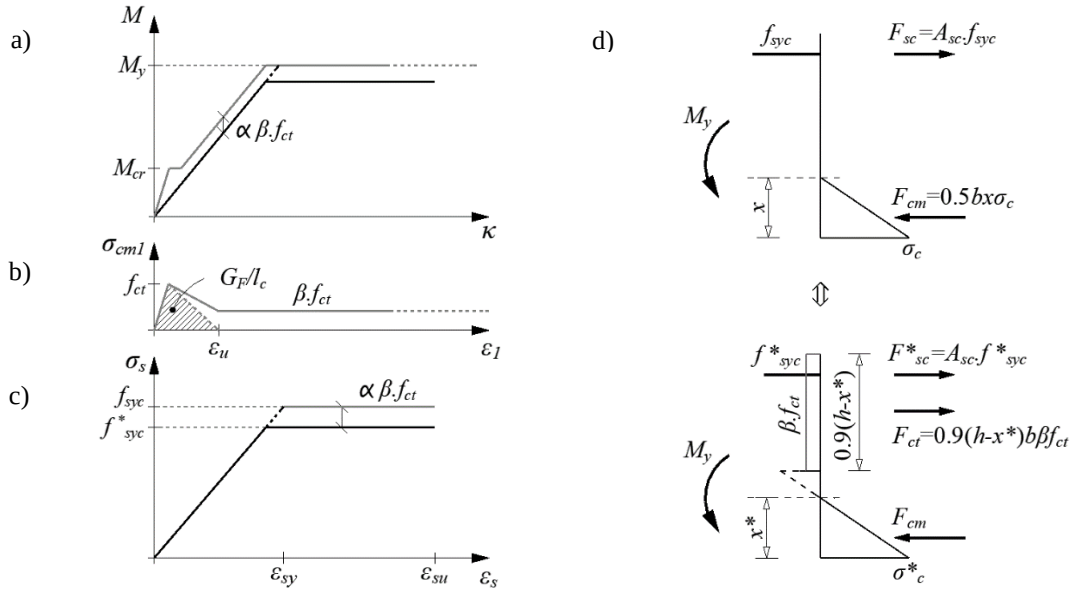

Figure 108. Constitutive laws for modelling the nonlinear moment-curvature relation including tension-stiffening: (a) idealized moment-curvature(M-κ) relation; (b) average principal concrete tensile stresses versus the principal average tensile strains; (c) average steel stresses versus the average tensile strains (d) equilibrium expressed in terms of forces at the cracks (top) and in terms of average forces (bottom).

After cracking, concrete keeps constant stress, reduced with β=0.4, considered to be an integration factor for the steel strain along the transmission length (fib 2012b). The concrete tensile strength is calculated considering a lower value according to $f'_{ct}=0.33f_{cm}^{1/2}$ (Vecchio and Collins 1986), which provides good agreement with the cracking load.

A bilinear stress-strain model is adopted for the reinforcement, with a hardening branch after yielding. The ultimate strain is limited at ε_{su}=10%.

6.2.4. Simplified moment-rotation curve

For practical purposes, Muttoni (2008) proposed a simplified relationship for reinforced concrete elements assuming a parabola of exponent a=3/2 for the rotation as a function of the ratio V/V_{flex} (Eq. (48)), also implemented in the MC2010 for the LoA II approach. Asa will be seen in the validation examples, this simplified relation can be adjusted for the case of the composite slabs considering a cubic exponent, i.e. a=3.

$$\psi=1.5\frac{r_s}{d_{sc}}\frac{f_{sy}}{E_s}\left(\frac{V}{V_{flex}}\right)^a \tag{48}$$

The flexural strength can be readily calculated considering Eq. (49) using the yield line method of an isolated circular slab:

$$V_{flex}=2\pi m_R\frac{r_s}{r_q\text{-}r_c} \tag{49}$$

where m_R is the nominal moment capacity per unit width and r_s is the radius of the circular isolated slab element. Herein, r_s is assumed to be equal to half the side of the isolated slabs, i.e., $r_s \approx B/2$.

Considering the geometric conditions of the series of slabs tested here, and in accordance with Eq. (49), the flexural strength can be approximated to $V_{flex}=7.7m_R$. For series SAMD and PBM, it becomes $V_{flex}=7.2m_R$ and $V_{flex}=7m_R$, respectively. In the case of moment transfer (eccentricity) in respect to series PE and the parametric study (6.3.3), Eq. (50) derived from MC2010 (fib 2012b) was used.

$$V_{flex}=\frac{m_R}{\frac{1}{7.7}+\frac{e}{3r_s}} \tag{50}$$

For calculation of m_R (Eq. (27)), the simplified analytical model was applied (Figure 109), as described in Chapter 3. For most hybrid slabs reinforced with standard ribbed rebars, it is considered that m_R occurs when the reinforcement in the RC substrate starts yielding and the UHPFRC layer is softening (point C). In the case of the RU layer, at this point, the reinforcement is also yielding. However, when high-strength steel is used in the strengthening overlay and/or a UHPFRC with significant strain hardening, m_R occurs when the reinforcement in the RU starts yielding and/or the UHPFRC tensile strength is reached (point B').

It is considered that the reinforcement is in the middle of the UHPFRC layer ($d_{sU}=d_U$), and a bi-linear stress-strain law is adopted. The formulas for calculating forces, the depth of the compressive zone, x, and corresponding auxiliary coefficients are presented in Table 4.

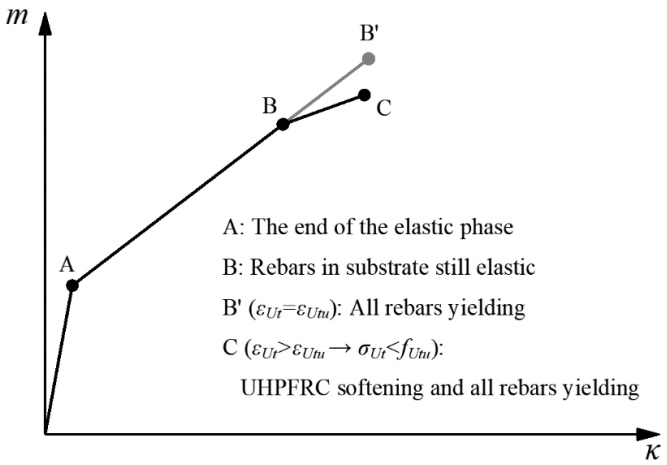

Figure 109. Simplified analytical *M-κ* relation for RC-(R)U cross-section.

The UHPFRC tensile behaviour is defined according to Figure 46 (c-d), and for the transformation of crack openings into strains, a crack-bandwidth equal to l_c=2/3h is considered (AFGC 2013).

6.2.5. Results of the punching shear calculation

The NLFEA and the simplified models were validated for accuracy in predicting the punching shear strength considering the intersection point between each slab's *V-ψ* relation and the corresponding failure criterion. The experimental punching shear strength point ($V_{R,exp}$; $\psi_{R,exp}$) refers to the maximum force of the dashed curves presented in Figure 110. The curves of the NLFEA models were interrupted on the intersection point with the failure criterion curves. As for the simplified approach, the *V-ψ* relations calculated according to the procedure presented in section 6.2.4 were not limited and show the flexural strength, V_{flex}.

For the NLFEA, the rotations were calculated for all concentrically loaded slabs by dividing the vertical central deflections by the distance between the column face and the reaction points (Guandalini 2005). The column face was considered to be located at the distance r_c=2c/π (Muttoni 2008; Bastien-Masse and Brühwiler 2016a). Nonetheless, the NLFEA rotations, ψ_{NLFEA}, for the rectangular (PRC-R-RU) and the eccentrically (PE-RU2) loaded slabs were calculated considering a constant slope of the deformation profile regarding the symmetry axes, N-S and W-E, using the relative deflection between the points normal to the vertical reactions.

It was observed that for slab PRC-R-RU, the rotations along both symmetry axes were nearly coincident. It was slightly higher as expected in the N-S direction, where the longest dimension of the rectangular loading area is aligned.

The results are presented in Figure 110. In general excellent agreement is achieved between the NLFEA and the experimental results. The agreement with simplified method based on the analytical force-rotation curve is also good, although the NLFEA fits the experimental curves better, as should be expected.

The structural response of the reference PRC (Figure 110 (a)) and PC-RC (Figure 110 (e)) slabs intersected the CSCT failure criterion after the start of the plastic deformations, whereas both the NLFEA and simplified curves intersected the failure criterion in the pre-yielding of the reinforcement. Although Muttoni (2008) establishes an exponent of 3/2 for the simplified model (more conservative for low reinforcement ratios), here, it was used 3 for the sake of comparison with the composite slabs.

No intersection between the slab PRC-U force-rotation curve and failure criterion CFC was achieved (Figure 110 (b)). Therefore, the NLFEA punching shear strength was considered equal to the maximum force reached by the model. For this slab, it is important to mention that the punching shear failure occurred after large slab deformation, and differently to the RU overlayered slabs, flexural cracks were clearly visible. Even though the simplified model predicts the punching shear resistance quite well, it underestimates the stiffness before the intersection with the CFC on one side, and on the other side, it overestimates the flexural capacity after the intersection point. This is also true for the PC-RU (Figure 110 (f)), SAMD2 (Figure 110 (j)) and PBM1 (Figure 110 (k)) slabs.

Very good agreement between the numerical, simplified and experimental curves is observed for the slabs PRC-RU (Figure 110 (c)), PRC-R-RU (Figure 110 (d)), PE-RU1 (Figure 110 (g)), PBM2 (Figure 110 (l)) and PBM4 (Figure 110 (n)). The NLFEA and simplified model curves slightly overestimate the experimental curve for both slabs strengthened with high-strength steel, SAMD1 (Figure 110 (i)) and PBM3 (Figure 110 (m)).

The punching shear capacity is affected by the force eccentricity in slab PE-RU2, relatively to PE-RU1. The rotations of the former refer to the eccentric side and to the direction S. These rotations were greater than those in the N- and W/E-directions (Figure

110 (h)). Besides, to take the eccentricity effect into account, the control perimeter in RC substrate and RU overlay was reduced by the coefficient of eccentricity k_e=0.75 and 0.80, respectively, determined according to Eq. (47). Also in this slab good agreement is shown using the simplified approach.

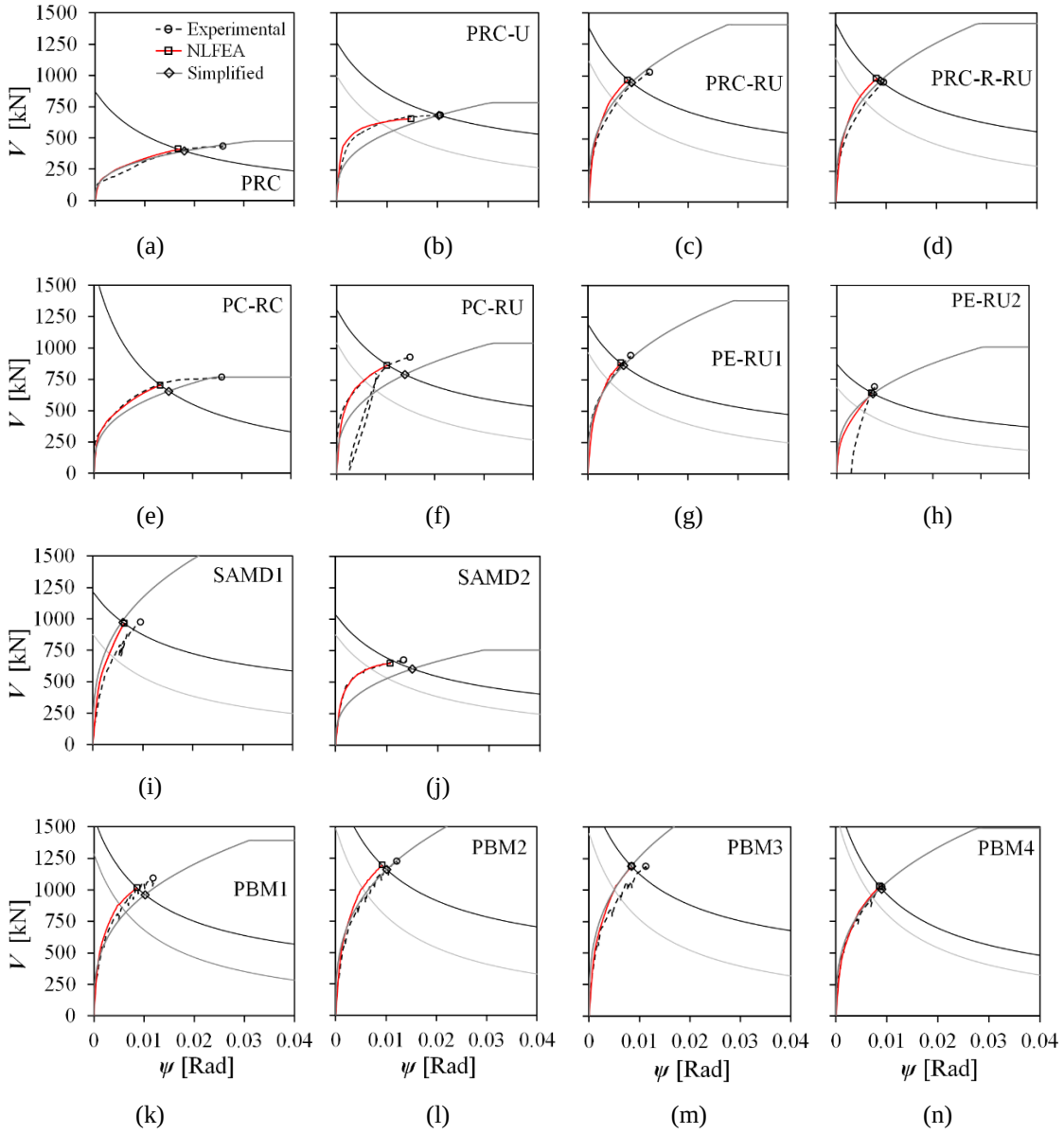

Figure 110. Punching shear strength prediction (a-d) PRC, (e-f) PC, (g-h) PE, (i-j) SAMD (Wuest 2007) and (k-n) PBM (Bastien-Masse 2015) series.

The punching shear strength obtained in the experiments and using the NLFEA and the simplified approach are presented in Table 22 The predictions were close, and the average of the ratio between the experimental and NLFEA punching shear strength of the composite slabs is about 1.04, with a standard deviation of 0.04, whereas it is 1.06 and

0.06 in the case of the simplified approach. The individual ratios are plotted in Figure 111 in terms of the equivalent reinforcement ratio.

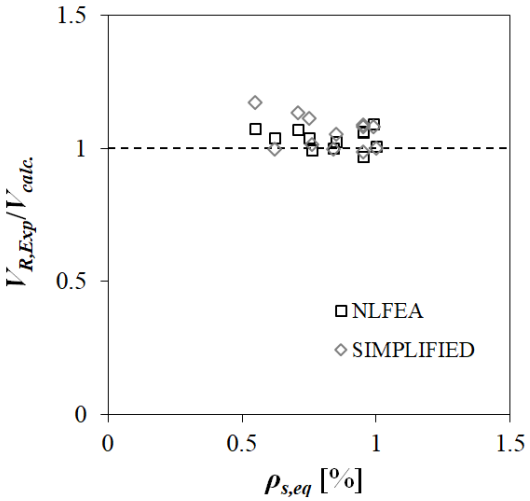

Figure 111. Validation of models for calculation of the punching shear.

The eccentricity effect in series PE can also be well predicted with both approaches, as presented in Figure 112.

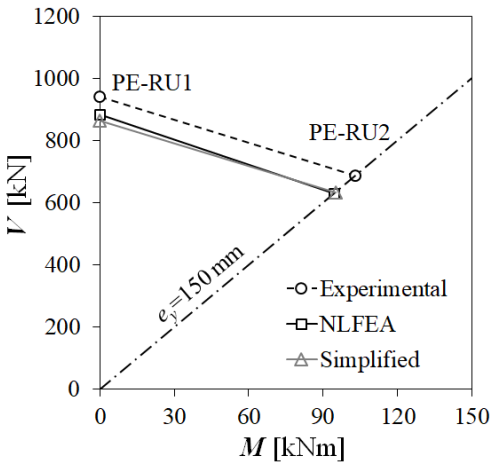

Figure 112. Experimental and NLFEA eccentricity effect.

The accuracy of the NLFEA and the simplified approach to predict the punching shear strength is evidence enough to validate both models.

Table 22. Punching shear prediction.

Specimens	$V_{R,Exp.}$ [kN]	$\psi_{R,Exp.}$ [mRad]	$V_{R,NLFEA}$ [kN]	$\psi_{R,NLFEA.}$ [mRad]	$V_{c,NLFEA.}$ [kN]	V_U [kN]	V_{flex} [kN]	$V_{R,Simp.}$ [kN]	$\psi_{R,Simp.}$ [mRad]	$V_{R,Exp.}/V_{R,NLFEA}$	$V_{R,Exp.}/V_{R,Simp.}$	$\psi_{R,Exp.}/\psi_{R,NLFEA}$	$\psi_{R,Exp.}/\psi_{R,Simp.}$
PRC	431	25.8	411	16.8	411	-	477	396	18.0	1.05	1.09	1.54	1.43
PRC-U	682	20.7	656	14.8	389	267	785	685	20.3	1.04	1.00	1.40	1.02
PRC-RU	1024	12.4	968	7.8	700	267	1407	948	8.6	1.06	1.08	1.58	1.44
PRC-R-RU	952	9.6	982	8.1	709	273	1418	964	8.9	0.97	0.99	1.18	1.07
PC-RC	766	26.0	701	13.5	701	-	766	655	15.2	1.09	1.17	1.93	1.71
PC-RU	929	15.0	865	10.3	597	267	1041	792	13.9	1.07	1.17	1.46	1.08
PE-RU1	940	8.6	883	6.6	657	225	1379	865	7.1	1.06	1.09	1.31	1.21
PE-RU2	686	8.0	628	7.3	441	187	1006	634	7.6	1.09	1.08	1.10	1.05
SAMD1	971	9.6	965	6.3	626	339	1670	973	6.0	1.01	1.00	1.52	1.60
SAMD2	675	13.4	650	10.7	489	160	756	608	15.0	1.04	1.11	1.25	0.89
PBM1	1089	11.9	1016	8.6	730	286	1393	962	10.2	1.07	1.13	1.38	1.17
PBM2	1223	12.2	1195	9	819	376	1684	1161	10.1	1.02	1.05	1.36	1.21
PBM3	1186	11.3	1188	10.5	828	359	1841	1191	8.4	1.00	1.00	1.08	1.35
PBM4	1023	9.1	1029	8.6	872	157	1492	1008	9.0	0.99	1.01	1.06	1.01
									Average	1.04	1.06	1.31	1.18
									Std. Dev.	0.04	0.06	0.18	0.20

6.3. PARAMETRIC STUDY

A parametric study is herein carried out to evaluate the strengthening efficiency associated to the use of UHPFRC and RC layers. The reference parameters for the parametric study are presented in Table 23. It is worth comparing the contributions of the UHPFRC an RC overlays. The RC overlay comprehends a class C45, whereas the chosen UHPFRC is defined by f_{Utu}=8 MPa and f_{Utu}/f_{Ute}=1.

Table 23. Reference parameters.

Geometry		**Material**	
General		**Concrete**	
B	2250	**RC substrate**	C25 (MC 2010)
C	250	**RC overlay**	C45 (MC 2010)
r_q	1082	f_{cm}	f_{ck}+8
RC substrate		E_c	$22(f_{cm}/10)^{0.3}$
h_c	180	f_{ct}	$0.3f_{ck}^{2/3}$
d_{sc}	150	**UHPFRC**	
ρ_{sc}	A_{sc}/bd_{sc}=0.75% (#ϕ12@100)	f_{Uc}	180
RC overlay		E_U	45
h_{c2}	50	f_{Ute}	8
d_{sc2}	$h_c+h_{c2}/2$	f_{Utu}/f_{Ute}	1
ρ_{sc2}	A_{sc2}/bh_{c2}=1.57% (#ϕ10@100)	ε_{Utu}	0.25
UHPFRF overlay		**Steel**	
h_U	50	E_s	200
d_{sU}	$h_c+h_U/2$	$f_{sy}=f_{su}$	500
ρ_{sU}	A_{sU}/bh_U=1.57% (#ϕ10@100)	ε_{su}	10

Units: Dimensions [mm]; Stresses, f_i [MPa]; Young's modulus, E_i [GPa]; Strains, ε_i [%]

It must be noted that according to Eq. (46), the CFC failure criterion does not normalize similarly to the CSCT due to the variables f_{ct} and h_U. Thus, the NLFEA results will be presented using normalized or absolute values of the force and rotations whenever justifiable. It is also interesting to compare the technique effectiveness relative to the corresponding substrate resistance, V_{Rc}.

For the general overview of each property effect, the variations of the NLFEA and the simplified approach model results will be presented. However, the discussion will be made in terms of the NLFEA results.

6.3.1. Substrate concrete strength and reinforcement ratio

As it was seen when comparing slabs PRC-RU and PC-RU with the same RU overlay but different reinforcement ratios on the substrate, the strengthening efficiency depends on how much the RC substrate can contribute to the resulting RC-RU composite section. Considering that the existing substrate condition is fixed, it is necessary to assess how it affects structural behaviour.

The compressive strength of the compression struts is strongly influenced by their state of transverse strains in the shear-critical region (Ruiz and Muttoni 2009). This is very important for slabs with transverse reinforcement, where larger rotations are expected (Ruiz, Muttoni, and Kunz 2011; Stefan, Ruiz, and Muttoni 2012). The crushing strength of RC slabs can be estimated using the failure criterion of slabs without transverse reinforcement (Eq. (43)) multiplied by an empirical parameter k_{sys} set to be 2.8 for double-headed studs (fib 2012b). Although no transverse reinforcement is accounted for in the slabs studied here, the UHPFRC overlay delays the formation of the critical shear-crack up to NIC formation, which is a function of the concrete tensile strength. Most probably, the formation of NIC will occur before the strut under compression crushes. Nevertheless, even by considering the default value of k_{sys}=2, the resulting crushing strength is above the CFC for all the cases presented hereafter. As a matter of fact, since the UHPFRC overlay enhances the bending stiffness, the risk for the concrete strut in the substrate to crush is associated with larger thicknesses (h_U>120 mm, h_U/h_c>2/3), which are impractical for this strengthening technique.

The parameters to be investigated in this section refer on one side to the substrate concrete strength by means of classes C16, C20, C25, C30 and C35 (fib 2012a), and on the other side, to the reinforcement ratios ρ_{sc}=0%, 0.19% (#ϕ6@100), 0.34% (#ϕ8@100), 0.52% (#ϕ10@100), 0.75% (#ϕ12@100), 1.34% (#ϕ16@100) and 2.1% (#ϕ20@100).

The effect of the reinforcement ratio on the punching shear strength is evidenced in Figure 113 (b). Low reinforcement ratios can result from either misplacing or corrosion

(reduction of effective cross-section) of rebars, which the worst-case scenario accounts for no flexural steel reinforcement. For low reinforcement ratios, ρ_{sc}<0.5%, $V_{Rc}=V_{flex}$, whereas for large ρ_{sc}>1%, it is $V_{Rc}<<V_{flex,}$ and the punching failure is very brittle. Although increasing the reinforcement ratio increases the punching capacity, it strongly decreases the deformation capacity (Muttoni 2008).

It is interesting to notice that according to the CSCT the normalized value of the resistance decreases with increasing concrete compressive strength (Figure 113 (a)).

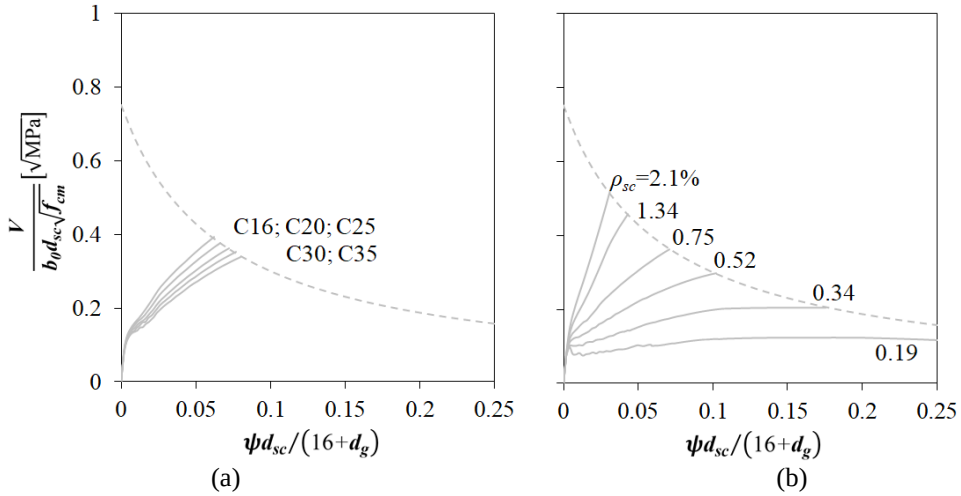

Figure 113. Variation of RC substrate (a) concrete strength and (b) reinforcement ratio.

The influence of the substrate concrete strength in slabs strengthened with RC overlay is similar to the reference RC slabs (Figure 114 (a)). It becomes even more relevant in composite slabs RC-RU because its tensile strength influences the UHPFRC layer contribution to the global punching shear resistance (Figure 114 (b)).

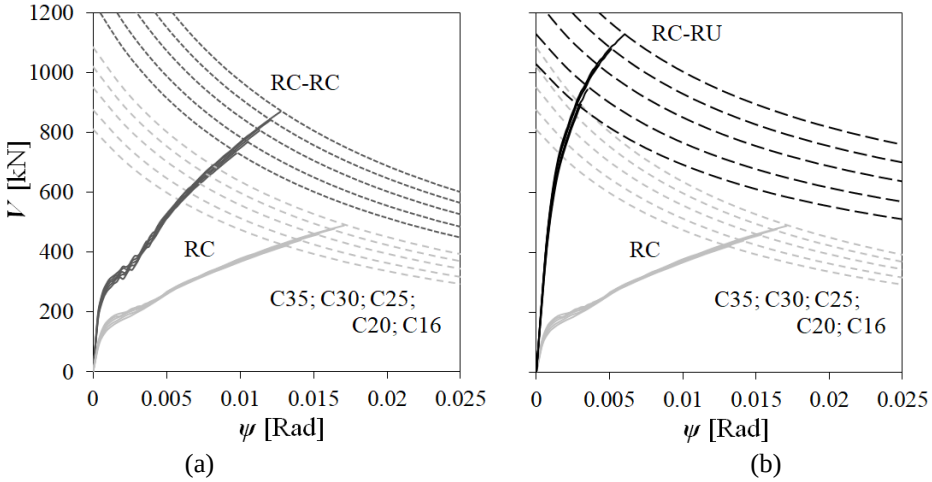

Figure 114. Variation of the substrate concrete strength ($h_{c2}=h_U$=50 mm and $\rho_{sc2}=\rho_{sU}$=1.57%) on (a) RC-RC and (b) RC-RU.

With the increase of the substrate reinforcement ratio, there is also an increase in resistance for both techniques (Figure 115). Although the relative resistance varies significantly in both cases, it is in RC-RC slabs where the absolute resistance depends more on the substrate reinforcement ratio. The same observation was made by (Lapi et al. 2018b). It is worth mentioning that even the composite section with no reinforcement on the substrate resists more than the highest reinforced RC-RC cross-section against the punching shear. In this case, the resistance is close to flexural capacity.

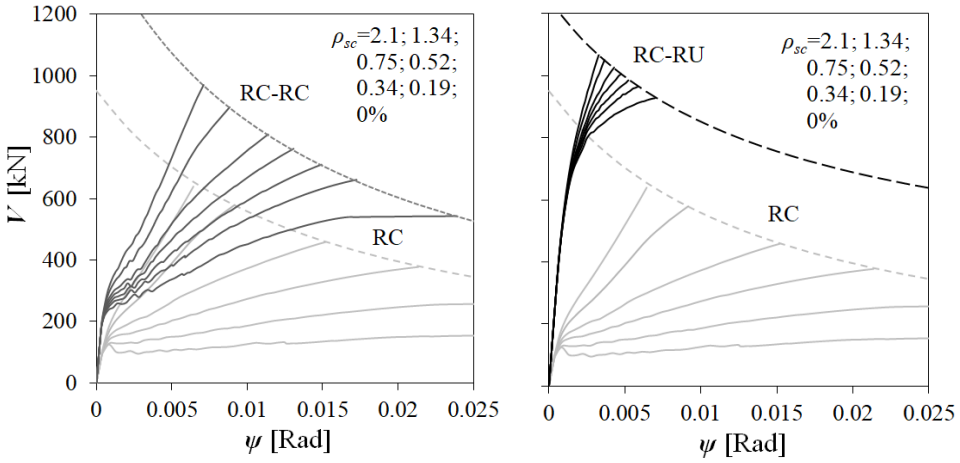

Figure 115. Variation of the substrate reinforcement ratio (h_{c2}=h_U=50 mm and ρ_{sc2}=ρ_{sU}=1.57%) on (a) RC-RC and (b) RC-RU.

The ratio $V_{RC\text{-}RC}/V_{Rc}$ is practically constant with the concrete strength, whereas a slight increase is seen in $V_{RC\text{-}RU}/V_{Rc}$ (Figure 116 (a)).

For lower reinforcement ratios of the substrate, the addition of a new UHPFRC overlay is significantly more efficient when compared with the RC overlay. However, for the continuous increase of the reinforcement ratios, the difference of punching shear resistance between both is reduced, as shown in Figure 116 (b). Although the simplified approach is more conservative relative to the NLFEA, the trends of the latter are also observed on the former.

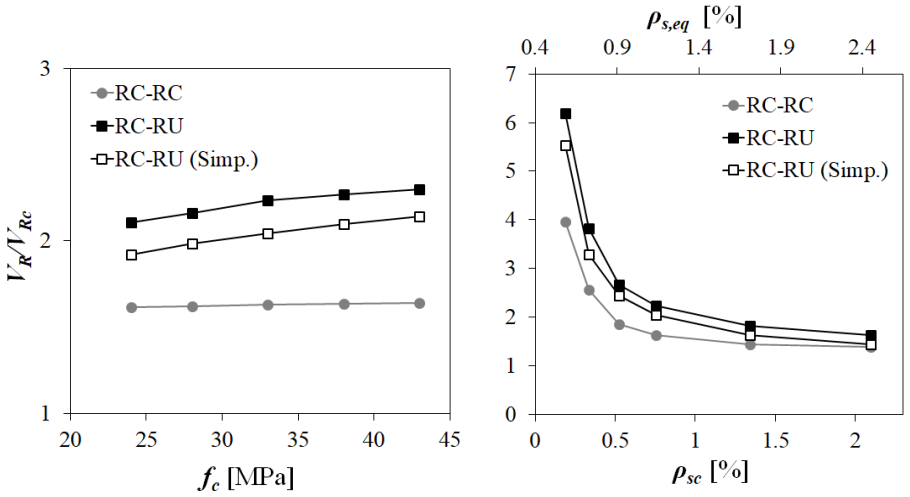

(a) (b)

Figure 116. Relative variation of the substrate (h_{c2}=h_U=50 mm and ρ_{sc2}=ρ_{sU}=1.57%) on (a) concrete strength and (b) reinforcement ratio.

6.3.2. Overlay thickness and reinforcement ratio

Two geometric characteristics are investigated for the flexural reinforcement: the overlay thickness and the reinforcement ratio, while the substrate is kept constant (C25 and ρ_{sc}=0.75%).

With the thickness increase, the effective depth and the flexural response are increased. However, on the negative side, the self-weight is also proportionally increased. For the RC-RC section, the increase in resistance is barely noticed (Figure 117 (a)), as reported by (Lapi et al. 2018b), and from thicknesses of 40 to 60 mm, the ratio $V_{RC\text{-}RC}/V_{Rc}$ varies only slightly (Figure 119 (a)). On the other side, the thickness variation is relevant in the composite slabs, as shown in Figure 117 (b), and analytically observed by (Bastien-Masse and Brühwiler 2016b). Not to mention the reinforced RU overlay, note that even the plain UHPFRC with h_U=40 mm resists more than the reinforced RC overlay with h_{c2}=40 mm and ρ_{sc2}=1.31%.

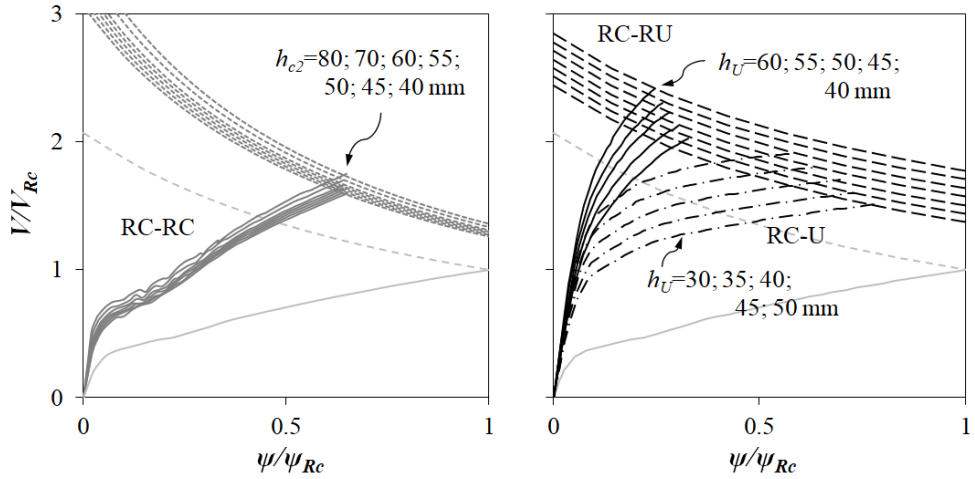

Figure 117. Variation of the overlay thickness (h_c=180 mm and ρ_{sc}=0.75%) on (a) RC-RC and (b) RC-U and RC-RU.

The substrate reinforcement ratio is more impactful in RC-RC (Figure 118 (a)) than it is in RC-RU (Figure 118 (b)) configurations.

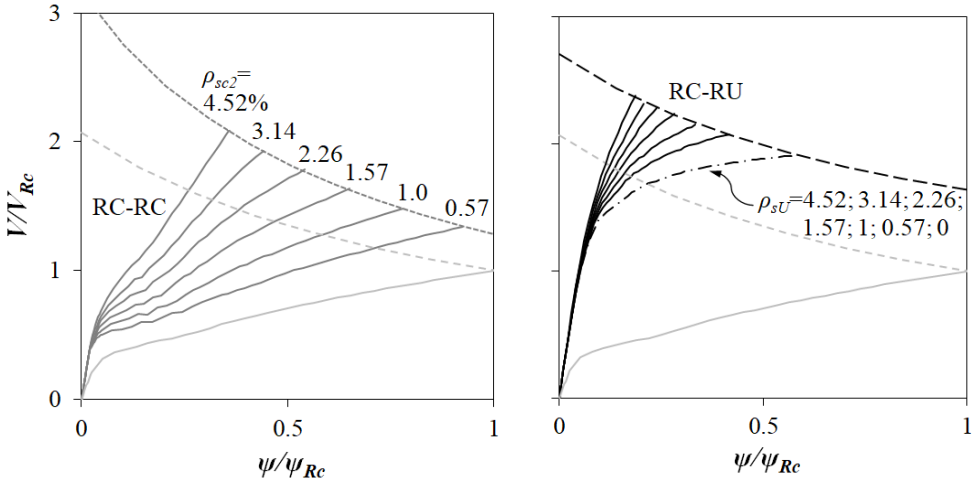

Figure 118. Variation of overlay reinforcement ratio (h_c=180 mm and ρ_{sc}=0.75%) on (a) RC-RC and (b) RC-RU.

The variation of the punching shear resistance with the reinforcement ration in the overlay of the RC-RC is higher than the RC-RU counterpart, as shown in Figure 119 (b). Nevertheless, it is observed that the punching shear strength for the RU configurations with low reinforcement ratio is comparable with the large reinforcement ratio of the RC overlay.

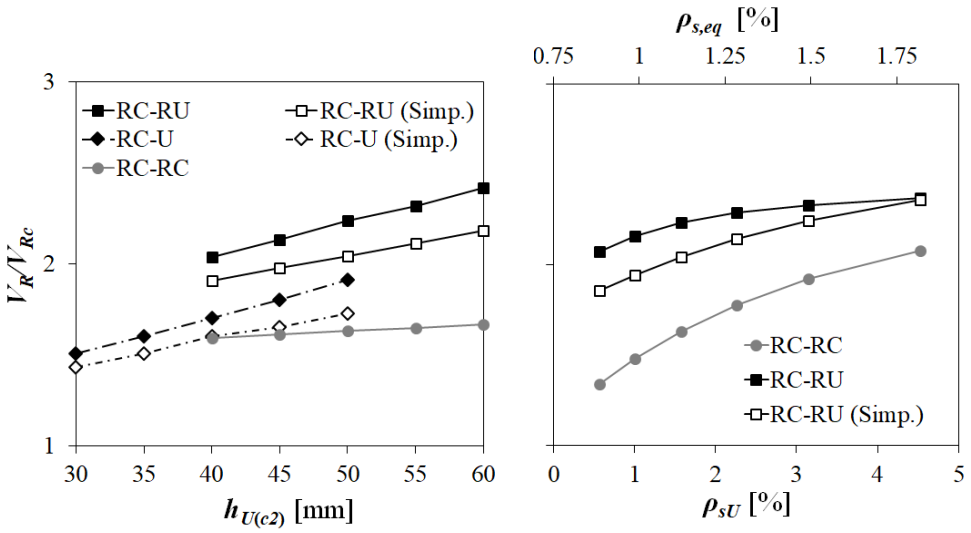

(a) (b)

Figure 119. Relative variation of the overlay (h_c=180 mm and ρ_{sc}=0.75%) on (a) thickness and (b) reinforcement ratio.

6.3.3. Force eccentricity

For the force eccentricity effect, the ratios e/c=0, 0.5, 1 and 1.5 were studied, keeping all other characteristics of the slabs constant. Again, the resistances of the strengthened slabs were normalized relative to the reference RC slabs with the same eccentricity (Figure 120). The control perimeters for both substrate and overlay were reduced to account for the eccentricity of the force, employing Eq. (47).

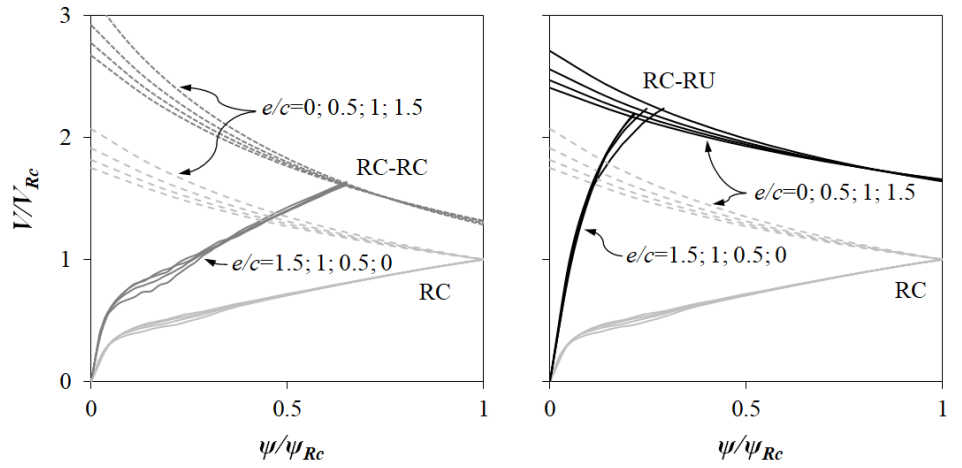

(a) (b)

Figure 120. Variation of the eccentricity (h_c=180, $h_{c2(U)}$=50 mm, ρ_{sc}=0.75 and ρ_{sc}=1.57%) on (a) RC-RC and (b) RC-RU.

The variation of the strengthening effectiveness with the eccentricity is negligible. Moreover, the slopes of the lines V_R-M of all cross-section types are practically equal, except for the simplified approach, in which predictions become rather conservative with the increase of the eccentricity (Figure 121).

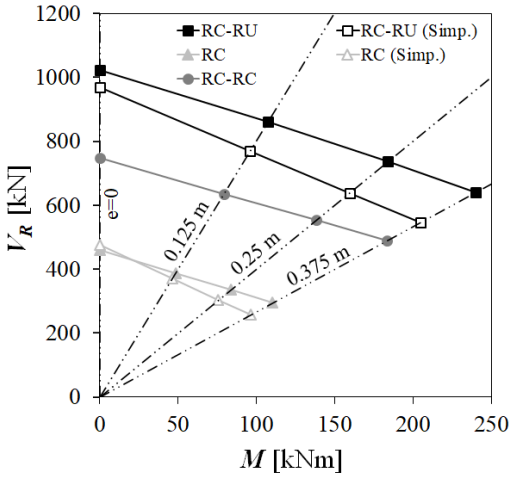

Figure 121. Eccentricity effect.

6.3.4. UHPFRC tensile strength and strain

The flexural strength of the composite section is larger for UHPFRC mixtures with higher tensile strength. Similarly, the ductility is improved with the ductility of the UHPFRC (Habel, Denarié, and Brühwiler 2006; Pimentel et al. 2017). Regarding punching shear strength, the increase is due to the flexural stiffness and is relatively small for RC-RU but with more relevance for the plain UHPFRC overlay, as shown in Figure 122 (a) and observed by (Bastien-Masse and Brühwiler 2016b) as well. On the other hand, Figure 122 (b) shows that for hybrid cross-sections, the extent of the hardening phase of the UHPFRC has a negligible effect.

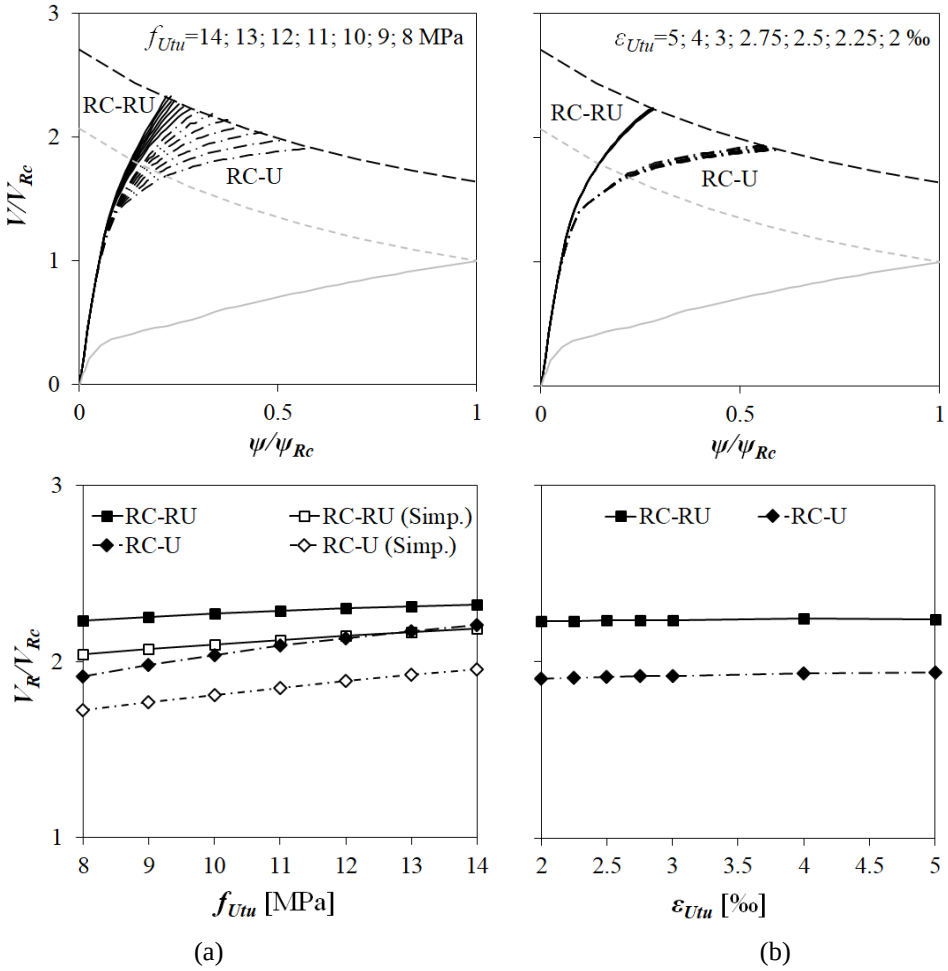

Figure 122. Variation of UHPFRC tensile properties (h_c=180 mm and ρ_{sc}=0.75%) (a) f_{Utu} and (b) ε_{Utu}.

6.3.5. Post-installed overlay

The flexural capacity of the strengthened RC flat slab is barely affected by the pre-existing loading and deformations/rotations (Lapi et al. 2018b; Bastien-Masse and Brühwiler 2016a), but the same is not valid for the punching shear strength since it is dependent on rotations (Koppitz, Kenel, and Keller 2015). The new UHPFRC layer can be placed over the existing substrate with the slab still supporting its self-weight because it does not need to be pre-deformed to activate its shear resistance (Bastien-Masse and Brühwiler 2016a) as it is the case of post-installed shear reinforcement (Ruiz, Muttoni, and Kunz 2011). However, the concrete might be partially cracked, and it can precipitate the formation of failure mechanism. Strengthening for load levels similar to the substrate strength leads to the poor efficiency of the system, whereas the efficiency is larger for lower loading levels (D. M. V. Faria et al. 2014).

For studying the effect of post-installed (PI) overlays, two substrates were considered, one with low and another with intermediate reinforcement ratios, ρ_{sc}=0.34% and 0.75%, respectively.

The investigation of the low reinforcement ratio case consisted of four strengthening stages. The first stage refers to the complete cross-section since the beginning of loading, and the latter refers to the extreme scenario in which layer is applied at the onset of reinforcement yielding (Figure 123 (a)).

The slab with intermediate reinforcement included three strengthening stages before the yielding of the reinforcement, and the last being closer to the punching shear strength (Figure 123 (b)).

The curves in Figure 123 (c-d) show that the punching shear resistance is negatively affected by the higher loading at the time of the strengthening intervention, V_{PI}, for both RC and RU overlayered cross-sections.

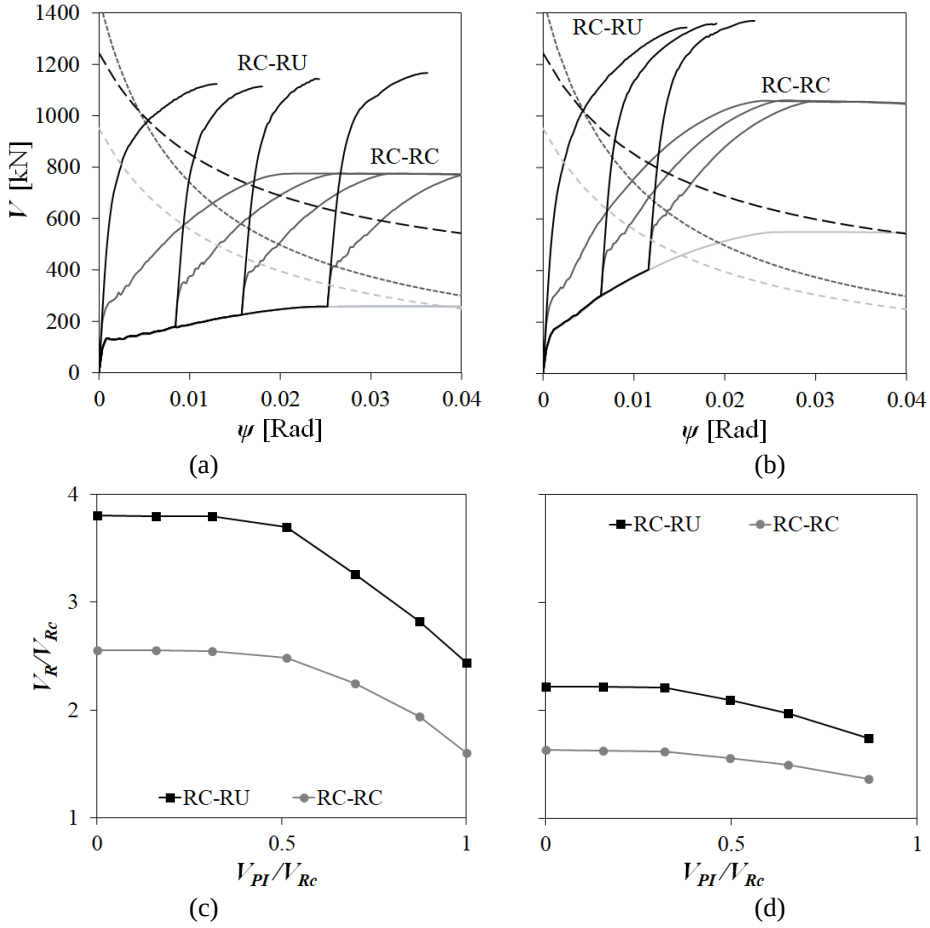

Figure 123. Variation of loading step for strengthening (h_c=180 mm) for (a-c) low (ρ_{sc}=0.34%) and (b-d) intermediate (ρ_{sc}=0.75%) reinforcement ratios of the substrate.

6.4. CONCLUSIONS

This work used the NLFEA to model the flexural response of RC and composite isolated flat slabs through layered shell finite elements. Additionally, it was also used a simplified approach. The force-rotation curves derived from the numerical and simplified models allowed predicting the punching shear strength through the intersection with suitable failure criterions based on the CSCT. The obtained results are in accordance with the experimental results and have shown good accuracy.

After the validation, a parametric study was carried out considering the variation of the substrate concrete strength and reinforcement ratio, the RC and UHPFRC overlay thickness and reinforcement ratio, the force eccentricity, the tensile strength and the extension of the strain-hardening phase of the UHPFRC and the effect of the post-installed overlay.

The results of the composite slabs were compared with those of RC-RC cross-sections. In all the cases, the former presented superior punching shear strength and bending stiffness.

7. Conclusion and Future Work

7.1. CONCLUSIONS

In Chapter 2, further theoretical developments were made and extensive experimental evidence was presented substantiating the NDT magnetic method for quality control of thin UHPFRC elements containing short steel fibres. A mathematical description of the fibre orientation was presented and used to derive the directional variation of the scalar descriptors of the fibre orientation. The simplified physical model of the composite was generalized to accommodate more realistic 2D fibre orientation distributions. The model predicts that the in-plane relative magnetic permeability of the composite is well approximated by a second-order tensor, which allows describing the anisometry of the fibre distribution in thin elements based on only three non-collinear inductance measurements. The validity of the fibre content and fibre orientation indicators was assessed using the developed model, substantiating the equations relating these indicators with V_f and $\alpha_{0,i}$. The influence on the relative magnetic permeability estimates of factors that the model cannot describe, such as the element thickness, surface finishing, the fibre sedimentation across the thickness, and the probe's distance to the boundaries, were assessed experimentally. Finally, a methodology was systematized for estimating the post-cracking strength of the UHPFRC based on the NDT measurements. The procedure was validated, and good agreement with the experiments was achieved. Therefore, it can be concluded that the NDT method used here is a valuable tool for quality control on real applications.

In Chapter 3, the results of flexural tests on RC-U and RC-RU slab strips with the UHPFRC layer under tension were presented. It is confirmed that in the case of reinforced UHPFRC layers, the flexural behaviour is less dependent on the fibre content and orientation in the UHPFRC. The moment-curvature curves could be well reproduced using a layered cross-sectional model with realistic material stress-strain laws. A simplified analytical model relying on a multilinear approximation of the real curve was

developed for use in engineering practice, which shows good agreement with the experiments.

In Chapter 4, an experimental campaign for testing composite RC-(R)U and reference RC beams failing in shear was carried out. The analysed variables were the reinforcement ratios in the RC substrate and the UHPFRC layer, the location of the UHPFRC layer (tension or compression side), the UHPFRC layer thickness and the size effect. In all cases, a significant stiffness and shear strength increase could be achieved with respect to the reference beams. The effect of the reinforcement ratio in the substrate on the shear strength of the composite beams is shown to be significant, as well as that in the UHPFRC layer. The size effect was similar in the strengthened and the reference beams. The specimens with the UHPFRC layer cast on the compressive side have also exhibited the formation of an alternative load-bearing mechanism after the formation of the critical shear crack, which allowed a substantial ductility increase with respect to the reference beams. A composite failure criterion based on the Critical Shear Crack Theory (CSCT) contemplating the contribution of the UHPFRC layer was shown to accurately predict the shear force V_{crit} corresponding to the sudden propagation of the diagonal flexural-shear crack. In the specimens with a thinner UHPFRC layer (h_U/h_c=0.15) and stronger substrate concrete (f_c=50MPa), V_{crit} coincided with the failure load. The model well reproduced the influence of all the studied variables. The model proposed by (Noshiravani and Brühwiler 2014; Bastien-Masse and Brühwiler 2016b) and adopted in the Swiss code (SIA 2016) was employed for determining the shear strength corresponding to the load-bearing mechanism developing after the NIC and critical shear crack propagation. This model is shown to provide safe estimates of the shear strength for the small scale specimens representing the thickness of typical building or bridge deck slabs. However, being rooted in the plasticity theory, the model is by definition size-independent and provided unsafe predictions of the failure load for the larger specimens of the series VS.

In Chapter 5, an experimental investigation is presented comprising six RC flat slabs strengthened with a thin UHPFRC overlay failing under punching shear. Two additional reference slabs were tested for comparison: one unstrengthened RC specimen and one specimen strengthened with a new RC overlay. The investigation allowed studying essential variables that affect the contribution of the UHPFRC for the punching shear strength of the composite slabs, namely the reinforcement ratio in the existing concrete

substrate, the reinforcement in the strengthening layer, the shape of the column and the eccentricity of the force. In addition, the tests significantly extend the existing experimental evidence and provide a wide range of data for model validation. All the composite RC-(R)U slabs failed in punching shear. The saw cuts revealed that the conical punching shear cracks do not cross the UHPFRC layer. Instead, a horizontal crack propagates just below the interface between the UHPFRC and the concrete (the NIC), promoting the separation between the two materials and allowing the development of the failure mechanism. The experimental results confirm the significant contribution of the UHPFRC thin overlay to the punching shear capacity. The failure loads were compared to the estimates obtained using the composite failure criterion (CFC) proposed by Bastien-Masse and Brühwiler (2016a). The slab tested with a rectangular loading plate with a ratio between the maximum and minimum side C_y/C_x=2 has shown that the term V_U in the CFC can still be calculated assuming a uniform tensile stress distribution around rectangular columns at least $C_y/C_x \leq 2.0$. As for the effect of the load eccentricity, reasonable estimates of the failure load were also obtained with the CFC considering suitably reduced control perimeters for taking into account the non-uniform stress distribution, following the recommendations of the fib Model Code 2010.

In Chapter 6, a nonlinear finite element analysis model using layered shell elements was developed for reproducing the flexural response of RC(-RC) and RC-(R)U composite slabs. Together with the composite failure criterion (CFC), the model was used to determine the punching shear strength of all the slabs tested within this thesis and also those available in the literature. Excellent agreement was obtained, proving an extensive validation of the approach. A simple equation of the load-rotation curve of RC-(R)U composite slabs were also validated, allowing the method to be applied in current engineering design practice. A parametric study was developed highlighting the effect on the strengthening ratio of the main variables governing the punching shear behaviour. The effect of the construction sequence was also analysed considering applying the strengthening layer on a slab supporting increasing forces due to its self-weight.

7.2. FUTURE WORK

The NDT method further developed in Chapter 2 revealed great potential for use in real applications. Dissemination of this work looking for its acceptance by the scientific and technical community is now required to foster its introduction in standard quality control practices. Still, some particular aspects deserve further research. For example, the dimensions of the ferrite core need to be modified to use the method in thicker elements with longer fibres, which can be of interest if the method is to be extended for fibre reinforced concrete (FRC). Also of interest would be the development of a new setup allowing the determination of the fibre content and orientation in cases where a quasi-2D fibre orientation distribution is not acceptable. In this case, the inductance measurement along three orthogonal axes is required, for instance, using cubic specimens.

As for the flexural behaviour of RC-(R)U beams and slabs, it is shown that the deformation capacity of the composite element is decreased due to the very good bond between the reinforcement and the UHPFRC, which promotes the robust localization of the strains in the reinforcement in the post-yield stage. Moreover, a softening behaviour in the moment-curvature curve is observed after the reinforcement yielding. In the case of statically undetermined structures, this *a priori* excludes the use of plastic analysis methods. The application of a reinforced UHPFRC layer is shown to be especially suitable to strengthen hogging moment regions of beams and slabs. The increase in the flexural hogging capacity can be pretty significant, and the use of elastic analysis with redistribution of moments could be useful in cases where the sagging bending moment region has a strength deficit. The definition of redistribution limits is still to be established and must be based on suitable flexural analysis models capable of reproducing the post-yield stage and the flexural deformation capacity of RC-(R)U sections.

Concerning the (one-way) shear strength of beams and slabs, further experimental evidence is required on larger specimens to evaluate the size-effect in cases where the post-critical shear strength is more significant than that leading to the propagation of the critical shear crack. Furthermore, a suitable mechanical model capable of reproducing the size effect in the post-critical stage is yet to be developed.

As for the punching shear behaviour of RC-(R)U composite flat slabs, there is no experimental evidence on the effect of the post-installed strengthening in an unpropped

slab supporting its own weight. The same occurs for one-way shear. In this case, the strengthening layer is only activated for the forces acting in the posterior stages, and the strentghening system's effectiveness may decrease. The model described in Chapter 6 is, in theory, capable of reproducing this effect, but experimental validation is required. Furthermore, the effects of cyclic loading patterns on the strengthening efficiency should also be analysed to evaluate the adequacy of this strengthening system for flat slabs of buildings located in earthquake prone regions. Also, the effects of moment redistribution and compressive membrane action occurring in continuous flat slabs should be assessed using an NLFEA in conjunction with CFC failure criteria, as presented in Chapter 6, but considering a realistic static scheme of a flat slab and not the isolated panel scheme that reproduces the experimental setups.

The observed punching failure mode of the RC-RU slabs and the good agreement of the CFC with the experimental failure loads confirm that the punching shear failure of the composite slabs is triggered by the formation of the NIC, which is still governed by the concrete tensile strength of the existing substrate. Therefore, despite the significant strength increase achieved in the RC-RU slabs, this suggests that if the NIC formation could be delayed or even prevented using suitable mechanical connection systems, like that schematized Figure 124, the punching shear strength would be even higher and eventually limited by concrete crushing in the vicinity of the column. More important, the ductility of the response would be larger, which may be determinant in cases of column-to-slab connection subjected to cyclic loadings

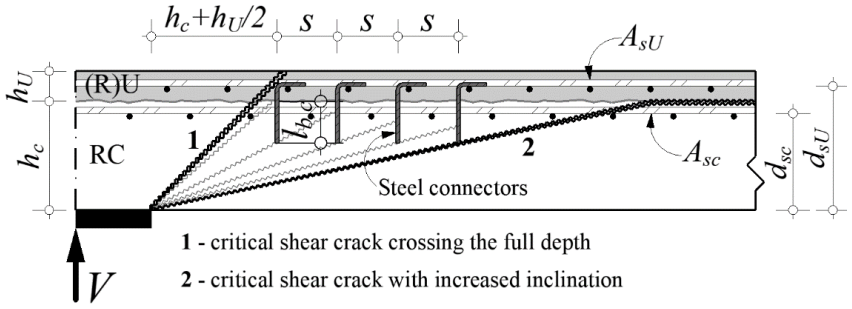

Figure 124. Proposed solution to improve the ductility associated with the punching shear failure mode of composite slabs.

Appendix

A. 1. DETERMINATION OF THE PROBABILITY DENSITY FUNCTIONS

From the function given in spherical coordinates:

$\Psi(\theta,\varphi)=\cosh(k_g\cos\theta)$

The equivalence between Cartesian and spherical coordinates are:

$r=\sqrt{x^2+y^2+z^2}$

$x= r\cos\theta$

$y=r\sin\theta\cos\varphi$

$z = r\sin\theta\sin\varphi$

so, the function can be rewritten in cartesian coordinates as:

$$\Psi(x,y,z)=\cosh\left(k_g\frac{x}{\sqrt{x^2+y^2+z^2}}\right)$$

The transformation of coordinates for any preferential orientation β_0 is given by:

$x'= x\cos\beta_0 + y\sin\beta_0$

$y'= y\cos\beta_0 - x\sin\beta_0$

Thus, the distribution function for any rotation β_0 is given by:

$$\Psi(x,y,z)=\cosh\left(k_g\frac{x\cos\beta_0 + y\sin\beta_0}{\sqrt{x^2+y^2+z^2}}\right)$$

or again in spherical coordinates by:

$$\Psi(\theta,\varphi)=\cosh\left\{k_g\left[\cos\theta\cos\beta_0 + \sin\theta\cos\varphi\sin\beta_0\right]\right\}$$

To normalize the function $\Psi(\theta,\varphi)$, and therefore to obtain the probability density function $\psi(\theta,\varphi)$, the former has to be divided by the total area so that the following property can be satisfied:

$$\int_{\varphi=0}^{2\pi}\int_{\theta=0}^{\frac{\pi}{2}} \psi(\theta,\varphi)\,\sin\theta\,d\theta\,d\varphi = 1$$

Note that $\sin\theta$ is the Jacobian determinant on the coordinate system transformation.

Then, the 3D-normalized probability density function is:

$$\psi(\theta,\varphi) = \frac{\cosh\left[k_g\left(\cos\theta\cos\beta_0 + \sin\theta\cos\varphi\sin\beta_0\right)\right]}{\int_{\varphi=0}^{2\pi}\int_{\theta=0}^{\frac{\pi}{2}}\cosh\left[k_g\left(\cos\theta\cos\beta_0 + \sin\theta\cos\varphi\sin\beta_0\right)\right]\sin\theta\,d\theta\,d\varphi}$$

$$= \frac{k_g}{2\pi\,\sinh k_g}\cosh\left[k_g\left(\cos\theta\cos\beta_0 + \sin\theta\cos\varphi\sin\beta_0\right)\right]$$

To obtain the 2D-normalized probability density function, similar deductions can be made, buy neglecting the *z*-axis and considering $\varphi = 0^{\circ}$:

$$\psi(\theta) = \frac{\cosh\left[k_g\left(\cos\theta\cos\beta_0 + \sin\theta\sin\beta_0\right)\right]}{\int_{\theta=0}^{\pi}\cosh\left[k_g\left(\cos\theta\cos\beta_0 + \sin\theta\sin\beta_0\right)\right]d\theta}$$

A. 2. VARIATION OF FIBRE ORIENTATION FACTOR WITH THE RATIO h_U/l_f

Zone *c*:

All the fibres located in zone *c* can freely rotate at any orientation, according to θ and φ. In this case, all the possible orientations of a fibre describe a surface of a sphere.

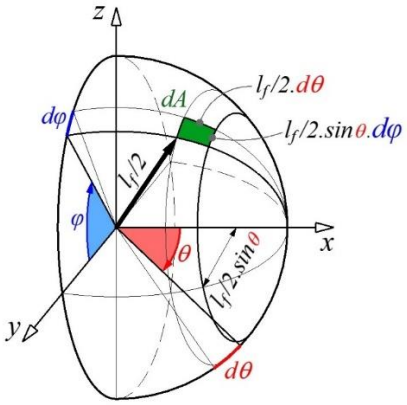

If considered just half of the sphere, the maximum values of θ and φ will be equal to $\pi/2$ and 2π, respectively.

$$dA = \frac{l_f^2}{4}\sin\theta d\theta d\varphi$$

$$A = \int_{\varphi=0}^{\varphi=2\pi}\int_{\theta=0}^{\theta=\frac{\pi}{2}} \frac{l_f^2}{4}\sin\theta d\theta d\varphi = \frac{\pi l_f^2}{2}$$

$$\psi(\theta,\varphi) = \frac{dA}{A} = \frac{1}{2\pi}\sin\theta d\theta d\varphi$$

$$p_x(\theta,\varphi) = \cos\theta$$

$$\alpha_{0,x}^c = \int_{\varphi=0}^{\varphi=2\pi}\int_{\theta=0}^{\theta=\frac{\pi}{2}} \frac{1}{2\pi}\sin\theta\cos\theta d\theta d\varphi = \int_{\theta=0}^{\theta=\frac{\pi}{2}} \frac{1}{2}\sin 2\theta d\theta = 0.5$$

Zone *w*:

In the region subjected to the wall effect, *w*, the freedom of a fibre to rotate will be limited as much closer the centre of the fibre will be to the upper and lower surfaces of the specimen. In this case, all the possible orientations of the fibre describe the surface of the spherical segment limited with z_{crit}. Therefore, the total area can be integrated into two

parts with respect to the boundary introduced with z_{crit}, i.e., one (A_1) is calculated as stated above but with the upper bound limit up to θ_{crit}. All the calculations are made considering half of the sphere.

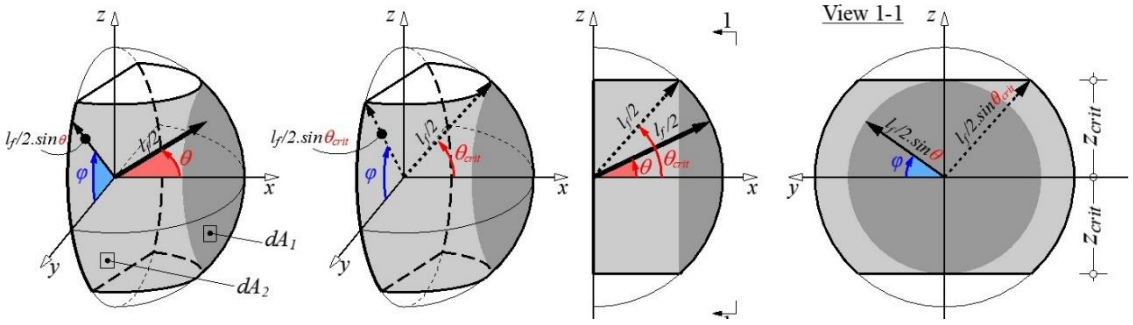

$$\theta_{crit}=\arcsin\left(\frac{2z_{crit}}{l_f}\right);\ 0\le z_{crit}\le\frac{l_f}{2}$$

$$dA_1=\frac{l_f^2}{4}\sin\theta d\theta d\varphi;\ \theta\le\theta_{crit}$$

$$\mathrm{d}A_2=l_f^2\sin\theta d\theta d\varphi;\ \ \theta_{crit}\le\theta\le\frac{\pi}{2}\ \text{and}\ \varphi\le\arcsin\left(\frac{2z}{l_f\sin\theta}\right)$$

$$dA=dA_1+dA_2$$

$$A=A_1+A_2=\frac{1}{2}A_{spherical\ segment}=\frac{1}{2}\times2\pi\times\frac{l_f}{2}\times2z=\pi\,l_f z$$

It is worth mentioning that in this region, the value of the fibre orientation factor depends on distance z between the fibre's gravity point and the upper or lower surfaces, so that:

$$\alpha_{0,x}^{w}(z)=\int_{\varphi=0}^{\varphi=2\pi}\int_{\theta=0}^{\theta=\theta_{crit}}\frac{l_f}{4\pi z}\sin\theta\cos\theta d\theta d\varphi+\int_{\varphi=0}^{\varphi=\arcsin\left(\frac{2z}{L_F\sin\theta}\right)}\int_{\theta=\theta_{crit}}^{\theta=\frac{\pi}{2}}\frac{l_f}{\pi z}\sin\theta\cos\theta d\theta d\varphi$$

has to be integrated, taking into account the whole distance z up to half the length of the fibre.

$$\alpha_{0,x}^{w}=\frac{2}{l_f}\int_{z=0}^{z=\frac{l_f}{2}}\left[\int_{\theta=0}^{\theta=\theta_{crit}}\frac{l_f}{2z}\sin\theta\cos\theta d\theta+\int_{\theta=\theta_{crit}}^{\theta=\frac{\pi}{2}}\frac{l_f}{\pi z}\sin\theta\cos\theta\arcsin\left(\frac{2z}{l_f\sin\theta}\right)d\theta\right]dz$$

The general fibre orientation will result from the weight of both zones. So, it can be computed by:

$$\alpha_{0,x} = \begin{cases} \dfrac{\alpha_{0,x}^{w} . l_f + \alpha_{0,x}^{c} \left(h_U - l_f \right)}{h_U} \; ; & \text{for } h_U > l_f \\ \alpha_{0,x}^{w} \quad ; & \text{for } h_U \leq l_f \end{cases}$$

For thin elements ($h_U / l_f \leq 3$) the value of fibre orientation factor is not smaller 0.532.

h_U/l_f	$\alpha_{0,x}$	h_U/l_f	$\alpha_{0,x}$	h_U/l_f	$\alpha_{0,x}$	h_U/l_f	$\alpha_{0,x}$	h_U/l_f	$\alpha_{0,x}$	h_U/l_f	$\alpha_{0,x}$
0	0.6366	1	0.5959	2	0.5480	3	**0.5320**	4	0.5240	5	0.5192
0.1	0.6356	1.1	0.5872	2.1	0.5457	3.1	0.5309	4.1	0.5234	6	0.5160
0.2	0.6346	1.2	0.5799	2.2	0.5436	3.2	0.5300	4.2	0.5228	7	0.5137
0.3	0.6328	1.3	0.5738	2.3	0.5417	3.3	0.5291	4.3	0.5223	8	0.5120
0.4	0.6302	1.4	0.5685	2.4	0.5400	3.4	0.5282	4.4	0.5218	9	0.5107
0.5	0.6269	1.5	0.5640	2.5	0.5384	3.5	0.5274	4.5	0.5213	10	0.5096
0.6	0.6228	1.6	0.5600	2.6	0.5369	3.6	0.5266	4.6	0.5209	20	0.5048
0.7	0.6178	1.7	0.5564	2.7	0.5355	3.7	0.5259	4.7	0.5204	30	0.5032
0.8	0.6118	1.8	0.5533	2.8	0.5343	3.8	0.5252	4.8	0.5200	40	0.5024
0.9	0.6046	1.9	0.5505	2.9	0.5331	3.9	0.5246	4.9	0.5196	50	0.5019

A. 3. EXPERIMENTAL RESULTS OF FIBRE ANISOMETRY

Author(s)	Specimen		V_f [%]	h_U [mm]	l_f [mm]	h_U/l_f	$\alpha_{0,i}$	$\alpha_{0,j}$	$\alpha_{0,j}/\alpha_{0,i}$
DEWST2	**190B**		1	30	13	2.3	0.73	0.4	0.48
	1RB						0.46	0.64	1.39
	290B		2				0.91	0.16	0.17
	30A		3				0.17	0.85	5.07
	4RA		4				0.48	0.59	1.21
(Oesterlee 2010)	**T2H**		3.14	40	13	3.1	0.79	0.19	0.24
	T6H-1		3.07				0.49	0.67	1.37
	T6H-2		2.96				0.39	0.74	1.90
	T7H-1		3.07				0.36	0.79	2.19
	T2V		3.17				0.53	0.63	1.19
	T4V		2.76				0.55	0.75	1.36
	T6V		4.13				0.50	0.53	1.06
(Ferrara, Ozyurt, and di Prisco 2011)	**A**		1.27	30	13	2.3	0.85	0.44	0.52
	B						0.76	0.54	0.71
(Wuest 2007)	**CM22-94-T5**	1	5.09	49	10	4.9	0.61	0.75	1.23
		3	5.27				0.59	0.80	1.36
	CM0-98-T4	1	6.24	49	10	4.9	0.62	0.58	0.94
		2	6.22				0.56	0.48	0.86
		3	6.22				0.7	0.48	0.69
		5	6.18				0.65	0.58	0.89
		7	6.17				0.62	0.58	0.94
		9	6.41				0.6	0.52	0.87
	CM23-P-T1	2	6.7	49	10	4.9	0.73	0.53	0.73
		6	6.68				0.6	0.56	0.93
		8	7.06				0.66	0.50	0.76
		10-2	6.81				0.7	0.48	0.69
		12-2	6.66				0.69	0.47	0.68
	HIFCOM-14-T2	1	4.27	49	13	3.8	0.65	0.35	0.54
	CM0-05-22-TE1	2	5.73	49	10	4.9	0.24	0.80	3.33
		5	5.79				0.53	0.74	1.40
		7	6.02				0.33	0.75	2.27
	CM22-3-e	1	6.25	49	10	4.9	0.66	0.52	0.79
		3	6.25				0.61	0.51	0.84
	SAMD2	1	6	23	10	2.3	0.52	0.68	1.31
		2					0.71	0.58	0.82
		2-2					0.71	0.53	0.75
		3					0.60	0.69	1.15
		3-2					0.72	0.47	0.65

		4					0.77	0.39	0.51
		5					0.55	0.75	1.36
		5-2					0.6	0.59	0.98
		6					0.8	0.54	0.68
(Bastien-Masse, Denarié, and Brühwiler 2016)	**III**		3	50	13	3.8	0.6	0.54	0.90
	IV						0.52	0.49	0.94
(Babut 1985)	P1		0.5	100	25	4	0.53	0.54	1.01
	P2		1				0.45	0.52	1.15
	P3		1.5				0.46	0.46	1.00
	P10		2				0.50	0.51	1.02
	P11		2.5				0.47	0.50	1.08
	P12		3				0.48	0.46	0.97
	P4		1.5				0.43	0.51	1.18
	P5		1.5				0.51	0.52	1.02
	P6		1.5				0.49	0.42	0.86
	P7		1.5				0.56	0.46	0.82
	P8		1.5				0.52	0.46	0.89
	P9		1.5				0.52	0.46	0.87
	P1		0.5				0.53	0.54	1.01
	P2		1				0.45	0.52	1.15

A. 4. EXPERIMENTAL RESULTS OF FIBRE ORIENTATION STATE INDICATORS

Authors	Specimens	V_f [%]	l_f [mm]	d_f [mm]	h_U [mm]	h_U/l_f	α_0	α_1	η_θ	η_θ^2
(Duque and Graybeal 2017)	**UTT1**	2	13	0.2	50	3.8	0.43	0.83	0.71	0.50
							0.33	0.66	0.60	0.36
							0.36	0.72	0.65	0.42
							0.52	0.84	0.70	0.49
							0.57	0.87	0.75	0.56
							0.63	0.92	0.77	0.59
							0.75	0.95	0.86	0.74
							0.71	0.96	0.83	0.69
							0.70	0.98	0.80	0.64
(Abrishambaf, Pimentel, and Nunes 2017)	**UTT2**	1.2	12	0.175	40	3.3	0.90	0.99	0.89	0.79
							0.87	0.99	0.90	0.81
							0.79	0.99	0.88	0.77
							0.84	0.99	0.88	0.77
							0.82	0.99	0.88	0.77
							0.55	0.86	0.72	0.52
							0.62	0.84	0.74	0.55
							0.56	0.81	0.70	0.48
							0.52	0.74	0.68	0.46
		2.3					0.78	0.96	0.87	0.76
							0.80	0.97	0.88	0.77
							0.80	0.96	0.88	0.77
							0.81	0.95	0.86	0.74
		3					0.73	0.98	0.88	0.77
							0.73	0.99	0.87	0.76
							0.66	0.97	0.85	0.72
							0.73	0.99	0.89	0.79
							0.71	0.98	0.88	0.77
							0.47	0.80	0.73	0.53
							0.51	0.83	0.77	0.59
							0.47	0.80	0.75	0.56
							0.46	0.79	0.73	0.53
							0.46	0.80	0.71	0.50
							0.45	0.81	0.70	0.49
							0.46	0.79	0.70	0.49
							0.44	0.77	0.69	0.48
(Shen and Brühwiler 2020)	**UTT3**	3.8	13	0.175	50	3.8	0.68	0.96	-	-
							0.62	0.94	-	-
							0.53	0.92	-	-
							0.53	0.93	-	-
							0.52	0.92	-	-
(Nunes et al. 2017)	**DEWST1**	1.5	12	0.175	25	2.1	0.89	0.99	0.93	0.86
							0.83	0.98	0.90	0.80
							0.65	0.87	0.75	0.56
							0.27	0.41	0.48	0.23

							0.18	0.27	0.41	0.17
		3					0.81	1.00	0.93	0.86
							0.77	0.98	0.90	0.81
							0.49	0.87	0.77	0.59
							0.51	0.86	0.74	0.55
							0.39	0.62	0.62	0.39
							0.28	0.57	0.56	0.32
DEWST2	**DEWST2**	1	13	0.2	30	2.3	0.70	0.93	0.78	0.61
							0.75	0.94	0.85	0.73
		2					0.69	0.94	0.81	0.65
							0.92	0.98	0.93	0.87
							0.46	0.75	0.69	0.47
		3					0.71	0.86	0.76	0.58
							0.83	0.98	0.92	0.85
							0.58	0.88	0.73	0.53
		4					0.57	0.90	0.72	0.52
							0.61	0.89	0.71	0.51
							0.51	0.85	0.77	0.60
FPBT	**LP1**	3	12	0.175	30	2.5	0.57	0.90	0.78	0.62
							0.49	0.85	0.73	0.53
	SP1						0.41	0.63	0.59	0.34
							0.40	0.59	0.57	0.32
	SP2						0.48	0.87	0.76	0.58
							0.41	0.81	0.70	0.49

A. 5. THEORETICAL MODEL OF THE NDT METHOD

In a simple magnetic circuit Figure A. 5. 1 (a), the inductance, L, is defined as the ability of a coil of N turns to generate a magnetic flux, Φ, induced by an electric current, I, that crosses the circuit:

$$L=\frac{N.\Phi}{I}$$

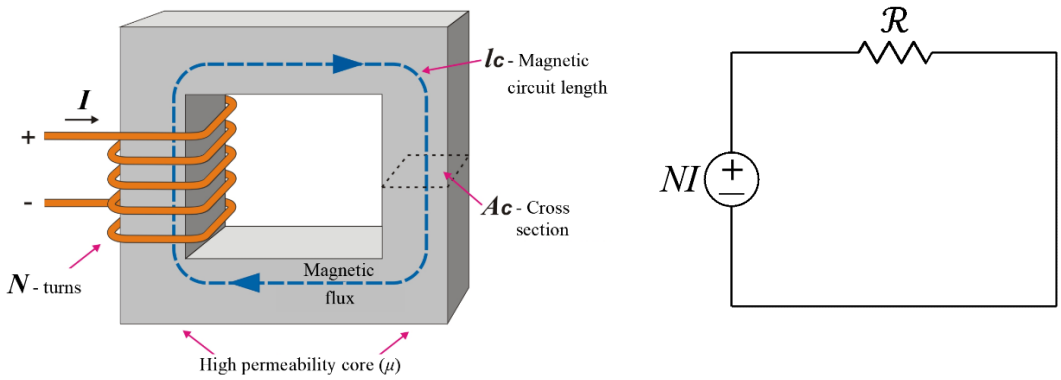

(a) (b)

Figure A. 5. 1. Magnetic circuit: (a) schematic representation (Fitzgerald, Kingsley, and Umans 2003) and (b) electrical equivalent.

The magnetic circuit, equivalent to an electric circuit (Figure A. 5. 1 (b)), is established based on Hopkinson's law for magnetic circuits – the reluctance, $\mathcal{R}$, of the magnetic circuit that holds the flux is the counterpart of the resistance, R, in the electric circuit, the magnetomotive force, F_m, is analogous to the electromotive force, ε, and the magnetic flux is analogous to electric current. Therefore, an equivalent Ohm's law for the magnetic circuit can be expressed by:

$$\Phi=\frac{F_m}{\mathcal{R}}=\frac{N.I}{\mathcal{R}}$$

where the reluctance is defined as

$$\mathcal{R}=\frac{l_c}{\mu_0.\mu_r.A_c}$$

where $\mu_0=4\pi\times10^{-7}(H/m)$; l_c is the magnetic circuit length, and A_c is the cross-section of the core.

Considering the previous equations, the inductance can be alternatively given by:

$$L=\frac{N^2}{\mathcal{R}}$$

For notation, of Figure A. 5. 2 and Figure A. 5. 3, let superscripts: *c* – ferrite core, *m* – UHPFRC cementitious matrix, *f* - fibres, *p* – parallel association of reluctances, *s* - series association of reluctances, *v* – vertical projection of fibres, and *h* – horizontal projection of fibres.

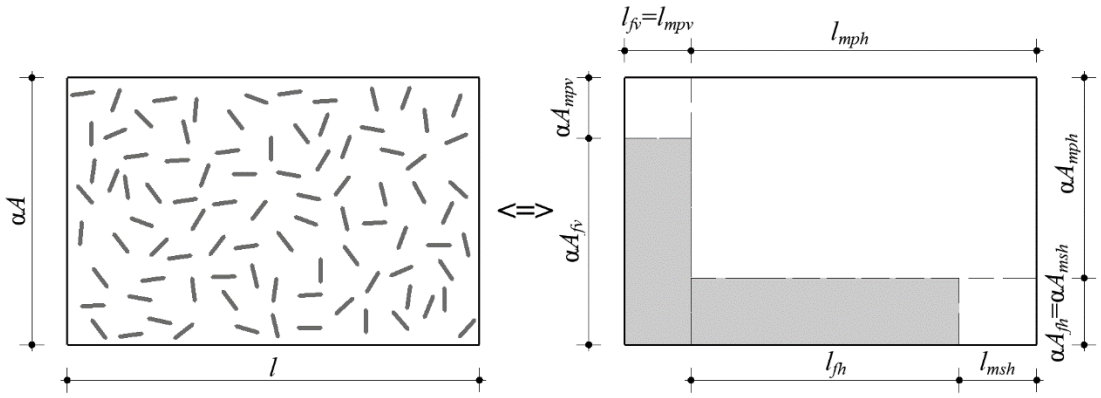

Figure A. 5. 2. Simplified physical model of UHPFRC 2D layer, adapted from (2016a).

The magnetic circuit resulting from placing the probe over the UHPFRC layer is characterized by the association of reluctance related to the ferrite core, $\mathcal{R}_c$, fibres, $\mathcal{R}_f$, and the UHPFRC cementitious matrix, $\mathcal{R}_m$ (Figure A. 5. 3).

The equivalent magnetic reluctance from the association of the reluctances of the UHPFRC phases is given as:

$$\mathcal{R}_{UHPFRC}=\frac{\mathcal{R}_{mph}.\left(\mathcal{R}_{fh}+\mathcal{R}_{msh}\right)}{\mathcal{R}_{mph}+\mathcal{R}_{fh}+\mathcal{R}_{msh}}+\frac{\mathcal{R}_{mpv}.\mathcal{R}_{fv}}{\mathcal{R}_{mpv}+\mathcal{R}_{fv}}$$

and the total equivalent magnetic reluctance of the circuit, including the ferrite core, is given as:

$$\mathcal{R}_{total}=\mathcal{R}_c+\mathcal{R}_{UHPFRC}$$

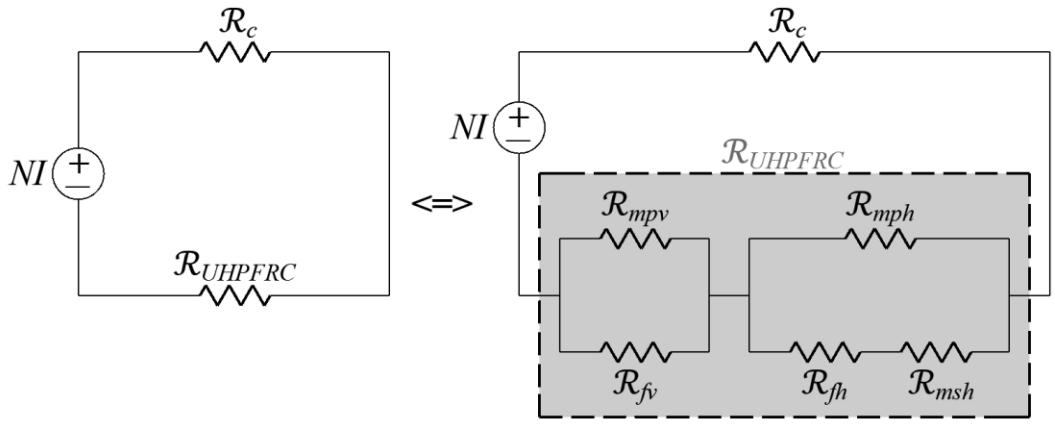

Figure A. 5. 3. Magnetic circuit of the probe and the simplified physical model, adapted from (2016a).

The total equivalent magnetic reluctance of the circuit can also be expressed as:

$$\mathcal{R}_{total} = \frac{l_c}{\mu_0 . \mu_{rc} . A_c} + \frac{l}{\mu_0 . \mu_{r,\beta} . A}$$

so, the inductance of the composite for a given β-direction is computed by:

$$L_\beta = \frac{N^2 . \mu_0}{\frac{l_c}{\mu_{r,c} . A_c} + \frac{l}{\mu_{r,\beta} . A}}$$

where $\mu_{r,c}$ e $\mu_{r,\beta}$ are respectively the relative magnetic permeability of the ferrite core and the UHPFRC composite layer for the given direction β; l e A are the length and cross-section crossed by the magnetic flux in the composite layer.

Since $\mu_{r,c} \approx 2000$ (Nunes and Pimentel 2016) and l_c=189 mm and A_c=28x30 mm^2, the contribution of the ferrite core can be neglected in the previous equation, resulting on:

$$L_\beta \approx \frac{N^2 . \mu_0 . \mu_{r,\beta}}{l/A}$$

Knowing that the inductance of the air, $L_{air} = N^2 \mu_0 / (l/A)$, and assuming that l/A is a constant shape factor (Nunes, Pimentel, and Carvalho 2016a), then the relative magnetic permeability of UHPFRC along with the measuring orientation, β, is approximated to:

$$\mu_{r,\beta} \approx \frac{L_\beta}{L_{air}}$$

It can be computed by the following equation:

$$\mu_{r,\beta}=\left\{\begin{array}{c}\dfrac{\left[1-(1-\gamma)\sum V_{f,n}.\sin^2(\beta-\theta_n)\right].\left(\mu_{r,f}.\gamma+1-\gamma\right)}{\left[1-(1-\gamma)\sum V_{f,n}.\cos^2(\beta-\theta_i)\right].\left(\mu_{r,f}.\gamma+1-\gamma\right)+(1-\gamma)\mu_{r,f}.\sum V_{f,n}.\cos^2(\beta-\theta_n)}\ldots \\ \\ \ldots+\dfrac{(1-\gamma)\sum V_{f,n}.\sin^2(\beta-\theta_n)}{\gamma+(1-\gamma)\mu_{r,f}.}\end{array}\right\}^{-1}$$

where $\mu_{r,f}$ is the relative magnetic permeability of the steel fibres, varying from 500 and 5000 (Andrade 2010); $\gamma \approx 0.33$ - 0.35 (Nunes, Pimentel, and Carvalho 2016b) is the model parameter expressing the fact that the fibres are discontinuous steel filaments.

A. 6. UHPFRC MIX-PROPORTIONS [kg/m^3]

Constituent materials	V_f**=1%**	V_f **=2%**	V_f **=3%**	V_f **=4%**
Cement	794.9			
Silica fume	79.49			
Limestone filler	311.43			
Water	145.36			
Superplasticizer	30			
Sand	993.56	967.26	940.96	914.66
Fibres	78.4	157	235	314

References

Abrishambaf, Amin, Joaquim A. O. Barros, and Vitor M. C. F. Cunha. 2013. "Relation between Fibre Distribution and Post-Cracking Behaviour in Steel Fibre Reinforced Self-Compacting Concrete Panels." *Cement and Concrete Research* 51: 57–66. https://doi.org/10.1016/J.CEMCONRES.2013.04.009.

Abrishambaf, Amin, Mário Pimentel, and Sandra Nunes. 2017. "Influence of Fibre Orientation on the Tensile Behaviour of Ultra-High Performance Fibre Reinforced Cementitious Composites." *Cement and Concrete Research*, 28–40. https://doi.org/10.1016/j.cemconres.2017.03.007.

———. 2019. "A Meso-Mechanical Model to Simulate the Tensile Behaviour of Ultra-High Performance Fibre-Reinforced Cementitious Composites." *Composite Structures* 222. https://doi.org/10.1016/j.compstruct.2019.110911.

———. 2020. "An Eco-Friendly UHPC for Structural Application: Tensile Mechanical Response." In *BEFIB2020, RILEM-Fib X International Symposium on Fibre Reinforced Concrete*, 30:1056–67. Valencia, Spain. https://doi.org/10.1007/978-3-030-58482-5_93.

Advani, Suresh G., and Charles L. Tucker. 1987. "The Use of Tensors to Describe and Predict Fiber Orientation in Short Fiber Composites." *Journal of Rheology* 31 (8): 751–84. https://doi.org/10.1122/1.549945.

AFGC. 2002. *Béton Fibrés à Ultra-Hautes Performances (Ultra High Performance Fibrereinforced Concretes)-Recommandations Provisoires*.

———. 2013. *Bétons Fibrés à Ultra-Hautes Performances (Ultra High Performance Fibrereinforced Concretes)-Recommandations*.

AFNOR. 2016a. *NF P 18-710: National Addition to Eurocode 2 - Design of Concrete Structures: Specific Rules for UHPFRC*. France.

———. 2016b. *Norme PR NF P18-470|Bétons Fibrés à Ultra Hautes Performances Spécification, Performance, Production et Conformité*. France.

———. 2016c. *Norme PR NF P18-710|Complément National à l'Eurocode 2 Calcul Des Structures En Béton: Règles Spécifiques Pour Les Bétons Fibrés à Ultra-Hautes Performances (BFUP)*. France.

Afonso, Carlos Liberal Moreno. 2010. "Lajes Fungiformes. Contribuições Para a Compreensão Do Seu Comportamento." Faculdade de Engenharia da Universidade do Porto.

Al-Osta, M. A., M. N. Isa, M. H. Baluch, and M. K. Rahman. 2017. "Flexural Behavior of Reinforced Concrete Beams Strengthened with Ultra-High Performance Fiber

Reinforced Concrete." *Construction and Building Materials* 134: 279–96. https://doi.org/10.1016/j.conbuildmat.2016.12.094.

Alaee, Farshid Jandaghi, and Bhushan Lal Karihaloo. 2003. "Retrofitting of Reinforced Concrete Beams with CARDIFRC." *JOURNAL OF COMPOSITES FOR CONSTRUCTION © ASCE* 7 (3): 174–86. https://doi.org/10.1061/ASCE1090-0268(2003)7:3(174).

Andrade, Fabiano. 2010. "MATERIAIS ELÉTRICOS - MEL."

ASTM. 2001. "Standard Test Method for Measuring Pavement Macrotexture Depth Using a Volumetric Technique: E 965." ASTM.

Aveston, J., and A. Kelly. 1973. "Theory of Multiple Fracture of Fibrous Composites." *Journal of Materials Science* 8 (3): 352–62. https://doi.org/10.1007/BF00550155.

Babut, R. 1985. "Structural Investigation of Steel Fibre Reinforced Concrete." *Heron* 31 (2): 29–43.

Baby, Florent, Benjamin A. Graybeal, Pierre Marchand, and François Toutlemonde. 2013. "UHPFRC Tensile Behavior Characterization: Inverse Analysis of Four-Point Bending Test Results." *Materials and Structures* 46 (8): 1337–54. https://doi.org/10.1617/s11527-012-9977-0.

Baby, Florent, Benjamin Graybeal, Pierre Marchand, and François Toutlemonde. 2012. "Proposed Flexural Test Method and Associated Inverse Analysis for Ultra-High-Performance Fiber-Reinforced Concrete." *ACI Materials Journal* 109 (5): 545–55.

Bache, Hans H. 1981. "Densified Cement Ultrafine Particle-Based Materials." In *2nd International Conference on Superplasticizers in Concrete*, 33.

Barnett, Stephanie J., Jean Francois Lataste, Tony Parry, Steve G. Millard, and Marios N. Soutsos. 2010. "Assessment of Fibre Orientation in Ultra High Performance Fibre Reinforced Concrete and Its Effect on Flexural Strength." *Materials and Structures/Materiaux et Constructions* 43 (7): 1009–23. https://doi.org/10.1617/s11527-009-9562-3.

Bastien-Masse, Malena. 2015. "Structural Behavior of R-UHPFRC-RC Composite Slabs." École Plytechnique Fédérale de Lausanne.

Bastien-Masse, Malena, and Eugen Brühwiler. 2015. "Experimental Investigation on Punching Resistance of R-UHPFRC–RC Composite Slabs." *Materials and Structures* 49: 1573–90. https://doi.org/10.1617/s11527-015-0596-4.

———. 2016a. "Composite Model for Predicting the Punching Resistance of R-UHPFRC–RC Composite Slabs." *Engineering Structures* 117: 603–16. https://doi.org/10.1016/j.engstruct.2016.03.017.

———. 2016b. "Contribution of R-UHPFRC Strengthening Layers to the Shear

Resistance of RC Elements." *Structural Engineering International*, 365–74. https://doi.org/10.2749/101686616X14555429843924.

———. 2016c. "Contribution of R-UHPFRC Strengthening Layers to the Shear Resistance of RC Elements." In *Proceedings of HiPerMat 2016-4th International Symposium on Ultra-High Performance Concrete and High Performance Materials*. https://doi.org/10.2749/101686616X14555429843924.

Bastien-Masse, Malena, Emmanuel Denarié, and Eugen Brühwiler. 2016. "Effect of Fiber Orientation on the In-Plane Tensile Response of UHPFRC Reinforcement Layers." *Cement and Concrete Composites*, 111–25. https://doi.org/10.1016/j.cemconcomp.2016.01.001.

Belletti, Beatrice, Mário Pimentel, Matteo Scolari, and Joost C. Walraven. 2015. "Safety Assessment of Punching Shear Failure According to the Level of Approximation Approach." *Structural Concrete* 16 (3): 366–80. https://doi.org/10.1002/suco.201500015.

Blais, Pierre Y., and Marco Couture. 1999. "Precast, Prestressed Pedestrian Bridge World's First Reactive Powder Concrete Structure." *PCI Journal*, 60–71.

Brühwiler, Eugen. 2017. "Strengthening of Existing Structures Using R-Uhpfrc : Principles and Conceptual Design." In *AFGC-ACI-Fib-RILEM Int. Symposium on Ultra-High Performance Fibre-Reinforced Concrete*, 993–1002. Montpellier.

———. 2020. "UHPFRC Technology to Enhance the Performance of Existing Concrete Bridges." *Structure and Infrastructure Engineering* 16 (1): 94–105. https://doi.org/10.1080/15732479.2019.1605395.

Brühwiler, Eugen, Malena Bastien-Masse, Hartmut Mühlberg, Bernard Houriet, Blaise Fleury, Stéphane Cuennet, Philippe Schär, Frédéric Boudry, and Marco Maurer. 2015. "Strengthening the Chillon Viaducts Deck Slabs with Reinforced UHPFRC." In *IABSE Conference – Structural Engineering: Providing Solutions to Global Challenges*. Geneva.

Brühwiler, Eugen, and Emmanuel Denarié. 2013. "Rehabilitation and Strengthening of Concrete Structures Using Ultra-High Performance Fibre Reinforced Concrete." *Structural Engineering International* 23 (4): 450–57. https://doi.org/10.2749/101686613X13627347100437.

Cavalaro, Sergio H.P., Rubén López-Carreño, Josep María Torrents, Antonio Aguado, and Pablo Juan-García. 2016. "Assessment of Fibre Content and 3D Profile in Cylindrical SFRC Specimens." *Materials and Structures/Materiaux et Constructions* 49 (1–2): 577–95. https://doi.org/10.1617/s11527-014-0521-2.

Charron, Jean-Philippe, Emmanuel Denarié, and Eugen Brühwiler. 2007. "Permeability of Ultra High Performance Fiber Reinforced Concretes (UHPFRC) under High Stresses." *Materials and Structures* 40: 269–77. https://doi.org/10.1617/s11527-006-9105-0.

———. 2008. “Transport Properties of Water and Glycol in an Ultra High Performance Fiber Reinforced Concrete (UHPFRC) under High Tensile Deformation.” *Cement and Concrete Research* 38 (5): 689–98. https://doi.org/10.1016/J.CEMCONRES.2007.12.006.

Choi, Jung, Woo Lim, and Sung Hong. 2016. “Strengthening T-Shaped RC Beams with UHPC.” In *Proceedings of HiPerMat 2016-4th International Symposium on Ultra-High Performance Concrete and High Performance Materials*.

Clément, Thibault, António Pinho Ramos, Miguel Fernández Ruiz, and Aurelio Muttoni. 2014. “Influence of Prestressing on the Punching Strength of Post-Tensioned Slabs.” *Engineering Structures* 72: 56–69. https://doi.org/10.1016/j.engstruct.2014.04.034.

Deeb, R., B. L. Karihaloo, and S. Kulasegaram. 2014. “Reorientation of Short Steel Fibres during the Flow of Self-Compacting Concrete Mix and Determination of the Fibre Orientation Factor.” *Cement and Concrete Research* 56 (February): 112–20. https://doi.org/10.1016/J.CEMCONRES.2013.10.002.

Denarié, Emmanuel, and Eugen Brühwiler. 2006. “Structural Rehabilitations with Ultra-High Performance Fibre Reinforced Concretes (UHPFRC).” *Restoration of Buildings and Monuments* 12 (5/6): 453–68.

Denarié, Emmanuel, Damien Jacomo, Nicolas Fady, and Dominique Corvez. 2013. “Rejuvenation of Maritime Signalisation Structures with UHPFRC.” In *RILEM-Fib-AFGC Int. Symposium on Ultra-High Performance Fibre-Reinforced Concrete*. Marseille.

Dupont, David, and Lucie Vandewalle. 2005. “Distribution of Steel Fibres in Rectangular Sections.” *Cement and Concrete Composites* 27 (3): 391–98. https://doi.org/10.1016/j.cemconcomp.2004.03.005.

Duque, Luis Felipe Maya, and Benjamin Graybeal. 2017. “Fiber Orientation Distribution and Tensile Mechanical Response in UHPFRC.” *Materials and Structures/Materiaux et Constructions* 50 (1). https://doi.org/10.1617/s11527-016-0914-5.

Einpaul, Jürgen, Miguel Fernández Ruiz, and Aurelio Muttoni. 2015. “Influence of Moment Redistribution and Compressive Membrane Action on Punching Strength of Flat Slabs.” *Engineering Structures* 86: 43–57. https://doi.org/10.1016/j.engstruct.2014.12.032.

Faifer, Marco, Liberato Ferrara, Roberto Ottoboni, and Sergio Toscani. 2013. “Low Frequency Electrical and Magnetic Methods for Non-Destructive Analysis of Fiber Dispersion in Fiber Reinforced Cementitious Composites: An Overview.” *Sensors (Switzerland)* 13 (1): 1300–1318. https://doi.org/10.3390/s130101300.

Farghaly, Ahmed Sabry, and Tamon Ueda. 2011. “Prediction of Punching Shear Strength of Two-Way Slabs Strengthened Externally with FRP Sheets.” *JOURNAL OF COMPOSITES FOR CONSTRUCTION* 15 (2): 181–93.

https://doi.org/10.1061/(ASCE)CC.1943-5614.0000177.

Faria, Duarte M. V., Jürgen Einpaul, António M. P. Ramos, Miguel Fernández Ruiz, and Aurelio Muttoni. 2014. "On the Efficiency of Flat Slabs Strengthening against Punching Using Externally Bonded Fibre Reinforced Polymers." *Construction and Building Materials* 73 (December): 366–77. https://doi.org/10.1016/j.conbuildmat.2014.09.084.

Faria, Duarte M.V., Válter J.G. Lúcio, and A. Pinho Ramos. 2012. "Post-Punching Behaviour of Flat Slabs Strengthened with a New Technique Using Post-Tensioning." *Engineering Structures* 40: 383–97. https://doi.org/10.1016/j.engstruct.2012.03.014.

Feenstra, Peter H., and René De Borst. 1996. "A Composite Plasticity Model for Concrete." *International Journal of Solids and Structures* 33 (5): 707–30. https://doi.org/10.1016/0020-7683(95)00060-N.

Fernandes, Hugo Daniel Pereira. 2019. "Strengthening of Flat Slabs with Reinforced Concrete Overlay – Analysis and Development of the Solution." Universidade Nova de Lisboa.

Fernandes, Hugo, Válter Lúcio, and António Ramos. 2017. "Strengthening of RC Slabs with Reinforced Concrete Overlay on the Tensile Face." *Engineering Structures* 132: 540–50. https://doi.org/10.1016/j.engstruct.2016.10.011.

Fernández Ruiz, Miguel, Aurelio Muttoni, and J Sagaseta. 2015. "Shear Strength of Concrete Members without Transverse Reinforcement: A Mechanical Approach to Consistently Account for Size and Strain Effects." *Engineering Structures*, no. 99: 360–72.

Ferrara, Liberato, Massimiliano Cremonesi, Marco Faifer, Sergio Toscani, Luca Sorelli, Marc-Antoine Baril, Julien Réthoré, Florent Baby, François Toutlemonde, and Sébastien Bernardi. 2017. "Structural Elements Made with Highly Flowable UHPFRC: Correlating Computational Fluid Dynamics (CFD) Predictions and Non-Destructive Survey of Fiber Dispersion with Failure Modes." *Engineering Structures* 133: 151–71. https://doi.org/10.1016/J.ENGSTRUCT.2016.12.026.

Ferrara, Liberato, Marco Faifer, Muhaxheri Milot, and Sergio Toscani. 2012. "A Magnetic Method for Non Destructive Monitoring of Fiber Dispersion and Orientation in Steel Fiber Reinforced Cementitious Composites. Part 2: Correlation to Tensile Fracture Toughness." *Materials and Structures* 45: 591–98. https://doi.org/10.1617/s11527-011-9794-x.

Ferrara, Liberato, Marco Faifer, and Sergio Toscani. 2012. "A Magnetic Method for Non Destructive Monitoring of Fiber Dispersion and Orientation in Steel Fiber Reinforced Cementitious Composites—Part 1: Method Calibration." *Materials and Structures* 45 (4): 575–89. https://doi.org/10.1617/s11527-011-9793-y.

Ferrara, Liberato, and Alberto Meda. 2007. "Relationships between Fibre Distribution,

Workability and the Mechanical Properties of SFRC Applied to Precast Roof Elements." *Materials and Structures* 39 (4): 411–20. https://doi.org/10.1617/s11527-005-9017-4.

Ferrara, Liberato, Nilufer Ozyurt, and Marco di Prisco. 2011. "High Mechanical Performance of Fibre Reinforced Cementitious Composites: The Role of 'Casting-Flow Induced' Fibre Orientation." *Materials and Structures* 44 (1): 109–28. https://doi.org/10.1617/s11527-010-9613-9.

FHWA. 2021. "North American Bridges Employing UHPC." 2021. https://usdot.maps.arcgis.com/apps/webappviewer/index.html?id=41929767ce164eba934d70883d775582.

fib. 2012a. *Fib Bulletin 65: Model Code 2010 - Volume 1*. Lausanne: fib.

———. 2012b. *Fib Bulletin 66: Model Code 2010 - Volume 2*. Vol. 2. Lausanne: fib. https://doi.org/10.1017/CBO9781107415324.004.

———. 2021. "Update on the Journey to Fib MC2020." 2021. https://www.fib-international.org/blog/367-update-on-the-journey-to-fib-mc2020.html.

Fitzgerald, A. E. (Arthur Eugene), Charles Kingsley, and Stephen D. Umans. 2003. *Electric Machinery*. McGraw-Hill.

Gardner, N. J., Jungsuck Huh, and Lan Chung. 2002. "Lessons from the Sampoong Department Store Collapse." *Cement and Concrete Composites* 24 (6): 523–29. https://doi.org/10.1016/S0958-9465(01)00068-3.

Gowripalan, N., and Ian R. Gilbert. 2000. *Design Gudelines for Ductal Prestressed Concrete Beams*. Sidney: VSL (Aust) Pty Ltd.

Graybeal, Benjamin A., and Florent Baby. 2013. "Development of Direct Tension Test Method for Ultra-High-Performance Fiber-Reinforced Concrete." *ACI Materials Journal*, no. 110: 177–86. https://doi.org/10.14359/51685532.

Graybeal, Benjamin, Eugen Brühwiler, Byung-Suk Kim, François Toutlemonde, Yen Lei Voo, and Arash Zaghi. 2020. "International Perspective on UHPC in Bridge Engineering." *Journal of Bridge Engineering* 25 (11). https://doi.org/10.1061/(ASCE)BE.1943-5592.0001630.

Graybeal, Benjamin, and Marshall Davis. 2008. "Cylinder or Cube : Strength Testing of 80 to 200 MPa (11 . 6 to 29 Ksi) Ultra-High-Performance Fiber-Reinforced Concrete." *ACI Materials Journal* 105 (6): 603–9.

Guandalini, Stefano. 2005. "Poinçonnement Symétrique Des Dalles En Béton Armé." École Polytechnique Fédérale de Lausanne.

Guenet, Thomas. 2016. "Modélisation Du Comportement Des Bétons Fibrés à Ultra-Hautes Performances Par La Micromécanique : Effet de l'orientation Des Fibres à

l'échelle de La Structure." Université Paris-Est.

Habel, Katrin. 2004. "Structural Behavior of Elements Combining Ultra-High Performance Fibre Reinforced Concretes (UHPFRC) and Reinforced Concrete." École Polytechnique Fédérale de Lausanne.

Habel, Katrin, Emmanuel Denarié, and Eugen Brühwiler. 2006. "Structural Response of Elements Combining and Reinforced Concrete." *Journal of Structural Engineering* 132 (November): 1793–1800. https://doi.org/10.1061/?ASCE?0733-9445?2006?132:11?1793?

———. 2007. "Experimental Investigation of Composite Concrete and Conventional Concrete Members." *ACI Structural Journal*, no. 104: 93–101. https://doi.org/10.14359/18437.

Haber, Zachary B., Igor De La Varga, and Benjamin A. Graybeal. 2018. "Properties and Behavior of UHPC-Class Materials."

Haber, Zachary B., Jose F. Munoz, I. De la Varga, and Benjamin A. Graybeal. 2018. "Ultra-High Performance Concrete for Bridge Deck Overlays."

Habert, G., Emmanuel Denarié, A. Šajna, and Pierre Rossi. 2013. "Lowering the Global Warming Impact of Bridge Rehabilitations by Using Ultra High Performance Fibre Reinforced Concretes." *Cement and Concrete Composites* 38: 1–11. https://doi.org/10.1016/J.CEMCONCOMP.2012.11.008.

IPQ. 2010. *Eurocódigo 2-Projecto de Estruturas de Betão, Parte 1-1: Regras Gerais e Regras Para Edifícios*. Lisboa: IPQ.

JSCE. 2008. *Recommendations for Design and Construction of High Performance Fiber Reinforced Cement Composites with Multiple Fine Cracks (HPFRCC).*

Kang, Su Tae, and Jin Keun Kim. 2011. "The Relation between Fiber Orientation and Tensile Behavior in an Ultra High Performance Fiber Reinforced Cementitious Composites (UHPFRCC)." *Cement and Concrete Research* 41 (10): 1001–14. https://doi.org/10.1016/j.cemconres.2011.05.009.

King, Suzanne, and Norbert J. Delatte. 2004. "Collapse of 2000 Commonwealth Avenue: Punching Shear Case Study." *Journal of Performance of Constructed Facilities* 18 (1): 54–61. https://doi.org/10.1061/(asce)0887-3828(2004)18:1(54).

Kolisko, Jiri, David Citek, Petr Tej, and Milan Rydval. 2017. "Production of Footbridge with Double Curvature Made of UHPC." *Mater. Sci. Eng* 246. https://doi.org/10.1088/1757-899X/246/1/012009.

Koppitz, Robert, Albin Kenel, and Thomas Keller. 2013. "Punching Shear of RC Flat Slabs – Review of Analytical Models for New and Strengthening of Existing Slabs." *Engineering Structures* 52: 123–30. https://doi.org/10.1016/J.ENGSTRUCT.2013.02.014.

———. 2015. “Effect of Load History on Punching Shear Resistance of Flat Slabs.” *Engineering Structures* 90: 130–42. https://doi.org/10.1016/j.engstruct.2015.02.016.

Krenchel, H. 1975. “Fibre Spacing and Specific Fibre Surface.” *Fibre Reinforced Cement and Concrete: RILEM Symposium*.

Kwon, Sukmin, Tomoya Nishiwaki, Takatsune Kikuta, and Hirozo Mihashi. 2014. “Development of Ultra-High-Performance Hybrid Fiber-Reinforced Cement-Based Composites.” *ACI Materials Journal* 111 (3): 309–18. https://doi.org/10.14359/51686890.

Lapi, Massimo, Hugo Fernandes, Maurizio Orlando, António Ramos, and Válter Lúcio. 2018a. “Performance Assessment of Flat Slabs Strengthened with a Bonded Reinforced-Concrete Overlay.” *Magazine of Concrete Research* 70 (9): 433–51. https://doi.org/10.1680/jmacr.17.00037.

Lapi, Massimo, Hugo Fernandes, Maurizio Orlando, António Pinho Ramos, and Válter Lúcio. 2018b. “Performance Assessment of Flat Slabs Strengthened with a Bonded Reinforced Concrete Overlay.” *Magazine of Concrete Research* 70 (9): 433–51. https://doi.org/doi.org/10.1680/jmacr.17.00037.

Lapi, Massimo, António Pinho Ramos, and Maurizio Orlando. 2019. “Flat Slab Strengthening Techniques against Punching-Shear.” *Engineering Structures* 180: 160–80. https://doi.org/10.1016/j.engstruct.2018.11.033.

Laranjeira, F., A. Aguado, C. Molins, S. Grünewald, J. Walraven, and S. Cavalaro. 2012. “Framework to Predict the Orientation of Fibers in FRC: A Novel Philosophy.” *Cement and Concrete Research* 42 (6): 752–68. https://doi.org/10.1016/j.cemconres.2012.02.013.

Lataste, J. F., M. Behloul, and D. Breysse. 2008. “Characterisation of Fibres Distribution in a Steel Fibre Reinforced Concrete with Electrical Resistivity Measurements.” *NDT and E International* 41 (8): 638–47. https://doi.org/10.1016/j.ndteint.2008.03.008.

Leutbecher, Torsten, and Ekkehard Fehling. 2012. “Tensile Behavior of Ultra-High-Performance Concrete Reinforced with Reinforcing Bars and Fibers: Minimizing Fiber Content.” *ACI Structural Journal* 109 (2): 253–64. https://doi.org/10.14359/51683636.

Lew, H. S., N. J. Carino, S.G. Fattal, and M. E. Batts. 1982. “Investigation of Construction Failure of Harbour Cay Condominium in Cocoa.” Washington, DC. https://doi.org/10.6028/NBS.BSS.145.

Li, Lufan, Jun Xia, Chee Chin, and Steve Jones. 2020. “Fibre Distribution Characterization of Ultra-High Performance Fibre-Reinforced Concrete (Uhpfrc) Plates Using Magnetic Probes.” *Materials* 13 (22): 1–20. https://doi.org/10.3390/ma13225064.

Lopez, Juan Angel, Hugo Coll, Pedro Serna, and Fernando Galán. 2016. "The UHPFRC Pedestrian Bridge above the V-21 Highway in Puzol, Valencia: Design, Construction and Cost." *4th International Symposium on Ultra-High Performance Concrete and High Performance Materials*.

López, Juan Ángel, Pedro Serna, Juan Navarro-Gregori, and Esteban Camacho. 2015. "An Inverse Analysis Method Based on Deflection to Curvature Transformation to Determine the Tensile Properties of UHPFRC." *Materials and Structures* 48 (11): 3703–18. https://doi.org/10.1617/s11527-014-0434-0.

Lu, Cong, and Christopher K.Y. Leung. 2017. "Theoretical Evaluation of Fiber Orientation and Its Effects on Mechanical Properties in Engineered Cementitious Composites (ECC) with Various Thicknesses." *Cement and Concrete Research* 95: 240–46. https://doi.org/10.1016/j.cemconres.2017.02.024.

Lúcio, Válter, António Ramos, and Duarte Faria. 2008. "Reforço de Lajes Fungiformes-Anomalias, Causas e Soluções." In *SILE2008-Seminário Internacional Sobre Ligações Estruturais*, 51–72. Lisboa. https://doi.org/DOI: 10.13140/2.1.4059.1369.

Markovic, Ivan. 2006. "High-Performance Hybrid-Fibre Concrete - Development and Utilisation." Technische Universiteit Delft.

Martinie, L., and Nicolas Roussel. 2011. "Simple Tools for Fiber Orientation Prediction in Industrial Practice." *Cement and Concrete Research* 41 (10): 993–1000. https://doi.org/10.1016/J.CEMCONRES.2011.05.008.

Martinie, Laetitia, Jean François Lataste, and Nicolas Roussel. 2015. "Fiber Orientation during Casting of UHPFRC: Electrical Resistivity Measurements, Image Analysis and Numerical Simulations." *Materials and Structures/Materiaux et Constructions* 48 (4): 947–57. https://doi.org/10.1617/s11527-013-0205-3.

Matos, Ana Mafalda, Sandra Nunes, and José L. Barroso Aguiar. 2019. "Capillary Transport of Water in Cracked and Non-Cracked UHPFRC Specimens." *Journal of Advanced Concrete Technology* 17 (5): 244–59. https://doi.org/10.3151/jact.17.244.

Matos, Ana Mafalda, Sandra Nunes, Carla Costa, and José L. Barroso-Aguiar. 2019. "Spent Equilibrium Catalyst as Internal Curing Agent in UHPFRC." *Cement and Concrete Composites* 104. https://doi.org/10.1016/j.cemconcomp.2019.103362.

Matthews, Stuart. 2021. "MC2020: Fib Model Code for Concrete Structures-Advances in Design and Life-Cycle Management." In *Fib Symposium*. Lisbon.

MCS-EPFL. 2021. "UHPFRC Map Switzerland." 2021. https://www.epfl.ch/labs/mcs/mcs-laboratory-for-maintenance-and-safety-of-structures/uhpfrc-map-switzerland/.

Meda, Alberto, Serena Mostosi, and Paolo Riva. 2014. "Shear Strengthening of Reinforced Concrete Beam with High-Performance Fiber-Reinforced Cementitious Composite Jacketing." *ACI Structural Journal* 111 (5): 1059–68.

https://doi.org/10.14359/51686807.

Muttoni, Aurelio. 2008. “Punching Shear Strength of Reinforced Concrete Slabs without Transverse Reinforcement.” *ACI Structural Journal* 105 (4): 440–50.

Muttoni, Aurelio, and Miguel Fernández Ruiz. 2008. “Shear Strength of Members without Transverse Reinforcement as Function of Critical Shear Crack Width.” *ACI Structural Journal* 105 (2): 163–72.

Muttoni, Aurelio, and Miguel Fernández Ruiz. 2012. “The Levels-of-Approximation Approach in MC 2010: Application to Punching Shear Provisions.” *Structural Concrete* 13 (1): 32–41. https://doi.org/10.1002/suco.201100032.

Naaman, Antoine E. 1972. “A Statistical Theory of Strength for Fiber Reinforced Concrete.” Massachusetts Institute of Technology.

———. 2008. “High Performance Fiber Reinforced Composites.” In *High-Performance Construction Materials: Science and Applications*, edited by Caijun Shi and Y L Mo, 91–153. World Scientific Publishing Co. Pte. Ltd.

Naaman, Antoine E., and Kay Wille. 2012. “The Path to Ultra-High Performance Fiber Reinforced Concrete (UHP-FRC): Five Decades of Progress.” In *Proceedings of HiperMat 2012 (Kassel, March 7-9, 2012)*, 3–15.

Nemati, Kamran M., and Piet Stroeven. 2001. “Stereological Analysis of Micromechanical Behavior of Concrete.” *Materials and Structures/Mat~riaux et Constructions*. Vol. 34.

Nguyen, Duy Liem, Dong Joo Kim, Gum Sung Ryu, and Kyung Taek Koh. 2013. “Size Effect on Flexural Behavior of Ultra-High-Performance Hybrid Fiber-Reinforced Concrete.” *Composites Part B: Engineering* 45 (1): 1104–16. https://doi.org/10.1016/j.compositesb.2012.07.012.

Nhumaio, Fulgêncio. 2015. “Inspecção Patológica, Avaliação Da Segurança Estrutural e Reforço de Um Edifício Em Estrutura de Betão Armado de Lajes Fungiformes Maciças.” Universidade Eduardo Mondlane.

Noshiravani, Talayeh. 2012. “Structural Response of R-UHPFRC – RC Composite Members Subjected to Combined Bending and Shear.” École Polytechnique Fédérale de Lausanne.

Noshiravani, Talayeh, and Eugen Brühwiler. 2013a. “Experimental Investigation on Reinforced Ultra-High- Performance Fiber-Reinforced Concrete Composite Beams Subjected to Combined Bending and Shear.” *ACI Structural Journal* 110 (2): 251–61.

———. 2013b. “Rotation Capacity and Stress Redistribution Ability of R-UHPFRC-RC Composite Continuous Beams: An Experimental Investigation.” *Materials and Structures/Materiaux et Constructions* 46 (12): 2013–28.

https://doi.org/10.1617/s11527-013-0033-5.

———. 2014. “Analytical Model for Predicting Response and Flexure-Shear Resistance of Composite Beams Combining Reinforced Ultrahigh Performance Fiber-Reinforced Concrete and Reinforced Concrete.” *Journal of Structural Engineering*. https://doi.org/10.1061/(ASCE)ST.1943-541X.0000902.

Nunes, Sandra, Helena Figueiras, Joaquim Figueiras, Joana Sousa Coutinho, Rui Faria, Mário Pimentel, João Rio, Diogo Azevedo, and Filipe Ribeiro. 2012. “PTDC/ECM/122446/2010 Betofibra-Betões de Elevado Desempenho Reforçado Com Fibras Em Soluções Inovadoras: Concepção, Caracterização e Controlo de Qualidade-Parte 2 - Formulação, Otimização Da Composição e Ensaios de Caracterização à Tração.” Porto.

Nunes, Sandra, and Mário Pimentel. 2016. “PTDC/ECM/122446/2010: Characterization and Comparison of Two Magnetic Probes.” Porto.

Nunes, Sandra, Mário Pimentel, and Adriano Carvalho. 2016a. “Non-Destructive Assessment of Fibre Content and Orientation in UHPFRC Layers Based on a Magnetic Method.” *Cement and Concrete Composites* 72: 66–79. https://doi.org/10.1016/j.cemconcomp.2016.05.024.

———. 2016b. “Non-Destructive Assessment of Fibre Content and Orientation in UHPFRC Reinforcement Layers.” In *Proceedings of 4th International Symposium on Ultra-High Performance Concrete and High Performance Materials (HiPerMat)*, edited by Ekkehard Fehling, Bernhard Middendorf, and Jenny Thiemicke. Kassel, Germany.

Nunes, Sandra, Mário Pimentel, Filipe Ribeiro, P. Milheiro-Oliveira, and Adriano Carvalho. 2017. “Estimation of the Tensile Strength of UHPFRC Layers Based on Non-Destructive Assessment of the Fibre Content and Orientation.” *Cement and Concrete Composites* 83: 222–38. https://doi.org/10.1016/j.cemconcomp.2017.07.019.

Oesterlee, Cornelius. 2010. “Structural Response of Reinforced UHPFRC and RC Composite Members.” École Polytechnique Fédérale de Lausanne.

Park, Seung Hun, Dong Joo Kim, Gum Sung Ryu, and Kyung Taek Koh. 2012. “Tensile Behavior of Ultra High Performance Hybrid Fiber Reinforced Concrete.” *Cement and Concrete Composites* 34: 172–84. https://doi.org/10.1016/j.cemconcomp.2011.09.009.

Perry, Vic H., and Katrin Habel. 2017. “Standardization of Ultra-High Performance Concrete the Canadian Pespective.” In *AFGC-ACI-Fib-RILEM Int. Symposium on Ultra-High Performance Fibre-Reinforced Concrete*, 555–64. Montpellier.

Perry, Vic H., and Royce P. E. Mathew. 2010. “INNOVATIVE FIELD-CAST UHPC JOINTS FOR PRECAST BRIDGE DECKS (SIDE-BY-SIDE DECK BULB-TEES), VILLAGE OF LYONS, NEW YORK: DESIGN, PROTOTYPING,

TESTING AND CONSTRUCTION." In *3rd Fib International Congress*, 13.

Perry, Vic H., and Peter J. Seibert. 2013. "FIFTEEN YEARS OF UHPC CONSTRUCTION EXPERIENCE IN PRECAST BRIDGES IN NORTH AMERICA." In *RILEM-Fib-AFGC Int. Symposium on Ultra-High Performance Fibre-Reinforced Concrete*, 229–38. Marseille.

Perry, Vic H., Paul White, and Theresa M. Ahlborn. 2016. "The First North American Broad Based Structural Design Guide on UHPC – ACI 239C." In *First International Interactive Symposium on UHPC*.

Pimentel, Mário, and Sandra Nunes. 2016a. "Determination of the Fibre Content and Orientation in UHPFRC Layers Using NDT-Application to the Simulation of the Behaviour of Strengthened Beams." In *IABMAS 2016 - Proceedings of the 8th International Conference on Bridge Maintenance, Safety and Management*, 547–53. Foz do Iguaçu, Brazil. https://doi.org/10.1201/9781315207681-73.

———. 2016b. "Determination of the Tensile Response of UHPFRC Layers Using a Non-Destructive Method for Assessing the Fiber Content and Orientation." In *Proceedings of the 9th International Conference on Fracture Mechanics of Concrete and Concrete Structures*, edited by V. Saouma, J. Bolander, and E. Landis. Berkeley, California.

———. 2016c. "Experimental Tests on RC Beams Reinforced with a UHPFRC Layer Failing in Bending and Shear." In *Proceedings of 4th International Symposium on Ultra-High Performance Concrete and High Performance Materials (HiPerMat)*, edited by Ekkehard Fehling, Bernhard Middendorf, and Jenny Thiemicke. Kassel, Germany.

———. 2016d. "On the Double-Edge Wedge-Splitting Test for the Characterisation of HPFRC in Uniaxial Tension." In *Proceedings of 4th International Symposium on Ultra-High Performance Concrete and High Performance Materials (HiPerMat)*, edited by Ekkehard Fehling, Bernhard Middendorf, and Jenny Thiemicke. Kassel, Germany.

Pimentel, Mário, Aurélio Sine, Amin Abrishambaf, and Sandra Nunes. 2017. "Flexural Behaviour of Hybrid RC-UHPFRC Elements in the Context of Strengthening and Rehabilitation." In *2nd International Conference on Recent Advances in Nonlinear Models – Design and Rehabilitation of Structures - CoRASS 2017*, edited by Helena Barros, Carla Ferreira, M. José Adam, and Norb Delatte, 291–300. Coimbra. https://doi.org/978-989-96461-8-6.

Prisco, Marco di, Liberato Ferrara, and Marco G. L. Lamperti. 2010. "Double-Edge Wedge Splitting Test: Preliminary Results." *Fracture Mechanics of Concrete and Concrete Structures (FraMCoS-7)*, 1579–86.

———. 2013. "Double Edge Wedge Splitting (DEWS): An Indirect Tension Test to Identify Post-Cracking Behaviour of Fibre Reinforced Cementitious Composites." *Materials and Structures* 46 (11): 1893–1918. https://doi.org/10.1617/s11527-013-

0028-2.

Pyo, Sukhoon, Sherif El-Tawil, and Antoine E. Naaman. 2016. "Direct Tensile Behavior of Ultra High Performance Fiber Reinforced Concrete (UHP-FRC) at High Strain Rates." *Cement and Concrete Research* 88: 144–56. https://doi.org/10.1016/j.cemconres.2016.07.003.

Qian, Shunzhi, and Victor C Li. 2007. "Simplified Inverse Method for Determining the Tensile Strain Capacity of Strain Hardening Cementitious Composites." *Journal of Advanced Concrete Technology* 5 (2): 235–46.

Redaelli, Dario. 2009. "Comportement et Modélisation Des Éléments de Structure En Béton Fibré à Ultra-Hautes Performances Avec Armatures Passives." École Polytchnique Fédérale de Lausanne.

Richard, Pierre, and Marcel Cheyrezy. 1995. "COMPOSITION OF REACTIVE POWDER CONCRETES." *Cement and Concrete Research* 25 (7): 1501–11.

Rocha, Daphne Wojciechowki. 2012. "Flexural Strengthening By Means of a Rc Overlay in the Tension Zone." Universidade Nova de Lisboa.

Rossi, Pierre. 1997. "High Performance Multimodal Fiber Reinforced Cement Composite (HPMFRCC): The LCPC Experience." *ACI Materials Journal* 94 (6): 478–83.

Ruiz, Miguel Fernández, and Aurelio Muttoni. 2009. "Applications of Critical Shear Crack Theory to Punching of Reinforced Concrete Slabs with Transverse Reinforcement." *ACI Structural Journal* 106 (4): 485–94. https://doi.org/10.14359/56614.

Ruiz, Miguel Fernández, Aurelio Muttoni, and Jakob Kunz. 2011. "Strengthening of Flat Slabs against Punching Shear Using Post-Installed Shear Reinforcement." *ACI Structural Journal* 107 (4): 434–42.

Sadouki, Hamid, Emmanuel Denarié, and Eugen Brühwiler. 2017. "Validation of a FEA Model of Structural Response of RC-Cantilever Beams Strengthened with a (R-) UHPFRC Layer." *Construction and Building Materials* 140: 100–108. https://doi.org/10.1016/j.conbuildmat.2017.02.090.

Sagaseta, J., M. Fernández Ruiz, and A. Muttoni. 2009. "Non-Symmetrical Punching of Flat Slabs and Slab Bridges without Transverse Reinforcement." In *11th Annual International Fib Symposium - Concrete: 21st Century Superhero: Building a Sustainable Future*.

Sagaseta, J., L. Tassinari, M. Fernández Ruiz, and A. Muttoni. 2014. "Punching of Flat Slabs Supported on Rectangular Columns." *Engineering Structures* 77: 17–33. https://doi.org/10.1016/j.engstruct.2014.07.007.

Sagaseta, Juan, Aurelio Muttoni, Miguel Fernández Ruiz, and Luca Tassinari. 2011. "Non-Axis-Symmetrical Punching Shear around Internal Columns of RC Slabs

without Transverse Reinforcement." *Magazine of Concrete Research* 63 (6): 441–57. https://doi.org/10.1680/macr.10.00098.

SAMARIS D22. 2005. "Full Scale Application of UHPFRC for the Rehabilitation of Bridges, for the European Project 5th FWP/SAMARIS – Sustainable and Advanced Materials for Road Infrastructures – WP 14: HPFRCC. Report D22."

Shen, Xiujiang, and Eugen Brühwiler. 2020. "Influence of Local Fiber Distribution on Tensile Behavior of Strain Hardening UHPFRC Using NDT and DIC." *Cement and Concrete Research* 132. https://doi.org/10.1016/j.cemconres.2020.106042.

SIA. 2014. *PrSIA 2052:2014-04 Béton Fibré Ultra-Performant (BFUP)-Matériaux, Dimensionnement et Exécution*. Zurique.

———. 2016. *SIA 2052-2016: Béton Fibré Ultra-Performant (BFUP)-Matériaux, Dimensionnement et Exécution*. Suiça.

Sirieix, Colette, Jean François Lataste, Denys Breysse, Samuel Naar, and Xavier Dérobert. 2007. "Comparison of Nondestructive Testing: Infrared Thermography, Electrical Resisitivity and Capacity Methods for Assessing a Reinforced Concrete Structure." *Journal of Building Appraisal* 3 (1): 77–88. https://doi.org/10.1057/palgrave.jba.2950065.

Stähli, Patrick, Rocco Custer, and Jan G. M. van Mier. 2008. "On Flow Properties, Fibre Distribution, Fibre Orientation and Flexural Behaviour of FRC." *Materials and Structures* 41 (1): 189–96. https://doi.org/10.1617/s11527-007-9229-x.

Stähli, Patrick, and Jan G.M. van Mier. 2007. "Manufacturing, Fibre Anisotropy and Fracture of Hybrid Fibre Concrete." *Engineering Fracture Mechanics* 74 (1–2): 223–42. https://doi.org/10.1016/J.ENGFRACMECH.2006.01.028.

Stefan, Lips, Miguel Fernández Ruiz, and Aurelio Muttoni. 2012. "Experimental Investigation on Punching Strength and Deformation Capacity of Shear-Reinforced Slabs." *ACI Structural Journal Journal* 109 (6): 889–900.

Stroeven, Piet. 1986. "Stereology of Concrete Reinforced with Short Steel Fibres." *Heron* 31 (2).

———. 2009. "Stereological Principles of Spatial Modeling Applied to Steel Fiber-Reinforced Concrete in Tension" 106 (3): 213–22.

Stroeven, Piet, and J Hu. 2006. "Effectiveness near Boundaries of Fibre Reinforcement in Concrete." *Materials and Structures* 39: 1001–13. https://doi.org/10.1617/s11527-006-9101-4.

Torabian, Ala, Brisid Isufi, Davood Mostofinejad, and António Pinho Ramos. 2020. "Flexural Strengthening of Flat Slabs with FRP Composites Using EBR and EBROG Methods." *Engineering Structures* 211. https://doi.org/10.1016/j.engstruct.2020.110483.

Torrents, Josep M., Ana Blanco, Pablo Pujadas, Antonio Aguado, Pablo Juan-García, and Miguel Ángel Sánchez-Moragues. 2012. "Inductive Method for Assessing the Amount and Orientation of Steel Fibers in Concrete." *Materials and Structures* 45 (10): 1577–92. https://doi.org/10.1617/s11527-012-9858-6.

Trüb, Martin. 2011. "Numerical Modeling of High Performance Fiber Reinforced Cementitious Composites." Swiss Federal Institure of Technology.

UN. 2015. "THE 17 GOALS | Sustainable Development." 2015. https://sdgs.un.org/goals.

Valente, Rui, Mário Pimentel, and Sandra Nunes. 2021. "Tensile Response of Reinforced UHPFRC Elements." In *Fib Lisbon Symposium*, 4095–4504.

Vaz Rodrigues, Rui. 2007. "Shear Strength of Reinforced Concrete Bridge Deck Slabs." École polytechnique Fédérale de Lausanne.

Vecchio, Frank J., and Michael P. Collins. 1986. "The Modified Compression-Field Theory for Reinforced Concrete Elements Subjected to Shear." *ACI Journal*, 2019–2231.

Wille, Kay, Sherif El-Tawil, and Antoine E. Naaman. 2014. "Properties of Strain Hardening Ultra High Performance Fiber Reinforced Concrete (UHP-FRC) under Direct Tensile Loading." *Cement and Concrete Composites* 48: 53–66. https://doi.org/10.1016/j.cemconcomp.2013.12.015.

Wille, Kay, and Antoine E. Naaman. 2010. "Fracture Energy of UHP-FRC under Direct Tensile Loading." *Korea Concrete Institute*, 978–89.

Woo, L. Y., S. Wansom, N. Ozyurt, B. Mu, S. P. Shah, and T. O. Mason. 2005. "Characterizing Fiber Dispersion in Cement Composites Using AC-Impedance Spectroscopy." *Cement and Concrete Composites* 27 (6): 627–36. https://doi.org/10.1016/j.cemconcomp.2004.06.003.

Wood, Jonathan G. M. 2003. "Pipers Row Car Park Wolverhampton: Quantitative Study of the Causes of the Partial Collapse on 20th March 1997." *Health and Safety Executive*. The United Kingdom.

Wuest, John. 2007. "Comportement Structural Des Bétons de Fibres Ultra Performants En Traction Dans Des Éléments Composés." École Polytchnique Fédérale de Lausanne.

Youm, H S, and S G Hong. 2018. "Evaluation for Punching Shear Strength of Slab-Column Connections with Ultra High Performance Fiber-Reinforced Concrete Overlay." *International Journal of Structural and Construction Engineering* 12 (1): 56–61.

Zhou, Bo, and Yuichi Uchida. 2017a. "Influence of Flowability, Casting Time and Formwork Geometry on Fiber Orientation and Mechanical Properties of UHPFRC."

Cement and Concrete Research 95: 164–77. https://doi.org/10.1016/j.cemconres.2017.02.017.

———. 2017b. "Relationship between Fiber Orientation/Distribution and Post-Cracking Behaviour in Ultra-High-Performance Fiber-Reinforced Concrete (UHPFRC)." *Cement and Concrete Composites* 83: 66–75. https://doi.org/10.1016/j.cemconcomp.2017.07.007.